

**2D DIRECT CURRENT RESISTIVITY MODELING  
AND INVERSION WITH HYBRID FD-FE  
TECHNIQUE AND  
3D CONTROLLED-SOURCE ELECTROMAGNETIC  
MODELING AND INVERSION WITH  
SCATTERED-FIELD TECHNIQUE**

**CHATCHAI VACHIRATIENCHAI**

**A THESIS SUBMITTED IN PARTIAL FULFILLMENT  
OF THE REQUIREMENTS FOR  
THE DEGREE OF DOCTOR OF PHILOSOPHY  
(PHYSICS)  
FACULTY OF GRADUATE STUDIES  
MAHIDOL UNIVERSITY  
2013**

**COPYRIGHT OF MAHIDOL UNIVERSITY**

Thesis  
entitled

**2D DIRECT CURRENT RESISTIVITY MODELING  
AND INVERSION WITH HYBRID FD-FE  
TECHNIQUE AND  
3D CONTROLLED-SOURCE ELECTROMAGNETIC  
MODELING AND INVERSION WITH  
SCATTERED-FIELD TECHNIQUE**

.....  
Mr. Chatchai Vachiratienchai  
Candidate

.....  
Assoc. Prof. Weerachai Siripunvaraporn,  
Ph.D. (Geophysics)  
Major advisor

.....  
Asst. Prof. Phichet Kittara,  
Ph.D. (Astrophysics)  
Co-advisor

.....  
Lect. Withoon Chunwachirasiri,  
Ph.D. (Physics)  
Co-advisor

.....  
Prof. Banchong Mahaisavariya,  
M.D., Dip Thai Board of Orthopedics  
Dean  
Faculty of Graduate Studies  
Mahidol University

.....  
Asst. Prof. Narin Nuttavut,  
Ph.D. (Applied Optics)  
Program Director  
Doctor of Philosophy Program  
in Physics  
Faculty of Science  
Mahidol University

Thesis  
entitled  
**2D DIRECT CURRENT RESISTIVITY MODELING  
AND INVERSION WITH HYBRID FD-FE  
TECHNIQUE AND  
3D CONTROLLED-SOURCE ELECTROMAGNETIC  
MODELING AND INVERSION WITH  
SCATTERED-FIELD TECHNIQUE**

was submitted to the Faculty of Graduate Studies, Mahidol University  
for the degree of Doctor of Philosophy (Physics)

on  
March 18, 2013

.....  
Mr. Chatchai Vachiratienchai  
Candidate

.....  
Lect. Siriporn Chaisri,  
Ph.D. (Geophysics)  
Chair

.....  
Assoc. Prof. Weerachai Siripunvaraporn,  
Ph.D. (Geophysics)  
Member

.....  
Lect. Withoon Chunwachirasiri,  
Ph.D. (Physics)  
Member

.....  
Asst. Prof. Phichet Kittara,  
Ph.D. (Astrophysics)  
Member

.....  
Prof. Banchong Mahaisavariya,  
M.D., Dip Thai Board of Orthopedics  
Dean  
Faculty of Graduate Studies  
Mahidol University

.....  
Prof. Skorn Mongkolsuk,  
Ph.D.  
Dean  
Faculty of Science  
Mahidol University

## ACKNOWLEDGEMENTS

I would like to express my gratitude to my advisor, Assoc. Prof. Weerachai Siripunvarporn, for his kindness, patience and suggestion. I also would like to express my gratitude to Prof. Gary Egbert for his suggestions. I am also highly grateful to Dr. Phichet Kittara, Dr. Withoon Chunwachirasiri and Dr. Siriporn Chaisri for their invaluable comments to improve this thesis. I gratefully acknowledge Royal Golden Jubilee (RGJ) scholarship for financial support through my study. I also thank the staffs in the Department of Physics, particularly Miss Nipaporn Suwannawong.

I greatly appreciate L<sup>A</sup>T<sub>E</sub>X class file by Asst. Prof. Michael Allen and also thank Tawat Rung-Arunwan for his suggestions about L<sup>A</sup>T<sub>E</sub>X

For much help and encouragement, I would like to thank the members of Geophysics Research Unit, Mahidol university, Puwis Amatyakul, Songkhun Boonchaisuk, Weerachai Sarakorn, Suntaree Unhapipat, Ananya Satitpitakul, Patchawee Nualkhow and all of the undergrad students.

And I thank my family for their kind support. The thesis is dedicated to my dad. THANK YOU ALL.

Chatchai Vachiratienchai

2D DIRECT CURRENT RESISTIVITY MODELING AND INVERSION WITH HYBRID FD-FE TECHNIQUE AND 3D CONTROLLED-SOURCE ELECTROMAGNETIC MODELING AND INVERSION WITH SCATTERED-FIELD TECHNIQUE.

CHATCHAI VACHIRATIENCHAI 5137842 SCPY/D

Ph.D. (PHYSICS)

THESIS ADVISORY COMMITTEE : WEERACHAI SIRIPUNVARAPORN, Ph.D. (GEOPHYSICS), PHICHET KITTARA, Ph.D. (ASTROPHYSICS), WITHOON CHUNWACHIRASIRI, Ph.D. (PHYSICS)

#### ABSTRACT

Both direct current resistivity (DCR) and controlled-source electromagnetic (CSEM) surveys are used for measuring resistivity variation of the subsurface. The goal of this research was to develop modeling and inversion programs for 2D DC resistivity surveys and also the 3D CSEM modeling that can be used inside the existing ModEM program. For 2-D DCR modeling, we developed a hybrid finite difference (FD) - finite element (FE) method. The technique was most efficient in both CPU time and memory when the surface elevation is incorporated into the survey. For inversion, we implemented our 2-D hybrid FD-FE method for the sensitivity calculation. The inversion algorithm was based on the data-space Occam's inversion. Both hybrid and data-space results in an efficient inversion program that can be used with topography. For CSEM modeling, the modeling is based on the scattered-field technique. Its accuracy greatly depends on the grid discretization. ModEM is a modular electromagnetic inversion system developed under a general mathematical framework for solving the EM inverse problem. Here, we implemented our CSEM modeling into the ModEM code. Our preliminary results showed that a 3-D CSEM is still not practical and requires further investigation.

KEY WORDS : HYBRID FD-FE TECHNIQUE / DCR SURVEY /  
SCATTERED-FIELD TECHNIQUE / CSEM SURVEY /  
MODEM / MODELING / INVERSION

128 pages

การแก้ปัญหาไปข้างหน้าและย้อนกลับในสองมิติของข้อมูลจากการสำรวจไฟฟ้ากระแสตรงโดยใช้เทคนิคลูกผสมระหว่างไฟไนต์ดิฟเฟอเรนซ์และไฟไนต์เอลิเมนต์และการแก้ปัญหาไปข้างหน้าและย้อนกลับในสามมิติของข้อมูลจากการสำรวจคลื่นแม่เหล็กไฟฟ้าชนิดควบคุมแหล่งกำเนิดโดยใช้เทคนิคคลื่นกระเจิง

2D DIRECT CURRENT RESISTIVITY MODELING AND INVERSION WITH HYBRID FD-FE TECHNIQUE AND 3D CONTROLLED-SOURCE ELECTROMAGNETIC MODELING AND INVERSION WITH SCATTERED-FIELD TECHNIQUE

นัตรชัย วชิระธีรชัย 5137842 SCPY/D

ปร.ด. (ฟิสิกส์)

คณะกรรมการที่ปรึกษาวิทยานิพนธ์ : วีระชัย สิริพันธ์วรารณ, Ph.D. (GEOPHYSICS), พิเชษฐ กิจธารา, Ph.D. (ASTROPHYSICS), วิฑูร ชื่นวชิรศิริ, Ph.D. (PHYSICS)

#### บทคัดย่อ

การสำรวจไฟฟ้ากระแสตรงและการสำรวจคลื่นแม่เหล็กไฟฟ้าชนิดควบคุมแหล่งกำเนิดถูกนำมาใช้ศึกษาสภาพต้านทานไฟฟ้าใต้ดินเป้าหมายของงานวิจัยชิ้นนี้คือทำการพัฒนาการแก้ปัญหาไปข้างหน้าและย้อนกลับในสองมิติของการสำรวจไฟฟ้ากระแสตรง และ ในสามมิติของการสำรวจคลื่นแม่เหล็กไฟฟ้าชนิดควบคุมแหล่งกำเนิดที่สามารถนำไปใช้กับโปรแกรมมอดีเอ็มสำหรับสำรวจไฟฟ้ากระแสตรงเทคนิคลูกผสมระหว่างไฟไนต์ดิฟเฟอเรนซ์และไฟไนต์เอลิเมนต์ ซึ่งทำงานได้อย่างมีประสิทธิภาพเมื่อสภาพพื้นผิวมีการเปลี่ยนแปลง ในการแก้ปัญหาย้อนกลับเราทำการพัฒนาส่วนคำนวณความว่องไวโดยใช้เทคนิคลูกผสม ระบบการคำนวณย้อนกลับพัฒนาตามแบบออกแคมภายใต้ปฏิกิริยาข้อมูล และการคำนวณแบบลูกผสม โปรแกรมคำนวณที่ได้มีประสิทธิภาพในสภาพพื้นผิวมีการยกระดับ สำหรับการคำนวณไปข้างหน้าของการสำรวจคลื่นแม่เหล็กไฟฟ้าได้ถูกพัฒนาภายใต้เทคนิคคลื่นกระเจิง ซึ่งความแม่นยำนั้นขึ้นกับวิธีการแบ่งตาราง มอดีเอ็มเป็นระบบการคำนวณแบบแยกส่วนของการคำนวณย้อนกลับสำหรับข้อมูลแม่เหล็กไฟฟ้าซึ่งถูกพัฒนาขึ้นภายใต้โครงสร้างทั่วไป สำหรับการแก้ปัญหาย้อนกลับของข้อมูลคลื่นแม่เหล็กไฟฟ้าในที่นี้เราทำการพัฒนาการแก้ปัญหาไปข้างหน้าและนำไปใช้กับมอดีเอ็ม ผลที่ได้ในขั้นต้นนั้นพบว่าโปรแกรมยังต้องการพัฒนาเพิ่มเติม

# CONTENTS

	<b>Page</b>
<b>ACKNOWLEDGEMENTS</b>	<b>iii</b>
<b>ABSTRACT (ENGLISH)</b>	<b>iv</b>
<b>ABSTRACT (THAI)</b>	<b>v</b>
<b>LIST OF TABLES</b>	<b>viii</b>
<b>LIST OF FIGURES</b>	<b>x</b>
<b>CHAPTER I Introduction</b>	<b>1</b>
1.1 Introduction	1
1.2 Scope of Study	5
1.3 Thesis Outline	5
<b>CHAPTER II An Efficient 2-D DC Resistivity Inversion</b>	<b>6</b>
2.1 Fundamentals of DCR Surveys	6
2.2 DCR Field Procedure and Data Plotting	12
2.3 2D DC Resistivity Modeling	16
2.3.1 Governing Equation	17
2.3.2 Finite Difference Method	18
2.3.3 Finite Element Method	24
2.3.4 Wavenumber $k_y$ selection	31
2.3.5 Accuracy Tests for Wavenumber Selection	34
2.3.6 Validation and Numerical comparisons I	34
2.3.7 Validation and Numerical comparisons II	42
2.3.8 A hybrid finite difference and finite element method	46

## CONTENTS (cont.)

	Page
2.3.9 Topographic gradient limitation	52
2.4 2D DC Resistivity Inversion	53
2.4.1 Occam's inversion	55
2.4.2 Inversion Parameters	57
2.4.3 Lagrange multiplier $\lambda^{-1}$	67
2.4.4 Synthetic Test	68
2.4.5 Real Case Test	74
2.5 Conclusion	79
<b>CHAPTER III Controlled-Source Electromagnetic Inversion</b>	<b>81</b>
3.1 Controlled-Source Electromagnetic Surveys	81
3.1.1 CSEM Sounding	82
3.1.2 2-D and 3-D CSEM imagings	90
3.2 3D CSEM modeling and Inversion	91
3.3 Maxwell's Equations and the Governing Equations	92
3.4 Staggered Grid	94
3.5 ModEM	95
3.6 NLCG inversion	100
3.7 Adapting ModEM to CSEM	102
3.8 Synthetic Test	102
3.8.1 Forward Modeling	103
3.8.2 Inversion	107
3.9 Conclusion	108



**CONTENTS (cont.)**

	<b>Page</b>
<b>REFERENCES</b>	<b>117</b>
<b>BIOGRAPHY</b>	<b>128</b>

## LIST OF TABLES

	Page
1.1 Resistivity (in $\Omega\text{m}$ ) for water-bearing rocks of various types. . . . .	1
2.1 The eight wavenumbers set and their weighting parameters $g$ supporting distances from 1.0-30.0 meters . . . . .	34
2.2 Vertical grid is used in the synthetic tests. . . . .	42
2.3 The relative error [%] defined as $(1/N) \sum_{i=1}^N ( \rho_a^{\text{cal}} - \rho_a^{\text{true}} ) / \rho_a^{\text{true}}$ , where $\rho_a^{\text{true}}$ is true apparent resistivity from the analytical formula (model A and B), and from the RES2DMOD program (model C), $\rho_a^{\text{cal}}$ is the apparent resistivity calculated from FD, or FE methods with 2-, 3- and 4-horizontal blocks between a pair of electrodes. Model A, B and C are shown in figure 2.21a-c, respectively. . . . .	43
2.4 The percentage accuracy difference and CPU time for all three arrays for testing the FD and FE forward modeling schemes. . . . .	46
2.5 The memory usage for all three arrays for testing the FD and FE forward modeling schemes. . . . .	46
2.6 The relative error [%] defined as $(1/N) \sum_{i=1}^N ( \rho_a^{\text{cal}} - \rho_a^{\text{true}} ) / \rho_a^{\text{true}}$ , where $\rho_a^{\text{true}}$ is the true apparent resistivity from analytical formula (model A and B), and from RES2DMOD program (model C), $\rho_a^{\text{cal}}$ is the apparent resistivity calculated from FD, FE, or HB methods with 2-, 3- and 4-horizontal blocks between a pair of electrodes. Models A, B and C are shown in figure 2.21a-c, respectively. . . . .	50
2.7 The percentage accuracy difference and CPU time for all three arrays for testing the three different forward modeling schemes. . . . .	51
2.8 The memory usage for all three arrays for testing the three different forward modeling schemes. . . . .	51
2.9 Summary of the number of grid between a pair of electrodes that makes the average error less than 1% for each $\theta$ . . . . .	54

## LIST OF TABLES (cont.)

	Page
2.10 The data-misfit and memory usage for FD, FE and HB inversions for three common arrays. . . . .	71
2.11 The descriptions of the inversions for line 1 and line 2 of the real surveys by Occam's inversen for both full Jacobian calculation (FJC) and Broyden's update (BU) and the commercial RES2DINV code. After the 21st iteration, RES2DINV was terminated as the change in the model was relatively small. . . . .	78
3.1 The 1-D resistivity model corresponding to the synthetic model (figure 3.15). . . . .	104
3.2 The number of grid in $x$ or $y$ direction, the total number of model parameter and its calculation time for evaluating sounding curve for the synthetic model (figure 3.15). . . . .	105
3.3 The minimum offset of which its relative error is less than 1%. <b>Ex</b> is the inline electric field of which the sounding curves are represented in figure 3.16 for amplitude and figure 3.17 for phase. <b>By</b> is broadside magnetic field of which sounding curves are represented in figure 3.18 for amplitude and figure 3.19 for phase. . . . .	106
3.4 The minimum offset for which its relative error is less than 2%. <b>Ex</b> is inline electric field of which the sounding curves are represented in figure 3.16 for amplitude and figure 3.17 for phase. <b>By</b> is broadside magnetic field of which sounding curves are represented in figure 3.18 for amplitude and figure 3.19 for phase. . . . .	106

## LIST OF FIGURES

	Page
1.1 A schematic diagram of direct current resistivity survey. <b>A</b> and <b>B</b> represent positive and negative current electrodes. <b>M</b> and <b>N</b> represent a pair of potential electrodes. . . . .	3
1.2 The apparent resistivity of 600 $\Omega\text{m}$ half-space, sinusoidal topography model (Figure 1.3). . . . .	3
1.3 The 600 $\Omega\text{m}$ half-space model with sinusoidal topography. . . . .	4
1.4 (a) A 2D seismic section. Several channel systems can be extracted from the seismic data and represent potential hydrocarbon-filled structures. The prospect marked with a green circle is the largest and a well target. (b) Adding resistivity information to the seismic data using CSEM technology shows that only the two shallower targets are filled with hydrocarbons (Hesthammer <i>et al.</i> , 2010). . . . .	4
2.1 Hemisphere pattern of electric potential when current is injected into homogeneous structure. . . . .	7
2.2 shows a four-electrode DCR measurement. Current electrodes are labeled by <b>A</b> and <b>B</b> , and potential electrodes are labeled by <b>M</b> and <b>N</b> . . . . .	8
2.3 Four arrays are illustrated (a) Wenner, (b) Schlumberger, (c) Dipole-Dipole, and (d) Pole-Pole array where $a$ is electrode spacing, $n$ is the investigation level, and $x$ is distance to “infinite-electrodes” in Pole-Pole array. . . . .	9
2.4 relative effect of a thin resistive layer bed in homogeneous earth for Wenner, Schlumberger and Dipole-Dipole arrays (Milsom, 2003). . . . .	11
2.5 The example of resistivity sounding or VEF: (a) illustrates the two-layer models which is 100 $\Omega\text{-m}$ and 30 m thick and is overlaid on 10 $\Omega\text{-m}$ uniform media and (b) sounding curve of the two-layers model. The y-axis is the apparent resistivity value and the x-axis is half of the distance between electrode <b>A</b> and <b>B</b> . . . . .	13

## LIST OF FIGURES (cont.)

	Page
2.6 The example of resistivity profiling: (a) illustrates the vertical-contact models which has 10 $\Omega$ -m uniform media on the left hand side of the model and 1,000 $\Omega$ -m uniform media on the right hand side of model and (b) profiling curve of the vertical-contact model. The y-axis is the apparent resistivity value and the x-axis is the central position of the array.	13
2.7 Pseudo section plotting for Wenner array. Each dot represents a datum.	14
2.8 A example of resistivity imaging: (a) illustrates the one-block models which has a 1 $\Omega$ -m conductive block buried in 100 $\Omega$ -m homogeneous media, (b), (c), and (d) illustrate pseudo sections for Wenner, Schlumberger and Dipole-Dipole arrays, representatively. . . . .	15
2.9 shows the rectangular grid and the discretized area $\Delta A_{i,j}$ around node $(i, j)$ . . . . .	18
2.10 the sparsity pattern of the capacitance matrix $\mathbf{C}$ . . . . .	24
2.11 shows (a) “left-slope” triangular element and (b) “right-slope” triangular element. . . . .	25
2.12 an example of the problem domain divided by “left-slope” triangular elements. . . . .	25
2.13 an example of the problem domain divided by “right-slope” triangular elements. . . . .	26
2.14 an example of the problem domain divided by a mix of “left-slope” and “right-slope” triangular elements that produces a maximum node connection. . . . .	26
2.15 an example of the problem domain divided by a mix of “left-slope” and “right-slope” triangular elements that produces a minimum connection.	27
2.16 shows an example of triangular element. . . . .	27
2.17 the sparsity pattern of the stiffness matrix $\mathbf{K}$ when the problem domain is discretized by “left-slope” triangular element. The sparsity pattern of $\mathbf{K}_k$ is close to the sparsity pattern of $\mathbf{C}$ except that has two extra bands (gray) which correspond to the top-left and bottom-right nodes. . . . .	32

## LIST OF FIGURES (cont.)

	Page
2.18 The relative error of $\nu$ for distance $\tilde{r}$ from 1.0-40.0 meters. . . . .	35
2.19 A schematic diagram of the general two-layers model. . . . .	35
2.20 The five situations of four electrodes spread over a vertical contact. The first one is “all electrodes on the left-hand side”, the second one is “electrode <b>B</b> ” on the right-hand side, the third one is “electrode <b>B</b> and <b>N</b> on the right-hand side”, the fourth one is “electrode <b>B</b> , <b>M</b> and <b>N</b> on the right-hand side” and the last one is “all electrodes on the right-hand side”. . . . .	37
2.21 Non-topography models used to validate FD, FE and our hybrid methods. (a) Model A: wet soil (10 $\Omega\text{m}$ ) lying on top of a resistive limestone (1000 $\Omega\text{m}$ ). (b) Model B: two different rocks with a vertical boundary. The left side is conductive (1 $\Omega\text{m}$ ) and the right side is resistive (1000 $\Omega\text{m}$ ). (c) Model C: two different anomalies buried in a 100 $\Omega\text{m}$ half-space. The left and right anomalies are 1 $\Omega\text{m}$ and 1000 $\Omega\text{m}$ , respectively. Forty-eight electrodes are deployed at the surface with 1-m spacing for all models. Integers indicate the electrode number. . . . .	39
2.22 Pseudo-sections of model A (figure 2.21a) for (a) Wenner, (b) Schlumberger, and (c) Dipole-Dipole arrays. . . . .	40
2.23 Pseudo-sections of model B (figure 2.21b) for (a) Wenner, (b) Schlumberger, and (c) Dipole-Dipole arrays. . . . .	40
2.24 Pseudo-sections of model C (figure 2.21c) for (a) Wenner, (b) Schlumberger, and (c) Dipole-Dipole arrays. . . . .	41
2.25 The extreme topography model with two steep hills and high contrast resistivity structures beneath. The white region is an air-filled cavity. . . . .	44
2.26 The pseudo-section of the extreme topography model for the Wenner array computed by the (a) FD method and (b) FE method. . . . .	44
2.27 The pseudo-section of the extreme topography model for a Schlumberger array computed by the (a) FD method and (b) FE method. . . . .	45
2.28 The pseudo-section of the extreme topography model for a Dipole-Dipole array computed by the (a) FD method and (b) FE method. . . . .	45

## LIST OF FIGURES (cont.)

	Page
2.29 Contour plots of electrical potentials calculated from (a) FD method, (b) FE method and (c) their difference. Both are generated from the same pair of injecting current electrodes and the same boundary conditions. Notice that the maximum differences are in the order of $10^{-3}$ . . . . .	48
2.30 Examples of mixed FD and FE grids for our hybrid FD – FE method for (a) left-slope model, (b) right-slope model, (c) ridge model and (d) valley model. Solid white circles are FE nodes. Black circles are FD nodes. Topography is denoted by black solid lines. . . . .	49
2.31 Grid discretization for the hybrid FD-FE method. The slope areas are discretized with FE (white nodes) and the others with FD (black nodes). Number of elements is given at the center of the rectangular or triangular elements. The number of nodes is indexed inside the black nodes for FD and the white nodes for FE (after Vachiratienchai & Siripunvaraporn, 2013). . . . .	49
2.32 Pseudo-section of the “extreme” topography model (figure 2.25) for (a) Wenner, (b) Schlumberger and (c) Dipole-Dipole arrays. . . . .	52
2.33 The left-slope model for “topographic gradient” study . . . . .	53
2.34 The structure of data vector $\mathbf{d}$ . . . . .	57
2.35 The structure of model vector $\mathbf{m}$ corresponding to the discretized model in figure 2.31. The FD superscript indicates a FD element and the FE superscript indicates a FE element. . . . .	58
2.36 2D section plot for the 20 <sup>th</sup> row of $\mathbf{J}_k$ calculated from (a) FD method, (b) FE method, and (c) HB method. (d) and (e) represents the difference of sensitivity value calculated from FD with FE and HB, respectively. All of these are generated from a Schlumberger array. Notice that the maximum differences are in the order of $10^{-4}$ . . . . .	64
2.37 The components of $\mathbf{C}$ matrix depending on $\sigma_j$ . . . . .	65

## LIST OF FIGURES (cont.)

	Page
2.38 The pattern of $\frac{\partial \mathbf{C}_{k_{yp}}}{\partial \sigma_j}$ . $N_z$ is the number of nodes in the $z$ -direction and $N_T$ is the total number of nodes. The coefficients in first, second, third, and fourth rows are coefficients for the top-left, bottom-left, bottom-right, and top-right nodes, respectively. . . . .	65
2.39 The pattern of the <b>M2P</b> matrix. The first $M$ rows store $\partial \mathbf{C}_{k_{yp}} / \partial \sigma_j$ for the top-left node, the second $M$ rows is for the bottom-left node, the third $M$ rows is for the bottom-right node and the fourth $M$ rows is for the top-right node. . . . .	66
2.40 Pseudo-section of the “extreme” topography model (figure 2.25) for (a) Wenner, (b) Schlumberger and (c) Dipole-Dipole arrays which are used as observed data for Synthetic test. . . . .	68
2.41 The final inverted results of the “extreme” topography model (figure 2.25a). Figures a, b and c are inverted results for Wenner, Schlumberger and Dipole-Dipole arrays computed by the FD method. . . . .	69
2.42 The final inverted results of the “extreme” topography model (figure 2.25a). Figures a, b and c are inverted results for Wenner, Schlumberger and Dipole-Dipole arrays computed by the HB method. . . . .	70
2.43 Data misfit versus $\lambda$ for each iteration. . . . .	72
2.44 (a) the inverted model of the Schlumberger data generated from extreme topography model (Figure 2.25a) when the Jacobain matrix is estimated by Broyden’s update (equation (2.142)) and (b) the change of data misfit with CPU time for FJC and BU. . . . .	73
2.45 The inverted model of the Schlumberger data generated from an extreme topography model (Figure 2.25a) when the controlling parameter $\eta$ is (a) 1, (b) 2, (c) 4 and (d) 8. . . . .	75
2.46 The change of data misfit with iteration for $\eta$ is 1, 2, 4 and 8. . . . .	76



## LIST OF FIGURES (cont.)

	Page
2.47 Field test area inside Mahidol University, Kanchanaburi campus, western Thailand. The two profiles (L1 & L2) are illustrated in the map with red and black profiles, respectively. The caves exposed at the surface are marked on the map as caves A and B (after Vachiratienchai & Siripunvaraporn, 2013). . . . .	76
2.48 Line 1 showing (a) the observed Schlumberger data, (b) the forward response, (c) the inverted model from our inversion (FJC) and (d) the inverted model from RES2DINV. The RMS misfits and number of iterations for this figure can be seen in Table 2.11 (after Vachiratienchai & Siripunvaraporn, 2013). . . . .	77
2.49 Line 2 showing (a) the observed Schlumberger data, (b) the forward response, (c) the inverted model from our inversion (FJC) and (d) the inverted model from RES2DINV. The RMS misfits and number of iterations for this figure can be seen in Table 2.11 (after Vachiratienchai & Siripunvaraporn, 2013). . . . .	77
3.1 Schematic diagram represents the horizontal electric dipole-dipole CSEM method. An EM transmitter is towed close to the seabed to maximize the coupling of electric and magnetic fields with seafloor rocks. These fields are recorded by instruments deployed on the seafloor. The instruments are also able to record magnetotelluric fields that have propagated through the seawater layer (after Constable & Srnka, 2007). . . . .	82
3.2 The canonical model for marine CSEM survey . . . . .	83
3.3 The diagram of a seafloor receiver. It consists of three induction magnetic coils and four plastic arms for measuring two components of the electric field ( <a href="http://marineemlab.ucsd.edu">http://marineemlab.ucsd.edu</a> ). . . . .	84
3.4 The sounding curve of inline ( $x$ ) electric field for the canonical model (indicated by asterisk) and homogeneous model (indicated by diamond). Figure (a) is amplitude and figure (b) is phase. The black solid line in figure (a) indicates the error floor of the receiver. . . . .	85

## LIST OF FIGURES (cont.)

	Page
3.5 The sounding curve of broadside ( $y$ ) electric field for the canonical model (indicated by asterisk) and homogeneous model (indicated by diamond). Figure (a) is amplitude and figure (b) is phase. The black solid line in figure (a) indicates the error floor of the receiver. . . . .	86
3.6 The sounding curve of inline ( $x$ ) magnetic field for the canonical model (indicated by asterisk) and homogeneous model (indicated by diamond). Figure (a) is amplitude and figure (b) is phase. The black solid line in figure (a) indicates the error floor of the receiver. . . . .	87
3.7 The sounding curve of broadside ( $y$ ) magnetic field for the canonical model (indicated by asterisk) and homogeneous model (indicated by diamond). Figure (a) is amplitude and figure (b) is phase. The black solid line in figure (a) indicates the error floor of the receiver. . . . .	88
3.8 The sounding curve of vertical ( $z$ ) magnetic field for the canonical model (indicated by asterisk) and homogeneous model (indicated by diamond). Figure (a) is amplitude and figure (b) is phase. The black solid line in figure (a) indicates the error floor of the receiver. . . . .	89
3.9 A schematic diagram of 3-D CSEM survey. The black arrow represents the transmitter and its orientation. Circles represent array of receivers where the white color indicates the radial receiver and the gray color indicates the azimuthal receiver. . . . .	90
3.10 Normal 3D finite difference or finite volume grid. Unknowns are defined at the corners of the rectangular block. . . . .	94
3.11 Staggered Grid Type I. Three components of electric field are defined at the edges on the cube and three components of magnetic field are defined at the face of the cube. The grid type is suitable for solving equation (3.10). . . . .	94
3.12 Staggered Grid Type II. Three components of electric field are defined at the faces on the cube and three components of magnetic field are defined at the edges of the cube. The grid type is suitable for solving equation (3.13). . . . .	95

## LIST OF FIGURES (cont.)

	Page
3.13 The schematic overview of ModEM. Individual modules are denoted by boxes, with dependencies indicated by arrows. Some boxes are marked with symbols to indicate the vectors and operators from Egbert & Kelbert (2012). The shaded small boxes indicate which dictionaries are used in each module. . . . .	98
3.14 Pseudo-code for non-linear conjugate gradient (NLCG) algorithm. Notation: $\mathbf{f}(\mathbf{m})$ represents the responses obtained from forward modeling; $\mathcal{P}_n$ and $\mathcal{P}'_n$ are values of the penalty functional and its derivative at the $n$ th iteration; $\mathbf{m}_n$ , $\mathbf{h}_n$ , $\mathbf{g}_n$ are vectors in the model space; $\alpha$ and $\beta$ represent real scalars; other symbols are as in the text ( <i>after Egbert, unpublished</i> ). . . . .	101
3.15 The synthetic model for testing the accuracy of CSEM modeling. Figure (a) is the top view at 1,000 m depth and figure (b) is the side view in the $y$ -direction. The white triangle represents the receiver position and the white dashed line is the tow direction. . . . .	103
3.16 The amplitude of the inline ( $x$ ) electric field for the synthetic model (figure 3.15) when the 0.25 Hz $x$ -direction horizontal electric dipole is towed at 50 meters above the seafloor receiver. The solid line is the reference data evaluated by the 1-D forward modeling program (Key, 2009), the diamond, circle, plus, cross, square and right-point triangle symbols are the numerical results from the 50m, 100m, 150m, 200m, 250m and 500m uniform grids, respectively. . . . .	109
3.17 The phase of the inline ( $x$ ) electric field for the synthetic model (figure 3.15) when 0.25 Hz $x$ -direction horizontal electric dipole is towed at 50 meters above the seafloor receiver. The solid line is the reference data evaluated by the 1-D forward modeling program (Key, 2009), the diamond, circle, plus, cross, square and right-point triangle symbols are the numerical results from the 50m, 100m, 150m, 200m, 250m and 500m uniform grids, respectively. . . . .	109

## LIST OF FIGURES (cont.)

	Page
3.18 The amplitude of the broadside ( $y$ ) magnetic field for the synthetic model (figure 3.15) when 0.25 Hz $x$ -direction horizontal electric dipole is towed at 50 meters above the seafloor receiver. The solid line is the reference data evaluated by the 1-D forward modeling program (Key, 2009), the diamond, circle, plus, cross, square and right-point triangle symbols are the numerical results from the 50m, 100m, 150m, 200m, 250m and 500m uniform grid model, respectively. . . . .	110
3.19 The phase of the broadside ( $y$ ) magnetic field for the synthetic model (figure 3.15) when the 0.25 Hz $x$ -direction horizontal electric dipole is towed at 50 meters above the seafloor receiver. The solid line is the reference data evaluated by the 1-D forward modeling program (Key, 2009), the diamond, circle, plus, cross, square and right-point triangle symbols are the numerical results from the 50m, 100m, 150m, 200m, 250m and 500m uniform grids, respectively. . . . .	110
3.20 The amplitude of the inline ( $x$ ) electric field for the synthetic model (figure 3.15) when the 0.25 Hz $x$ -direction horizontal electric dipole is towed at 50 meters above the seafloor receiver. The solid line is the reference data evaluated by the 1-D forward modeling program (Key, 2009), the circle, plus and left-point triangle symbols are the numerical results from the first, second and third non-uniform grids, respectively. .	111
3.21 The phase of the inline ( $x$ ) electric field for the synthetic model (figure 3.15) when 0.25 Hz $x$ -direction horizontal electric dipole is towed at 50 meters above the seafloor receiver. The solid line is the reference data evaluated by the 1-D forward modeling program (Key, 2009), the circle, plus and left-point triangle symbols are the numerical results from the first, second and third non-uniform grids, respectively. . . . .	111
3.22 The amplitude of the broadside ( $y$ ) magnetic field for the synthetic model (figure 3.15) when 0.25 Hz $x$ -direction horizontal electric dipole is towed at 50 meters above the seafloor receiver. The solid line is the reference data evaluated by the 1-D forward modeling program (Key, 2009), the circle, plus and left-point triangle symbols are the numerical results from the first, second and third non-uniform grids, respectively. . . . .	112

## LIST OF FIGURES (cont.)

	Page
3.23 The phase of the broadside ( $y$ ) magnetic field for the synthetic model (figure 3.15) when 0.25 Hz $x$ -direction horizontal electric dipole is towed at 50 meters above the seafloor receiver. The solid line is the reference data evaluated by the 1-D forward modeling program (Key, 2009), the circle, plus and left-point triangle symbols are the numerical results from the first, second and third non-uniform grids, respectively. . . . .	112
3.24 The error of the $E_x$ amplitude for the synthetic model (figure 3.15) when 0.25 Hz $x$ -direction horizontal electric dipole is towed at 50 meters above the seafloor receiver. The solid lines represent the 500m offset, the circle, plus and left-point triangle symbols are the numerical results from the first, second and third non-uniform grids, respectively. . . . .	113
3.25 The error of the $E_x$ phase for the synthetic model (figure 3.15) when 0.25 Hz $x$ -direction horizontal electric dipole is towed at 50 meters above the seafloor receiver. The solid lines represent the 500m offset, the circle, plus and left-point triangle symbols are the numerical results from the first, second and third non-uniform grids, respectively. . . . .	113
3.26 The error of the $B_y$ amplitude for the synthetic model (figure 3.15) when 0.25 Hz $x$ -direction horizontal electric dipole is towed at 50 meters above the seafloor receiver. The solid lines represent the 500m offset, the circle, plus and left-point triangle symbols are the numerical results from the first, second and third non-uniform grids, respectively. . . . .	114
3.27 The error of the $B_y$ phase for the synthetic model (figure 3.15) when 0.25 Hz $x$ -direction horizontal electric dipole is towed at 50 meters above the seafloor receiver. The solid lines represent the 500m offset, the circle, plus and left-point triangle symbols are the numerical results from the first, second and third non-uniform grids, respectively. . . . .	114
3.28 The two-blocks model for testing the reliability of CSEM inversion. The 0.1 $\Omega$ -m conductive and 10 $\Omega$ -m resistive anomalies are placed at the surface of 1 $\Omega$ -m sediment. The conductive anomaly is placed at the south of the resistive anomaly. Both anomalies have the same horizontal and vertical dimensions which are $1.2 \times 2.2 \times 0.4$ km. The white lines in figure (a) represent the lines of the receiver. . . . .	115

## LIST OF FIGURES (cont.)

	<b>Page</b>
3.29 The inverted result is generated by NLCG inversion when $\nu = 1.0$ . . . .	116

CHAPTER I

INTRODUCTION

1.1 Introduction

Resistivity is an intrinsic property of a material, which quantifies how strongly a material opposes the flow of electric current. In most rocks, the porosity and chemical content of the water filling the pore spaces are more important in governing resistivity than the conductivity of mineral grains of which the rock is composed. The range of resistivities among rocks is quite large, extending from under  $10^{-1}$  to over  $10^8 \Omega\text{m}$ . Rocks and minerals with resistivities below  $1.0 \Omega\text{m}$  are considered good conductors; those from 1 to  $100 \Omega\text{m}$  are intermediate conductors and those above  $100 \Omega\text{m}$  are poor conductors. Table 1.1 lists the ranges of resistivities for several types of water-bearing rocks. In civil engineering, the image of the Earth’s resistivity is used to locate water

Source: G. R. Keller, in "Handbook of Physical Constants," rev. ed., Geol. Soc. Am. Mem. 97, 1966.

Geologic age	Marine sand, shale, graywacke	Terrestrial sands, claystone, arkose	Volcanic rocks (basalt, rhyolite, tuffs)	Granite, gabbro, etc.	Limestone, dolomite, anhydrite salt
Quaternary, Tertiary	1-10	15-50	10-200	500-2,000	50-5,000
Mesozoic	5-20	25-100	20-500	500-2,000	100-10,000
Carboniferous	10-40	50-300	50-1,000	1,000-5,000	200-100,000
Pre-Carboniferous Paleozoic	40-200	100-500	100-2,000	1,000-5,000	10,00-100,000
Precambrian	100-2,000	300-5,000	200-5,000	5,000-20,000	10,00-100,000

Table 1.1: Resistivity (in  $\Omega\text{m}$ ) for water-bearing rocks of various types.

tables, detect utilities (e.g., buried water, gas, sewerage), map soft soil and overburden for geotechnical characterization. In the mining industry, a resistivity image is used for detecting a wide variety of base metal sulphide deposits via detection of conductivity anomalies which can be generated around sulphide bodies in the subsurface. In the hydrocarbon industry, a resistivity image is commonly used as a complement of a seismic

survey for classifying types of material in the appropriated structure. In statistic, about 90% of the appropriate structure are filled with saline (Constable, 2010).

To study the Earth's resistivity, there are various methods such as telluric, magnetotelluric, cross-well electromagnetic, controlled-source electromagnetic (CSEM), air-borne electromagnetic, transient/time-domain electromagnetic and direct current resistivity (DCR) survey. All of them can be separated into two types which are passive source and active source survey. The passive source survey measures the variation of natural EM fields and it can be applied for studying very deep structures such as plate tectonics, fault structures, etc. The magnetotelluric (MT) method is one of the most famous passive-source methods which measures both electric field and magnetic field variation at the Earth's surface. The MT method can be used not only for crustal study (e.g. Stanley *et al.*, 1990; Constable & Srnka, 2007; Boonchaisuk *et al.*, 2013) but also for hydrocarbon exploration, mining exploration and geothermal exploration.

For shallow or offshore surveys, active source surveys such as direct current resistivity surveys and controlled-source electromagnetic surveys are more practical. The direct current (DC) resistivity survey is one of the most popular geophysical techniques for shallow resistivity surveys. DC resistivity survey studies the Earth's resistivity by driving direct current into the ground via a pair of electrodes **A** and **B** and then measuring the induced potential field by a other pair or electrodes **M** and **N** as shown in figure 1.1.

In Thailand, DC resistivity surveys are commonly and widely used by many organizations such as department of mineral resources, department of groundwater resources, Chiang Mai University, Khon Kaen University, Prince of Sonhkla University and Mahidol University for studying near-surface resistivity variations. As the DC resistivity method is used for shallow survey, topography has a strong effect on DC resistivity data (Telford *et al.*, 1990). Topography causes localized dispersion and focusing of the current distribution near the surface and hence generates artifacts, i.e., terrain-induced conductive and resistive anomalies in field data. Figure 1.2 shows DC resistivity data of a 600  $\Omega\text{m}$  half-space, sinusoidal topography model (Figure 1.3).

In the theory, the DC resistivity data of half-space model must equal the resistivity of the half-space. In our case, the DC resistivity data should be equal to 600  $\Omega\text{m}$ . With the sinusoidal topography, DC resistivity data is not equal to 600  $\Omega\text{m}$  but it varies from 100-1000  $\Omega\text{m}$ . The topography effect is one of the most important effects in DC resistivity surveys and therefore should be taken into consideration when inverting the DCR data.

In the past decades, the controlled-source electromagnetic (CSEM) survey has become one of the most important tools for the hydrocarbon industry. It is used as a complementary tool for seismic reflection survey. Figure 1.4 shows one successful



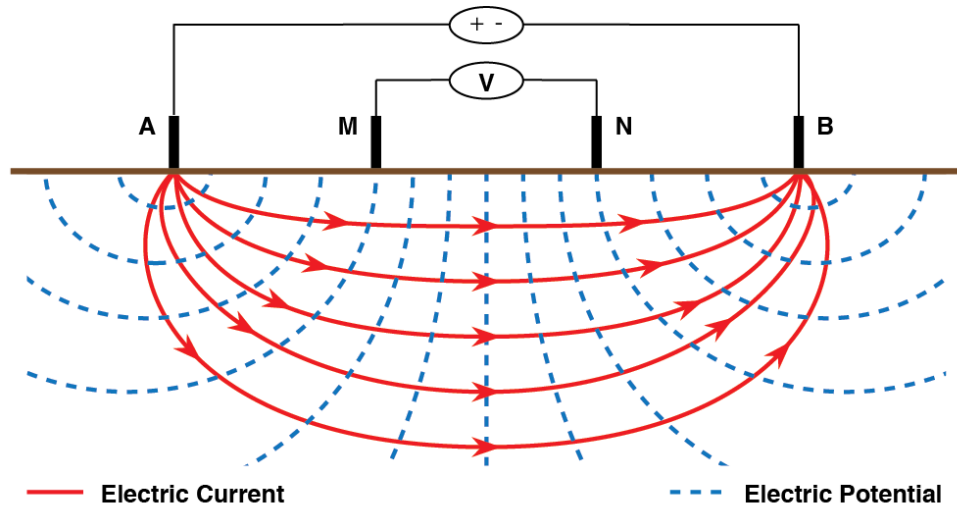


Figure 1.1: A schematic diagram of direct current resistivity survey. **A** and **B** represent positive and negative current electrodes. **M** and **N** represent a pair of potential electrodes.

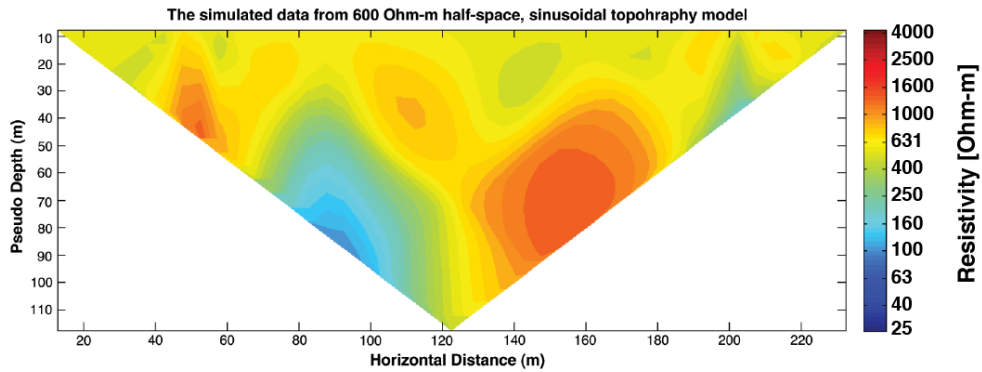


Figure 1.2: The apparent resistivity of 600  $\Omega\text{m}$  half-space, sinusoidal topography model (Figure 1.3).

CSEM survey for detecting a hydrocarbon reservoir which is done by Hesthammer & Boulaenko (2005). Figure 1.4a shows a 2D seismic section. Several channel systems can be extracted from the seismic data and represent potential hydrocarbon-filled structures. Figure 1.4b shows the same seismic section masked with resistivity information from a 2D CSEM survey. The result shows that only the two shallower targets are likely to be filled with hydrocarbons and the result was confirmed by drilling in 2008.

Nowadays, CSEM survey is used for not only detecting the presence of hydrocarbon reservoirs but also for estimating its volume. To estimate the volume of hydrocarbons, 3-D CSEM modeling and inversion are needed. The ModEM system is a modular electromagnetic inversion system which provides numerical tools for developing 3-D forward modeling and inversion. ModEM is also available as a free EM developing tool by Oregon State University. Here, we need to develop 3-D CSEM modeling to fit

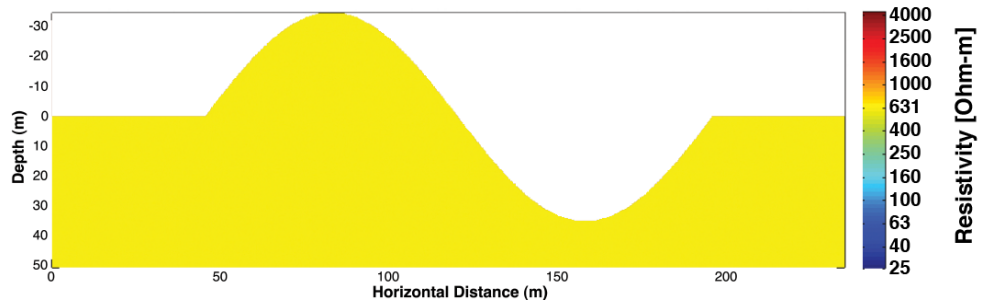


Figure 1.3: The 600  $\Omega\text{m}$  half-space model with sinusoidal topography.

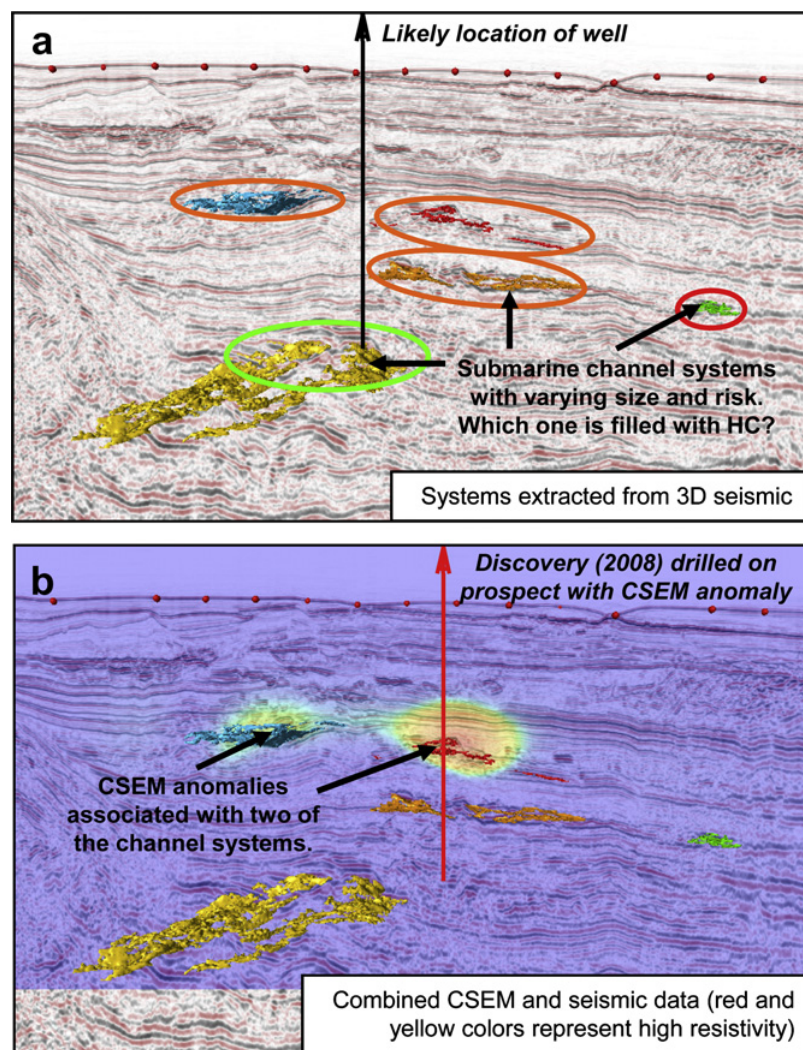


Figure 1.4: (a) A 2D seismic section. Several channel systems can be extracted from the seismic data and represent potential hydrocarbon-filled structures. The prospect marked with a green circle is the largest and a well target. (b) Adding resistivity information to the seismic data using CSEM technology shows that only the two shallower targets are filled with hydrocarbons (Hesthammer *et al.*, 2010).

the ModEM system in the hope that it can be readily used.

## 1.2 Scope of Study

In the thesis, we work on two areas which are (1) to develop an efficient 2D inversion program which can include topography effects in 2D DC resistivity survey and (2) to develop the 3-D CSEM modeling that can be used inside the ModEM system.

## 1.3 Thesis Outline

This thesis consists of 3 chapters for two projects. The first chapter is this chapter in which we give the introduction and the outline of the thesis.

The second chapter is the chapter for 2D DC resistivity forward modeling and inversion. In this chapter, we describe the basics of DC resistivity surveys and the hybrid finite difference-finite element technique that is introduced to solve the topography effect. The accuracy and reliability of new 2D DC resistivity forward modeling and inversion are also tested in this chapter.

The third chapter describes the basics of CSEM surveys and the scattered-field technique. In this chapter, we also describe how to develop CSEM forward modeling based on the scattered-field technique and then describe how to incorporate 3-D CSEM modeling into the ModEM system. Finally, the accuracy and reliability of 3-D CSEM forward modeling and inversion are tested at the end of this chapter.

## CHAPTER II

### AN EFFICIENT 2-D DC RESISTIVITY INVERSION

In this chapter, we develop an efficient 2-D DC resistivity inversion code that is fast, reliable and can also incorporate the topography. The technique we used for the modeling is the hybrid finite difference and finite element method. We start the chapter by briefly describing the fundamentals of the DC resistivity survey and also field acquisition. The DC Resistivity method relies on Ohm's law. In the next section, we describe two methods that are commonly used to solve Ohm's law for DC Resistivity surveys. They are the finite difference (e.g. Dey & Morrison, 1979; Vachiratienchai, 2007; Pidlisecky & Knight, 2008; Sun *et al.*, 2009) and the finite element methods (e.g. Tong & Yang, 1990; Sasaki, 1994; Li & Spitzer, 2002; Pain *et al.*, 2002; Boonchaisuk *et al.*, 2008). We start by developing our own codes based on the two methods. To confirm that our code works well, we validate the results through many synthetic examples and also compare them with the commercial code (RES2DINV). The results clearly show that FD is faster than FE but less efficient when incorporating the topography. The advantage of FD becomes a disadvantage of FE, and the disadvantage of FD becomes a advantage of FE. This has led us to the idea of combining both FD and FE to produce the hybrid method. In the next section, we describe the idea of the hybrid FD - FE method and then we examine our idea through the synthetic examples to show that our hybrid FD - FE method is the most efficient method.

The forward modeling computes the responses from the known model. In a real field survey, we collected the data and then inverted the data to obtain the resistivity model. We start the section by explaining the concept of the inversion and many different algorithms used for DC resistivity surveys. Then we focus on the data space Occam's inversion. This is because it is reliable and efficient. In the next section, we describe how we implement the hybrid FD - FE method inside the data space Occam's inversion to produce the efficient inversion. We validate and verify our codes through both synthetic examples and real field data.

### 2.1 Fundamentals of DCR Surveys

A DCR survey images the subsurface resistivity structure by measuring a series of induced-electric potentials along with the electric current and relative geometry

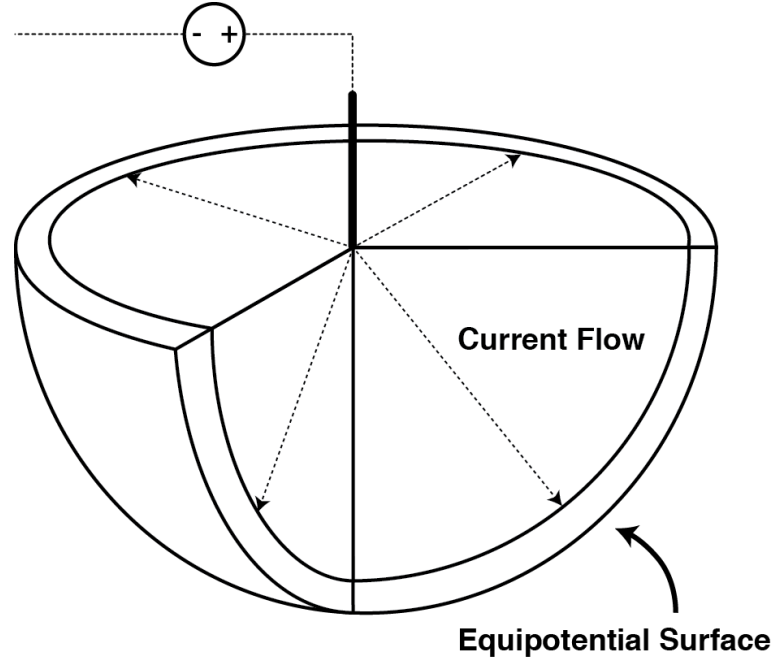


Figure 2.1: Hemisphere pattern of electric potential when current is injected into homogeneous structure.

of the four electrodes. For quality assessment or direct interpretation, the collected data are converted into a form which is related to the relevant physical property. For each measurement, it is theoretically equivalent of using Ohm's Law to calculate to resistivity i.e. the apparent resistivity.

Ohm's law states that the electric current through a material between two points is directly proportional to the potential difference between the two points. Ohm's law can be written as

$$\mathbf{J} = -\sigma \nabla \phi, \quad (2.1)$$

where  $\mathbf{J}$  is the current density,  $\sigma$  is the conductivity or the inverse of resistivity ( $\rho$ ) and  $\phi$  is the electric potential. For homogeneous earth, the injected electric current will flow out in any direction and produces an equipotential surface with a hemispherical shape (figure 2.1). In this case, equation (2.1) can be written as

$$\frac{I}{2\pi r^2} = -\frac{1}{\rho} \frac{\partial \phi}{\partial r}, \quad (2.2)$$

where  $I$  is strength of the injected current and  $r$  is radial distance from point source. Integrating (2.2) with respect to  $r$ , we obtain the relation between  $\phi$  and  $r$ ,

$$\phi(r) = \frac{\rho I}{2\pi r}. \quad (2.3)$$

For electrode arrays, the potential at any potential electrode is equal to the sum of the contributions from the individual current electrodes. In a four-electrode survey (figure

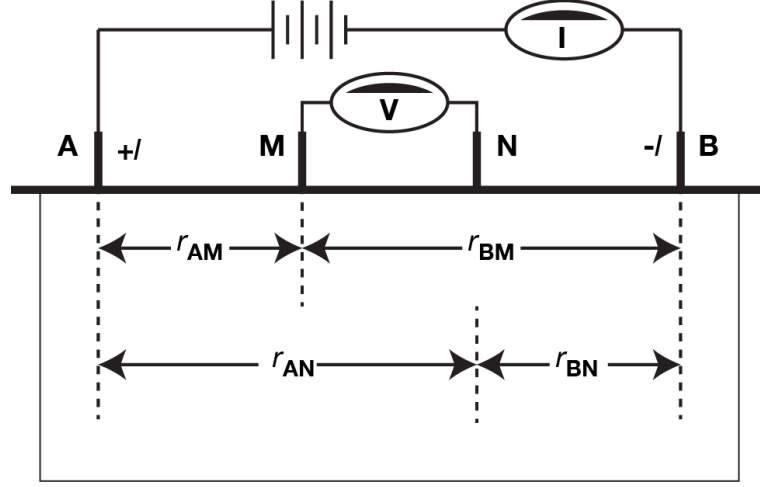


Figure 2.2: shows a four-electrode DCR measurement. Current electrodes are labeled by **A** and **B**, and potential electrodes are labeled by **M** and **N**.

2.2) over a homogeneous earth, the potential difference between potential electrode **M** and **N**,  $\phi_{MN}$ , is,

$$\phi_{MN} = \frac{\rho I}{2\pi} \left( \frac{1}{r_{AM}} - \frac{1}{r_{BM}} - \frac{1}{r_{AN}} + \frac{1}{r_{BN}} \right), \quad (2.4)$$

where  $r$  is distance from the current electrode to the potential electrode and the first subscript indicates the current electrode and the second subscript indicates the potential electrode.  $r_{AM}$  is the distance from current electrode **A** to potential electrode **M**. Rearranging equation (2.4), we obtain the equation for computing resistivity from the measurement as

$$\rho = G \frac{\phi_{MN}}{I}, \quad (2.5)$$

where the geometric factor

$$G = 2\pi \left( \frac{1}{r_{AM}} - \frac{1}{r_{BM}} - \frac{1}{r_{AN}} + \frac{1}{r_{BN}} \right)^{-1}. \quad (2.6)$$

The resistivity calculated by Ohm's law in equation (2.5) is equal to the true resistivity only in the homogeneous Earth case. In more complicated and heterogeneous cases, the resistivity calculated by equation (2.5) is called the apparent resistivity  $\rho_a$  and is measured as a function of the electrode spacing.

Although equation (2.5) can be used for all electrode arrays, it is impractical for use in field surveys. We need to express the geometric factor in term of electrode geometry. For common electrode arrays,  $G$  is summarized in figure 2.3 where  $a$  is the minimum electrode spacing and  $n$  is the investigation-depth level to indicate the survey depth. Each electrode array has a particular depth of investigation, resolution, and sensitivity to subsurface structure and telluric noise.

**The Wenner array** was popularized by the pioneering work carried out by the University of Birmingham research group (Griffiths & Turnbull, 1985; Griffiths *et al.*,

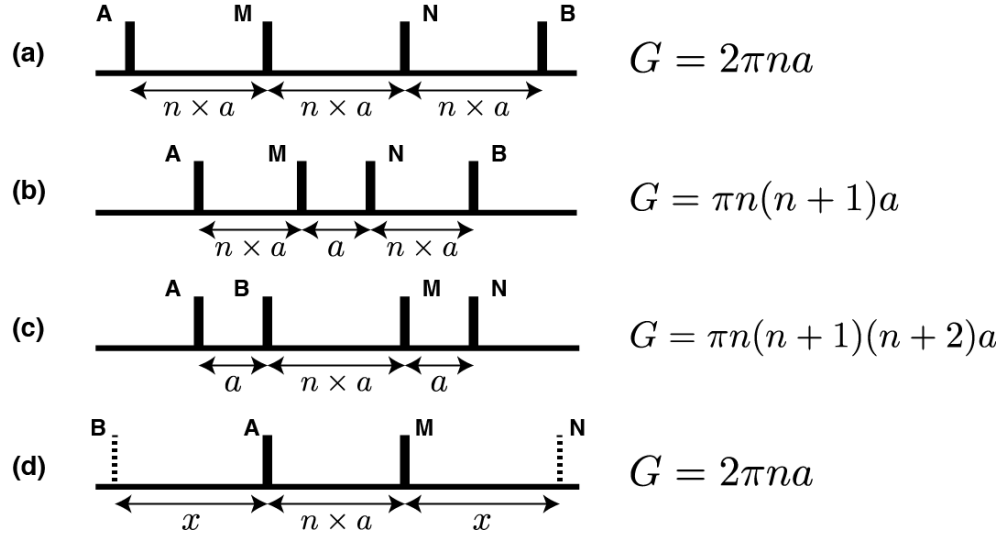


Figure 2.3: Four arrays are illustrated (a) Wenner, (b) Schlumberger, (c) Dipole-Dipole, and (d) Pole-Pole array where  $a$  is electrode spacing,  $n$  is the investigation level, and  $x$  is distance to “infinite-electrodes” in Pole-Pole array.

1990). Many of the early 2-D surveys were carried out with this array. A schematic diagram of the Wenner array is shown in Figure 2.3a. The Wenner array places current electrodes on different sides of the electrode array and measures the potential difference at the middle of the array. All distances between neighboring electrodes are equal to  $na$ . The Wenner array has best signal response and high resolution of vertical structures but it has a relatively shallow depth of investigation (Ward, 1990; Sharma, 1997; Loke, 2000). Its geometric factor is computed by

$$G = 2\pi na. \quad (2.7)$$

**The Schlumberger array** has been used since the 1920's for electrical sounding (1D electrical survey) and is still popular. Figure 2.3b illustrates a schematic diagram of The Schlumberger array. The way of placing electrodes of the Schlumberger array is close to that of the Wenner array except the distance between potential electrodes is always equal to  $a$ . Fixing the distance between potential electrodes makes the signal of the Schlumberger array weaker than the signal of the Wenner array. The Schlumberger array has the ability to resolve horizontal and vertical structures relatively well and has a greater depth of investigation than the Wenner array, and a wider horizontal data coverage than the Wenner array (Ward, 1990; Sharma, 1997; Loke, 2000). Its geometric factor is computed by

$$G = \pi n(n + 1)a. \quad (2.8)$$

**The Dipole-Dipole array** or Eltran array is more popular and practical for large scale DCR surveys than the Wenner and Schlumberger arrays and is also

popular in induced polarization (IP) surveys because the complete separation of current and voltage circuits reduces the vulnerability to inductive noise. A schematic diagram of the Dipole-Dipole array is shown in Figure 2.3c. The distance between electrode **A** and electrode **M** is equal to  $na$  while the distance between a pair of current electrodes and a pair of potential electrodes are always  $a$ . The Dipole-Dipole array has a greater depth of investigation than the Wenner and Schlumberger arrays but its signal strength is the weakest of all the arrays. Because of the weakness of its signal, the Dipole-Dipole array is more subject to telluric noise than the Wenner and Schlumberger arrays. The Dipole-Dipole array is considered inferior to Wenner and Schlumberger arrays for the resolution of horizontal and steeply dipping structures (Ward, 1990; Sharma, 1997; Loke, 2000). Its geometric factor is computed by

$$G = \pi n(n + 1)(n + 2)a. \quad (2.9)$$

**The Pole-Pole array** is very popular in archaeological surveys because it lends itself to rapid one-person operation. Unlike the other arrays, the Pole-Pole array places and fixes one current electrode and one potential electrode far away from the study area. The proper distance to a fixed electrode,  $x$ , should be 10-30 times the distance between any two mobile electrodes. The long cables required can impede field work and may also act as aerials, picking up stray electromagnetic signals (inductive noise) that can affect the readings. The Pole-Pole array has the deepest penetration of all arrays and the widest horizontal coverage for a given array length but the poorest resolution (Ward, 1990; Sharma, 1997; Loke, 2000; Milsom, 2003). Its geometric factor is computed by

$$G = 2\pi na. \quad (2.10)$$

Arrays are usually chosen at least partly for their depth of investigation. The depth of investigation is the depth to which a fraction of the current penetrates. It depends on the earth resistivity structure as well as the overall length of the electrode array (Loke, 2000). The wider the length of the electrode array, the deeper the depth of investigation. The depth of investigation of each electrode array can be determined by finding the array length at which the effect of a thin horizontal layer in the homogeneous earth is a maximum. The relative effects of a thin horizontal layer, for Wenner, Schlumberger and Dipole-Dipole arrays, are shown in figure 2.4. The peak of the Wenner array is located at the left of the graph while the peak of Dipole-Dipole array is located at the right of the graph. That means the Dipole-Dipole array is the most penetrative array and the Wenner array is the least penetrative array. The Wenner peak occurs when the length of array is 10 times the thin layer depth, and the Schlumberger array is only a little better. Figure 2.4 also shows the Wenner curve is the most sharply peaked, indicating superior vertical resolving power.



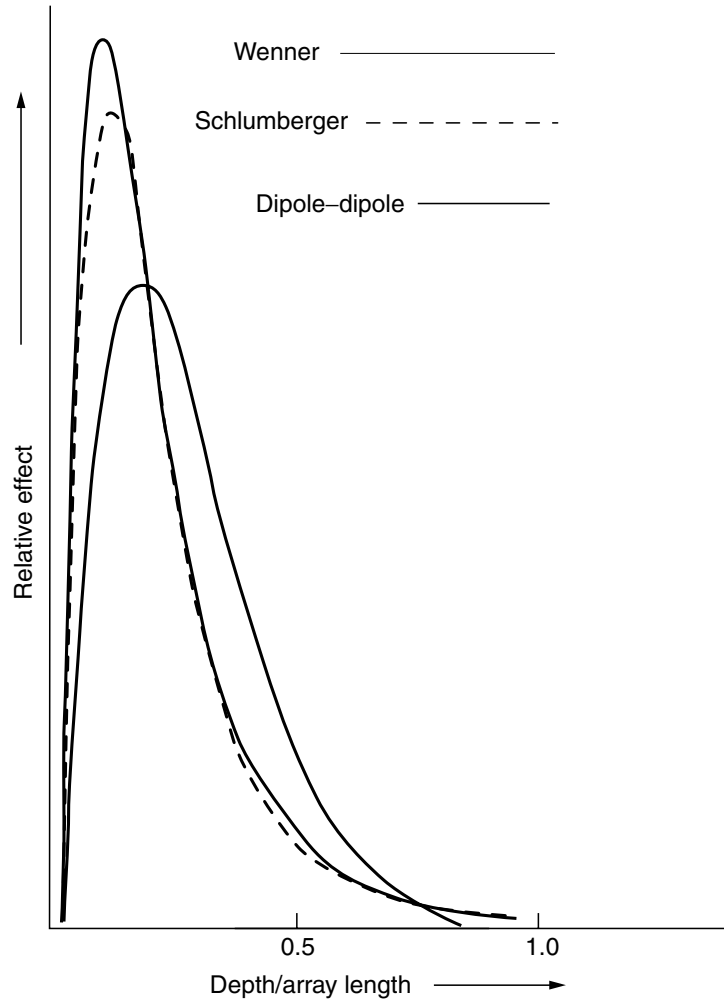


Figure 2.4: relative effect of a thin resistive layer bed in homogeneous earth for Wenner, Schlumberger and Dipole-Dipole arrays (Milsom, 2003).

Electrodes may in principle be positioned on the ground surface to any desired degree of accuracy (although errors are always possible and become more likely as separations increase). Most modern instruments provide current at one of a number of preset levels and fluctuations in supply are generally small and unimportant. Noise therefore enters the apparent resistivity values almost entirely via the voltage measurements, the ultimate limit being determined by voltmeter sensitivity. There may also be noise from induction in the cables and natural voltages, which may vary with time and so be incompletely cancelled by reversing the current flow and averaging. Large separations and long cables should be avoided if possible, but the most effective method of improving the signal to noise ratio is to increase the signal strength. There are physical limits to the amount of current any given instrument can supply to the ground and it may be necessary to choose arrays that give large voltages for a given current flow. The

Wenner and Pole-Pole arrays score more highly in this respect than most other arrays. For a given input current, the voltages measured using a Schlumberger array are always less than those for a Wenner array of the same overall length, because the separation between the potential electrodes is always smaller. For the Dipole-Dipole array, the comparison depends upon  $n$  but even for  $n = 1$ , the signal strength is smaller than for the Wenner array by a factor of three (Milsom, 2003).

## 2.2 DCR Field Procedure and Data Plotting

For a DC resistivity survey, there are 3 recording procedures which are (1) resistivity sounding, (2) resistivity profiling and (3) resistivity imaging.

**Resistivity sounding** or vertical electrical sounding (VES) is used when the earth's structure needs to be interpreted in terms of layers under a single location at the surface. The electrode locations are varied symmetrically about a central location. Therefore, data must be plotted as a function of electrode spacing rather than as a function of location in log-log scale. The resulting plot is called a sounding curve. Figure 2.5 shows the example curve on the two-layers model which is a 100  $\Omega$ -m and 30 m thick layer laid on a 10  $\Omega$ -m homogeneous medium. For small electrode spacings, electric current flows only in near-surface regions. Apparent resistivities are similar to the true resistivity of the top layer (100  $\Omega$ -m). As current flows deeper, apparent resistivities are influenced by the resistivity of deeper materials (10  $\Omega$ -m). At very large electrode spacings, the sounding curve reflects the deeper ground because most of the current is flowing in the deeper regions. The most common configurations for soundings are the Wenner and Schlumberger arrays.

**Resistivity profiling** is a common procedure for studying lateral changes by moving a fixed array along the survey line. Data is plotted as a function of the central position of the array in a log-linear scale. The resulting plot is called a profiling curve. Figure 2.6 shows the example profiling curve on the vertical-contact model which is 10  $\Omega$ -m uniform media on the left hand side (LHS) and 1,000  $\Omega$ -m uniform media on the right hand side (RHS). For all electrodes on the LHS, electric current flows only in the LHS media. Apparent resistivities are similar to the true resistivity of the LHS media (10  $\Omega$ -m). The apparent resistivities are influenced by the resistivity of the RHS materials (1,000  $\Omega$ -m). For electrodes on the RHS, the profiling curve reflects the RHS media because most of the current is flowing in the RHS regions. The most common configurations for profiling are Dipole-Dipole arrays.

**Resistivity imaging** or 2D DC resistivity surveying is a process for studying resistivity variation in both vertical and horizontal directions. Resistivity imaging is a combination of resistivity sounding and resistivity profiling. The electrode array is

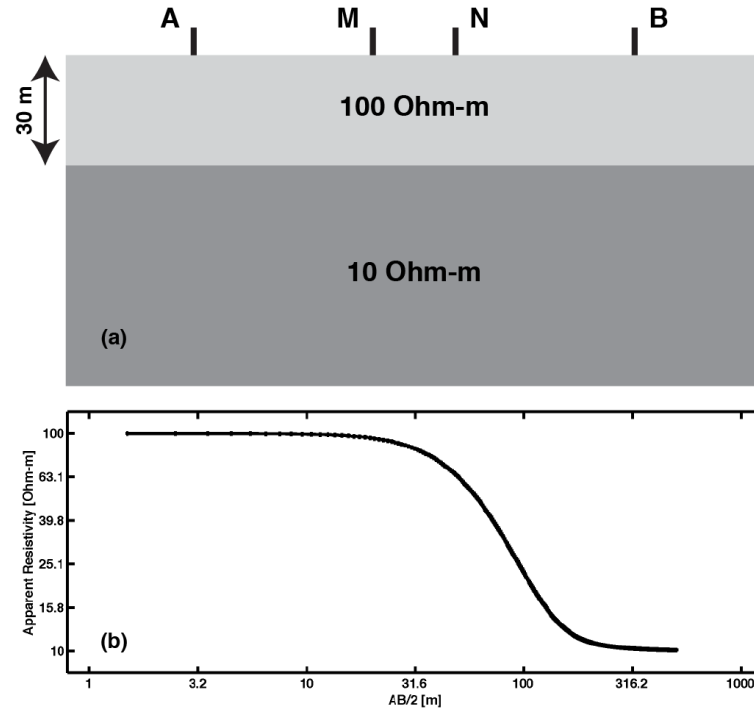


Figure 2.5: The example of resistivity sounding or VEF: (a) illustrates the two-layer models which is 100  $\Omega$ -m and 30 m thick and is overlaid on 10  $\Omega$ -m uniform media and (b) sounding curve of the two-layers model. The y-axis is the apparent resistivity value and the x-axis is half of the distance between electrode **A** and **B**.

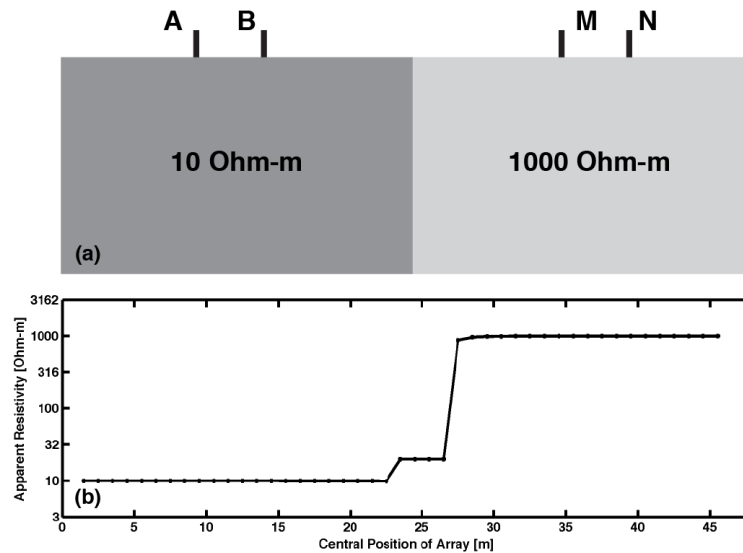


Figure 2.6: The example of resistivity profiling: (a) illustrates the vertical-contact models which has 10  $\Omega$ -m uniform media on the left hand side of the model and 1,000  $\Omega$ -m uniform media on the right hand side of model and (b) profiling curve of the vertical-contact model. The y-axis is the apparent resistivity value and the x-axis is the central position of the array.

moved along the survey line and its spacing is also changed. Therefore, data must be plotted as a function of electrode spacing and the central position of the array. The resulting plot is called a pseudo section. Figure 2.7 shows a schematic diagram of resistivity imaging for collecting data with a Wenner array. Figure 2.8 represents the examples of pseudo sections for a one-block model by using Wenner, Schlumberger and Dipole-Dipole arrays with 48 electrodes, 1-m electrode spacing and 15 investigation-depth levels. The x-axis of the pseudo section is the horizontal distance which is the central position of each electrode array and the y-axis is the pseudo depth which can be roughly estimated from the array type and electrode spacing. Following Milsom (2003), the pseudo depth is about 25%, 35% and 50% of the array length for Wenner, Schlumberger, and Dipole-Dipole arrays.

The pseudo section doesn't reflect the intrinsic earth's resistivity and it also depends on the array type and the Earth's structure. For interpretation, the pseudo section must be converted to true resistivity structure. It is done by a process called "inversion" as will be described in Section 2.4.

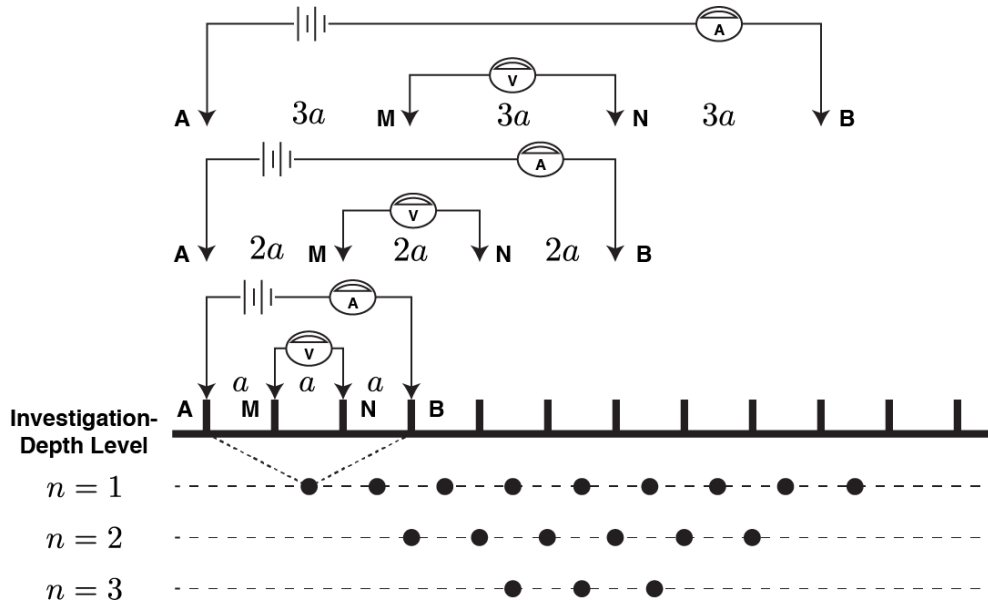


Figure 2.7: Pseudo section plotting for Wenner array. Each dot represents a datum.

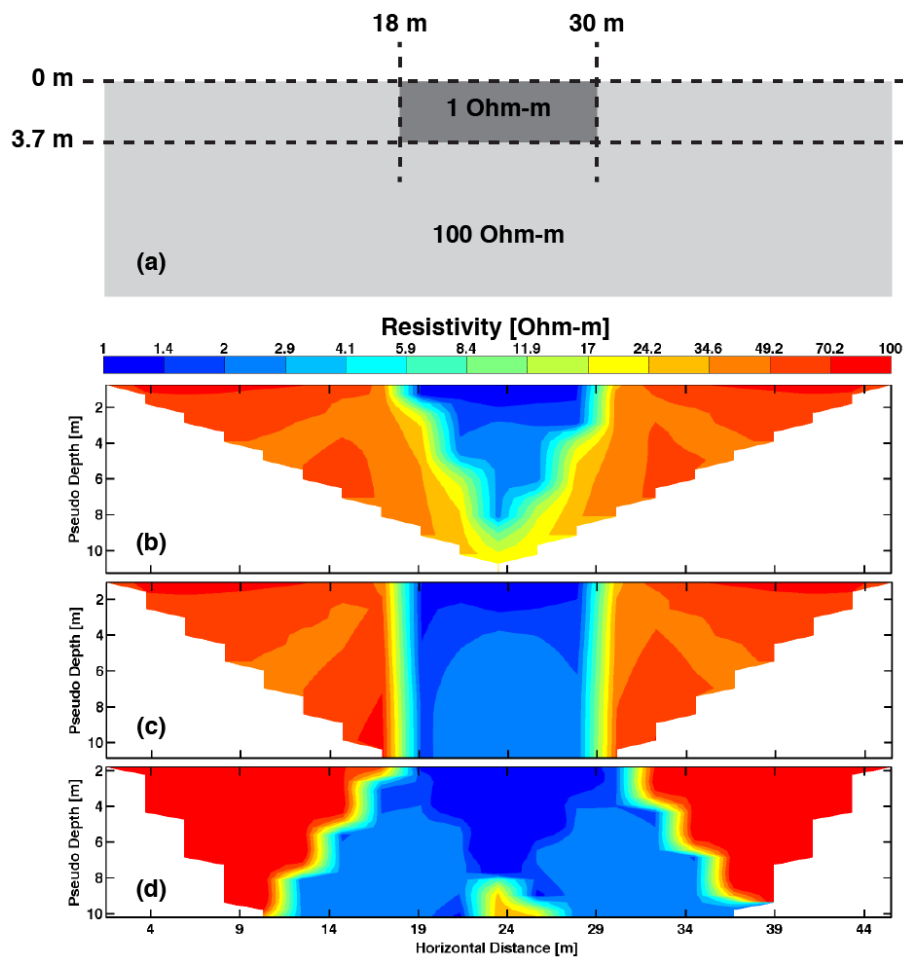


Figure 2.8: A example of resistivity imaging: (a) illustrates the one-block models which has a  $1\ \Omega\text{-m}$  conductive block buried in  $100\ \Omega\text{-m}$  homogeneous media, (b), (c), and (d) illustrate pseudo sections for Wenner, Schlumberger and Dipole-Dipole arrays, representatively.

## 2.3 2D DC Resistivity Modeling

DC resistivity modeling is an inverse process of inversion. DC resistivity modeling is a computational program for calculating the apparent resistivity,  $\rho_a$ , from a known resistivity model. There are various numerical techniques for developing 2D DC resistivity modeling such as (1) boundary element (BE) method (Okabe, 1981; Xu *et al.*, 1998; Ma, 2002), (2) finite element (FE) method (e.g., Coggon, 1971; Fox *et al.*, 1980; Tong & Yang, 1990; Sasaki, 1994; Tsourles *et al.*, 1999; Li & Spitzer, 2002; Pain *et al.*, 2002; Rücker *et al.*, 2006; Boonchaisuk, 2007; Boonchaisuk *et al.*, 2008; Erdogan *et al.*, 2008; Blome *et al.*, 2009; Vachiratienchai *et al.*, 2010), and (3) finite difference (FD) method (e.g., Dey & Morrison, 1979; Zhang *et al.*, 1995; Zhao & Yedlin, 1996; Vachiratienchai, 2007; Pidlisecky & Knight, 2008; Vachiratienchai *et al.*, 2010). Unlike other methods, the BE method transforms the governing equation from a partial differential equation to a integral equation by using Green's theorem. This transformation significantly reduces the memory requirement and it makes the BE method the lowest memory method. Although the BE method can save memory, it can function only on a simple model as mentioned in Xu *et al.* (1998). The BE method is therefore not practical for use as a inversion kernel. For inversion, the FD and FE methods are commonly and widely used for developing forward modeling. Both methods have its advantages the FD method uses less time and memory than the FE method but the FE method is more flexible than the FD method.

The finite element method can handle complicated geometries more easily than the finite difference method. In DC resistivity modeling, the FE method is therefore applied when modeling with topography (e.g. Fox *et al.*, 1980; Tsourles *et al.*, 1999; Loke, 2000; Li & Spitzer, 2002; Erdogan *et al.*, 2008). However, if the topography is trivial, the FD method is much more computationally efficient (Li & Spitzer, 2002; Erdogan *et al.*, 2008). Because of its superior computational performance, there have been attempts to incorporate topography into the FD approach. Erdogan *et al.* (2008) applied a triangular discretization, instead of the commonly used rectangular discretization, to FD at the air-earth interface. With their approach, triangular FD is as accurate as triangular FE, but slightly less accurate than the FE distorted-mesh. However, their triangular FD algorithm is significantly faster than both FE approaches. Sun *et al.* (2009) applied a coordinate transformation to the FD mesh to increase the accuracy of their solutions when topography is present. The idea of coordinate transformation is similar to what was previously used by Baba & Seama (2002) to incorporate seafloor topography in electromagnetic modeling.

### 2.3.1 Governing Equation

For 2D DCR survey, the governing equation is the equation for computing the electric potential and can be derived from two basic physics principles which are Ohm's law (equation (2.1)) and the continuity equation,

$$\nabla \cdot \mathbf{J} = \frac{\partial q}{\partial t} \delta(x) \delta(y) \delta(z), \quad (2.11)$$

where  $q$  is the charge density specified at a point in the Cartesian  $x - y - z$  space by the Dirac delta function.

Substituting equation (2.1) into equation (2.11), we can write a generalized three-dimensional version of equation (2.11) as

$$-\nabla \cdot [\sigma(x, y, z) \nabla \phi(x, y, z)] = \frac{\partial q}{\partial t} \delta(x_s) \delta(y_s) \delta(z_s). \quad (2.12)$$

For the 2D assumption, the conductivity distribution in the strike ( $y$ ) direction is not changed, and so  $\frac{\partial}{\partial y} \sigma(x, y, z) = 0$ . Equation (2.12) can be written as

$$-\nabla \cdot [\sigma(x, z) \nabla \phi(x, y, z)] = \frac{\partial q}{\partial t} \delta(x_s) \delta(y_s) \delta(z_s). \quad (2.13)$$

In equation (2.13), potential  $\phi$  and source term  $\frac{\partial q}{\partial t} \delta(x_s) \delta(y_s) \delta(z_s)$  are functions of  $x$ ,  $y$ , and  $z$  while conductivity  $\sigma$  is a function of  $x$  and  $z$ . The most practical way is to solve equation (2.13) in Fourier transform space  $(x, k_y, z)$  by transforming  $y$  into the wavenumber  $k_y$  domain. This transformation is performed in the forward and backward direction by

$$\tilde{\phi}(x, k_y, z) = \int_0^\infty \phi(x, y, z) \cos(k_y y) dy, \quad (2.14)$$

and

$$\phi(x, y, z) = \frac{2}{\pi} \int_0^\infty \tilde{\phi}(x, k_y, z) \cos(k_y y) dk_y. \quad (2.15)$$

By the transformation of equation (2.14), the three-dimensional potential distribution  $\phi(x, y, z)$  due to a point source at  $(x_s, y_s, z_s)$  over a two-dimensional conductivity distribution  $\sigma(x, z)$  is reduced to the two-dimensional transformed potential  $\tilde{\phi}(x, k_y, z)$  which is a solution of the transformed equation (2.13),

$$-\nabla \cdot [\sigma(x, z) \nabla \tilde{\phi}(x, k_y, z)] + k_y^2 \sigma(x, z) \tilde{\phi}(x, k_y, z) = \tilde{Q} \delta(x_s) \delta(z_s), \quad (2.16)$$

where  $\tilde{Q}$  is the constant steady state current density in  $(x, k_y, z)$  space, given by

$$\tilde{Q} \delta(x_s) \delta(z_s) = \frac{I}{2\Delta A} \delta(x_s) \delta(z_s), \quad (2.17)$$

where  $I$  is the current injected at  $(x_s, z_s)$ , and  $\Delta A$  is a representative area in the  $x-z$  plane about the injection point  $(x_s, z_s)$ .

Equation (2.16) is the “governing equation” for the 2D DCR problem. To get the transformed electric potential  $\tilde{\phi}$  for an arbitrary resistivity structure, equation (2.16) is solved by applying the FD or FE method under mixed boundary conditions (Dey & Morrison, 1979). The general form of a mixed boundary condition is

$$\alpha(x, z)\tilde{\phi} + \beta(x, z)\frac{\partial \tilde{\phi}}{\partial \eta} = 0, \quad (2.18)$$

where

$$\alpha = 0 \quad \text{and} \quad \beta = \sigma \quad \text{for ground surface,}$$

$$\alpha = k_y \frac{K_1(k_y r)}{K_0(k_y r)} \quad \text{and} \quad \beta = 1 \quad \text{for left, right, and bottom boundaries,}$$

where  $k_y$  is the spatial wave number,  $r$  is the distance from source,  $K_0$  is the zeroth order modified Bessel function, and  $K_1$  is the first order modified Bessel function.

In the following sections, we derive the discrete form of the governing equation for the FD and FE methods. After that we describe the method for selecting the wavenumber.

### 2.3.2 Finite Difference Method

To solve equation (2.16) with the FD method, the conductivity model is first discretized into a rectangular grid as illustrated in figure 2.9. The conductivity  $\sigma_{i,j}$

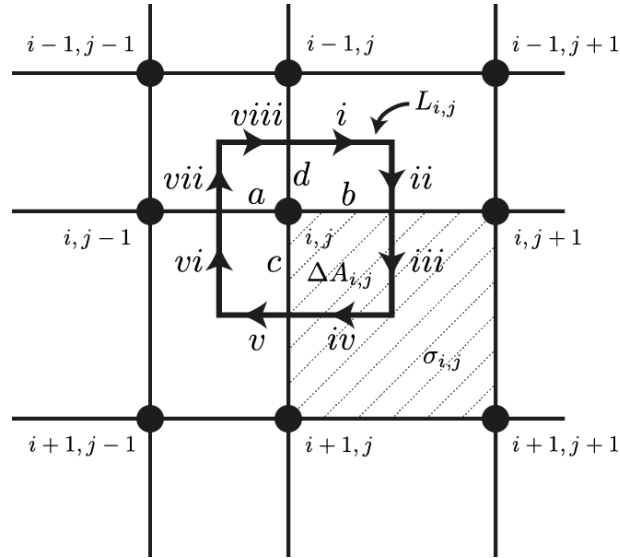


Figure 2.9: shows the rectangular grid and the discretized area  $\Delta A_{i,j}$  around node  $(i, j)$ .

indicates the conductivity in the region bounded by nodes  $(i, j)$ ,  $(i, j+1)$ ,  $(i+1, j)$ , and  $(i+1, j+1)$  which are defined at the corners of a rectangular grid. For node  $(i, j)$  in the interior, the representative area  $\Delta A_{i,j}$  is

$$\Delta A_{i,j} = \frac{(\Delta x_j + \Delta x_{j-1})(\Delta z_i + \Delta x_{i-1})}{4},$$



and the representative area  $\Delta A_{i,j}$  for node  $(i, j)$  at the ground surface is

$$\Delta A_{i,j} = \frac{(\Delta x_j + \Delta x_{j-1}) \Delta z_i}{4},$$

where  $\Delta x_j$  is the horizontal distance between node  $(i, j)$  and node  $(i, j+1)$ ,  $\Delta x_{j-1}$  is the horizontal distance between node  $(i, j)$  and node  $(i, j-1)$ ,  $\Delta z_i$  is the vertical distance between node  $(i, j)$  and node  $(i+1, j)$ , and  $\Delta z_{i-1}$  is the vertical distance between node  $(i, j)$  and node  $(i-1, j)$ .

For node  $(i, j)$  for which node  $\tilde{\phi}_{i,j}$  is unknown, equation (2.16) is integrated over the representative area  $\Delta A_{i,j}$  to obtain

$$-\iint_{\Delta A_{i,j}} \nabla \cdot [\sigma_{i,j} \nabla \tilde{\phi}_{i,j}] dx_j dz_i + \iint_{\Delta A_{i,j}} k_y^2 \sigma_{i,j} \tilde{\phi}_{i,j} dx_j dz_i = \frac{I}{2} \delta(x_s) \delta(z_s). \quad (2.19)$$

Applying Green's theorem to the first term of equation (2.19), we obtain

$$\iint_{\Delta A_{i,j}} \nabla \cdot [\sigma_{i,j} \nabla \tilde{\phi}_{i,j}] dx_j dz_i = \oint_{L_{i,j}} \sigma_{i,j} \frac{\partial \tilde{\phi}_{i,j}}{\partial \eta} dl, \quad (2.20)$$

where  $\eta$  is the outward normal direction, and  $L_{i,j}$  is the contour line which encloses the representative area  $\Delta A_{i,j}$  as shown in figure 2.9. The contour integral along the contour line  $L_{i,j}$  can be divided into eight parts as indicated by the arrow in figure 2.9. By applying central differences to approximate  $\frac{\partial \tilde{\phi}}{\partial \eta}$ , we obtain

$$\begin{aligned} \oint_{L_{i,j}} \sigma_{i,j} \frac{\partial \tilde{\phi}_{i,j}}{\partial \eta} dl &= \frac{\Delta x_j \sigma_{i-1,j}}{2} \left( \frac{\tilde{\phi}_{i-1,j} - \tilde{\phi}_{i,j}}{\Delta z_{i-1}} \right) + \frac{\Delta z_{i-1} \sigma_{i-1,j}}{2} \left( \frac{\tilde{\phi}_{i,j+1} - \tilde{\phi}_{i,j}}{\Delta x_j} \right) \\ &+ \frac{\Delta z_i \sigma_{i,j}}{2} \left( \frac{\tilde{\phi}_{i,j+1} - \tilde{\phi}_{i,j}}{\Delta x_j} \right) + \frac{\Delta x_j \sigma_{i,j}}{2} \left( \frac{\tilde{\phi}_{i-1,j-1} - \tilde{\phi}_{i,j}}{\Delta z_i} \right) \\ &+ \frac{\Delta x_{j-1} \sigma_{i,j-1}}{2} \left( \frac{\tilde{\phi}_{i-1,j-1} - \tilde{\phi}_{i,j}}{\Delta z_i} \right) + \frac{\Delta z_i \sigma_{i,j-1}}{2} \left( \frac{\tilde{\phi}_{i,j-1} - \tilde{\phi}_{i,j}}{\Delta x_{j-1}} \right) \\ &+ \frac{\Delta z_{i-1} \sigma_{i-1,j-1}}{2} \left( \frac{\tilde{\phi}_{i,j-1} - \tilde{\phi}_{i,j}}{\Delta x_{j-1}} \right) + \frac{\Delta x_{j-1} \sigma_{i-1,j-1}}{2} \left( \frac{\tilde{\phi}_{i-1,j} - \tilde{\phi}_{i,j}}{\Delta z_{i-1}} \right). \end{aligned} \quad (2.21)$$

In the similar way, the second term on the left-hand side of equation (2.19) can be expressed as

$$\begin{aligned} \iint_{\Delta A_{i,j}} k_y^2 \sigma_{i,j} \tilde{\phi}_{i,j} dx_j dz_i &= k_y^2 \tilde{\phi}_{i,j} \left[ \frac{\sigma_{i-1,j-1} \Delta x_{j-1} \Delta z_{i-1}}{4} + \frac{\sigma_{i,j-1} \Delta x_{j-1} \Delta z_i}{4} \right. \\ &\quad \left. + \frac{\sigma_{i,j} \Delta x_j \Delta z_i}{4} + \frac{\sigma_{i-1,j} \Delta x_j \Delta z_{i-1}}{4} \right], \\ &= \Lambda(\sigma_{i,j}, \Delta A_{i,j}) \tilde{\phi}_{i,j}. \end{aligned} \quad (2.22)$$

Substituting equation (2.21) and (2.22) into equation (2.19) and rearranging, we obtain

$$C_L^{ij} \tilde{\phi}_{i,j-1} + C_R^{ij} \tilde{\phi}_{i,j+1} + C_T^{ij} \tilde{\phi}_{i-1,j} + C_B^{ij} \tilde{\phi}_{i+1,j} + C_P^{ij} \tilde{\phi}_{i,j} = \frac{I}{2} \delta(x_s) \delta(z_s), \quad (2.23)$$

where

$$\begin{aligned}
C_L^{ij} &= - \left[ \frac{\Delta z_{i-1} \sigma_{i-1,j-1} + \Delta z_i \sigma_{i,j-1}}{2\Delta x_{j-1}} \right], \\
C_R^{ij} &= - \left[ \frac{\Delta z_{i-1} \sigma_{i-1,j} + \Delta z_i \sigma_{i,j}}{2\Delta x_j} \right], \\
C_T^{ij} &= - \left[ \frac{\Delta x_{j-1} \sigma_{i-1,j-1} + \Delta x_j \sigma_{i-1,j}}{2\Delta z_{i-1}} \right], \\
C_B^{ij} &= - \left[ \frac{\Delta x_{j-1} \sigma_{i,j-1} + \Delta x_j \sigma_{i,j}}{2\Delta z_i} \right], \\
C_P^{ij} &= - \left[ C_L^{ij} + C_R^{ij} + C_T^{ij} + C_B^{ij} - \Lambda(\sigma_{i,j}, \Delta A_{i,j}) \right], \\
\Lambda(\sigma_{i,j}, \Delta A_{i,j}) &= k_y^2 \left[ \frac{\sigma_{i-1,j-1} \Delta x_{j-1} \Delta z_{i-1}}{4} + \frac{\sigma_{i,j-1} \Delta x_{j-1} \Delta z_i}{4} \right. \\
&\quad \left. + \frac{\sigma_{i,j} \Delta x_j \Delta z_i}{4} + \frac{\sigma_{i-1,j} \Delta x_j \Delta z_{i-1}}{4} \right].
\end{aligned} \tag{2.24}$$

The parameter  $C_L^{ij}$ ,  $C_R^{ij}$ ,  $C_T^{ij}$ , and  $C_B^{ij}$  are coupling coefficients between nodes  $(i, j)$  and  $(i, j-1)$ ,  $(i, j+1)$ ,  $(i-1, j)$  and  $(i+1, j)$ , respectively, and  $C_P^{ij}$  is the self-coupling coefficient at node  $(i, j)$ . Equation (2.23) is called the self-adjoint difference equation that is derived for the interior node. The boundary nodes can be divided into 8 types which are

### Nodes located on the ground surface

The mesh region  $\Delta A_{i,j}$  is enclosed by the contour  $L_{i,j}$  defined by the sections  $iii, iv, v, vi, a$ , and  $b$  as shown in figure 2.9. For all nodes  $(1, j)$ ,  $j = 2, 3, \dots, N_x - 1$ , the discrete equation is given by

$$C_L^{ij} \tilde{\phi}_{i,j-1} + C_R^{ij} \tilde{\phi}_{i,j+1} + C_B^{ij} \tilde{\phi}_{i+1,j} + C_P^{ij} \tilde{\phi}_{i,j} = \frac{I}{2} \delta(x_s) \delta(z_s), \tag{2.25}$$

where

$$C_L^{ij} = - \left[ \frac{\Delta z_i \sigma_{i,j-1}}{2\Delta x_{j-1}} \right], \tag{2.26}$$

$$C_R^{ij} = - \left[ \frac{\Delta z_i \sigma_{i,j}}{2\Delta x_j} \right], \tag{2.27}$$

$$C_B^{ij} = - \left[ \frac{\Delta x_{j-1} \sigma_{i,j-1} + \Delta x_j \sigma_{i,j}}{2\Delta z_i} \right], \tag{2.28}$$

$$C_P^{ij} = - \left[ C_L^{ij} + C_R^{ij} + C_B^{ij} - \Lambda(\sigma_{i,j}, \Delta A_{i,j}) \right], \tag{2.29}$$

and

$$\Lambda(\sigma_{i,j}, \Delta A_{i,j}) = k_y^2 \left[ \frac{\sigma_{i,j-1} \Delta x_{j-1} \Delta z_i}{4} + \frac{\sigma_{i,j} \Delta x_j \Delta z_i}{4} \right]. \tag{2.30}$$

### Nodes located on the top-left and the top-right corners

For the top-left  $(1, 1)$  node and top-right  $(1, N_x)$ , the mesh region  $\Delta A_{i,j}$  is bounded by sections  $(iii, iv, c, \text{ and } b)$  and  $(v, vi, a, \text{ and } c)$ , respectively. The component of  $\mathbf{J}$  in the  $z$ -direction satisfies the Neumann condition and the component of  $\mathbf{J}$  in the  $x$ -direction satisfies the mixed boundary condition

$$\alpha(x, z)\tilde{\phi} \cos \theta + \frac{\partial \tilde{\phi}}{\partial \eta} = 0, \quad (2.31)$$

where  $\eta$  is the angle between the radial distance  $r$  from the source to the node  $(i, j)$  and the outward normal in  $x$ -direction. The discrete equation for the top-left corner node becomes

$$C_R^{ij} \tilde{\phi}_{i,j+1} + C_B^{ij} \tilde{\phi}_{i+1,j} + C_P^{ij} \tilde{\phi}_{i,j} = \frac{I}{2} \delta(x_s) \delta(z_s), \quad (2.32)$$

where

$$C_R^{ij} = - \left[ \frac{\Delta z_i \sigma_{i,j}}{2 \Delta x_j} \right], \quad (2.33)$$

$$C_B^{ij} = - \left[ \frac{\Delta x_j \sigma_{i,j}}{2 \Delta z_i} \right], \quad (2.34)$$

$$C_P^{ij} = - \left[ C_R^{ij} + C_B^{ij} - \Lambda(\sigma_{i,j}, \Delta A_{i,j}) \right] + \frac{\Delta z_i \sigma_{i,j} \alpha \cos \theta}{2}, \quad (2.35)$$

and

$$\Lambda(\sigma_{i,j}, \Delta A_{i,j}) = k_y^2 \left( \frac{\sigma_{i,j} \Delta x_j \Delta z_i}{4} \right). \quad (2.36)$$

For the top-right corner node, we get

$$C_L^{ij} \tilde{\phi}_{i,j-1} + C_B^{ij} \tilde{\phi}_{i+1,j} + C_P^{ij} \tilde{\phi}_{i,j} = \frac{I}{2} \delta(x_s) \delta(z_s), \quad (2.37)$$

where

$$C_L^{ij} = - \left[ \frac{\Delta z_i \sigma_{i,j-1}}{2 \Delta x_{j-1}} \right], \quad (2.38)$$

$$C_B^{ij} = - \left[ \frac{\Delta x_{j-1} \sigma_{i,j-1}}{2 \Delta z_i} \right], \quad (2.39)$$

$$C_P^{ij} = - \left[ C_L^{ij} + C_B^{ij} - \Lambda(\sigma_{i,j}, \Delta A_{i,j}) \right] + \frac{\Delta z_i \sigma_{i,j-1} \alpha \cos \theta}{2}, \quad (2.40)$$

and

$$\Lambda(\sigma_{i,j}, \Delta A_{i,j}) = k_y^2 \left( \frac{\sigma_{i,j-1} \Delta x_{j-1} \Delta z_i}{4} \right). \quad (2.41)$$

### Nodes located on the bottom edge

For nodes  $(N_z, j)$ ,  $j = 2, 3, \dots, N_x - 1$ , the region  $\Delta A_{i,j}$  is bounded by sections  $i, ii, b, a, vii$ , and  $viii$  and its discrete equation is

$$C_L^{ij} \tilde{\phi}_{i,j-1} + C_R^{ij} \tilde{\phi}_{i,j+1} + C_T^{ij} \tilde{\phi}_{i-1,j} + C_P^{ij} \tilde{\phi}_{i,j} = \frac{I}{2} \delta(x_s) \delta(z_s), \quad (2.42)$$

where

$$C_L^{ij} = - \left[ \frac{\Delta z_{i-1} \sigma_{i-1,j-1}}{2\Delta x_{j-1}} \right], \quad (2.43)$$

$$C_R^{ij} = - \left[ \frac{\Delta z_{i-1} \sigma_{i-1,j}}{2\Delta x_j} \right], \quad (2.44)$$

$$C_T^{ij} = - \left[ \frac{\Delta x_{j-1} \sigma_{i-1,j-1} + \Delta x_j \sigma_{i-1,j}}{2\Delta z_{i-1}} \right], \quad (2.45)$$

$$C_P^{ij} = - \left[ C_L^{ij} + C_R^{ij} + C_T^{ij} - \Lambda(\sigma_{i,j}, \Delta A_{i,j}) \right] + \left( \frac{\Delta x_{j-1} \sigma_{i-1,j-1} + \Delta x_j \sigma_{i-1,j}}{2} \right) \alpha \cos \theta, \quad (2.46)$$

and

$$\Lambda(\sigma_{i,j}, \Delta A_{i,j}) = k_y^2 \left[ \frac{\sigma_{i-1,j-1} \Delta x_{j-1} \Delta z_{i-1}}{4} + \frac{\sigma_{i-1,j} \Delta x_j \Delta z_{i-1}}{4} \right]. \quad (2.47)$$

### Nodes located on the bottom-left and bottom-right corner

For the bottom-left  $(N_z, 1)$  node and the bottom-right  $(N_z, N_x)$  node, the region  $\Delta A_{i,j}$  is bounded by the sections  $(i, ii, b, \text{and } d)$  and  $(d, a, vii, \text{and } viii)$ , respectively. Applying the mixed boundary condition, the discrete equation for the bottom-left is

$$C_R^{ij} \tilde{\phi}_{i,j+1} + C_T^{ij} \tilde{\phi}_{i-1,j} + C_P^{ij} \tilde{\phi}_{i,j} = \frac{I}{2} \delta(x_s) \delta(z_s), \quad (2.48)$$

where

$$C_R^{ij} = - \left[ \frac{\Delta z_{i-1} \sigma_{i-1,j}}{2\Delta x_j} \right], \quad (2.49)$$

$$C_T^{ij} = - \left[ \frac{\Delta x_j \sigma_{i-1,j}}{2\Delta z_{i-1}} \right], \quad (2.50)$$

$$C_P^{ij} = - \left[ C_R^{ij} + C_T^{ij} - \Lambda(\sigma_{i,j}, \Delta A_{i,j}) \right] + \left( \frac{\Delta x_j \sigma_{i-1,j}}{2} \right) \alpha \cos \theta_1 + \left( \frac{\Delta z_{i-1} \sigma_{i-1,j}}{2} \right) \alpha \cos \theta_2, \quad (2.51)$$

and

$$\Lambda(\sigma_{i,j}, \Delta A_{i,j}) = k_y^2 \left[ \frac{\sigma_{i-1,j} \Delta x_j \Delta z_{i-1}}{4} \right]. \quad (2.52)$$

$\theta_2$  and  $\theta_1$  are the angles between the radial distance  $r$  from the source and the  $x$ - and  $z$ -directions, respectively. For the bottom-right corner node, we get

$$C_L^{ij} \tilde{\phi}_{i,j-1} + C_T^{ij} \tilde{\phi}_{i-1,j} + C_P^{ij} \tilde{\phi}_{i,j} = \frac{I}{2} \delta(x_s) \delta(z_s), \quad (2.53)$$

where

$$C_L^{ij} = - \left[ \frac{\Delta z_{i-1} \sigma_{i-1,j-1}}{2\Delta x_{j-1}} \right], \quad (2.54)$$

$$C_T^{ij} = - \left[ \frac{\Delta x_{j-1} \sigma_{i-1,j-1}}{2\Delta z_{i-1}} \right], \quad (2.55)$$

$$C_P^{ij} = - \left[ C_L^{ij} + C_R^{ij} + C_T^{ij} - \Lambda(\sigma_{i,j}, \Delta A_{i,j}) \right] + \left( \frac{\Delta x_{j-1} \sigma_{i-1,j-1}}{2} \right) \alpha \cos \theta_1 \\ + \left( \frac{\Delta z_{i-1} \sigma_{i-1,j-1}}{2} \right) \alpha \cos \theta_2, \quad (2.56)$$

and

$$\Lambda(\sigma_{i,j}, \Delta A_{i,j}) = k_y^2 \left[ \frac{\sigma_{i-1,j-1} \Delta x_{j-1} \Delta z_{i-1}}{4} \right]. \quad (2.57)$$

### Nodes located on the left boundary

For the nodes  $(i, 1), i = 2, 3, \dots, N_z - 1$ , the region  $\Delta A_{i,j}$  is bounded by the contour  $L_{i,j}$  with the sections  $i, ii, iii, iv, c$ , and  $d$ . Applying the mixed boundary condition, we get the discrete equation

$$C_R^{ij} \tilde{\phi}_{i,j+1} + C_T^{ij} \tilde{\phi}_{i-1,j} + C_B^{ij} \tilde{\phi}_{i+1,j} + C_P^{ij} \tilde{\phi}_{i,j} = \frac{I}{2} \delta(x_s) \delta(z_s), \quad (2.58)$$

where

$$C_R^{ij} = - \left[ \frac{\Delta z_{i-1} \sigma_{i-1,j} + \Delta z_i \sigma_{i,j}}{2 \Delta x_j} \right], \quad (2.59)$$

$$C_T^{ij} = - \left[ \frac{\Delta x_j \sigma_{i-1,j}}{2 \Delta z_{i-1}} \right], \quad (2.60)$$

$$C_B^{ij} = - \left[ \frac{\Delta x_j \sigma_{i,j}}{2 \Delta z_i} \right], \quad (2.61)$$

$$C_P^{ij} = - \left[ C_R^{ij} + C_T^{ij} + C_B^{ij} - \Lambda(\sigma_{i,j}, \Delta A_{i,j}) \right] + \frac{\Delta z_i \sigma_{i,j} + \Delta z_{i-1} \sigma_{i-1,j}}{2} \alpha \cos \theta, \quad (2.62)$$

and

$$\Lambda(\sigma_{i,j}, \Delta A_{i,j}) = k_y^2 \left[ \frac{\sigma_{i,j} \Delta x_j \Delta z_i}{4} + \frac{\sigma_{i-1,j} \Delta x_j \Delta z_{i-1}}{4} \right]. \quad (2.63)$$

### Nodes located on the right boundary

For the nodes  $(i, N_x), i = 2, 3, \dots, N_z - 1$ , the region  $\Delta A_{i,j}$  is bounded by the contour  $L_{i,j}$  with the sections  $d, c, v, vi, vii$ , and  $viii$ . Applying the mixed boundary condition, we get the discrete equation

$$C_L^{ij} \tilde{\phi}_{i,j-1} + C_T^{ij} \tilde{\phi}_{i-1,j} + C_B^{ij} \tilde{\phi}_{i+1,j} + C_P^{ij} \tilde{\phi}_{i,j} = \frac{I}{2} \delta(x_s) \delta(z_s), \quad (2.64)$$

where

$$C_L^{ij} = - \left[ \frac{\Delta z_{i-1} \sigma_{i-1,j-1} + \Delta z_i \sigma_{i,j-1}}{2 \Delta x_{j-1}} \right], \quad (2.65)$$

$$C_T^{ij} = - \left[ \frac{\Delta x_{j-1} \sigma_{i-1,j-1}}{2 \Delta z_{i-1}} \right], \quad (2.66)$$

$$C_B^{ij} = - \left[ \frac{\Delta x_{j-1} \sigma_{i,j-1}}{2 \Delta z_i} \right], \quad (2.67)$$

$$C_P^{ij} = - \left[ C_L^{ij} + C_T^{ij} + C_B^{ij} - \Lambda(\sigma_{i,j}, \Delta A_{i,j}) \right] + \frac{\Delta z_i \sigma_{i,j-1} + \Delta z_{i-1} \sigma_{i-1,j-1}}{2} \alpha \cos \theta, \quad (2.68)$$

and

$$\Lambda(\sigma_{i,j}, \Delta A_{i,j}) = k_y^2 \left[ \frac{\sigma_{i-1,j-1} \Delta x_{j-1} \Delta z_{i-1}}{4} + \frac{\sigma_{i,j-1} \Delta x_{j-1} \Delta z_i}{4} \right]. \quad (2.69)$$

The self-adjoint difference equations are the “discrete equations” for the FD method. By applying the discrete equations to all nodes  $(i, j)$ , we obtain a set of simultaneous equations which can be written in the matrix form

$$\mathbf{C} \tilde{\Phi} = \mathbf{s}, \quad (2.70)$$

where  $\mathbf{C}$  is the coefficient matrix or “capacitance” matrix,  $\tilde{\Phi}$  is the potential vector, and  $\mathbf{s}$  is the source vector. The capacitance matrix is a 5-band sparse matrix as shown in figure 2.10 and its size is equal to  $N_T \times N_T$  where  $N_T$  is the number of nodes in the whole domain. The capacitance matrix is a function only of geometry, physical property

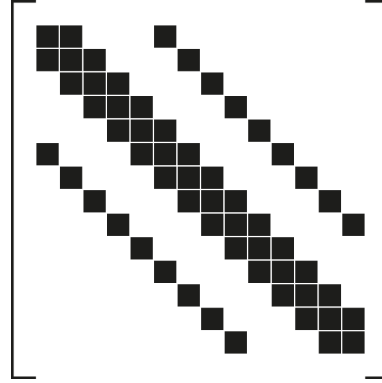


Figure 2.10: the sparsity pattern of the capacitance matrix  $\mathbf{C}$ .

distribution, and wavenumber  $k_y$ . Here we use  $LU$ -factorization to decompose  $\mathbf{C}$ , and then use backward and forward substitutions to solve the system.

### 2.3.3 Finite Element Method

In order to solve equation (2.16) with the FE method, the conductivity model is divided into many subdomains and each subdomain is called “element”. For the 2D problem, the common shape of a finite element is triangular because it easily handles any complex shape. Figure 2.11 represents two triangular elements which are used for dividing the conductivity model. In the FE method, one rectangle used in the FD method is divided into two triangular elements that are the upper and lower elements. For the “left-slope” triangular element as shown in figure 2.11a, the upper element is bounded by nodes  $(i, j)$ ,  $(i + 1, j + 1)$ , and  $(i, j + 1)$  while the lower element is bounded by nodes  $(i, j)$ ,  $(i + 1, j)$ , and  $(i + 1, j + 1)$ . For the “right-slope” triangular element as shown in figure 2.11b, the upper element is bounded by nodes  $(i, j)$ ,  $(i + 1, j)$ , and  $(i, j + 1)$  while the lower element is bounded by nodes  $(i + 1, j)$ ,  $(i + 1, j + 1)$ , and  $(i, j + 1)$ .

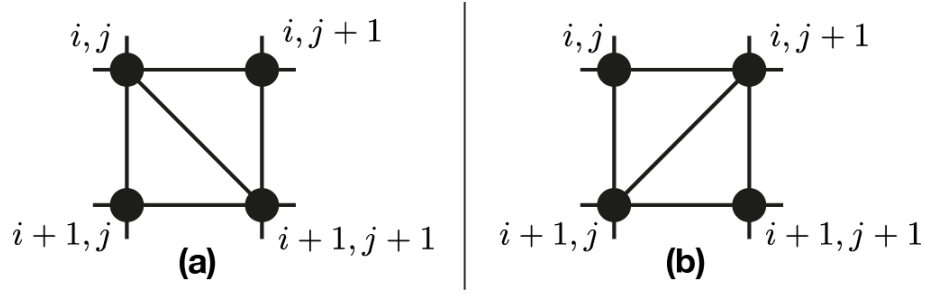


Figure 2.11: shows (a) “left-slope” triangular element and (b) “right-slope” triangular element.

Figure 2.12 illustrates an example of the conductivity model discretized by “left-slope” triangular elements. The conductivity  $\sigma_{i,j}^L$  indicates the conductivity in the lower triangular element bounded by nodes  $(i, j)$ ,  $(i+1, j)$ , and  $(i+1, j+1)$  and conductivity  $\sigma_{i,j}^U$  indicates the conductivity in the upper triangular element bounded by nodes  $(i, j)$ ,  $(i+1, j+1)$ , and  $(i, j+1)$ . By dividing the conductivity model with “left-slope” triangular elements only, node  $(i, j)$  is connected by nodes  $(i-1, j-1)$ ,  $(i, j-1)$ ,  $(i+1, j)$ ,  $(i+1, j+1)$ ,  $(i, j+1)$ , and  $(i-1, j)$ . In the contrast, if the conductivity model is divided with “right-slope” triangular elements only as shown in figure 2.13, node  $(i, j)$  is connected by nodes  $(i, j-1)$ ,  $(i+1, j-1)$ ,  $(i+1, j)$ ,  $(i, j+1)$ ,  $(i-1, j+1)$ , and  $(i-1, j)$ . Unlike the FD method, the node  $(i, j)$  of the FE method can connect to the neighboring node from 4 to 8 nodes depending on the discretization around the node  $(i, j)$ . Figure 2.14 shows the discretization that produces the maximum node connection and figure 2.15 shows the discretization that produces the minimum node connection. Due to the variation of discretization, FE method has no explicit

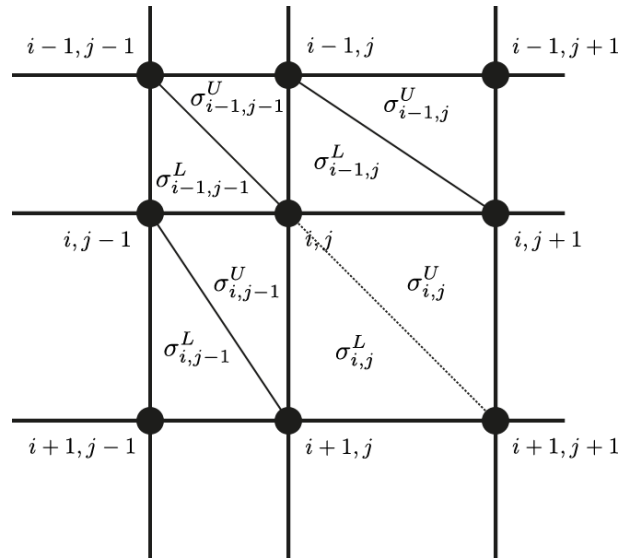


Figure 2.12: an example of the problem domain divided by “left-slope” triangular elements.

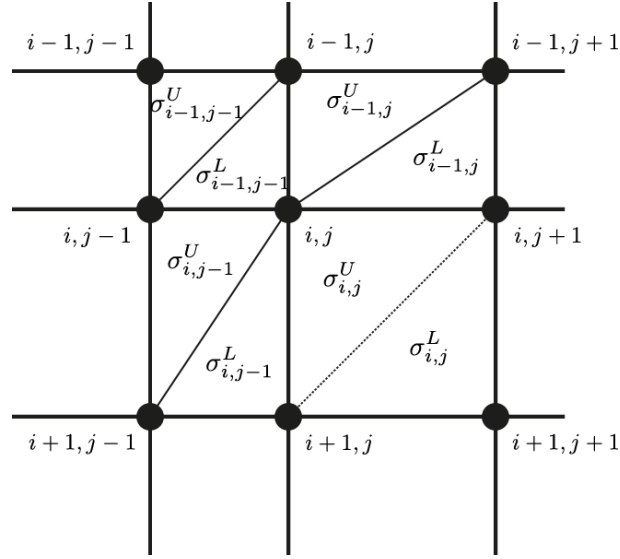


Figure 2.13: an example of the problem domain divided by “right-slope” triangular elements.

expression as equation (2.23) in the FD method. The common method for constructing the system of equations for the whole domain as equation (2.70) in the FD method is constructing the system of equations for each elements and then assembling the matrix elements into the global matrix which is the system of equations for the whole domain.

To derive an equation for constructing the matrix elements, we start by considering a subdomain shown in figure 2.16. The element has three nodes of which the corresponding coordinate values  $(x_i, z_i)$  and the nodal variables  $(\tilde{\phi}_i)$  are assigned.

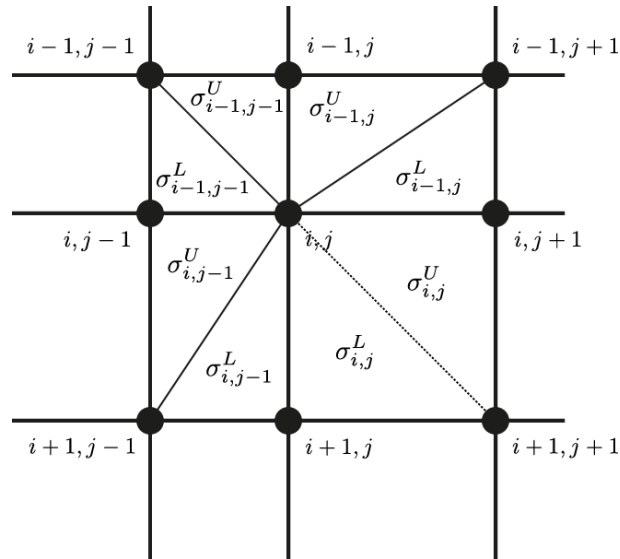


Figure 2.14: an example of the problem domain divided by a mix of “left-slope” and “right-slope” triangular elements that produces a maximum node connection.





where

$$A = \frac{1}{2} \begin{vmatrix} 1 & x_1 & z_1 \\ 1 & x_2 & z_2 \\ 1 & x_3 & z_3 \end{vmatrix}. \quad (2.74)$$

The magnitude of  $A$  is equal to the area of the linear triangular element. Its value is positive if the element node is numbered in the counter-clockwise direction, and vice versa. For the finite element method, the numbering direction has to be the same for every element in the domain.

Substituting the solution of equation (2.73) into equation (2.71), we obtain

$$\begin{aligned} \tilde{u}(x, k_y, z) &= \gamma_1(x, z)\tilde{\phi}_1 + \gamma_2(x, z)\tilde{\phi}_2 + \gamma_3(x, z)\tilde{\phi}_3, \\ &= \sum_{i=1}^3 \gamma_i(x, z)\tilde{\phi}_i, \end{aligned} \quad (2.75)$$

where  $\gamma$  is the shape function for the linear triangular element which can be expressed in the local coordinate system as

$$\begin{aligned} \gamma_1 &= \frac{1}{2A} [(x_2 z_3 - x_3 z_2) + (z_2 - z_3)x + (x_3 - x_2)z], \\ \gamma_2 &= \frac{1}{2A} [(x_3 z_1 - x_1 z_3) + (z_3 - z_1)x + (x_1 - x_3)z], \\ \gamma_3 &= \frac{1}{2A} [(x_1 z_2 - x_2 z_1) + (z_1 - z_2)x + (x_2 - x_1)z]. \end{aligned} \quad (2.76)$$

These shape function satisfy the conditions

$$\gamma_i(x_j, z_j) = \delta_{ij}, \quad (2.77)$$

where  $\delta$  is the Kronecker delta function and

$$\sum_{i=1}^3 \gamma_i = 1. \quad (2.78)$$

Substituting  $\tilde{u}(x, k_y, z)$  into equation (2.16), we obtain

$$R = \nabla \cdot [\sigma(x, z) \nabla \tilde{u}] - k_y^2 \sigma(x, z) \tilde{u} + \tilde{Q} \delta(x_s) \delta(z_s). \quad (2.79)$$

Because  $\tilde{u}(x, k_y, z)$  is not the exact solution, the residual  $R$  is not, in general, zero. Hence the residual doesn't vanish everywhere in the subdomain. To reduce the error, the method of weighted residuals (MWR) is applied. The notion in the MWR is to force the residual to zero in some average sense over the domain. That is

$$\int_{\Omega} w_i R d\Omega = 0 \quad \text{for } i = 1, \dots, n, \quad (2.80)$$

where  $w_i$  is the weight function, and  $n$  is the number of nodal variables  $\tilde{\phi}_i$ . For a triangular element as in our case,  $n$  is 3 for each subdomain. MWR can be divided into

5 methods corresponding to the weight function (Grandin, 1991). These five methods are (1) the collocation method, (2) subdomain method, (3) the least squares method, (4) the Galerkin method, and (5) the method of moment. Here, the Galerkin method is used for determining the weight function. For the Galerkin method, the weight function is the derivative of the trial function  $\tilde{u}$  with respect to the nodal variable  $\tilde{\phi}_i$ ,

$$w_i = \frac{\partial \tilde{u}}{\partial \tilde{\phi}_i} = \gamma_i. \quad (2.81)$$

Consider the subdomain  $\Omega^{(e)}$  for which the conductivity  $\sigma^{(e)}$  is, in general, constant the MWR equation can be written as

$$\sigma^{(e)} \int_{\Omega^{(e)}} w_i \nabla^2 \tilde{u} d\Omega^{(e)} - \sigma^{(e)} \int_{\Omega^{(e)}} w_i k_y^2 \tilde{u} d\Omega^{(e)} + \int_{\Omega^{(e)}} w_i \tilde{Q} \delta(x_s) \delta(z_s) d\Omega^{(e)} = 0. \quad (2.82)$$

Consider  $\int_{\Omega^{(e)}} w_i \frac{\partial^2 \tilde{u}}{\partial x^2} d\Omega^{(e)}$ . The domain integral can be rewritten as

$$\int_{\Omega^{(e)}} w_i \frac{\partial^2 \tilde{u}}{\partial x^2} d\Omega^{(e)} = \int_{z_1}^{z_2} \left( \int_{x_1}^{x_2} w_i \frac{\partial^2 \tilde{u}}{\partial x^2} dx \right) dz.$$

Applying integration by parts with respect to  $x$ , we obtain

$$\int_{\Omega^{(e)}} w_i \frac{\partial^2 \tilde{u}}{\partial x^2} d\Omega^{(e)} = - \int_{z_1}^{z_2} \left( \int_{x_1}^{x_2} \frac{\partial w_i}{\partial x} \frac{\partial \tilde{u}}{\partial x} dx \right) dz + \int_{z_1}^{z_2} \left[ w_i \frac{\partial \tilde{u}}{\partial x} \right]_{x_2}^{x_1} dz.$$

Rewriting the expression using the domain and boundary integrations results in

$$\int_{\Omega^{(e)}} w_i \frac{\partial^2 \tilde{u}}{\partial x^2} d\Omega^{(e)} = - \int_{\Omega^{(e)}} \frac{\partial w_i}{\partial x} \frac{\partial \tilde{u}}{\partial x} d\Omega^{(e)} + \oint w_i \frac{\partial \tilde{u}}{\partial x} \mathbf{n}_x d\Gamma^{(e)}, \quad (2.83)$$

where  $\mathbf{n}_x$  is the  $x$ -component of the unit normal vector which is positive in the outward direction and the boundary integral is positive in the counter-clockwise direction, and  $\Gamma^{(e)}$  is the boundary of the subdomain  $\Omega^{(e)}$ .

Similarly,  $\int_{\Omega^{(e)}} w_i \frac{\partial^2 \tilde{u}}{\partial z^2} d\Omega^{(e)}$  can be written as

$$\int_{\Omega^{(e)}} w_i \frac{\partial^2 \tilde{u}}{\partial z^2} d\Omega^{(e)} = - \int_{\Omega^{(e)}} \frac{\partial w_i}{\partial z} \frac{\partial \tilde{u}}{\partial z} d\Omega^{(e)} + \oint w_i \frac{\partial \tilde{u}}{\partial z} \mathbf{n}_z d\Gamma^{(e)}, \quad (2.84)$$

Combining equation (2.83) with (2.84), we obtain

$$\int_{\Omega^{(e)}} w_i \nabla^2 \tilde{u} d\Omega^{(e)} = - \int_{\Omega^{(e)}} \left( \frac{\partial w_i}{\partial x} \frac{\partial \tilde{u}}{\partial x} + \frac{\partial w_i}{\partial z} \frac{\partial \tilde{u}}{\partial z} \right) d\Omega^{(e)} + \oint w_i \frac{\partial \tilde{u}}{\partial \mathbf{n}} d\Gamma^{(e)}, \quad (2.85)$$

where

$$\frac{\partial \tilde{u}}{\partial \mathbf{n}} = \frac{\partial \tilde{u}}{\partial x} \mathbf{n}_x + \frac{\partial \tilde{u}}{\partial z} \mathbf{n}_z.$$

Substituting equation (2.85) into equation (2.82), we obtain

$$\begin{aligned} & - \sigma^{(e)} \int_{\Omega^{(e)}} \left( \frac{\partial w_i}{\partial x} \frac{\partial \tilde{u}}{\partial x} + \frac{\partial w_i}{\partial z} \frac{\partial \tilde{u}}{\partial z} \right) d\Omega^{(e)} + \sigma^{(e)} \oint w_i \frac{\partial \tilde{u}}{\partial \mathbf{n}} d\Gamma^{(e)} \\ & - \sigma^{(e)} \int_{\Omega^{(e)}} w_i k_y^2 \tilde{u} d\Omega^{(e)} + \int_{\Omega^{(e)}} w_i \tilde{Q} \delta(x_s) \delta(z_s) d\Omega^{(e)} = 0. \end{aligned} \quad (2.86)$$

From the mixed boundary condition (2.18), the second term of equation (2.86) becomes

$$\sigma^{(e)} \oint w_i \frac{\partial \tilde{u}}{\partial \mathbf{n}} d\Gamma^{(e)} = - \int_{\Gamma^{(e)}} w_i \beta^{(e)} \tilde{u} d\Gamma^{(e)}.$$

Therefore equation (2.86) is rewritten as

$$\begin{aligned} & \sigma^{(e)} \int_{\Omega^{(e)}} \left( \frac{\partial w_i}{\partial x} \frac{\partial \tilde{u}}{\partial x} + \frac{\partial w_i}{\partial z} \frac{\partial \tilde{u}}{\partial z} \right) d\Omega^{(e)} + \int_{\Gamma^{(e)}} w_i \beta^{(e)} \tilde{u} d\Gamma^{(e)} \\ & + \sigma^{(e)} \int_{\Omega^{(e)}} w_i k_y^2 \tilde{u} d\Omega^{(e)} = \int_{\Omega^{(e)}} w_i \tilde{Q} \delta(x_s) \delta(z_s) d\Omega^{(e)}. \end{aligned} \quad (2.87)$$

Substituting equation (2.75) into equation (2.87) and applying the Galerkin method, we obtain

$$\begin{aligned} & \sum_{j=1}^3 \left[ \int_{\Omega^{(e)}} \sigma^{(e)} \nabla \gamma_i \cdot \nabla \gamma_j d\Omega^{(e)} + \int_{\Gamma^{(e)}} \beta^{(e)} \gamma_i \gamma_j d\Gamma^{(e)} + k_y^2 \int_{\Omega^{(e)}} \sigma^{(e)} \gamma_i \gamma_j d\Omega^{(e)} \right] \tilde{\phi}_j \\ & = \int_{\Omega^{(e)}} \frac{I}{2} \delta(x_s) \delta(z_s) \gamma_i d\Omega^{(e)} \quad \text{for } i = 1, \dots, 3. \end{aligned} \quad (2.88)$$

This equation can be written in matrix form as

$$(\mathbf{A}^{(e)} + \mathbf{B}^{(e)} + \mathbf{C}^{(e)}) \tilde{\mathbf{\Phi}}^{(e)} = \mathbf{F}^{(e)}, \quad (2.89)$$

where

$$\begin{aligned} A_{ij}^{(e)} &= \int_{\Omega^{(e)}} \sigma^{(e)} \nabla \gamma_i \cdot \nabla \gamma_j d\Omega^{(e)}, \\ B_{ij}^{(e)} &= \int_{\Gamma^{(e)}} \beta^{(e)} \gamma_i \gamma_j d\Gamma^{(e)}, \\ C_{ij}^{(e)} &= k_y^2 \int_{\Omega^{(e)}} \sigma^{(e)} \gamma_i \gamma_j d\Omega^{(e)}, \text{ and} \\ F_i^{(e)} &= \int_{\Omega^{(e)}} \frac{I}{2} \delta(x_s) \delta(z_s) \gamma_i d\Omega^{(e)}. \end{aligned}$$

Substituting the shape function (equation (2.76)) into equation (2.89) and evaluating the integration following (Gabàs, 2003), we obtain

$$\begin{aligned} A_{ij}^{(e)} &= \int_{\Omega^{(e)}} \sigma^{(e)} \nabla \gamma_i \cdot \nabla \gamma_j d\Omega^{(e)}, \\ &= \frac{\sigma^{(e)}}{4A} (b_i b_j + c_i c_j), \end{aligned} \quad (2.90)$$

where  $A$  is the area of the element calculated by  $A = \frac{1}{2} (c_i b_j - b_i c_j)$ ,  $b_1 = x_3 - x_2$ ,  $c_1 = z_3 - z_2$ , and the other constants are obtained by cyclic permutations.

$$B_{ij}^{(e)} = \int_{\Gamma^{(e)}} \beta^{(e)} \gamma_i \gamma_j d\Gamma^{(e)} = \begin{cases} 0 & \text{if } (x, z) \in \Gamma, \\ \frac{\beta^{(e)}}{6} L^{(e)} (1 + \delta_{ij}) & \text{if } (x, z) \notin \Gamma. \end{cases} \quad (2.91)$$

where  $L^{(e)}$  is the length of  $\Gamma^{(e)}$ , and  $\Gamma$  is the boundary of the whole computational domain.

$$\begin{aligned} C_{ij}^{(e)} &= k_y^2 \int_{\Omega^{(e)}} \sigma^{(e)} \gamma_i \gamma_j d\Omega^{(e)}, \\ &= \frac{1}{12} k_y^2 \sigma^{(e)} A (1 + \delta_{ij}). \end{aligned} \quad (2.92)$$

$$F_i^{(e)} = \int_{\Omega^{(e)}} \frac{I}{2} \delta(x_s) \delta(z_s) \gamma_i d\Omega^{(e)} = \begin{cases} 0 & \text{if } (x, z) \neq (x_s, z_s), \\ \frac{I}{2} & \text{if } (x, z) = (x_s, z_s). \end{cases} \quad (2.93)$$

We assemble the matrix elements and vector elements into the global matrix based on its the global-node number results in

$$\mathbf{K} \tilde{\Phi} = \mathbf{s}, \quad (2.94)$$

where  $\mathbf{K}$  is the coefficient matrix or “stiffness” matrix. Figure 2.17 shows an example of the stiffness matrix when the problem domain is discretized by “left-slope” triangular elements only. The stiffness matrix is only a function of geometry, physical property distribution, and wavenumber  $k_y$ . This is the same as with the capacitance matrix. As with FD, we use  $LU$ -factorization to decompose  $\mathbf{K}$ , and then use backward and forward substitutions to solve the system.

Both the rectangular FD and the right triangular FE define potential nodes at the same locations (Figure 2.9 and 2.12). For the same mesh, the number of unknowns  $\tilde{\phi}$  for both FE and FD would therefore be the same. The matrices  $\mathbf{C}$  and  $\mathbf{K}$  thus have the same dimension. However, since  $\mathbf{C}$  has only five bands, while  $\mathbf{K}$  has seven, the number of non-zero coefficients of FD is less than that of FE. Thus, FD would theoretically require smaller storage than FE. In addition, the calculation time for decomposing and solving (2.70) would be expected to be less than that for (2.94).

### 2.3.4 Wavenumber $k_y$ selection

After solving equation (2.70) or (2.94), we obtain the vector of transformed electric potential  $\tilde{\Phi}$ . In order to calculate electric potential  $\phi$  at a particular point  $p$ , the inverse Fourier transform is applied at the point. In theory, inverse the Fourier transform has to use an infinite number of wavenumbers  $k_y$  to calculate the electric potential (equation (2.15)). Here, the optimization approach proposed by Xu *et al.* (2000) is used for calculating the inverse Fourier transform. Following the optimization approach, the electric potential  $\phi$  is a linear combination of the transformed electric potential  $\tilde{\phi}$

$$\phi(x, z) = \sum_{p=1}^n \tilde{\phi}(r, k_{y_p}) g_p, \quad (2.95)$$

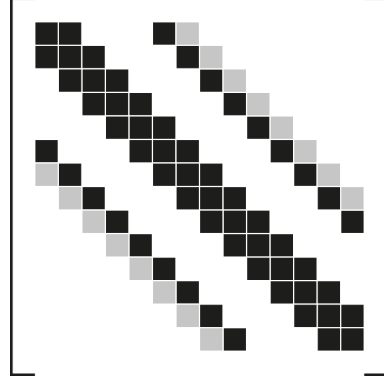


Figure 2.17: the sparsity pattern of the stiffness matrix  $\mathbf{K}$  when the problem domain is discretized by “left-slope” triangular element. The sparsity pattern of  $\mathbf{K}_k$  is close to the sparsity pattern of  $\mathbf{C}$  except that has two extra bands (gray) which correspond to the top-left and bottom-right nodes.

where  $n$  is the number of wavenumbers, and  $g_p$  is the weighting parameter. For the homogeneous half-space earth, the electric potential is a function of the earth resistivity  $\rho$  and the radial distance  $r = \sqrt{x^2 + y^2 + z^2}$  as shown in equation (2.3). Substituting equation (2.3) into equation (2.14), we obtain

$$\begin{aligned}\tilde{\phi}(x, k_y, z) &= \int_0^\infty \frac{\rho \cos(k_y y)}{2\pi \sqrt{x^2 + y^2 + z^2}} dy, \\ &= \frac{\rho}{2\pi} K_0(k_y \tilde{r}),\end{aligned}\tag{2.96}$$

where  $\tilde{r} = \sqrt{x^2 + z^2}$  is the radial distance in the transformed space. Substituting (2.3) and (2.96) into equation (2.15) and setting  $y$  equal to 0, we get

$$\frac{1}{\tilde{r}} = \frac{2}{\pi} \int_0^\infty K_0(k_y \tilde{r}) dk_y.\tag{2.97}$$

Rewriting equation (2.97) as a sum, we obtain

$$\frac{1}{\tilde{r}} \approx \sum_{p=1}^n K_0(k_{y_p} \tilde{r}) g_p.\tag{2.98}$$

In order to obtain the same relative errors for different values of  $\tilde{r}$ , equation (2.98) can be rewritten as

$$1 = \tilde{r}_h \sum_{p=1}^n K_0(k_{y_p} \tilde{r}_h) g_p = \nu_h,\tag{2.99}$$

and, in the matrix form as

$$\mathbf{E}\mathbf{g} = \boldsymbol{\nu},\tag{2.100}$$

where  $E_{h,p} = \tilde{r}_h K_0(\tilde{r}_h k_{y_p})$ . The values of  $k_{y_p}$  and  $g_p$  are computed by minimizing the objective function  $\Theta$ ,

$$\Theta = (\mathbf{I} - \boldsymbol{\nu})^T (\mathbf{I} - \boldsymbol{\nu}) = (\mathbf{I} - \mathbf{E}\mathbf{g})^T (\mathbf{I} - \mathbf{E}\mathbf{g}),\tag{2.101}$$

where  $\mathbf{I}$  is a unit column vector.

There are two steps for selection of  $k_{yp}$  and  $g_p$ . The first step is to determine the values of  $g_p$  from the given set of  $k_{yp}$ . For a given set of  $k_{yp}$ , a set of  $g_p$  can be determined by differentiating the objective function  $\Theta$  with respect to  $\mathbf{g}$  and setting the result equal to zero. The differential form of  $\Theta$  is

$$d\Theta = 2d\mathbf{g}^T \mathbf{E}^T (\mathbf{I} - \mathbf{E}\mathbf{g}). \quad (2.102)$$

In general,  $d\mathbf{g}^T$  is not equal to zero; therefore

$$\mathbf{E}^T (\mathbf{I} - \mathbf{E}\mathbf{g}) = 0 \quad \text{or} \quad \mathbf{g} = \mathbf{B}^{-1} \mathbf{c}, \quad (2.103)$$

where  $\mathbf{B} = \mathbf{E}^T \mathbf{E}$ , and  $\mathbf{c} = \mathbf{E}^T \mathbf{I}$ . The  $\mathbf{g}$  calculated from equation (2.103) is a set of  $g_p$  corresponding to a given set of  $k_{yp}$ . When another set of wavenumbers is given, we will get another set of  $g_p$ .

After this, we obtain the set of  $g_p$  corresponding to the given set of wavenumbers,  $\mathbf{k}_y^0$ . The second step is to determine  $\mathbf{k}_y$  which make the objective function  $\Theta$  reach a global minimum. To do that, we expand  $\nu$  with a Taylor series expansion about a set of initial values  $\mathbf{k}_y^0$ , and take the first-order term in  $d\mathbf{k}_y$ ,

$$\nu = \nu_0 + \frac{\partial \nu}{\partial \mathbf{k}_y} d\mathbf{k}_y. \quad (2.104)$$

Substituting equation (2.104) into equation (2.101), we obtain

$$\Theta = (\mathbf{I} - \nu_0 + \frac{\partial \nu}{\partial \mathbf{k}_y} d\mathbf{k}_y)^T (\mathbf{I} - \nu_0 + \frac{\partial \nu}{\partial \mathbf{k}_y} d\mathbf{k}_y). \quad (2.105)$$

Differentiating  $\Theta$  with respect to  $d\mathbf{k}_y$  and setting its result equal to zero, we obtain the expression for computing the new set of wavenumber  $\mathbf{k}_y^1$  as

$$\mathbf{k}_y^1 = \mathbf{k}_y^0 + \mathbf{M}^{-1} \mathbf{H}, \quad (2.106)$$

where

$$\mathbf{M} = \left( \frac{\partial \nu}{\partial \mathbf{k}_y} \right)^T \left( \frac{\partial \nu}{\partial \mathbf{k}_y} \right),$$

and

$$\mathbf{H} = \left( \frac{\partial \nu}{\partial \mathbf{k}_y} \right)^T (\mathbf{I} - \nu_0).$$

The new set of wavenumbers,  $\mathbf{k}_y^1$ , might not reach the global minimum because equation (2.106) is an approximate formula. We can obtain the optimum set of wavenumbers by taking  $\mathbf{k}_y^1$  as a new set of the initial values  $\mathbf{k}_y^0$  and repeating the above process.

### 2.3.5 Accuracy Tests for Wavenumber Selection

Here, the optimization algorithm for wavenumbers is tested to do the inverse Fourier transform for the distance  $\tilde{r}$  of 1.0-30.0 meters. This range of  $\tilde{r}$  corresponds to the distance between the current and potential electrodes for the Wenner array with 48 electrodes, 1 meter electrode spacing, and 15 investigation depth levels. This range also covers the distance between the current and potential electrode for the Dipole-Dipole array with 28 investigation depth levels and also covers the distance between current and potential electrode for the Schlumberger array with 61 electrodes, 1 meter electrode spacing, and 30 investigation depth levels.

Table 2.1 shows the set of wavenumbers and its weighting parameters calculated by the optimization algorithm. Its relative error is less than 0.05% for a  $f$  of 1.0-30.0 meters and it slightly increases when the distance is over 30.0 meters as shown in figure 2.18. It shows that the results for the optimization algorithm not only works well in the input  $\tilde{r}$  but also functions for some distance outside the input region. For

$k_y$	$g$
1.00191499e-02	2.05845911e-02
9.61319787e-02	6.37489791e-01
1.01458177e-01	-6.21186137e-01
1.89791636e-01	1.67781685e-01
5.04297173e-01	2.22301411e-01
7.86306211e-01	2.34362843e-01
1.31297930e+00	1.62692691e-01
1.97520393e+00	1.22197461e+00

Table 2.1: The eight wavenumbers set and their weighting parameters  $g$  supporting distances from 1.0-30.0 meters

the other electrode spacing ( $a$ ), we generate the appropriate wavenumber set by simply dividing the set of wavenumbers and its weighting parameters in table 2.1 by  $a$ .

### 2.3.6 Validation and Numerical comparisons I

To validate our FD and FE codes, three synthetic models are used as shown in figure 2.21. Model A (figure 2.21a) mimics the situation of wet soil (conductive layer) lying on top of limestone (resistive layer) which is commonly found in the western part of Thailand. For any two-layer models, the structure can be described by 3 parameters which are the resistivity of the 1st layer  $\rho_1$ , the resistivity of the 2nd layer  $\rho_2$ , and the thickness of the 1st layer  $z$  as shown in figure 2.19. The analytic solution of the apparent resistivity  $\rho_a$  for Wenner, Schlumberger, Dipole-Dipole, and other 4-electrodes array is



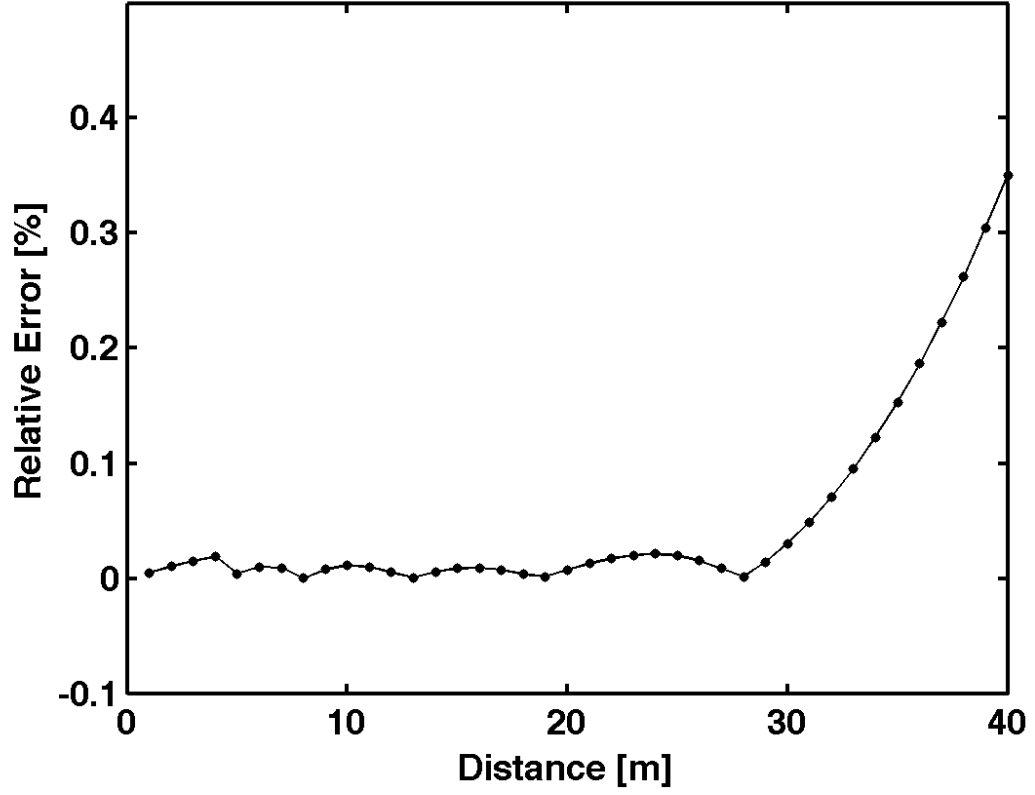
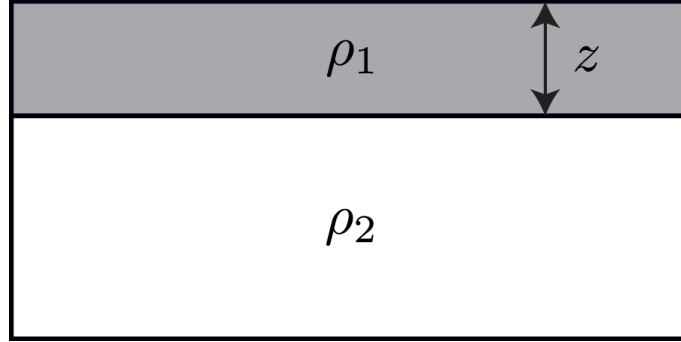
Figure 2.18: The relative error of  $\nu$  for distance  $\tilde{r}$  from 1.0-40.0 meters.

Figure 2.19: A schematic diagram of the general two-layers model.

given by

$$\rho_a = \rho_1 \left[ 1 + 2p \sum_{m=1}^{\infty} k^m \left\{ \frac{1}{(r_{\text{AM}}^2 + 4m^2 z^2)^{1/2}} - \frac{1}{(r_{\text{BM}}^2 + 4m^2 z^2)^{1/2}} - \frac{1}{(r_{\text{AN}}^2 + 4m^2 z^2)^{1/2}} + \frac{1}{(r_{\text{BN}}^2 + 4m^2 z^2)^{1/2}} \right\} \right] \quad (2.107)$$

where  $k = (\rho_2 - \rho_1) / (\rho_2 + \rho_1)$ ,  $p = \{1/r_{\text{AM}} - 1/r_{\text{BM}} - 1/r_{\text{AN}} + 1/r_{\text{BN}}\}^{-1}$ , and  $r$  is distance between the electrodes as shown in figure 2.2.

Model B resembles a vertical fault or boundary between two different rocks with resistive rock on one side and conductive rock on another side (figure 2.21b). The analytic solution of the model B can be divided into five situations, depending on the electrode positions with respect to the contact as shown in figure 2.20.

For the Wenner and Schlumberger arrays, the analytical solutions for model B are as follows.

(1) All electrodes on left-hand side:

$$\begin{aligned} \rho_a = \rho_1 p \left[ \left( \frac{1}{r_{AM}} - \frac{1}{r_{BM}} \right) - \left( \frac{1}{r_{AN}} - \frac{1}{r_{BN}} \right) \right. \\ \left. + k \left\{ \left( \frac{1}{2s - r_{AM}} - \frac{1}{2s - 2r_{AM} - r_{BM}} \right) \right. \right. \\ \left. \left. - \left( \frac{1}{2s - r_{AN}} - \frac{1}{2s - 2r_{AN} - r_{BN}} \right) \right\} \right], \end{aligned} \quad (2.108)$$

(2) Electrode **B** on the right-hand side:

$$\begin{aligned} \rho_a = \rho_1 p \left[ \left( \frac{1}{r_{AM}} - \frac{1}{r_{BM}} \right) - \left( \frac{1}{r_{AN}} - \frac{1}{r_{BN}} \right) \right. \\ \left. + k \left\{ \left( \frac{1}{2s - r_{AM}} - \frac{1}{r_{BM}} \right) - \left( \frac{1}{2s - r_{AN}} - \frac{1}{r_{BN}} \right) \right\} \right], \end{aligned} \quad (2.109)$$

(3) Electrode **B** and **N** on the right-hand side:

$$\begin{aligned} \rho_a = \rho_1 p \left[ \left( \frac{1}{r_{AM}} - \frac{1}{r_{BM}} \right) - k^* \left( \frac{1}{r_{AN}} - \frac{1}{r_{BN}} \right) \right. \\ \left. + k \left\{ \left( \frac{1}{2s - r_{AM}} - \frac{1}{r_{BM}} \right) \right. \right. \\ \left. \left. + k^* \left( \frac{1}{r_{AN}} - \frac{1}{2r_{AN} + r_{BN} - 2s} \right) \right\} \right], \end{aligned} \quad (2.110)$$

(4) Electrode **B**, **M** and **N** on the right-hand side:

$$\begin{aligned} \rho_a = \rho_1 p k^* \left[ \left( \frac{1}{r_{AM}} - \frac{1}{r_{BM}} \right) - \left( \frac{1}{r_{AN}} - \frac{1}{r_{BN}} \right) \right. \\ \left. - k \left\{ \left( \frac{1}{r_{AM}} - \frac{1}{2r_{AM} + r_{BM} - 2s} \right) \right. \right. \\ \left. \left. - \left( \frac{1}{r_{AN}} - \frac{1}{2r_{AN} + r_{BN} - 2s} \right) \right\} \right], \end{aligned} \quad (2.111)$$

(5) All electrodes on the right-hand side:

$$\begin{aligned} \rho_a = \rho_1 p k^* \left[ \left( \frac{1}{r_{AM}} - \frac{1}{r_{BM}} \right) - \left( \frac{1}{r_{AN}} - \frac{1}{r_{BN}} \right) \right. \\ \left. - k \left\{ \left( \frac{1}{2s + r_{AM}} - \frac{1}{2s + 2r_{AM} + r_{BM}} \right) \right. \right. \\ \left. \left. - \left( \frac{1}{2s + r_{AN}} - \frac{1}{2s + 2r_{AN} + r_{BN}} \right) \right\} \right], \end{aligned} \quad (2.112)$$

where  $s$  is the distance between the fault line and current electrode **A**, and

$$\begin{aligned} k &= (\rho_2 - \rho_1) / (\rho_2 + \rho_1), \\ k^* &= (1 + k) / (1 - k), \\ p &= \{1/r_{\mathbf{AM}} - 1/r_{\mathbf{BM}} - 1/r_{\mathbf{AN}} + 1/r_{\mathbf{BN}}\}^{-1}. \end{aligned} \quad (2.113)$$

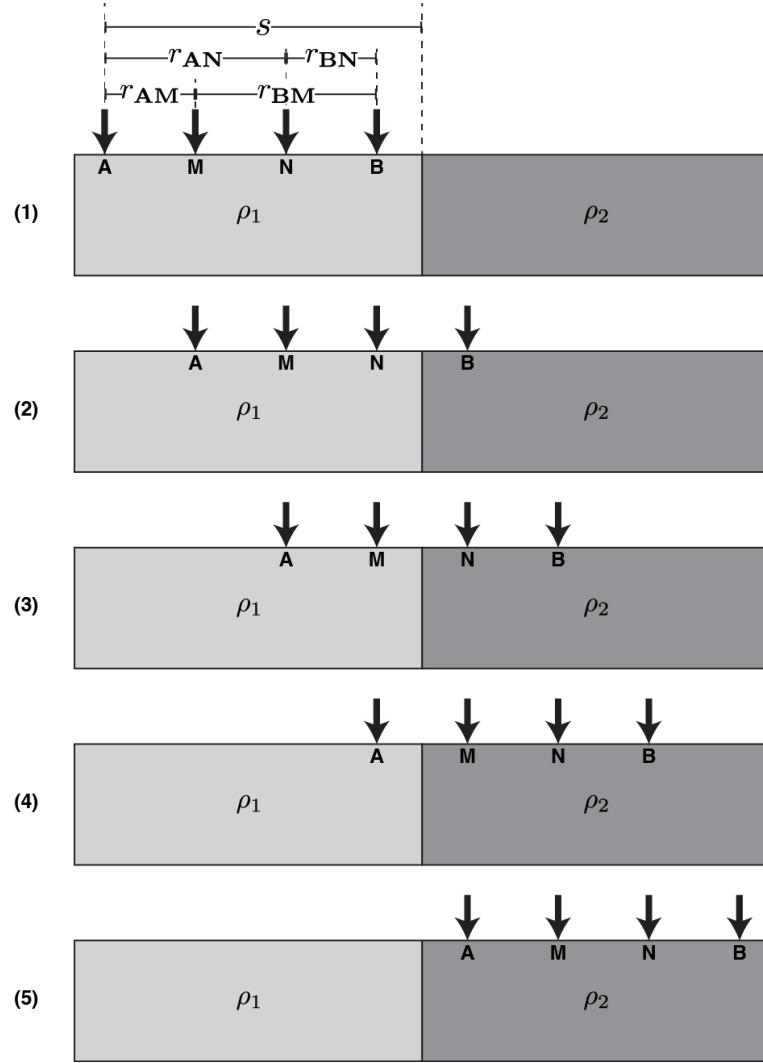


Figure 2.20: The five situations of four electrodes spread over a vertical contact. The first one is “all electrodes on the left-hand side”, the second one is “electrode **B**” on the right-hand side, the third one is “electrode **B** and **N** on the right-hand side”, the fourth one is “electrode **B**, **M** and **N** on the right-hand side” and the last one is “all electrodes on the right-hand side”.

For the Dipole-Dipole array (potential electrodes placed on the right-hand side of current electrodes),  $r_{\mathbf{AM}} = r_{\mathbf{BN}} = r$ ,  $r_{\mathbf{AN}} = r - l$ ,  $r_{\mathbf{BM}} = r + l$  where  $l$  is the distance between the pair of current electrodes. Then the analytic solution for a vertical-contact model is given by

(1) all four electrodes on the left-hand side

$$\rho_a \approx \rho_1 \left\{ 1 - \frac{kr^3}{(2s+r)^3} \right\}, \quad (2.114)$$

(2) dipole straddles contact:

$$\rho_a \approx \rho_1(1+k), \quad (2.115)$$

(3) all four electrodes on right:

$$\rho_a \approx \rho_1 k^* \left\{ 1 - \frac{kr^3}{(2s+r)^3} \right\}, \quad (2.116)$$

The last model (model C) consists of two different anomalies buried in a host layer (figure 2.21c). In this model, there is no analytical solution. Commercial software (RES2DMOD; Loke & Barker (1996)) is therefore used to generate the solutions for comparison. In all models, 48 electrodes are deployed at the surface with 1m spacing. Three configurations (Schlumberger, Wenner and DipoleDipole arrays) are used to generate the apparent resistivities up to 15 levels ( $n = 115$ ). To compare and validate the responses, a relative error  $\xi$  is used as an index to describe the accuracy of the codes and is defined as

$$\xi = \frac{1}{N} \sum_{i=1}^N \frac{|\rho_a^{\text{cal}} - \rho_a^{\text{true}}|}{\rho_a^{\text{true}}} \times 100\%, \quad (2.117)$$

where  $N$  is the total number of data points,  $\rho_a^{\text{cal}}$  is the calculated apparent resistivity from our FD or FE by forward modeling routines, and  $\rho_a^{\text{true}}$  is the apparent resistivity from the analytical solution for models A and B and the numerical solution from RES2DMOD for model C. Pseudo-sections for all three configurations of models A, B, and C are illustrated in figure 2.22, 2.23, and 2.24, respectively. In theory, fine grid discretization would produce the most accurate result but would have resulted in a large CPU time and large memory requirements. This might prohibit a run on some complicated large models. It is therefore necessary to have an automatic mesh generation scheme which can generate an optimized mesh that requires less calculation time and memory but can still produce the responses at an acceptable level of accuracy.

In this section, we study the effect of grid discretization on FD and FE by using 8 wavenumbers (table 2.1). To calculate the responses with FD or FE, the model must be discretized as in figure 2.9 for FD or figure 2.12 for FE. In the vertical direction, the top layer spacing is set as  $0.025a$  where  $a$  is the electrode spacing. The spacing between the next layers is then logarithmically increased with depth to a maximum of about  $220a$ . With this technique, the number of blocks in the vertical direction for the models in figure 2.21 is set at 26 blocks as shown in table 2.3.6. For horizontal direction, the left and right boundaries are extended beyond the first and last electrodes to at least

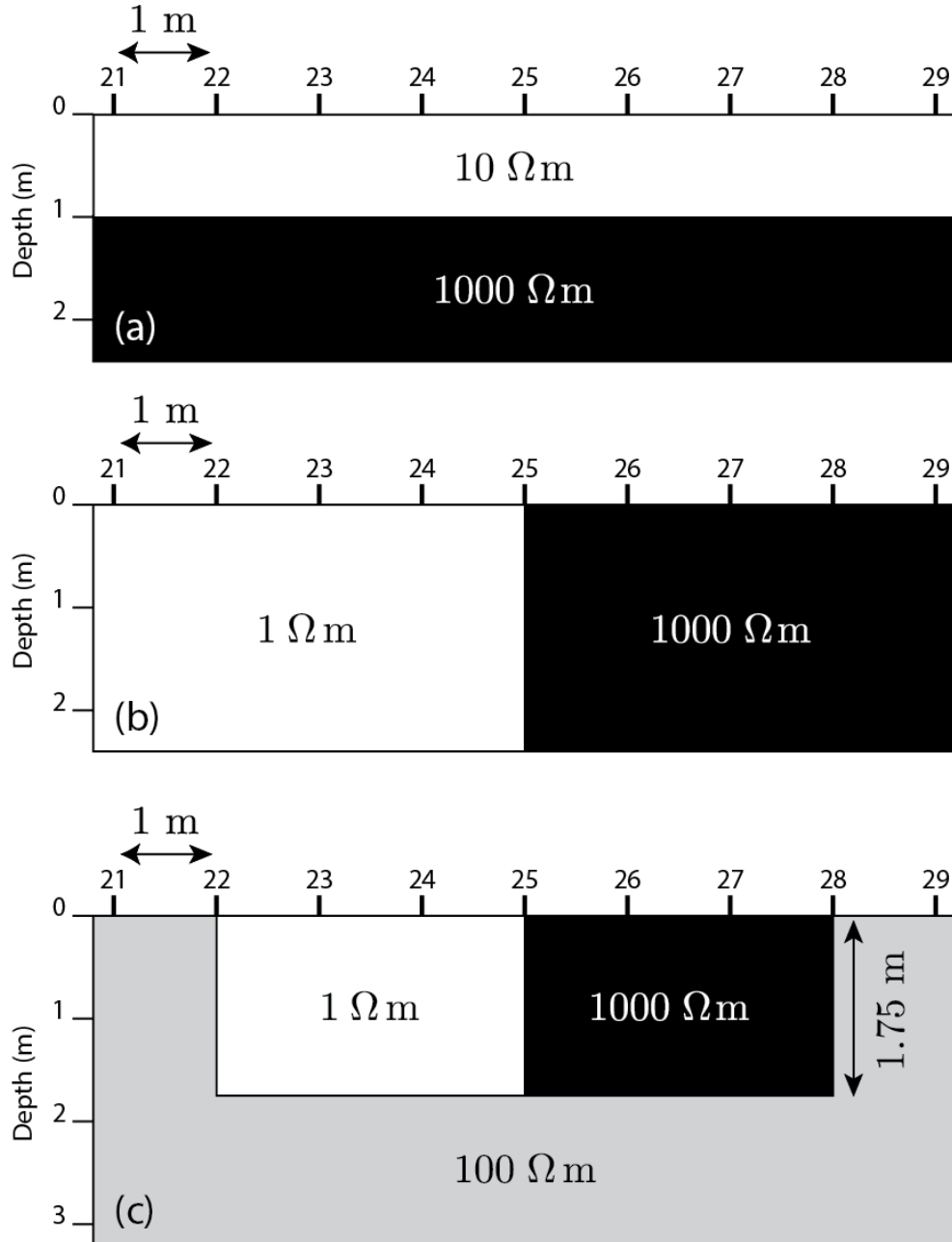


Figure 2.21: Non-topography models used to validate FD, FE and our hybrid methods. (a) Model A: wet soil (10  $\Omega\text{m}$ ) lying on top of a resistive limestone (1000  $\Omega\text{m}$ ). (b) Model B: two different rocks with a vertical boundary. The left side is conductive (1  $\Omega\text{m}$ ) and the right side is resistive (1000  $\Omega\text{m}$ ). (c) Model C: two different anomalies buried in a 100  $\Omega\text{m}$  half-space. The left and right anomalies are 1  $\Omega\text{m}$  and 1000  $\Omega\text{m}$ , respectively. Forty-eight electrodes are deployed at the surface with 1-m spacing for all models. Integers indicate the electrode number.

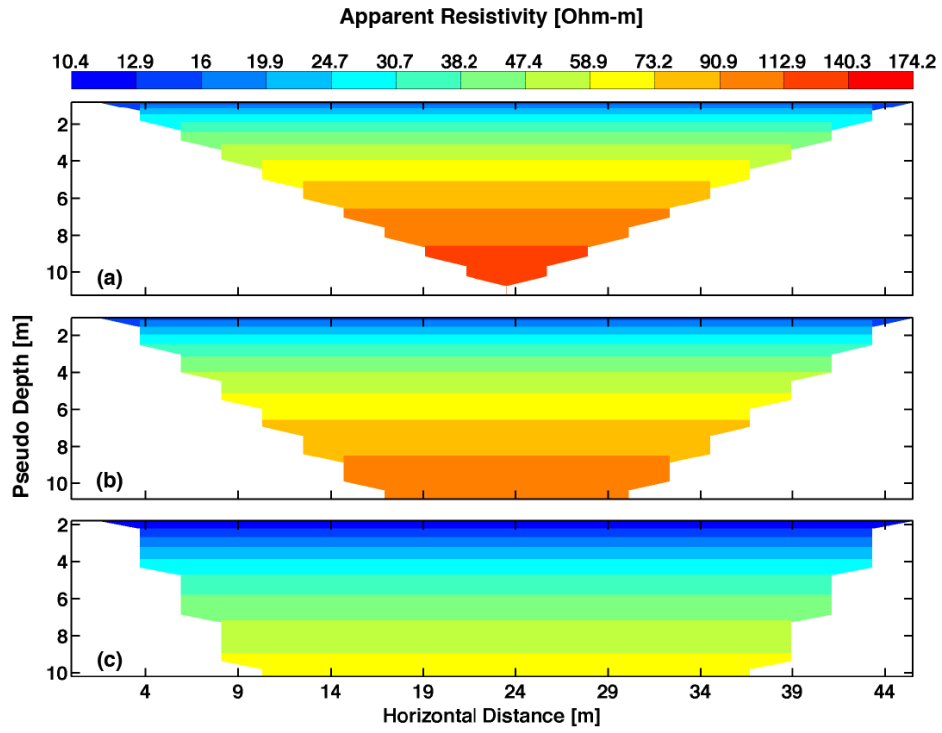


Figure 2.22: Pseudo-sections of model A (figure 2.21a) for (a) Wenner, (b) Schlumberger, and (c) Dipole-Dipole arrays.

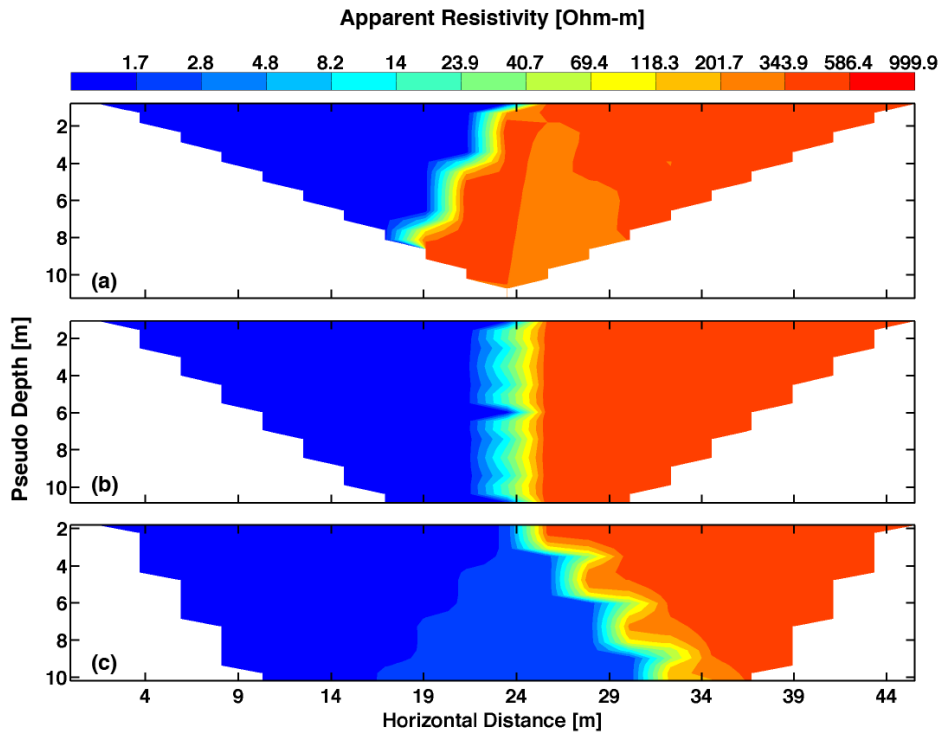


Figure 2.23: Pseudo-sections of model B (figure 2.21b) for (a) Wenner, (b) Schlumberger, and (c) Dipole-Dipole arrays.

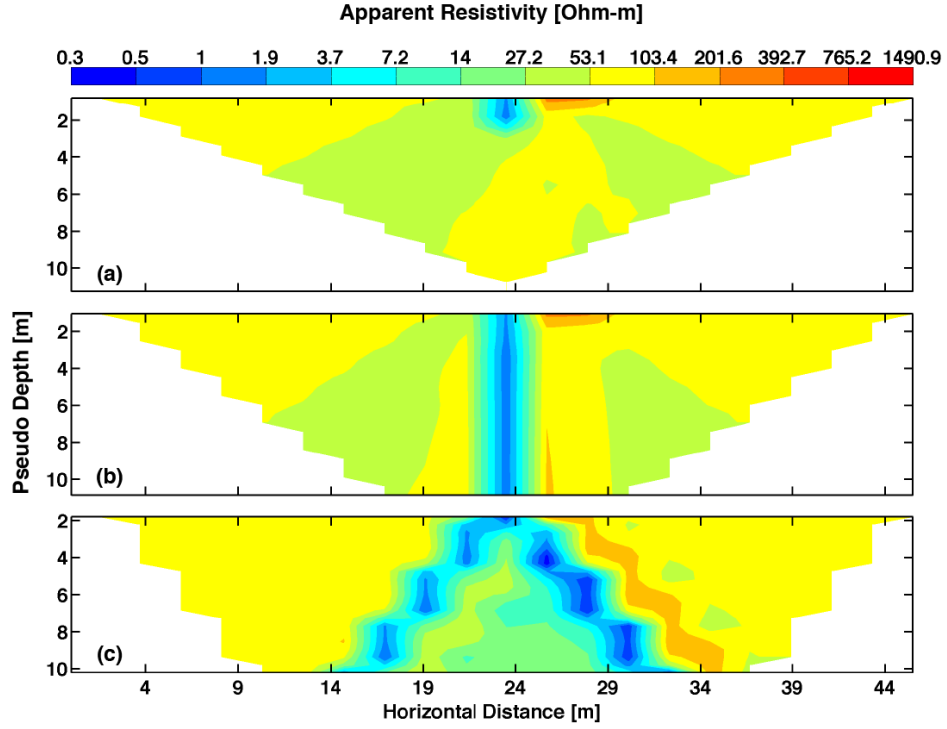


Figure 2.24: Pseudo-sections of model C (figure 2.21c) for (a) Wenner, (b) Schlumberger, and (c) Dipole-Dipole arrays.

about  $1000a$  to make sure that the current injection from the first and last electrodes would not interfere with the boundaries.

The grid spacing beyond the first and last electrodes increases exponentially to minimize the number of horizontal blocks. Between a pair of electrodes, a simple discretization is to divide the spacing equally into many different numbers of blocks. Here we present results from the studies of dividing the spacing distance between a pair of electrode into 2-blocks, 3-blocks and 4-blocks cases in the horizontal direction. This mesh generation led to a  $114 \times 26$  model in the  $x$ - and  $z$ -directions, respectively, for the 2-blocks case, and a  $161 \times 26$  model for the 3-blocks case, and a  $208 \times 26$  model for the 4-blocks case for all models. The number of unknowns at the nodes for both FD and FE would therefore be at 2990, 4374 and 5103 for  $114 \times 26$ ,  $161 \times 26$  and  $208 \times 26$  discretizations, respectively.

The number of unknowns for both methods are exactly the same but coefficient matrices  $\mathbf{C}$  and  $\mathbf{K}$  are still different as already described in the previous section. Because  $\mathbf{K}$  has two more bands than  $\mathbf{C}$ , the FE matrix  $\mathbf{K}$  has 32,723 non-zero terms while  $\mathbf{C}$  has 23,571 terms.  $\mathbf{K}$  therefore has about 38% more non-zero terms than  $\mathbf{C}$ . FE requires 3.29-3.62 times more CPU time than FD to solve the system of equations eight times (for  $8 k_y$ ). The relative errors of models A, B and C obtained when using the FD and FE methods with 2-blocks, 3-blocks and 4-blocks discretizations in the horizontal

Level	Depth [m]	Level	Depth [m]
<b>1</b>	0.025	<b>14</b>	3.700
<b>2</b>	0.050	<b>15</b>	4.545
<b>3</b>	0.075	<b>16</b>	5.815
<b>4</b>	0.100	<b>17</b>	7.715
<b>5</b>	0.125	<b>18</b>	10.570
<b>6</b>	0.500	<b>19</b>	14.850
<b>7</b>	0.750	<b>20</b>	21.270
<b>8</b>	1.000	<b>21</b>	30.900
<b>9</b>	1.350	<b>22</b>	45.350
<b>10</b>	1.735	<b>23</b>	67.002
<b>11</b>	2.160	<b>24</b>	99.525
<b>12</b>	2.625	<b>25</b>	148.280
<b>13</b>	3.135	<b>26</b>	221.815

Table 2.2: Vertical grid is used in the synthetic tests.

direction are 0.1-1.5% (Table 2.3.6). If the model is discretized with only 1 block per electrode pair, both FE and FD codes produce results with relative errors larger than 10% for all models. Using more than 5-blocks between a pair of electrodes, the accuracy is improved but is not significantly different from the 4-blocks case.

Although all the relative errors are at an acceptable level ( $\xi < 1\%$ ), it should be noted that FD is more accurate than FE for the 2- blocks case, the errors are comparable for the 3-blocks case, but FE is more accurate in the 4-blocks case. We also see that FD 2-blocks discretization is about as accurate as FE 3-blocks discretization. This result is very important and will be used for the mixed grid hybrid FD-FE method. However, in later section, we show that in the case of topography with a large slope, the number of blocks between a pair of electrodes must be increased.

### 2.3.7 Validation and Numerical comparisons II

In this section, FD and FE codes will be tested on models that include topography. Here, we mimic the situation of cavity detection in a karst terrain, where limestone is the base lithology whose variable erosion yields varying topography. The synthetic model contains extreme topography with two  $60^\circ$  hills (figure 2.25). Beneath the left hill is an air-filled high resistivity cavity and beneath the right hill there is a high conductivity zone. At greater depth, a high and a low resistivity structure are buried inside an otherwise homogeneous region with a resistivity of  $1000 \Omega\text{m}$ . 48 electrodes are deployed with 4 m horizontal spacing to cover a distance of 188 m. The three major configurations (Wenner, Schlumberger and Dipole-Dipole arrays) are used to test the accuracy and efficiency of the FD and FE codes.



Model	Method	#Block	Wenner	Schlumberger	Dipole	Time [s]
A (Fig. 2.21a)	FD	2	0.25	0.23	0.33	0.55
		3	0.15	0.15	0.27	0.83
		4	0.15	0.14	0.29	1.13
	FE	2	0.44	0.41	0.66	1.99
		3	0.18	0.17	0.26	2.85
		4	0.10	0.09	0.21	3.78
B (Fig. 2.21b)	FD	2	0.89	0.67	0.55	0.55
		3	0.76	0.58	0.44	0.83
		4	0.72	0.55	0.41	1.15
	FE	2	1.20	0.99	1.15	1.98
		3	0.66	0.51	0.57	2.87
		4	0.47	0.36	0.41	3.78
C (Fig. 2.21c)	FD	2	0.96	0.84	0.89	0.55
		3	0.81	0.72	0.49	0.83
		4	0.76	0.73	0.44	1.14
	FE	2	1.31	1.26	1.55	2.00
		3	0.75	0.67	0.71	2.86
		4	0.56	0.55	0.50	3.78

Table 2.3: The relative error [%] defined as  $(1/N) \sum_{i=1}^N (|\rho_a^{\text{cal}} - \rho_a^{\text{true}}|) / \rho_a^{\text{true}}$ , where  $\rho_a^{\text{true}}$  is true apparent resistivity from the analytical formula (model A and B), and from the RES2DMOD program (model C),  $\rho_a^{\text{cal}}$  is the apparent resistivity calculated from FD, or FE methods with 2-, 3- and 4-horizontal blocks between a pair of electrodes. Model A, B and C are shown in figure 2.21a-c, respectively.

The FD and FE methods use the same grid ( $209 \times 59$ ) which are discretized by an “automatic grid discretization” routine, but the FD method requires air layers on top of the Earth domain. As a result, the FD method has 12,331 unknown nodes whereas the FE methods have only 8,560. These unknown nodes result in 61,119 non-zero coefficients in the  $\mathbf{C}$  matrix of FD, and 58,982 in the  $\mathbf{K}$  matrix of FE. The potentials obtained from each method are then used to calculate the apparent resistivities for each configuration. The pseudo-section of the Wenner, Schlumberger, and Dipole-Dipole arrays are shown, respectively, in figures 2.26, 2.27, and 2.28 where (a) is for FD and (b) is for FE methods.

Generally, because FE can approximate the topography better than FD, the FE solution is therefore more accurate than FD as proven in Erdogan *et al.* (2008). For this model, there is no analytical formulation and it also cannot be solved by the RES2DMOD program. The apparent resistivity responses from the FE method are therefore used as the reference solution  $\rho_{\text{true}}$  for comparison.

Table 2.3.7 shows that relative errors of the apparent resistivity responses of the FD method range from 3% for the Wenner array to almost 8% for the Dipole-Dipole array although topography is incorporated. The inaccuracy of the FD method results

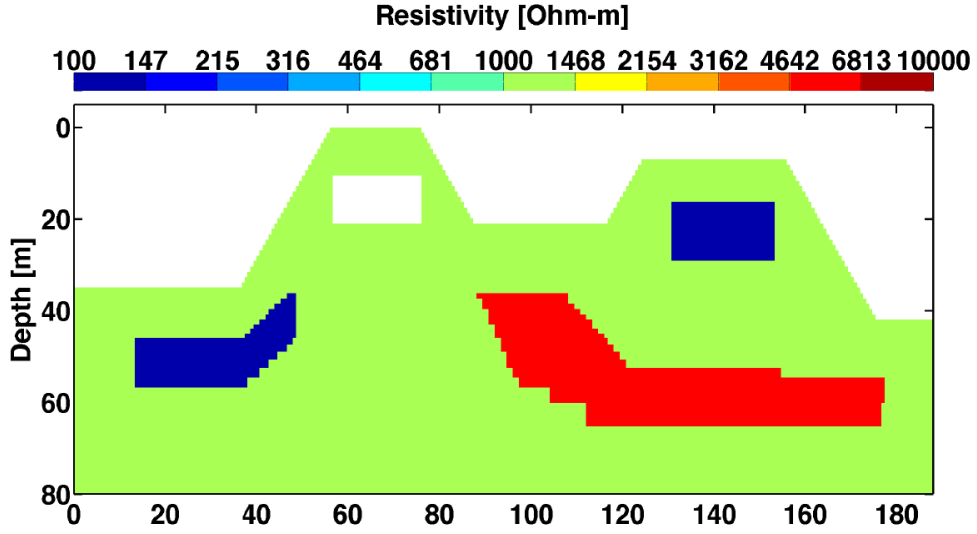


Figure 2.25: The extreme topography model with two steep hills and high contrast resistivity structures beneath. The white region is an air-filled cavity.

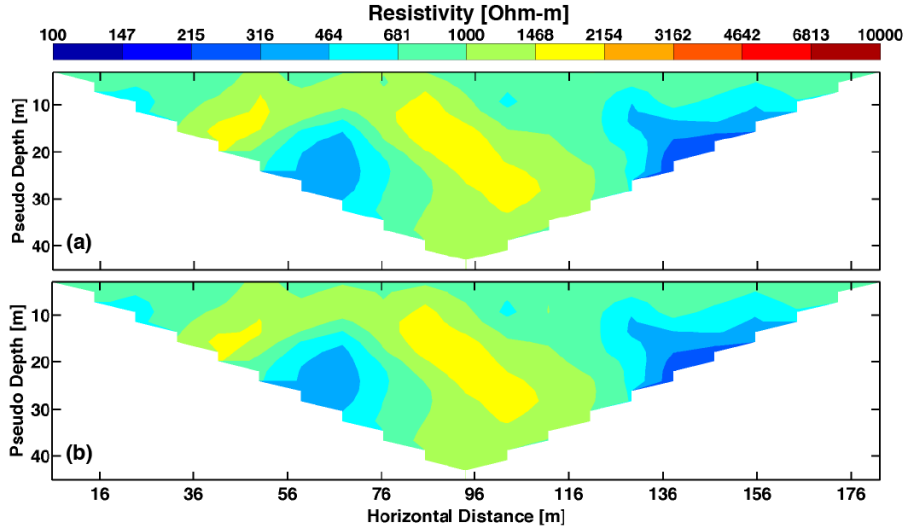


Figure 2.26: The pseudo-section of the extreme topography model for the Wenner array computed by the (a) FD method and (b) FE method.

from using a rectangular mesh to model the steeper slope which is not realistic. In theory, to increase the FD accuracy one must discretize the model domain more finely. This increases the number of the unknown nodes and consequently the CPU time and the memory requirement. However, in practice, even if we try to discretize the model domain more finely, particularly in the slope and the near surface region, we cannot obtain an error lower than 2%.

In terms of CPU time, the FE (without air) method requires 1.93 times more CPU time than the FD (with air) method. This is because the FE method doesn't have the explicit formula for forming its system of equations as with the FD method. The

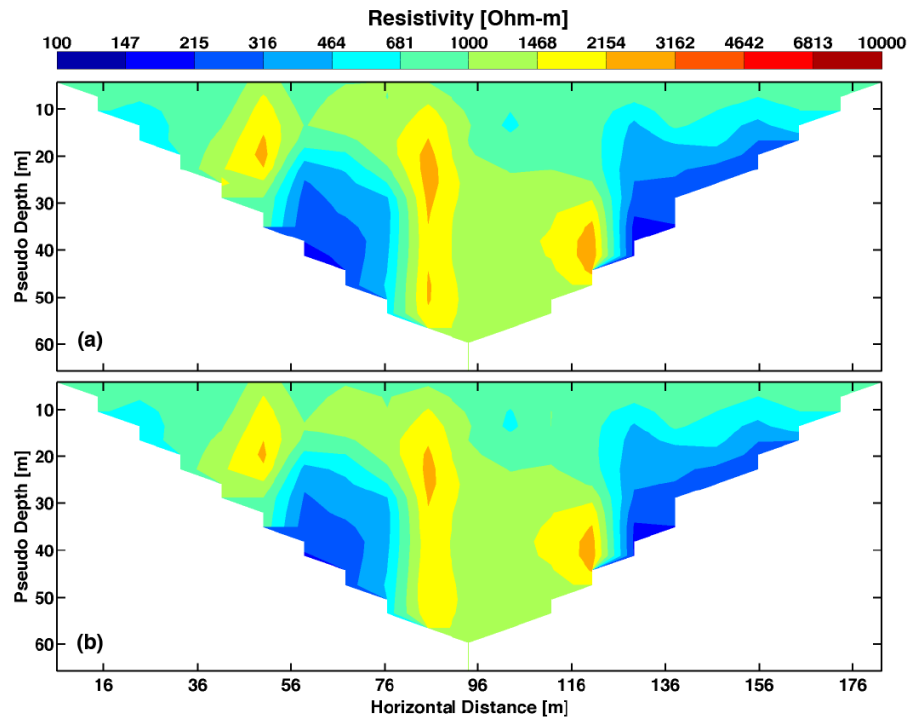


Figure 2.27: The pseudo-section of the extreme topography model for a Schlumberger array computed by the (a) FD method and (b) FE method.

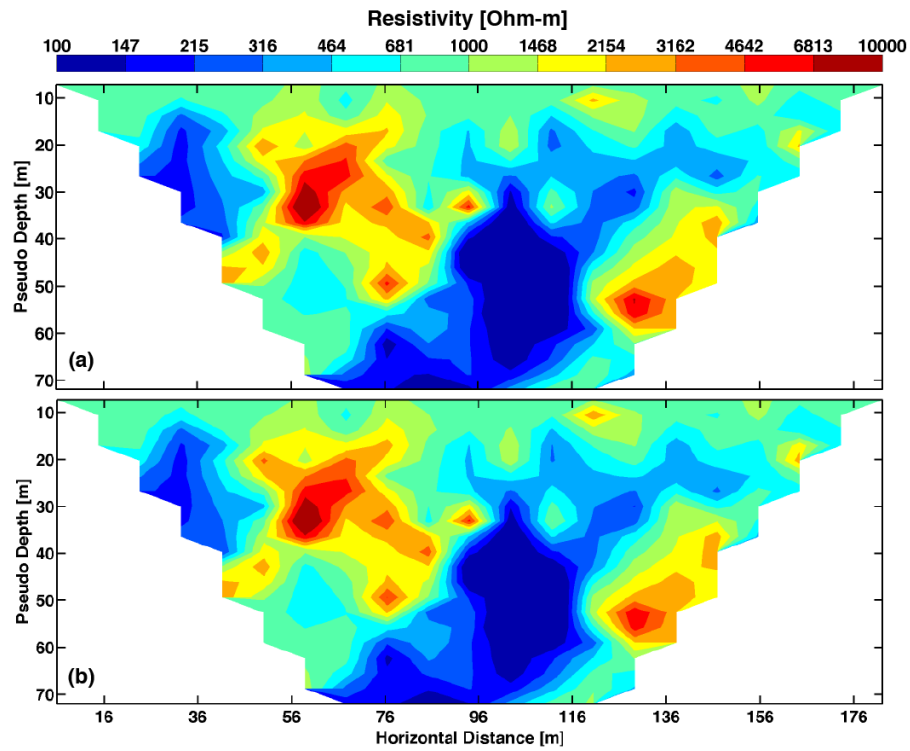


Figure 2.28: The pseudo-section of the extreme topography model for a Dipole-Dipole array computed by the (a) FD method and (b) FE method.

FE method requires a for loop to form its system of equations while the FD method forms its system of equations by using only matrix operations. In MATLAB, a matrix operation is more efficient than a for loop. For performing the same calculation, a matrix operation needs less CPU time than a for loop. 83.7-88.8% of the CPU time of FE method is for forming the stiffness matrix ( $\mathbf{K}$ ), while the rest is used to solve equation (2.94) for all eight wavenumbers. In contrast, the FE method without air requires a lot less memory than FD methods. The majority of the memory is used to store the  $\mathbf{L}$  and  $\mathbf{U}$  matrices for each wavenumber (as in Table 2.3.7). The storing of  $\mathbf{L}$  and  $\mathbf{U}$  makes the code most efficient when solving equation (2.70) or (2.94) with different right-hand sides.

This experiment shows that when topography exists, the FD method is still faster than the FE method but it produces inaccurate results and its memory requirement is greater than for the FE method.

Method	Accuracy Difference [%]			CPU time [s]
	Wenner	Schlumberger	Dipole-Dipole	
<b>FD</b>	3.13	5.33	7.82	3.35
<b>FE</b>	-	-	-	6.46

Table 2.4: The percentage accuracy difference and CPU time for all three arrays for testing the FD and FE forward modeling schemes.

Method	Memory Usage [MB]		
	C or $\mathbf{K}$ or $\alpha\mathbf{C} + \beta\mathbf{K}$	L or U	Total (for 8 $k_y$ )
<b>FD</b>	1.05	14.98	242.25
<b>FE</b>	0.99	8.83	145.68

Table 2.5: The memory usage for all three arrays for testing the FD and FE forward modeling schemes.

### 2.3.8 A hybrid finite difference and finite element method

The advantage of FD over FE was demonstrated in the previous section and has also been shown in Erdogan *et al.* (2008). However, when topography is present, the right triangular elements of FE are more suitable for modeling a surface with topography than the rectangular blocks of FD. FE therefore produces a more accurate result than FD (Erdogan *et al.*, 2008). Here we introduce a hybrid FD-FE method which combines the advantages of both FD and FE together, and avoids the deficiencies of both methods. The concept of hybrid methods are not new. They have been applied in various applications, e.g., in elastic wave modeling (Jianfeng & Tielinm, 2002; Galis *et al.*, 2008) and in hydrology (Simpson, 2003), among many others.

Both FD and FE are approximation methods. It has been proven that both FE and FD yield similar discrete approximations when applied to the same grid (see Zienkiewicz & Cheung, 1965). This is very crucial information for the hybrid method. If there are any large differences between both approximations, a hybrid method would be invalid. In this case, a transition zone from FD to FE and vice versa must be introduced similar to that of Galis *et al.* (2008).

To confirm this important point, the electrical potentials  $\tilde{\phi}_{\mathbf{FE}}$  and  $\tilde{\phi}_{\mathbf{FD}}$  at all nodes calculated with FE and FD methods, respectively, from the same pair of current injection electrodes were compared. One example generated from model A (figure 2.21a) and is plotted in figure 2.29. In all comparisons,  $\tilde{\phi}_{\mathbf{FD}}$  and  $\tilde{\phi}_{\mathbf{FE}}$  at all nodes are almost identical as shown in figure 2.29a and b, respectively. The maximum absolute differences between  $\tilde{\phi}_{\mathbf{FE}}$  and  $\tilde{\phi}_{\mathbf{FD}}$  are in the order of  $10^{-3}$  (figure 2.29c).

Due to the small discrepancies between  $\tilde{\phi}_{\mathbf{FE}}$  and  $\tilde{\phi}_{\mathbf{FD}}$ , it is reasonable to linearly combine equation (2.70) and (2.94) to form the single system of equations for the hybrid method,

$$(\alpha\mathbf{C} + \beta\mathbf{K})\tilde{\Phi} = \mathbf{s}, \quad (2.118)$$

where  $\alpha$  and  $\beta$  are diagonal matrices whose diagonal elements can be either 0 or 1. At node  $i$  (or row  $i$ ), if FD is used,  $\alpha_{ii} = 1$  and  $\beta_{ii} = 0$ . If FE is used at node  $i$ ,  $\alpha_{ii} = 0$  and  $\beta_{ii} = 1$ . If every node is approximated with FD, equation (2.118) reduces to equation (2.70), and similarly if every node is approximated with FE, equation (2.118) reduces to equation (2.94). Clearly, the system of equations (2.118) is not symmetric if both FD and FE grids are used. Similar to FD and FE, *LU*-factorization is used to decompose and solve equation (2.118).

To discretize the model with the hybrid technique, the model is first discretized with FD rectangular blocks (white circles in figure 2.30). Then, wherever there is topography, FE triangular elements (black circles in figure 2.30) are inserted to replace the FD rectangular blocks. Figure 2.30 shows that any kinds of topography can be easily modeled with left-diagonal or right-diagonal triangular elements. The left- and right-slope models (figure 2.30a and b) can be discretized at the slope with left- and right-diagonal triangular FE elements, respectively. For the ridge and valley models (figure 2.30c and d), we use both left-diagonal and right-diagonal triangular elements depending on the directions of the slopes. Since there are many more FD blocks than FE triangular elements, it seems likely that the hybrid method will maintain the advantages of FD in terms of computational resources, while gaining accuracy from FE when topography is present.

Figure 2.31 shows the example of hybrid grid discretization, its node-index system, and its element-index system. The node numbers for the hybrid method are

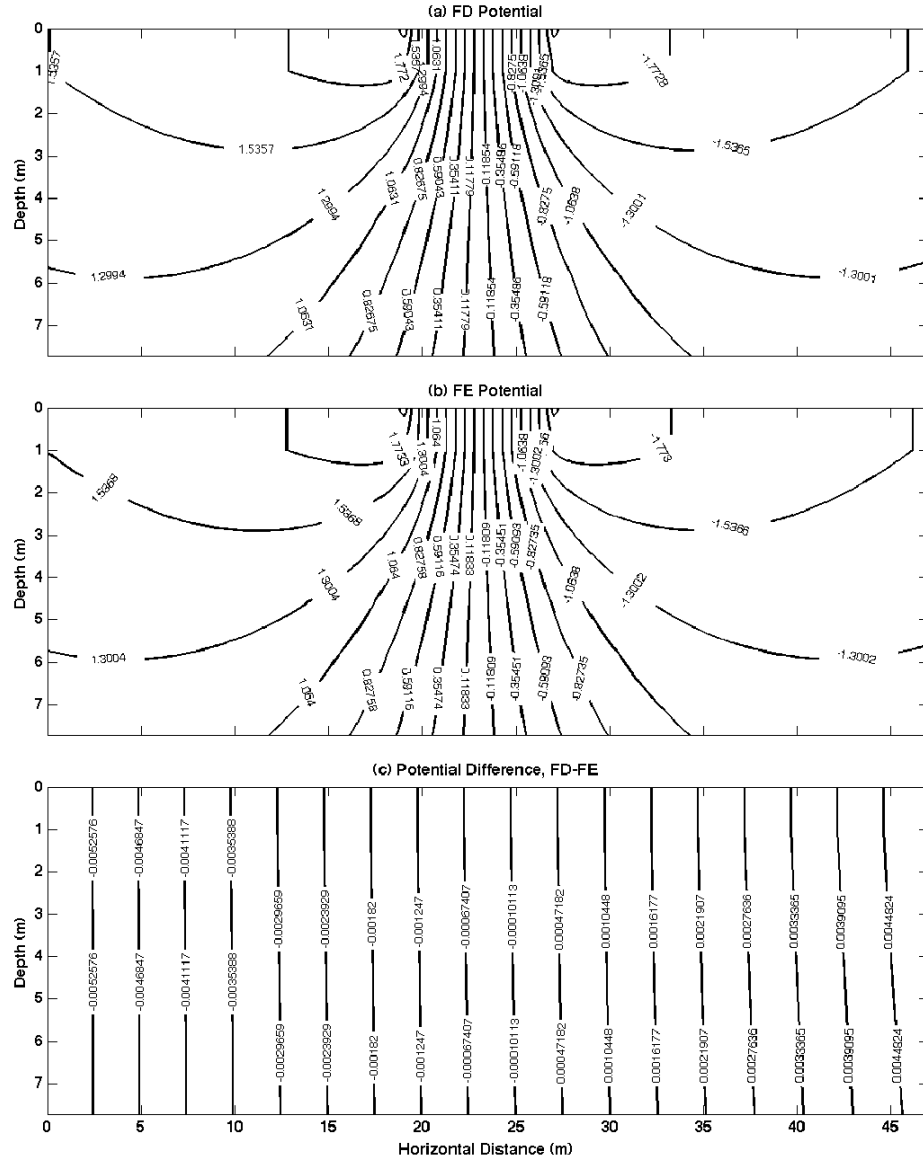


Figure 2.29: Contour plots of electrical potentials calculated from (a) FD method, (b) FE method and (c) their difference. Both are generated from the same pair of injecting current electrodes and the same boundary conditions. Notice that the maximum differences are in the order of  $10^{-3}$ .

indexed from top to bottom and left to right (figure 2.31). The element numbers are similarly indexed from top to bottom and left to right, but starting first with the FD elements and then the FE elements.

### Theoretical comparison

All three methods (FD, FE and HB) share the same number of unknowns for each model discretization. The coupling coefficient matrices ( $\mathbf{C}$ ,  $\mathbf{K}$  and  $\alpha\mathbf{C} + \beta\mathbf{K}$ ) therefore have the same dimension, but different numbers of non-zero coefficients. For

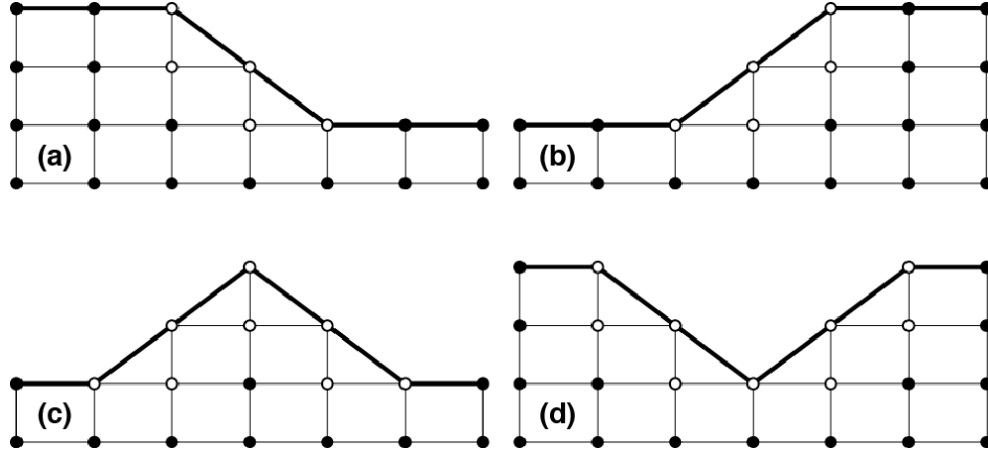


Figure 2.30: Examples of mixed FD and FE grids for our hybrid FD-FE method for (a) left-slope model, (b) right-slope model, (c) ridge model and (d) valley model. Solid white circles are FE nodes. Black circles are FD nodes. Topography is denoted by black solid lines.

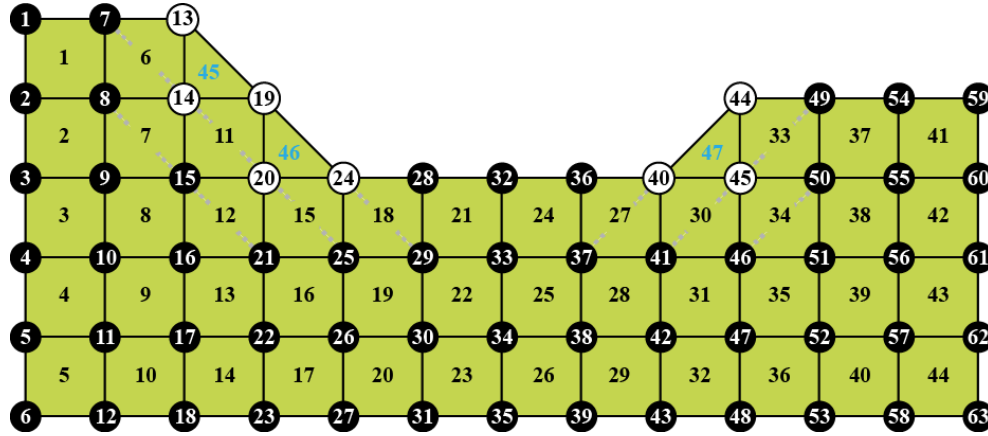


Figure 2.31: Grid discretization for the hybrid FD-FE method. The slope areas are discretized with FE (white nodes) and the others with FD (black nodes). Number of elements is given at the center of the rectangular or triangular elements. The number of nodes is indexed inside the black nodes for FD and the white nodes for FE (after Vachiratienchai & Siripunvaraporn, 2013).

a hybrid method, where FD and FE grids are mixed, the number of non-zero bands would be equal to that of FE, i.e. 7. However, because the majority of nodes are from FD, the number of non-zero entries would be less than that of FE and slightly more than that of FD. Hence the memory and CPU time requirements of the hybrid method should be slightly more than that of FD, but less than that of FE.

### Validation of the hybrid FD-FE method I

Before applying a hybrid FD-FE method to a model with topography, we must first check that our hybrid code can also produce accurate results even with a model that has no topography. The validation tests were performed on the previous three models (figure 2.21a-c). For these models with no topography, we used FE triangular elements beneath the surface and FD rectangular blocks for the rest of the models. The same mesh generation scheme used earlier for FD and FE methods is also applied for the hybrid method. This would lead to the same number of unknowns and same matrix dimensions for the 2-blocks, 3-blocks, and 4-blocks cases, as previously applied.

Model	Method	#Block	Wenner	Schlumberger	Dipole	Time [s]
A (Fig. 2.21a)	FD	2	0.25	0.23	0.33	0.55
		3	0.15	0.15	0.27	0.83
		4	0.15	0.14	0.29	1.13
	FE	2	0.44	0.41	0.66	1.99
		3	0.18	0.17	0.26	2.85
		4	0.10	0.09	0.21	3.78
	HB	2	0.30	0.28	0.36	0.57
		3	0.18	0.17	0.27	0.88
		4	0.14	0.14	0.29	1.19
B (Fig. 2.21b)	FD	2	0.89	0.67	0.55	0.55
		3	0.76	0.58	0.44	0.83
		4	0.72	0.55	0.41	1.15
	FE	2	1.20	0.99	1.15	1.98
		3	0.66	0.51	0.57	2.87
		4	0.47	0.36	0.41	3.78
	HB	2	1.10	0.88	0.98	0.59
		3	0.90	0.72	0.83	0.88
		4	0.75	0.56	0.41	1.18
C (Fig. 2.21c)	FD	2	0.96	0.84	0.89	0.55
		3	0.81	0.72	0.49	0.83
		4	0.76	0.73	0.44	1.14
	FE	2	1.31	1.26	1.55	2.00
		3	0.75	0.67	0.71	2.86
		4	0.56	0.55	0.50	3.78
	HB	2	1.06	0.93	0.94	0.58
		3	0.86	0.75	0.50	0.89
		4	0.78	0.75	0.44	1.19

Table 2.6: The relative error [%] defined as  $(1/N) \sum_{i=1}^N (|\rho_a^{\text{cal}} - \rho_a^{\text{true}}|) / \rho_a^{\text{true}}$ , where  $\rho_a^{\text{true}}$  is the true apparent resistivity from analytical formula (model A and B), and from RES2DMOD program (model C),  $\rho_a^{\text{cal}}$  is the apparent resistivity calculated from FD, FE, or HB methods with 2-, 3- and 4-horizontal blocks between a pair of electrodes. Models A, B and C are shown in figure 2.21a-c, respectively.



The number of non-zero coefficients of HB is slightly less than 1% above that of FD, but almost about 30% less than that of FE. The memory requirement for the hybrid method is about 7% more than that of FD, and 20% less than that of FE. In terms of computational time to solve the system of equations 8 times (for 8  $k_y$ ) HB needs on average about 5% more CPU time than FD. Table 2.3.8 shows that the relative errors of HB can be either larger than both FD and FE or in between the values of both FD and FE or smaller than both FD and FE. However, they are all at about the same acceptable level. Thus we conclude that our hybrid method can yield apparent resistivities as accurately as the FD and FE methods where topography is not present.

### Validation of the hybrid method II

In this section, our hybrid method will be tested on an extreme topography model (figure 2.25). In this test, the model is also divided into  $209 \times 59$  elements. Since the hybrid method doesn't require the air portion like the FE method, the hybrid method therefore also has 8,560 unknown nodes. These unknown nodes result in 42,604 non-zero coefficients in the  $\alpha\mathbf{C} + \beta\mathbf{K}$  matrix. The HB method is used to calculate the apparent resistivities for Wenner, Schlumberger, and Dipole-Dipole configurations and its results are summarized in table 2.3.8.

Method	Accuracy Difference [%]			CPU time [s]
	Wenner	Schlumberger	Dipole-Dipole	
<b>FD</b>	3.13	5.33	7.82	3.35
<b>FE</b>	-	-	-	6.46
<b>HB</b>	0.47	0.29	0.29	2.62

Table 2.7: The percentage accuracy difference and CPU time for all three arrays for testing the three different forward modeling schemes.

Method	Memory Usage [MB]		
	C or K or $\alpha\mathbf{C} + \beta\mathbf{K}$	L or U	Total (for 8 $k_y$ )
<b>FD</b>	1.05	14.98	242.25
<b>FE</b>	0.99	8.83	145.68
<b>HB</b>	0.73	6.89	113.31

Table 2.8: The memory usage for all three arrays for testing the three different forward modeling schemes.

Figure 2.32 is the forward response of Wenner, Schlumberger and Dipole-Dipole arrays computed by the HB method. The apparent resistivity responses of the hybrid method differ by less than 0.5% from those of the FE methods for all configurations and the hybrid method requires 0.41 and 0.78 less CPU time than FE (without air) and FD (with air) methods, respectively. This is because the systems of equations

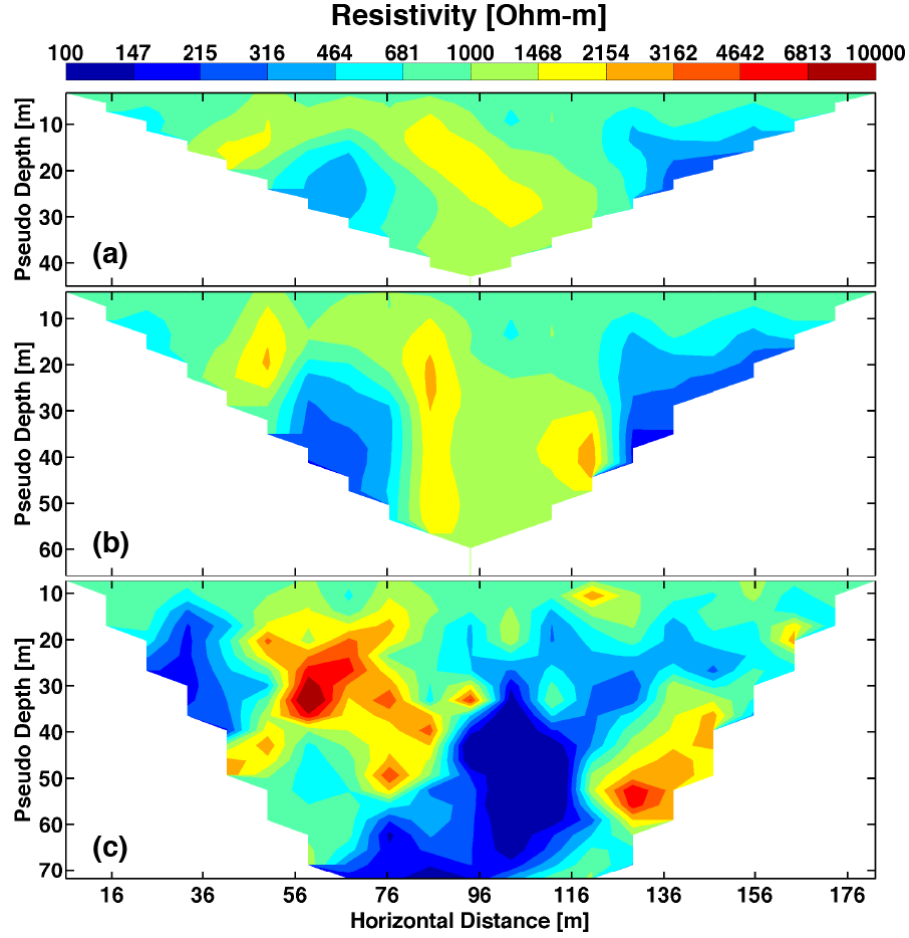


Figure 2.32: Pseudo-section of the “extreme” topography model (figure 2.25) for (a) Wenner, (b) Schlumberger and (c) Dipole-Dipole arrays.

for FD and FE are larger due to the larger numbers of unknowns. 60-70% of the CPU time of the hybrid method is for forming the coefficient matrix ( $\alpha\mathbf{C} + \beta\mathbf{K}$ ), while the rest is used to solve equation (2.118) for all eight wave numbers. Similarly, the hybrid method without air requires a lot less memory than both the FD and FE methods.

This experiment shows the advantage of the hybrid FD-FE method over the conventional FD and FE methods. However, the reduction in CPU time depends greatly on the topography. If the topography is smooth, the relative reduction in CPU time of the hybrid method would be less than the results in Table 2.3.8.

### 2.3.9 Topographic gradient limitation

The topographic gradient can vary from almost flat to almost vertical. In previous examples where the gradients are  $60^\circ$ , the “automatic grid discretization” routine works well and the accuracy is quite high. The “automatic grid discretization” routine is designed based on the “topographic gradient” study.

In the topographic gradient study, the left-slope model (figure 2.33) is tested with different topographic gradients from  $5^\circ$  up to  $85^\circ$ . Most electrodes were placed

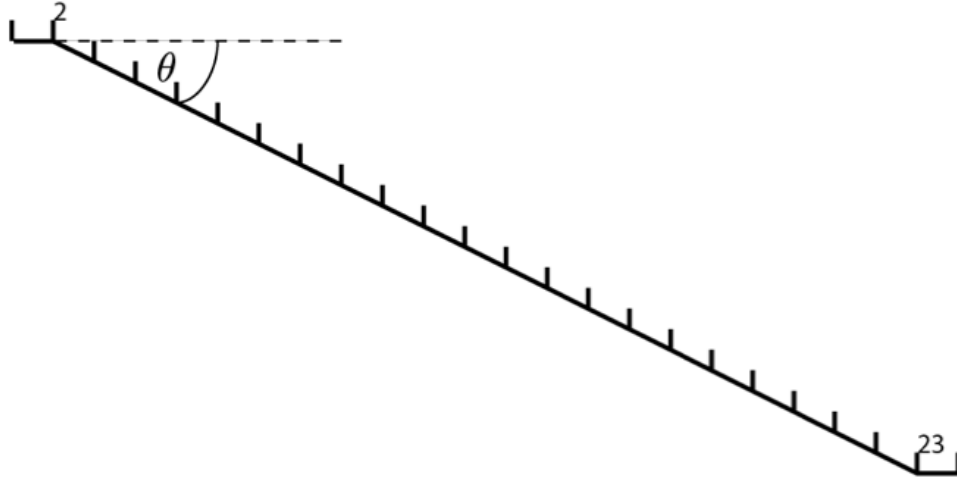


Figure 2.33: The left-slope model for “topographic gradient” study

on the slope. The finite element with fine grid (20 blocks between a pair of electrodes) is used as a base solution. The vertical grid discretization was automatically adjusted so that the right triangular elements matched well with the slope. All of these models were tested with the hybrid method where the slope was discretized with right triangular elements and the interiors with rectangular grids. Results of the “topographic gradient” study are summarized in table 2.3.9. By using the default grid generation with 3-blocks between electrodes, for gradients below  $45^\circ$ , the errors at all electrodes were on average below 1%. The error increases with slopes of more than  $45^\circ$ . This is because the right triangular elements with 3-blocks between electrodes do not fit well with the slopes of large gradients. The biggest errors occur near the corners. Therefore, to lower the errors, the number of blocks between electrodes should be increased where there are large slopes. Based on our studies, to obtain relative errors of less than 1%, the number of blocks between electrodes must be 3, 4, 5, 6 and 7 for gradients less than  $45^\circ$ ,  $46-50^\circ$ ,  $51-55^\circ$ ,  $56-70^\circ$ , and  $71-75^\circ$ , respectively. However, when the slopes are larger than  $75^\circ$ , the average errors are larger than 5% with any number of blocks between electrodes. The  $75^\circ$  slope appears to mark the limit of our hybrid scheme when incorporating the slope. However, this would not be a problem because regions with a large slope are often avoided in most field surveys.

## 2.4 2D DC Resistivity Inversion

Efficient inversions for two-dimensional direct current (DC) resistivity data are available both commercially (e.g. Oldenburg & Li, 1994; Loke & Barker, 1996)

$\theta$ [°]	No. of Grid	Average Error [%]
5	3	0.3674
10	3	0.3817
15	3	0.4221
20	3	0.4737
25	3	0.5302
30	3	0.5880
35	3	0.6466
40	3	0.7115
45	3	0.7698
50	4	0.4547
55	5	0.3363
60	6	0.2973
65	6	0.3239
70	7	0.3967
75	7	0.6405
80	10	6.1826
85	10	6.6160

Table 2.9: Summary of the number of grid between a pair of electrodes that makes the average error less than 1% for each  $\theta$ .

and academically (e.g. Tong & Yang, 1990; Olayinka & Yaramanci, 2000; Christiansen & Auken, 2004; Ha *et al.*, 2006; Athanasiou *et al.*, 2007; Boonchaisuk *et al.*, 2008; Kalscheuer *et al.*, 2010; Santos & El-Kaliouby, 2011; Ulugergerli, 2011). An efficient inversion in general is defined as one with a low CPU time and memory (RAM) requirement. This makes many of these programs applicable on notebook computers and therefore practical for field work. An efficient inversion should also be able to handle topography and many different DC resistivity configurations.

There are various inversion techniques such as Gauss-Newton, quasi-Newton, Occam's inversion and conjugate gradient (CG) methods. Gauss-Newton is the most direct approach for solving inverse problems (e.g. Sasaki, 1994; Li & Oldenburg, 1994; Loke & Dahlin, 1997). The Gauss-Newton method has a high convergence rate. It takes a few iterations to return the inverted result but it consumes a lot of CPU time and memory. To reduce CPU time, Broyden (1965) proposed other approach called the quasi-Newton method (Loke & Barker, 1996; Loke & Dahlin, 1997, 2002; Tsourlos *et al.*, 1998). Most of the quasi-Newton method is similar to the Gauss-Newton method except the quasi-Newton method avoids excessive computation by using Broyden's update technique. The quasi-Newton method is successful for reducing CPU time but has a lower convergence rate (Loke & Dahlin, 2002). It needs more iterations than the Gauss-Newton method and sometimes the quasi-Newton method produces a different result from the Gauss-Newton method. Occam's inversion is another variant of the

Gauss-Newton method. It was first proposed by Constable *et al.* (1987). Occam's inversion removes some unnecessary parameters from its algorithm. This makes Occam's inversion stabler than the Gauss-Newton method and its convergence rate is close to the Gauss-Newton method. Zhang *et al.* (1995) and Ellis & Oldenburg (1994) proposed inversion algorithm for 3D data based on the CG method. The CG method is introduced to the inverse problem for reducing memory usage. It can solve inverse problems without storing a huge matrix as in the Gauss-Newton method and its variant but its convergence rates are less than those of other methods (Siripunvaraporn & Egbert, 2007). The algorithm of the CG method is practical for 3D inverse problems but for 2D problems the Gauss-Newton method and its variants are more practical than CG method.

Here, we discuss about our attempt to develop an efficient Occam's inversion code on MATLAB. We start by reviewing the original and modified Occam's inversion algorithms proposed by Siripunvaraporn & Egbert (2000). Then we describe the algorithm of each of the necessary modules. Finally the reliability and stability of our inversions are tested on both synthetic data and real field data.

#### 2.4.1 Occam's inversion

Occam's inversion was first proposed by Constable *et al.* (1987) for magnetotelluric data and 1D DC resistivity data. Since then it has been applied to various geophysical data (e.g. deGroot-Hedlin & Constable, 1990; LaBrecque & Ward, 1990; Siripunvaraporn & Egbert, 2000; Siripunvaraporn *et al.*, 2005; Greenhalgh, 2006; Boonchaisuk, 2007; Vachiratienchai, 2007; Boonchaisuk *et al.*, 2008). The philosophy of Occam's inversion is to find the smoothest model for which the response fits the observed data at the appropriate level. This philosophy can be translated into a minimization problem of an unconstrained functional  $U(\mathbf{m}, \lambda)$

$$U(\mathbf{m}, \lambda) = (\mathbf{m} - \mathbf{m}_0)^T \mathbf{C}_m^{-1} (\mathbf{m} - \mathbf{m}_0) + \lambda^{-1} \{ (\mathbf{d} - \mathbf{F}[\mathbf{m}])^T \mathbf{C}_d^{-1} (\mathbf{d} - \mathbf{F}[\mathbf{m}]) - \chi_d^{*2} \}, \quad (2.119)$$

where  $\mathbf{m}$  is the  $M$  column vector of the resistivity model,  $\mathbf{m}_0$  is the “prior” resistivity model,  $\mathbf{C}_m$  is the  $M \times M$  model covariance matrix,  $\mathbf{d}$  is the observed data with dimension  $N$ ,  $\mathbf{F}[\mathbf{m}]$  is the forward modeling response,  $\mathbf{C}_d$  is the  $N \times N$  data covariance matrix,  $\chi_d^*$  is the desired level of data misfit,  $\lambda^{-1}$  is a Lagrange multiplier,  $M$  is the number of model parameters and  $N$  is the number of data points. The first term on the right is the model objective function which is the square of model misfit  $\chi_m$  determining the consistency between  $\mathbf{m}_0$  and  $\mathbf{m}$ .  $\chi_m$  is zero when  $\mathbf{m}$  is perfectly matched with  $\mathbf{m}_0$ . The second term on the right is the data objective function which is the square of data misfit  $\chi_d$  determining the difference between the observed data  $\mathbf{d}$  and the forward response  $\mathbf{F}[\mathbf{m}]$ .

Instead of directly minimizing equation (2.119), Constable *et al.* (1987) considers the penalty functional  $W_\lambda(\mathbf{m})$ ,

$$W_\lambda(\mathbf{m}) = (\mathbf{m} - \mathbf{m}_0)^T \mathbf{C}_m^{-1} (\mathbf{m} - \mathbf{m}_0) + \lambda^{-1} \{(\mathbf{d} - \mathbf{F}[\mathbf{m}])^T \mathbf{C}_d^{-1} (\mathbf{d} - \mathbf{F}[\mathbf{m}])\}. \quad (2.120)$$

When  $\lambda$  is fixed,  $\partial U / \partial \mathbf{m}$  is equal to  $\partial W_\lambda / \partial \mathbf{m}$ . Therefore, the minimum of  $U$  can be achieved by minimizing  $W_\lambda$  with a series of  $\lambda$ , and choosing the smallest value as the result. To obtain the stationary point of  $W_\lambda$  at the  $(k+1)$  iteration, we start by linearizing  $\mathbf{F}[\mathbf{m}_{k+1}]$  based on Taylor's series expansion,  $\mathbf{F}[\mathbf{m}_{k+1}] = \mathbf{F}[\mathbf{m}_k] + \mathbf{J}_k(\mathbf{m}_{k+1} - \mathbf{m}_k)$  where  $\mathbf{J}_k = \partial \mathbf{F}[\mathbf{m}_k] / \partial \mathbf{m}_k$  is the  $N \times M$  jacobian or sensitivity matrix at the  $k$  iteration. Substituting the result into equation (2.120) and solving for the stationary point, a series of iterative solutions is obtained,

$$\mathbf{m}_{k+1}(\lambda) = (\lambda \mathbf{C}_m^{-1} + \mathbf{J}_k^T \mathbf{C}_d^{-1} \mathbf{J}_k)^{-1} \mathbf{J}_k^T \mathbf{C}_d^{-1} \hat{\mathbf{d}} + \mathbf{m}_0, \quad (2.121)$$

where  $\hat{\mathbf{d}} = \mathbf{d} - \mathbf{F}[\mathbf{m}_k] + \mathbf{J}_k(\mathbf{m}_k - \mathbf{m}_0)$ . This equation is the “original” model-update equation for Occam's inversion. It requires us to solve a  $M \times M$  system of equations and we therefore call equation (2.121) “model-space” Occam's inversion.

Parker (1994) shows new approach to compute  $\mathbf{m}_{k+1}$ . The new approach requires us to solve a  $N \times N$  system of equations instead of a  $M \times M$  system of equations. The new approach of equation (2.121) is called the “data-space” Occam's inversion and its model-update equation is

$$\mathbf{m}_{k+1}(\lambda) = \mathbf{C}_m \mathbf{J}_k^T (\lambda \mathbf{C}_d + \mathbf{J}_k \mathbf{C}_m \mathbf{J}_k^T)^{-1} \hat{\mathbf{d}} + \mathbf{m}_0. \quad (2.122)$$

The “data-space” space inversion was first used for 2D magnetotelluric data by Siripunvaraporn & Egbert (2000). It has also been applied to 3D magnetotelluric data (Siripunvaraporn *et al.*, 2004, 2005), and 2D DC resistivity data (Boonchaisuk, 2007; Vachiratienchai, 2007; Boonchaisuk *et al.*, 2008).

“Model-space” and “data-space” Occam's inversion will produce the identical result if and only if all the same inverted parameters are used (Siripunvaraporn & Egbert, 2000; Siripunvaraporn *et al.*, 2005). As mentioned before, the “model-space” Occam's inversion requires memory based on the number of model parameter ( $M$ ) whereas the memory requirement of the “data-space” Occam's inversion is based on the number of data points ( $N$ ). In other words, if  $N$  is much less than  $M$  then the “data-space” Occam's inversion will be more effective than the “model-space” Occam's inversion. For 2D DC resistivity data, the  $M$  is usually much greater than the  $N$ . Therefore, the “data-space” Occam's inversion is a practical algorithm for 2D DC resistivity data. The comparison between “model-space” and “data-space” Occam's inversion for 2D DC resistivity data can be seen in Vachiratienchai (2007).

Here, we develop a inversion for 2D DC resistivity data based on the “data-space” Occam’s inversion and the hybrid FD-FE methods. In the following, we describe the necessary inversion parameters and how we design the algorithm to fully take advantage of matrix operation in MATLAB. Finally, our inversion code is tested on both synthetic and real field data.

### 2.4.2 Inversion Parameters

As in equation (2.122), the “data-space” Occam’s inversion can function when the observed data  $\mathbf{d}$ , forward response  $\mathbf{F}[\mathbf{m}_k]$ , data-covariance matrix  $\mathbf{C}_d$ , model-covariance matrix  $\mathbf{C}_m$ , initial model  $\mathbf{m}_k$ , prior model  $\mathbf{m}_0$ , sensitivity matrix  $\mathbf{J}_k$ , and Lagrange multiplier  $\lambda^{-1}$  are known.

#### The structure of $\mathbf{d}$ , $\mathbf{F}[\mathbf{m}_k]$ , and $\mathbf{m}$

As in section 2.1, a DC resistivity survey studies subsurface resistivity  $\rho$  by collecting apparent resistivity  $\rho_a$  at the surface.  $\rho_a$  is therefore the observed data  $\mathbf{d}$  and  $\rho$  is the model parameter  $\mathbf{m}$  for inversion. By directly using  $\rho_a$  and  $\rho$ , the inversion is not stable and produces negative resistivity which is meaningless. To prevent this,  $\ln(\rho_a)$  is used as the observed data and  $\ln(\rho)$  is used as the model parameter. The structure of  $\mathbf{d}$  and  $\mathbf{F}[\mathbf{m}]$  is a  $N \times 1$  column vector as shown in figure 2.34 and the structure of  $\mathbf{m}$  is a  $M \times 1$  column vector of which element number is indexed from top to bottom and left to right of the model, starting with the FD elements and then the FE elements as shown in figure 2.35.

$$\mathbf{d} = \begin{bmatrix} \ln(\rho_{a_1}) \\ \ln(\rho_{a_2}) \\ \vdots \\ \ln(\rho_{a_{20}}) \\ \vdots \\ \ln(\rho_{a_{N-1}}) \\ \ln(\rho_{a_N}) \end{bmatrix}_{N \times 1}$$

Figure 2.34: The structure of data vector  $\mathbf{d}$ .

$$\mathbf{m} = \begin{bmatrix} \ln(\rho_1^{\text{FD}}) \\ \ln(\rho_2^{\text{FD}}) \\ \vdots \\ \ln(\rho_{22}^{\text{FD}}) \\ \vdots \\ \ln(\rho_{44}^{\text{FD}}) \\ \ln(\rho_{45}^{\text{FE}}) \\ \ln(\rho_{46}^{\text{FE}}) \\ \ln(\rho_{47}^{\text{FE}}) \end{bmatrix}_{M \times 1}$$

Figure 2.35: The structure of model vector  $\mathbf{m}$  corresponding to the discretized model in figure 2.31. The FD superscript indicates a FD element and the FE superscript indicates a FE element.

### Initial Model ( $\mathbf{m}_k$ ) and Prior Model ( $\mathbf{m}_0$ )

The prior model and initial model are different. The initial model is used for starting the inversion process and its resistivities are changed continually. The prior model is the reference model and the inversion tries to find a inverted result close to the prior model. The prior model is preserved for the whole inversion process. To achieve the smoothest model, the homogeneous earth model is usually used as the prior model. The resistivity is calculated by the geometric mean

$$\rho_{\text{avg}} = \sqrt[N]{\rho_a^1 \rho_a^2 \dots \rho_a^N}. \quad (2.123)$$

By default, the prior model is also used as the initial model.

### Data-Covariance Matrix $\mathbf{C}_d$

The data-covariance matrix  $\mathbf{C}_d$  has been added to the inversion to prevent the over-fit problem which always occurs in the inversion process when the observed data is contaminated by noise. If  $\mathbf{d}$  is the observed data then  $\mathbf{d}$  is the superposition of real signal  $\mathbf{d}_r$  and noise  $\mathbf{d}_n$

$$\mathbf{d} = \mathbf{d}_r + \mathbf{d}_n. \quad (2.124)$$

In DC resistivity surveys, noise comes from the installation, environment, and telluric noise from power lines. Noise is difficult to remove from observed data. To produce a model which perfectly fits with observed data, inversion can include non-geologically interpretable artifacts into the inverted model. These artifacts can result in a misleading interpretation.  $\mathbf{C}_d$  is used for solving this problem. In general,  $\mathbf{C}_d$  is the  $N \times N$  diagonal



matrix whose elements are errors  $\delta$  of the observed data

$$\mathbf{C}_d = \begin{pmatrix} \delta_1^2 & 0 & \cdots & 0 \\ 0 & \delta_2^2 & \cdots & 0 \\ \vdots & \vdots & \ddots & \vdots \\ 0 & 0 & \cdots & \delta_N^2 \end{pmatrix}.$$

In our work,  $\mathbf{d}$  is the natural logarithm of the observed data.  $\mathbf{C}_d$  therefore has to be created from the error in the natural logarithm scale  $\delta_i^{\log}$ . The error in the natural logarithm scale is equal to

$$\delta_i^{\log} = \frac{\delta_i^{\text{linear}}}{d_i}, \quad (2.125)$$

where  $\delta_i^{\text{linear}}$  is data error in linear scale.  $\mathbf{C}_d^{-1}$  is simply calculated by finding the inverse of  $\mathbf{C}_d$ . Note that  $\delta_i^{\text{linear}}$  is usually set as 1% of  $d_i$  for good quality data. For noisy data,  $\delta_i^{\text{linear}}$  is adjusted.

### Matrix $\mathbf{C}_m$ , $\mathbf{C}_m \mathbf{J}_k^T$ Multiplication and Controlling parameter $\eta$

The model-covariance matrix  $\mathbf{C}_m$  is introduced into the inversion for controlling the changing of the resistivity model in the inversion process. In other inversion algorithms including the “model-space” Occam’s inversion,  $\mathbf{C}_m^{-1}$  is used to control the inversion process and it is a roughness operator or Laplacian operator (e.g. Constable *et al.*, 1987; deGroot-Hedlin & Constable, 1990). The inverse of them are close to singular and cannot be used as  $\mathbf{C}_m$  in the “data-space” Occam’s inversion. Egbert *et al.* (1994) proposed using the diffusion equation to calculate  $\mathbf{C}_m \mathbf{u}$ , where  $\mathbf{u}$  is any vector, in their oceanography inversion. This idea was also reapplied for 2D magnetotelluric data by Siripunvaraporn & Egbert (2000), and 2D DC resistivity data by Boonchaisuk (2007); Vachiratienchai (2007); Boonchaisuk *et al.* (2008).

Here, we redesign the algorithm for computing  $\mathbf{C}_m \mathbf{u}$  to fully take advantage of the MATLAB environment. In the following, we review the main concepts of diffusion in previous work and then we show the new algorithm.

The general form of the diffusion equation is

$$\frac{\partial \mathbf{\Omega}}{\partial \tau} = \gamma \nabla^2 \mathbf{\Omega}, \quad (2.126)$$

where  $\tau$  is the pseudo-time, and  $\gamma$  is the diffusion parameter. Siripunvaraporn & Egbert (2000) avoids directly solving equation (2.126) because it consumes memory and time. To avoid solving the 2D diffusion equation, we solve the 1D diffusion equation alternatively between vertical ( $z$ -direction) and horizontal ( $x$ -direction) directions. This approach is similar to the operator splitting method (Press *et al.*, 1992). Considering the 1D diffusion equation in the vertical direction ( $z$ -direction),

$$\frac{\partial \mathbf{\Omega}}{\partial \tau} = \gamma \frac{\partial^2 \mathbf{\Omega}}{\partial z^2}. \quad (2.127)$$

For solving equation (2.127), there are two numerical methods which are the explicit and implicit methods. The explicit method is faster but less stable than the implicit method. Here the implicit method is used to solve (2.127). The time derivative, discretized using by the forward derivative, becomes

$$\frac{\partial \Omega_i}{\partial \tau} = \frac{\Omega_i^{n+1} - \Omega_i^n}{\tau}. \quad (2.128)$$

When  $\Omega_i$  is not located at the boundary, the second order derivative can be discretized by the center derivative,

$$\frac{\partial^2 \Omega_i}{\partial z^2} = \frac{2\gamma_i \Omega_{i+1}^{n+1}}{h_i(h_i + h_{i-1})} + \frac{2\gamma_i \Omega_{i-1}^{n+1}}{h_{i-1}(h_i + h_{i-1})} - \frac{2\gamma_i \Omega_i^{n+1}}{(h_i h_{i-1})}, \quad (2.129)$$

where  $h_{i-1}$  is the distance from  $\Omega_{i-1}$  to  $\Omega_i$  and  $h_i$  is the distance from  $\Omega_i$  to  $\Omega_{i+1}$ . When  $\Omega_i$  is located at the upper boundary, the second order derivative can be discretized by the forward derivative,

$$\frac{\partial^2 \Omega_i}{\partial z^2} = \frac{2\gamma_i \Omega_{i+2}^{n+1}}{h_{i+1}(h_{i+1} - h_i)} - \frac{2\gamma_i \Omega_{i+1}^{n+1}}{h_i(h_{i+1} - h_i)} + \frac{2\gamma_i \Omega_i^{n+1}}{(h_{i+1} h_i)}, \quad (2.130)$$

where  $h_{i+1}$  is the distance from  $\Omega_i$  to  $\Omega_{i+2}$ . When  $\Omega_i$  is located at the lower boundary, the second order derivative can be discretized by the backward derivative,

$$\frac{\partial^2 \Omega_i}{\partial z^2} = \frac{2\gamma_i \Omega_i^{n+1}}{(h_{i-2} h_{i-1})} - \frac{2\gamma_i \Omega_{i-1}^{n+1}}{h_{i-1}(h_{i-2} - h_{i-1})} + \frac{2\gamma_i \Omega_{i-2}^{n+1}}{h_{i-2}(h_{i-2} - h_{i-1})}, \quad (2.131)$$

where  $h_{i-2}$  is the distance from  $\Omega_{i-2}$  to  $\Omega_i$ . Equation (2.127) can be rewritten in matrix form as

$$\mathbf{\Omega}^{n+1} = (\mathbf{I} + \tau \mathbf{\Pi}_z)^{-1} \mathbf{\Omega}^n \quad (2.132)$$

$$= \mathbf{H}_z \mathbf{\Omega}^n, \quad (2.133)$$

where  $\mathbf{\Pi}_z$  is the discrete form of the second order derivative in the  $z$ -direction,  $\mathbf{H}_z$  is  $M_z \times M_z$  diffusion operator in  $z$ -direction, and  $M_z$  is the number of models in the  $z$ -direction. In the same way, we can create the 1D diffusion operator in  $x$ -direction ( $\mathbf{H}_x$  the size of which depends on the number of models in the  $x$ -direction). The model covariance can be written as

$$\mathbf{C}_m = [\mathbf{H}_z \mathbf{H}_x \mathbf{H}_x \mathbf{H}_z]^\zeta, \quad (2.134)$$

where  $\zeta$  is the number of iterations to apply the diffusion operator. For the “data-space” Occam’s inversion,  $\mathbf{C}_m$  is not constructed.  $\mathbf{C}_m \mathbf{J}_k^T$  is calculated by alternately multiplying  $\mathbf{H}_z$  and  $\mathbf{H}_x$ , following the pattern in equation (2.134), to  $\mathbf{J}_k^T$ . The algorithm for calculating  $\mathbf{C}_m \mathbf{J}_k^T$  used in Vachiratienchai (2007) is shown in algorithm 1:

**Data:**  $\mathbf{J}_k$ ,  $\mathbf{H}_z$ , and  $\mathbf{H}_x$   
**Result:**  $\mathbf{C}_m \mathbf{J}_k^T$   
 initialization;  
**while**  $ii \leq N$  **do**  
   read  $ii^{th}$  row of  $\mathbf{J}_k$ ;  
   rearrange into 2D format and save the result into  $\mathbf{Jk2D}$ ;  
   **while**  $jj \leq \zeta$  **do**  
     multiply  $\mathbf{H}_z$  to  $\mathbf{Jk2D}$ ;  
     transpose the result and then multiply it by  $\mathbf{H}_x \mathbf{H}_x$ ;  
     transpose the result and then multiply it by  $\mathbf{H}_z$ ;  
   **end**  
   rearrange the result into 1D format and save it into the  $ii^{th}$   
   column of  $\mathbf{C}_m \mathbf{J}_k^T$ ;  
**end**

**Algorithm 1:** Algorithm for calculating  $\mathbf{C}_m \mathbf{J}_k^T$  used in Vachiratienchai (2007).

Algorithm 1 needs a lot of CPU time to rearrange and transpose the matrix. The computational time is about 0.5-2 minutes depending on the number of model parameters and data. This algorithm requires matrix arrangement and matrix transpose because  $\mathbf{H}_z$  and  $\mathbf{H}_x$  are developed to operate on  $M_z \times M_x$  matrix. In other words, we can dispose of the matrix arrangement and matrix transpose from the  $\mathbf{C}_m \mathbf{J}_k^T$  calculation by redesigning  $\mathbf{H}_z$  and  $\mathbf{H}_x$  matrix. The new  $\mathbf{H}_z$  and  $\mathbf{H}_x$  matrix is designed to directly operate on the column of  $\mathbf{J}_k^T$  by rearranging the elements corresponding to the model element index as described earlier. The new algorithm for computing  $\mathbf{C}_m \mathbf{J}_k^T$  is described below

**Data:**  $\mathbf{J}_k$ ,  $\mathbf{H}_z$ , and  $\mathbf{H}_x$   
**Result:**  $\mathbf{C}_m \mathbf{J}_k^T$   
 initialization;  
 transpose  $\mathbf{J}_k$  and save the result into  $\mathbf{C}_m \mathbf{J}_k^T$ ;  
**while**  $jj \leq \zeta$  **do**  
   multiply  $\mathbf{H}_z$  to  $\mathbf{C}_m \mathbf{J}_k^T$ ;  
   multiply the result by  $\mathbf{H}_x \mathbf{H}_x$ ;  
   multiply it by  $\mathbf{H}_z$ ;  
**end**

**Algorithm 2:** New algorithm for calculating  $\mathbf{C}_m \mathbf{J}_k^T$ .

As mentioned before,  $\mathbf{C}_m$  is introduced for controlling the changing of the resistivity model. In our algorithm,  $\mathbf{C}_m$  has three adjustable parameters ( $\tau$ ,  $\zeta$ , and  $\gamma$ ). From semi-empirical tests, we found that the smoothness of the inverted model depends on  $\tau$  and  $\gamma$  and the stability of the inversion depends on  $\zeta$ . If  $\zeta$  is too small (e.g.  $\zeta = 1$ ), inversion fails. On other hand, if  $\zeta$  is too large then the inversion will spend a lot of CPU time computing  $\mathbf{C}_m \mathbf{J}_k^T$ . From semi-empirical tests, the proper value of  $\zeta$  is 10.

In physics, if we know the diffusion coefficient  $\gamma$  and its diffusion time  $\tau$  then we can approximate the diffusion length  $l$  by

$$l = \sqrt{4\gamma\tau}. \quad (2.135)$$

The diffusion length of  $\mathbf{C}_m$  can be used to determine the smoothness of model. A larger diffusion length corresponds to a smoother inverted model. In our inversion,  $\tau$  is fixed as 1 and  $\gamma$  is automatically adjusted based on the diffusion length. In this work, we assume that diffusion length in the  $x$ -direction is equal to the diffusion length in the  $z$ -direction and it is a function of the depth  $D$ ,

$$l = \kappa D, \quad (2.136)$$

where  $\kappa$  is real number and its value is also a function of depth. Its maximum value is 1 for  $D < a/\eta$  and its value is reduced by 0.1 until it reaches 0.2. In other words,  $\eta$  is used for controlling the smoothness of the inverted model and  $\mathbf{C}_m \mathbf{J}_k^T$ . Therefore,  $\eta$  is the controlling parameter for our  $\mathbf{C}_m$ . Here, the value of  $\eta$  is 1, 2, 4, or 8. If  $\eta = 8$ , inversion will add a superior anomaly to the inverted result for reducing the data misfit. If  $\eta = 1$ , inversion will return a smoother model but its data misfit is higher.

### Jacobian Matrix $\mathbf{J}_k$

The Jacobian matrix is introduced to the inversion for approximating the response of  $\mathbf{m}_{k+1}$  from the known response  $\mathbf{F}[\mathbf{m}_k]$  and model parameter  $\mathbf{m}_k$ . The Jacobian matrix is a  $N \times M$  matrix which stores the information about the gradient of the responses with respect to its model parameters,

$$\mathbf{J}_k^{ij} = \frac{\partial \mathbf{F}_i[\mathbf{m}_k]}{\partial \mathbf{m}_k^j}. \quad (2.137)$$

To prevent the occurrence of negative resistivity in the inverse,  $\ln(\rho_a)$  is used as the response and  $\ln(\rho)$  is used as the model parameter. Therefore, equation (2.137) can be rewritten as

$$\begin{aligned} \mathbf{J}_k^{ij} = & - \frac{\sigma_j}{\phi^{A_i, M_i} - \phi^{B_i, M_i} - \phi^{A_i, N_i} + \phi^{B_i, N_i}} \\ & \sum_{p=1}^n g_p \frac{\partial}{\partial \sigma_j} \left( \tilde{\phi}_{k_{yp}}^{A_i, M_i} - \tilde{\phi}_{k_{yp}}^{B_i, M_i} - \tilde{\phi}_{k_{yp}}^{A_i, N_i} + \tilde{\phi}_{k_{yp}}^{B_i, N_i} \right), \end{aligned} \quad (2.138)$$

where the superscript of  $\phi$  or  $\tilde{\phi}$  indicates its current ( $A_i$  or  $B_i$ ) and potential electrodes ( $M_i$  or  $N_i$ ). The direct and simplest way to get the derivative of  $\tilde{\phi}$  at potential electrodes is to differentiate equation (2.70), (2.94), or (2.118) with respect to  $\sigma_j$  and pick up the result only at its potential electrode,

$$\frac{\partial}{\partial \sigma_j} \tilde{\Phi}_{k_{yp}}^{A_i} = - \left( \alpha \mathbf{C}_{k_{yp}} + \beta \mathbf{K}_{k_{yp}} \right)^{-1} \frac{\partial \left( \alpha \mathbf{C}_{k_{yp}} + \beta \mathbf{K}_{k_{yp}} \right)}{\partial \sigma_j} \tilde{\Phi}_{k_{yp}}^{A_i}. \quad (2.139)$$

This straightforward technique consumes a lot of computational resource because it requires one to compute the derivative for the whole domain before using some elements.

For example, if the resistivity model has  $100 \times 25$  elements, we will have 2,626 nodes. If we use equation (2.139), we have to calculate the derivative of 2,626 nodes before only 2 points corresponding to the M and N electrodes are used to construct the Jacobian. For solving this problem, we introduce the extract operator  $\mathbf{E}_p$  for extracting the interesting nodes from the whole vector. The size of extracting operator  $\mathbf{E}_p$  is the number of interesting points  $\times N_T$  or  $2 \times 2,626$  for the previous example. Each row of  $\mathbf{E}_p$  has only one non-zero element that corresponds to the position of potential electrodes and its value is 1.

The  $p^{th}$  node of the derivative of the transformed potential can be obtained by multiplying the column vector  $\frac{\partial}{\partial \sigma_j} \tilde{\Phi}_{k_{yp}}^{A_i}$  by the extracting operator  $\mathbf{E}_p$ ,

$$\begin{aligned} \frac{\partial}{\partial \sigma_j} \tilde{\phi}_{k_{yp}}^{A_i,p} &= \mathbf{E}_p \frac{\partial}{\partial \sigma_j} \tilde{\Phi}_{k_{yp}}^{A_i} \\ &= -\mathbf{E}_p \left( \alpha \mathbf{C}_{k_{yp}} + \beta \mathbf{K}_{k_{yp}} \right)^{-1} \frac{\partial \left( \alpha \mathbf{C}_{k_{yp}} + \beta \mathbf{K}_{k_{yp}} \right)}{\partial \sigma_j} \tilde{\Phi}_{k_{yp}}^{A_i}. \end{aligned} \quad (2.140)$$

When coefficient matrix is symmetric (as in pure FD or FE), equation (2.140) can be rewritten as,

$$\frac{\partial}{\partial \sigma_j} \tilde{\phi}_{k_{yp}}^{A_i,p} = -\psi_p^T \frac{\partial \left( \alpha \mathbf{C}_{k_{yp}} + \beta \mathbf{K}_{k_{yp}} \right)}{\partial \sigma_j} \tilde{\Phi}_{k_{yp}}^{A_i}, \quad (2.141)$$

where  $\psi_p = \left( \alpha \mathbf{C}_{k_{yp}} + \beta \mathbf{K}_{k_{yp}} \right)^{-1} \mathbf{E}_p^T$ . By using equation (2.141), we directly obtain the interesting element  $\partial \tilde{\phi}_{k_{yp}}^{A_i,p} / \partial \sigma_j$  without pre-calculating the whole vector  $\partial \tilde{\Phi}_{k_{yp}}^{A_i} / \partial \sigma_j$ . The term  $\psi_p$  is equivalent to solve forward modeling when the injected current is set as 2 A. This implementation is close to the adjoint Green's function technique proposed by McGillivray & Oldenburg (1990). They derived it by using the adjoint field method and they found that the derivative of  $\partial \tilde{\Phi}_{k_{yp}}^{A_i} / \partial \sigma_j$  at the  $p^{th}$  position can be computed by multiplying the adjoint field or  $\psi_p$  to "the sensitivity problem", and integrating it over domain. The main difference between our proof and McGillivray's prove is that the symmetric condition is not required in their proof. The other words, equation (2.141) can function not only in the symmetric case like pure FD or FE but also in non-symmetric cases like HB.

To confirm this point, we compute the Jacobian matrix by using equation (2.141) for FD, FE and HB and its results are shown in figure 2.36. In this test, a Schlumberger array with 48 electrodes, 4-m electrode spacing, and 22 investigation-depth levels is used. The tested model is a 1,000  $\Omega$ -m homogeneous model discretized into 26 elements in the  $z$ -direction and 161 elements in the  $x$ -direction. In the test, we have 528 data points and 4,186 model parameters. FD needs 12.6 s for computing the whole Jacobian matrix while FE needs 16.9 s and HB needs 13.2 s. Figure 2.36a, b, and c shows the 2D section of the 20<sup>th</sup> row of the Jacobian matrix for FD, FE, and HB

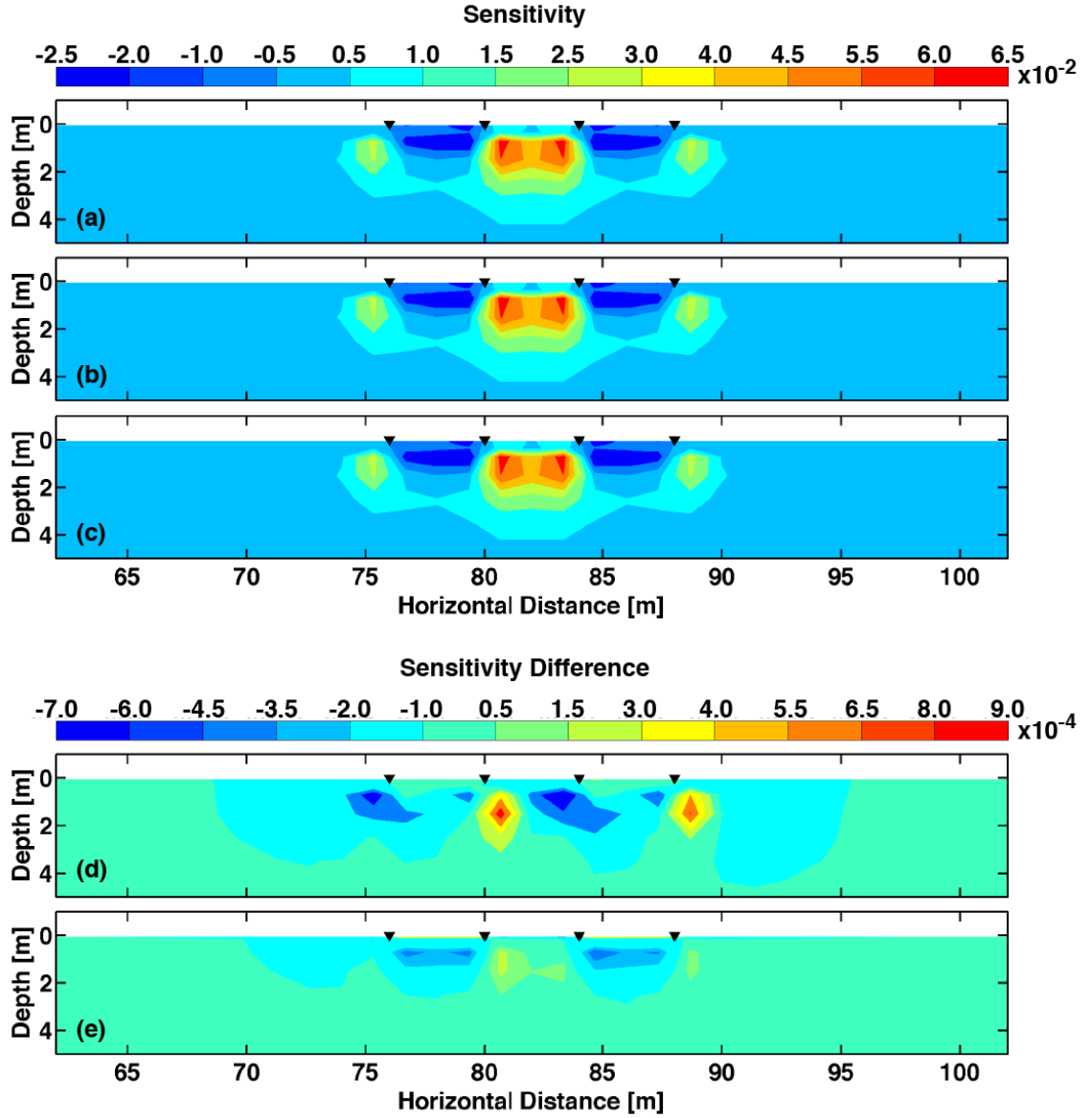


Figure 2.36: 2D section plot for the 20<sup>th</sup> row of  $\mathbf{J}_k$  calculated from (a) FD method, (b) FE method, and (c) HB method. (d) and (e) represents the difference of sensitivity value calculated from FD with FE and HB, respectively. All of these are generated from a Schlumberger array. Notice that the maximum differences are in the order of  $10^{-4}$ .

where the black triangles indicate electrode position. The sensitivity value is high in the region between the A and B electrodes and its highest value is about 1 m beneath the centre of the array. Figure 2.36d and e show the 2D section of the difference between FD and FE and between FD and HB, respectively. On average, the sensitivity value is in the order of  $10^{-2}$  but its difference is in the order of  $10^{-4}$ . From this test, we can conclude that equation (2.141) can function on both symmetric and non-symmetric system as HB, although equation (2.141) is derived for symmetric system only.

For the DCR problem, each electrode is used as both a current and a po-

tential electrode. It means that  $\psi_p$  have been calculated since solving the modeling problem. By using equation (2.141), we can get  $\partial \tilde{\phi}_{k_{yp}}^{A_i,p} / \partial \sigma_j$  by using only addition and multiplication. The challenge for developing a  $\mathbf{J}_k$  calculation module is to avoid using a for-loop. Equation (2.141) is used for calculating  $\partial \tilde{\phi}_{k_{yp}}^{A_i,p} / \partial \sigma_j$  for only one model parameter  $\sigma_j$ . If we develop simple code based on equation (2.141), we have to iterate the code  $M$  times or 4,186 times for the previous test and a for-loop in MATLAB is ineffective. To avoid using a for-loop in MATLAB, we design a new way to store  $\partial(\alpha \mathbf{C}_{k_{yp}} + \beta \mathbf{K}_{k_{yp}}) / \partial \sigma_j$  for all model parameters. Originally,  $\alpha \mathbf{C}_{k_{yp}} + \beta \mathbf{K}_{k_{yp}}$  has  $N_T \times N_T$  elements. Most of them vanish when its matrix is differentiated. For pure FD, there are 12 non-zero elements divided into 4 groups corresponding to top-left, bottom-left, bottom-right, and top-right nodes around the  $\sigma_j$  element as shown in figure 2.37.

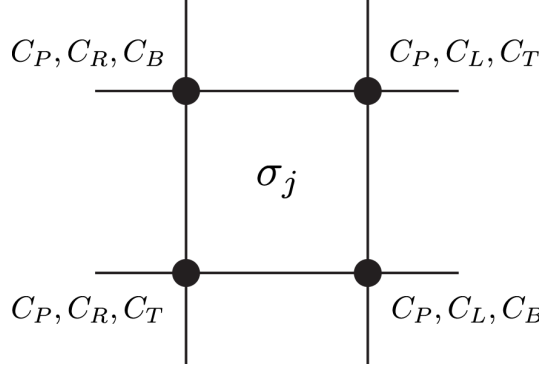


Figure 2.37: The components of  $\mathbf{C}$  matrix depending on  $\sigma_j$ .

Twelve elements of  $\partial \mathbf{C}_{k_{yp}} / \partial \sigma_j$  are in 4 rows of  $\partial \mathbf{C}_{k_{yp}} / \partial \sigma_j$  as shown in figure 2.38. When multiplying  $\partial \mathbf{C}_{k_{yp}} / \partial \sigma_j$  by  $\tilde{\Phi}_{k_{yp}}^{A_i}$ , we obtain a column vector contain-

$$\frac{\partial \mathbf{C}_{k_{yp}}}{\partial \sigma_j} = \begin{bmatrix} \frac{\partial C_{P_j}}{\partial \sigma_j} & \frac{\partial C_{B_j}}{\partial \sigma_j} & \frac{\partial C_{R_j}}{\partial \sigma_j} & \\ \frac{\partial C_{T_{j+1}}}{\partial \sigma_j} & \frac{\partial C_{P_{j+1}}}{\partial \sigma_j} & & \frac{\partial C_{R_{j+1}}}{\partial \sigma_j} \\ \frac{\partial C_{L_{j+N_z}}}{\partial \sigma_j} & & \frac{\partial C_{P_{j+N_z}}}{\partial \sigma_j} & \frac{\partial C_{B_{j+N_z}}}{\partial \sigma_j} \\ \frac{\partial C_{L_{j+N_z+1}}}{\partial \sigma_j} & & \frac{\partial C_{T_{j+N_z+1}}}{\partial \sigma_j} & \frac{\partial C_{P_{j+N_z+1}}}{\partial \sigma_j} \end{bmatrix}_{N_T \times N_T}$$

Figure 2.38: The pattern of  $\frac{\partial \mathbf{C}_{k_{yp}}}{\partial \sigma_j}$ .  $N_z$  is the number of nodes in the  $z$ -direction and  $N_T$  is the total number of nodes. The coefficients in first, second, third, and fourth rows are coefficients for the top-left, bottom-left, bottom-right, and top-right nodes, respectively.

ing 4 non-zero elements corresponding to the top-left (TL), bottom-left (BL), bottom-right (BR) and top-right (TR) node of  $\sigma_j$ . On other hand, there are only 4 rows of  $\partial \mathbf{C}_{k_{yp}} / \partial \sigma_j$  that are necessary for computing  $\frac{\partial \mathbf{C}_{k_{yp}}}{\partial \sigma_j} \tilde{\Phi}_{k_{yp}}^{A_i}$ . Following this idea, we can store  $\partial \mathbf{C}_{k_{yp}} / \partial \sigma_j$  for  $j = 1$  to  $M$  in a single matrix called **M2P** which has  $4 \times M$  rows and  $N_T$  columns. The first  $M$  rows store  $\partial \mathbf{C}_{k_{yp}} / \partial \sigma_j$  for the top-left node, the second  $M$  rows are for the bottom-left node, the third  $M$  rows are for the bottom-right node and the fourth  $M$  rows are for the top-right node as shown in figure 2.39. By multiplying

$$\mathbf{M2P} = \begin{bmatrix}
 \begin{array}{ccc}
 \frac{\partial C_{P_1}}{\partial \sigma_1} & \frac{\partial C_{B_1}}{\partial \sigma_1} & \frac{\partial C_{R_1}}{\partial \sigma_1} \\
 & \frac{\partial C_{P_j}}{\partial \sigma_j} & \frac{\partial C_{B_j}}{\partial \sigma_j} \\
 & & \frac{\partial C_{P_M}}{\partial \sigma_M} & \frac{\partial C_{B_M}}{\partial \sigma_M} & \frac{\partial C_{R_M}}{\partial \sigma_M}
 \end{array} & \text{TL Node} \\
 \hline
 \begin{array}{ccc}
 \frac{\partial C_{T_2}}{\partial \sigma_1} & \frac{\partial C_{P_2}}{\partial \sigma_1} & \frac{\partial C_{R_2}}{\partial \sigma_1} \\
 & \frac{\partial C_{T_{j+1}}}{\partial \sigma_j} & \frac{\partial C_{P_{j+1}}}{\partial \sigma_j} \\
 & & \frac{\partial C_{T_{M+1}}}{\partial \sigma_M} & \frac{\partial C_{P_{M+1}}}{\partial \sigma_M} & \frac{\partial C_{R_{M+1}}}{\partial \sigma_M}
 \end{array} & \text{BL Node} \\
 \hline
 \begin{array}{ccc}
 \frac{\partial C_{L_{1+N_z}}}{\partial \sigma_1} & \frac{\partial C_{P_{1+N_z}}}{\partial \sigma_1} & \frac{\partial C_{B_{1+N_z}}}{\partial \sigma_1} \\
 & \frac{\partial C_{L_{j+N_z}}}{\partial \sigma_j} & \frac{\partial C_{P_{j+N_z}}}{\partial \sigma_j} & \frac{\partial C_{B_{j+N_z}}}{\partial \sigma_j} \\
 & & \frac{\partial C_{L_{M+N_z}}}{\partial \sigma_M} & \frac{\partial C_{P_{M+N_z}}}{\partial \sigma_M} & \frac{\partial C_{B_{M+N_z}}}{\partial \sigma_M}
 \end{array} & \text{BR Node} \\
 \hline
 \begin{array}{ccc}
 \frac{\partial C_{L_{1+N_z+1}}}{\partial \sigma_1} & \frac{\partial C_{T_{1+N_z+1}}}{\partial \sigma_1} & \frac{\partial C_{P_{1+N_z+1}}}{\partial \sigma_1} \\
 & \frac{\partial C_{L_{j+N_z+1}}}{\partial \sigma_j} & \frac{\partial C_{T_{j+N_z+1}}}{\partial \sigma_j} & \frac{\partial C_{P_{j+N_z+1}}}{\partial \sigma_j} \\
 & & \frac{\partial C_{L_{M+N_z+1}}}{\partial \sigma_M} & \frac{\partial C_{T_{M+N_z+1}}}{\partial \sigma_M} & \frac{\partial C_{P_{M+N_z+1}}}{\partial \sigma_M}
 \end{array} & \text{TR Node}
 \end{bmatrix} 4M \times N_T$$

Figure 2.39: The pattern of the **M2P** matrix. The first  $M$  rows store  $\partial \mathbf{C}_{k_{yp}} / \partial \sigma_j$  for the top-left node, the second  $M$  rows is for the bottom-left node, the third  $M$  rows is for the bottom-right node and the fourth  $M$  rows is for the top-right node.

**M2P** by  $\tilde{\Phi}_{k_{yp}}^{A_i}$ , we get  $\frac{\partial \mathbf{C}_{k_{yp}}}{\partial \sigma_j} \tilde{\Phi}_{k_{yp}}^{A_i}$  for all  $j$ . Then we multiply the result by  $\psi_p$  to obtain  $\frac{\partial}{\partial \sigma_j} \tilde{\phi}_{k_{yp}}^{A_i, p}$  for all  $p$  and all  $j$ . By using this method, the CPU time is significantly reduced from more than 5 minutes to a few seconds (Vachiratienchai & Siripunvaraporn, 2010). Note that  $\partial \mathbf{C}_{k_{yp}} / \partial \sigma_j$  of FE and HB is different from FD. There are 9 or 14 non-zero elements for FE and 9, 12 or 14 non-zeros elements for HB but those elements are still in 4 rows of  $\partial \mathbf{C}_{k_{yp}} / \partial \sigma_j$ . Therefore this process can function for both FE and HB methods.

In the previous section, we describe about how to compute the whole Jaco-



bian matrix and it needs about 12.6 seconds of CPU time for the previous test. There is another approach for approximating the Jacobian matrix. It is called Broyden's update method (Broyden, 1965). Broyden's update method updates the Jacobian matrix using

$$\mathbf{J}_{k+1} = \mathbf{J}_k + \mathbf{u}_k \mathbf{p}_k^T, \quad (2.142)$$

where  $\mathbf{u}_k = (\mathbf{F}[\mathbf{m}_{k+1}] - \mathbf{F}[\mathbf{m}_k] - \mathbf{J}_k \mathbf{p}_k) / (\mathbf{p}_k^T \mathbf{p}_k)$  and  $\mathbf{p}_k = \mathbf{m}_{k+1} - \mathbf{m}_k$ . It needs only 0.02 seconds for the previous test. Broyden's update method has been applied to DC resistivity inversion by Loke & Barker (1996), Loke & Dahlin (1997), Loke & Dahlin (2002) and Christiansen & Auken (2004). In theory, the convergence rate of the approximate Jacobian matrix is less than that of the exact Jacobian matrix. Loke & Dahlin (2002) reported that if the resistivity contrast is greater than 10:1, there are significant differences in the results obtained by the two methods.

Here, we also integrate Broyden's update method into our inversion and we compare the convergence rate of both methods on both synthetic and real field data.

### 2.4.3 Lagrange multiplier $\lambda^{-1}$

The Lagrange multiplier is first introduced as the weighting parameter between the model objective function  $\chi_m^2$  and the data objective function  $\chi_d^2$ . Most of the inversions use  $\lambda$  for choosing the searching space and then vary another parameter to find the best model on that searching space. For example, Loke & Dahlin (2002) start their inversion with a large value of  $\lambda$ , and then progressively reduce  $\lambda$  after each iteration until it reaches the minimum limit ( $\lambda_m$ ). The  $\lambda_m$  is usually set as one-tenth of the initial  $\lambda$ . Loke & Dahlin (2002) have found that the initial  $\lambda$  is between 0.10 and 0.20 giving satisfactory results for most synthetic and field data sets. The  $\lambda$  is reduced by a factor of 2.5 after each iteration, and it reaches the minimum value after the fourth iteration. After the fourth iteration, the  $\lambda$  is kept constant at  $\lambda_m$ . For Occam's inversion,  $\lambda$  is treated in a different way. It is always used as the searching parameter for inversion. Its maximum and minimum values aren't set as in other inversions. Its value is automatically adjusted by the inversion to find the best result. On other hand, Occam's inversion automatically chooses its searching space while other inversions have to manually choose their searching spaces. This is the advantage of Occam's inversion over other inversions.

For our code, we use successive parabolic interpolation (SPI) for varying  $\lambda$  in logarithmic space. We start the process with 3 three initial values which are 1, 2, and 3. Then SPI estimates the new  $\lambda$  such that the data objective function is less than previous values. If  $\chi_d > \chi_d^*$ , this process terminates when the new  $\lambda$  differs from the previous  $\lambda$  by less than 20% or a parabolic curve is found. If  $\chi_d < \chi_d^*$ , this process terminates when the new  $\lambda$  differs from the previous  $\lambda$  by less than 0.001% or  $\chi_d$  differs

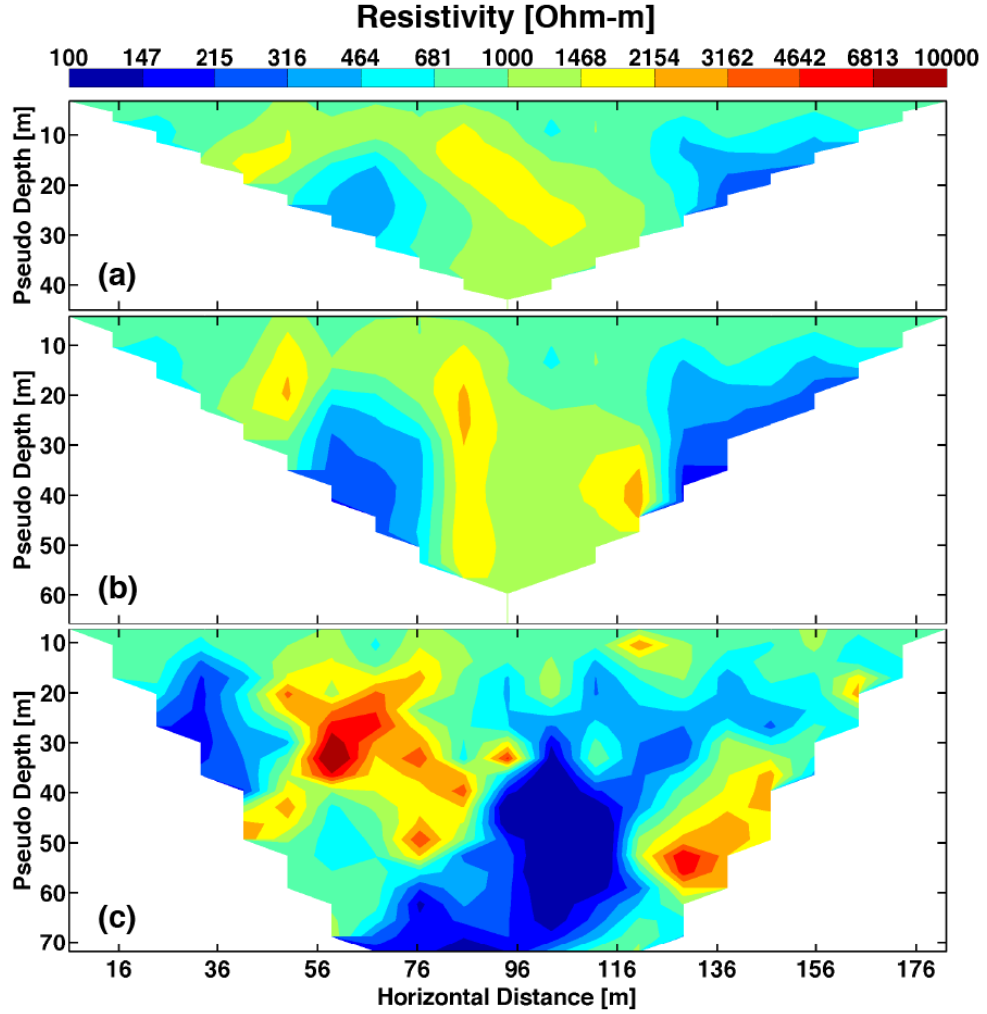


Figure 2.40: Pseudo-section of the “extreme” topography model (figure 2.25) for (a) Wenner, (b) Schlumberger and (c) Dipole-Dipole arrays which are used as observed data for Synthetic test.

from  $\chi_d^*$  by less than 5% of  $\chi_d^*$ . The resulting  $\lambda$  is used as the initial  $\lambda$  for the next iteration.

#### 2.4.4 Synthetic Test

In this section, the efficiency, robustness and reliability of our inversions are tested on synthetic data from an “extreme” topography model. All three common arrays (Wenner, Schlumberger and Dipole-Dipole arrays) are used in this test. Each array has 48 electrodes with 4-m horizontal electrode spacing. Figure 2.40 shows pseudo-sections for (a) Wenner, (b) Schlumberger and (c) Dipole-Dipole arrays.

Three percent random noise is added to the simulated data to make them as if they are collected from a real field survey and they are used as errorbars for the synthetic tests. In the inversion, the resistivity model is discretized into  $209 \times$

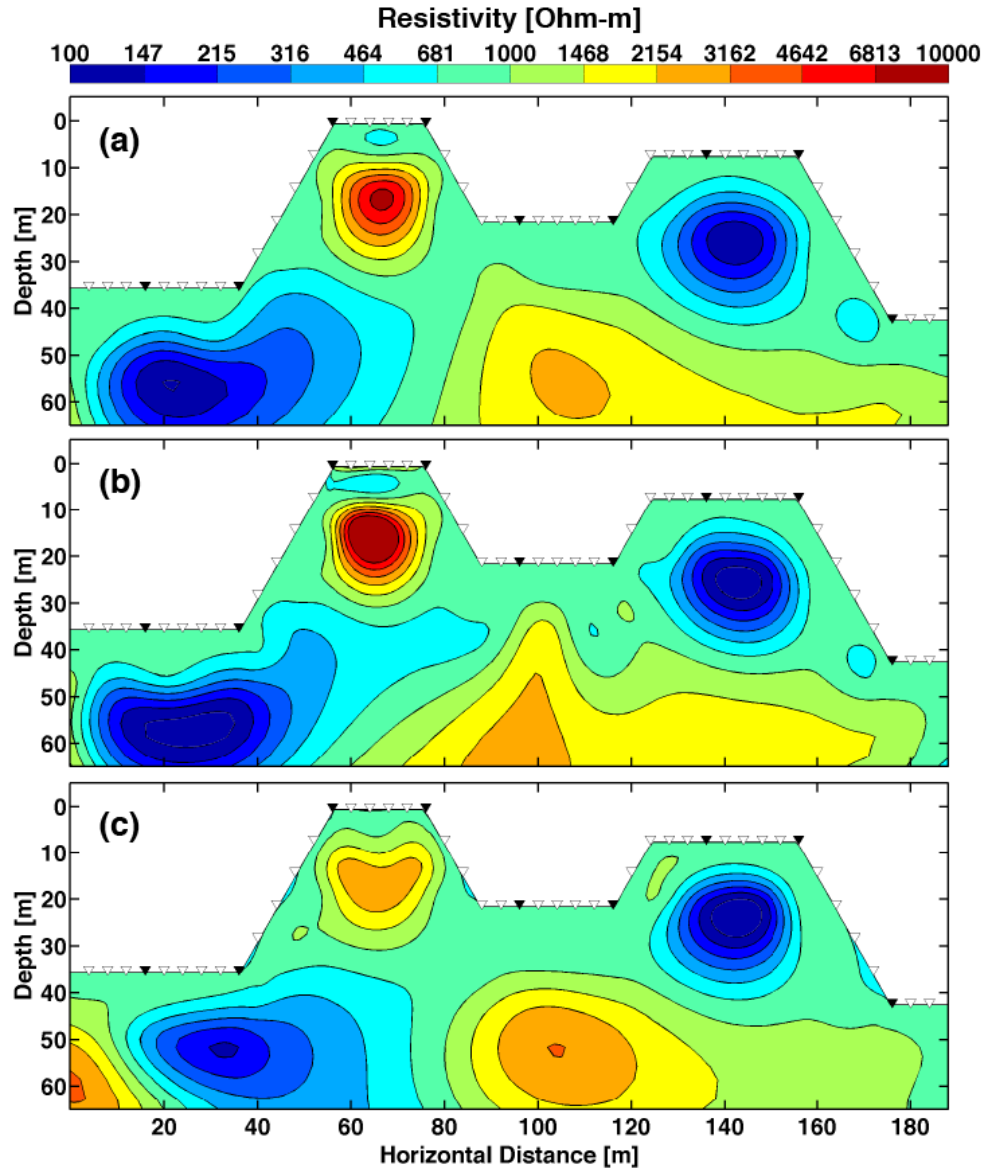


Figure 2.41: The final inverted results of the “extreme” topography model (figure 2.25a). Figures a, b and c are inverted results for Wenner, Schlumberger and Dipole-Dipole arrays computed by the FD method.

59 elements leading to 12,331 unknowns for FD and 8,560 unknowns for FE and HB. A homogeneous model is used as the initial and prior model of which the resistivity is computed from the geometric mean as described in Section 2.4.2. These resistivity values lead a data misfit of FD to 9.04% for Wenner, 12.11% for Schlumberger and 18.92% for Dipole-Dipole array and lead a data misfit of FE and HB to 9.06% for Wenner, 11.88% for Schlumberger and 18.24% for Dipole-Dipole array. The final data misfit, CPU time, memory of the synthetic tests are summarized in table 2.10 and the final inverted results computed by the FD method are shown in figure 2.41. Figure

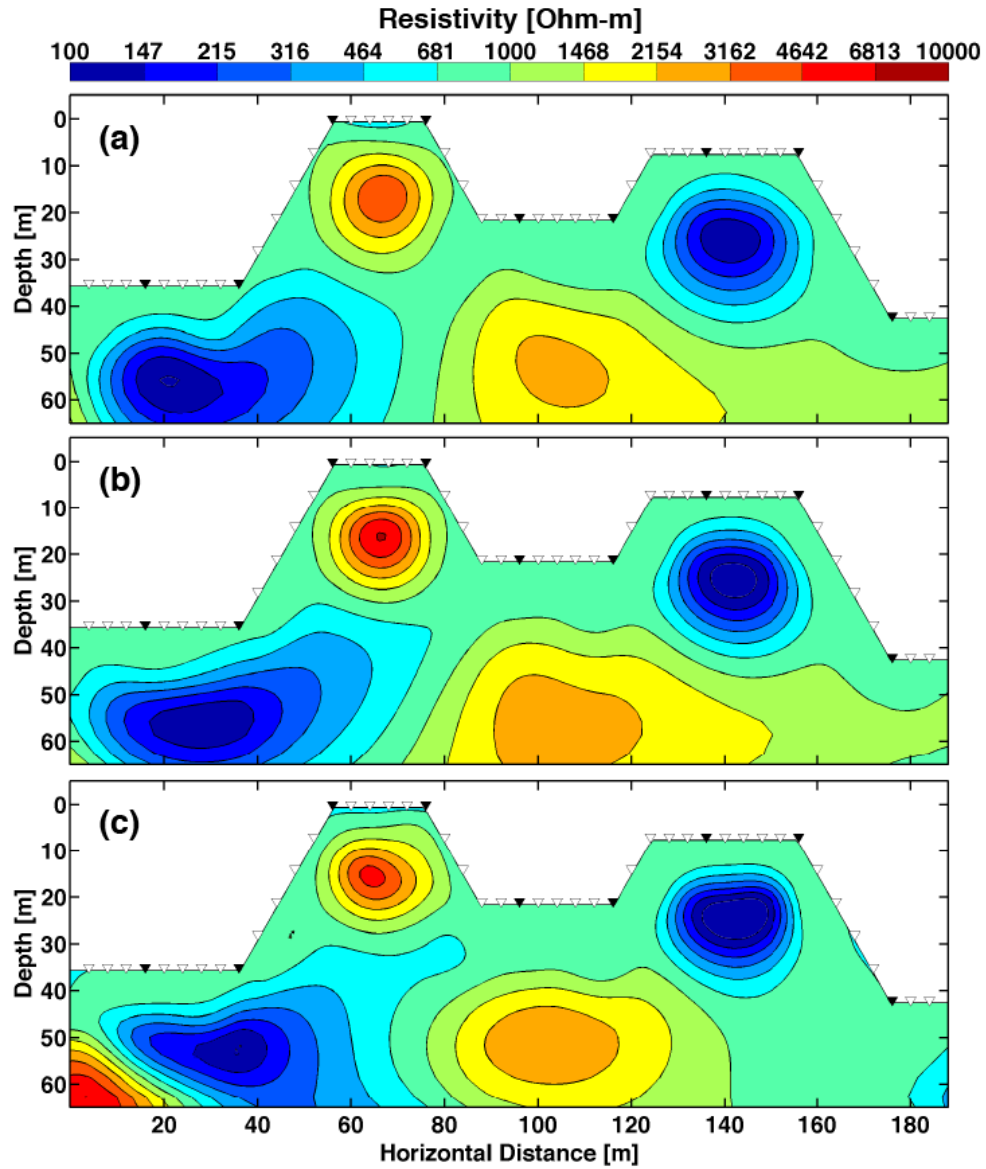


Figure 2.42: The final inverted results of the “extreme” topography model (figure 2.25a). Figures a, b and c are inverted results for Wenner, Schlumberger and Dipole-Dipole arrays computed by the HB method.

2.42 shows the inverted results computed by the HB method. The results from the FE method are similar to the results from the HB method.

The HB method produces the same results as the FE method for all arrays. For the Wenner and Schlumberger arrays, both methods can reach the target (1%) in 5 iterations. Both inversions can also recover all anomalies beneath the topography relatively well as shown in figure 2.42a and 2.42b. For FD, the inversion cannot reach the target misfit and its result is different from FE and HB as shown in figure 2.41. The main reason is that the FD response is inaccurate because of its topography approximation.

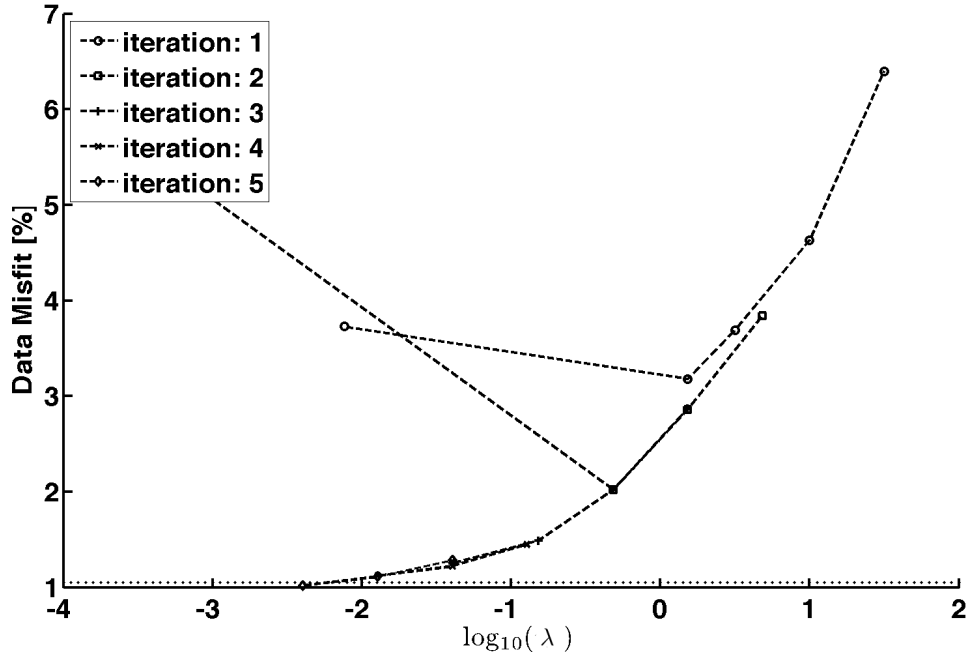
Table 2.10: The data-misfit and memory usage for FD, FE and HB inversions for three common arrays.

Array	Method	Data Misfit		CPU [min] (No. Iter)	Memory Usage [MB]	
		Initial	Final		Jacobian	Total
Wenner	FD	9.04	1.19	2.30 (3)	22.73	287.71
	FE	9.06	1.05	6.50 (5)	23.00	191.68
	HB	9.06	1.05	3.68 (5)	23.00	159.31
Schlumberger	FD	12.11	1.41	4.12 (5)	33.4	292.8
	FE	11.88	1.02	7.09 (5)	33.8	196.6
	HB	11.88	1.02	3.84 (5)	33.8	164.2
Dipole	FD	18.92	2.69	4.64 (5)	53.03	348.32
	FE	18.24	1.99	11.74 (5)	53.67	252.02
	HB	18.24	1.99	4.27 (5)	53.67	220.65

The inversion has to compensate for this inaccuracy by adding some artifacts into the model. For the Dipole-Dipole array, all methods cannot reach the target level. Data misfits are reduced from 18.92 to 2.69 in 5 iterations for the FD method and from 18.24 to 1.99 in 5 iterations for the FE and HB methods before diverging.

Figure 2.43 shows the variation of  $\lambda$  of each iteration for the HB method. The first iteration uses 5 values of  $\lambda$  to search for the minimum RMS. The minimum-RMS model of iteration 1 is then used as the initial model for the 2nd iteration. The process is then repeated for the next iteration. Figure 2.43 shows that, after each iteration,  $\lambda$  shifts to the left side, i.e., to a smaller value of  $\lambda$  for more structures and a rougher model. The inversion takes slightly less than 4 min for HB and close to 8 min for FE to converge to 1 RMS and also to reach the minimum RMS at the 5th iteration for FD. On average, each iteration takes around 40-50 s for HB, 88-105 s for FE, and 50-60 s for FD. More than 65% of this CPU time is used for the matrix-vector multiplication to form and store  $\mathbf{J}_k \mathbf{C}_m \mathbf{J}_k^T$ , while the rest is for solving and updating the model (equation (2.122)) for each  $\lambda$ .

Normally, the memory usage for inversion is dominated by the Jacobian matrix  $\mathbf{J}_k$  but this is not the case here. The memory usage in the forward modeling routines to keep all  $\mathbf{L}$  and  $\mathbf{U}$  matrices of all eight wave-numbers is a lot larger than that of the Jacobian matrix (Table 2.3.7 and Table 2.10). However, the total amount of memory required for the whole inversion process (Table 2.10) is currently not a problem for most computers for 2-D inversion. Therefore, storing all necessary matrices would be an advantage since we can repeatedly use them as many times as we like for different values of  $\lambda$ . These advantages are not possible in CG and NLCG inversions since such algorithms do not construct this large sensitivity matrix, and do not solve the system of equations with the direct method.

Figure 2.43: Data misfit versus  $\lambda$  for each iteration.

### Comparison of Jacobian calculation

In the previous section, we validated our FD, FE, and HB inversion and its results show that the HB method produces reliable results and has fewer requirements than other methods. Here, we test the effect of the Jacobian calculation on the inverted result by using the HB method. In this test, inversion uses the fully computed Jacobian matrix at the first iteration and after that uses Broyden's update technique (equation (2.142)) is used for updating the Jacobian matrix. The change in the data misfit with the CPU time for the full Jacobian calculation (FJC) and Broyden's update (BU) are reported in figure 2.44b and the final inverted result for Broyden's update is shown in 2.44a.

The data misfit decreases with each iteration and its reduction is largest after first three iterations for both methods. After the 4<sup>th</sup> iteration, the data misfit of BU is almost constant but the data misfit of FJC decreases until it reaches the target at the 5<sup>th</sup> iteration. The inversion process of BU is terminated at the 9<sup>th</sup> iteration because its data misfit is constant at 1.19. On average (except the first iteration), BU uses about 18-21 seconds to finish its iteration and uses only 0.025 seconds to update its Jacobian matrix. Although BU consumes less CPU time than FJC in each iteration, its CPU time for whole inversion is 3.53 min which is less than that of FJC by about 8% or 19 seconds. For its inverted result (figure 2.44a), four resistivity anomalies are recovered but its shapes are distorted from the FJC result (figure 2.42b), especially the

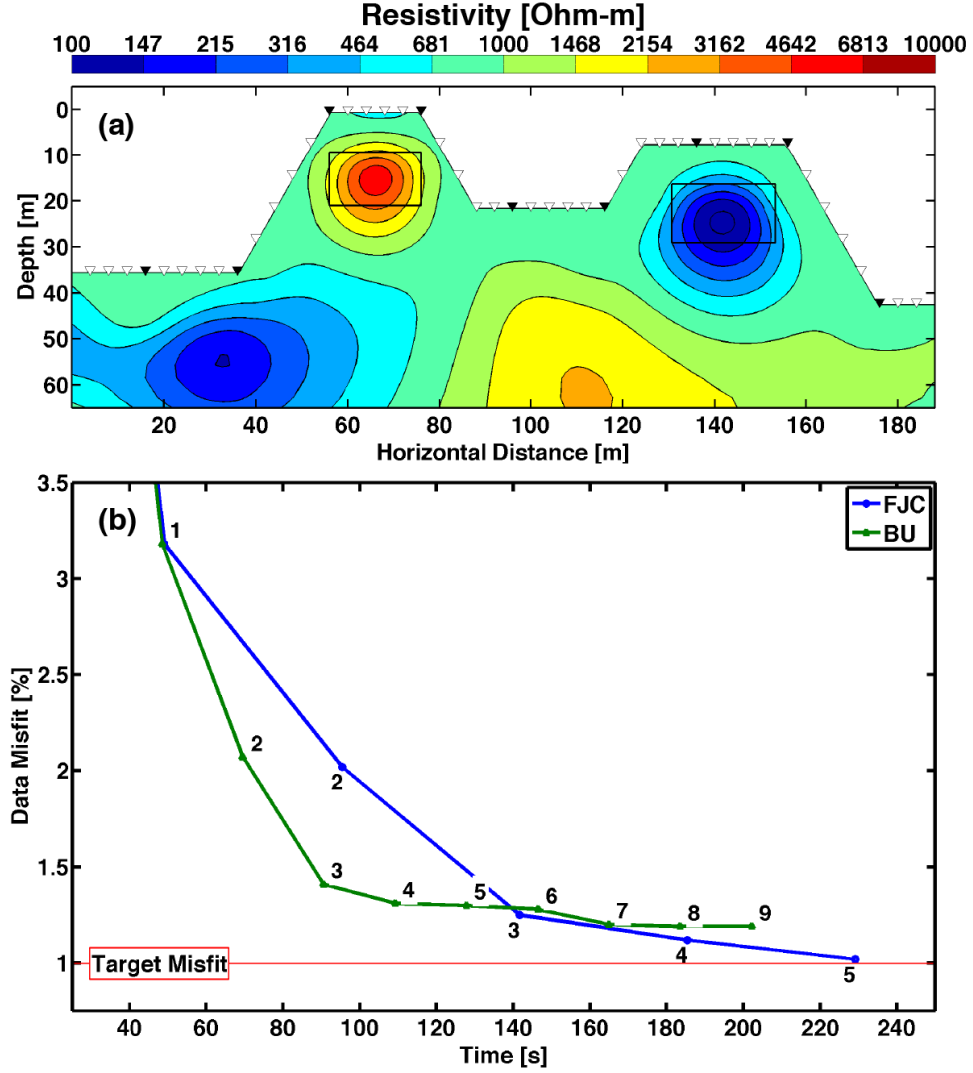


Figure 2.44: (a) the inverted model of the Schlumberger data generated from extreme topography model (Figure 2.25a) when the Jacobain matrix is estimated by Broyden's update (equation (2.142)) and (b) the change of data misfit with CPU time for FJC and BU.

two deeper anomalies.

Although BU can reduce the CPU time in each iteration, its overall CPU time is slightly less than that of FJC and this difference will decrease when the number of models or data points decrease. This difference is acceptable for real field work. Therefore, we highly recommend FJC for real field work.

### Comparison of the controlling parameter $\eta$

As described in Section 2.4.2, we redesign the module for computing  $\mathbf{C}_m \mathbf{J}_k^T$  and its smoothness is controlled by  $\eta$ . In this section, we study the affect of  $\eta$  by using the data from the Schlumberger array. Figure 2.45a, b, c, and d shows the inverted results

when  $\eta$  is 1, 2, 4 and 8, respectively. All of them can reach target level but its results are slightly different. The black rectangular block indicates the position of conductive and resistive anomalies beneath the hills. Following the results, two anomalies beneath the hills are recovered better than other anomalies for all values of  $\eta$ . For  $\eta = 1$ , the inverted result clearly shows 4 main anomalies and 1 small artifact at the surface of the left hill as shown in figure 2.45a. When  $\eta$  is increased to 2, the size of artifact increases as shown in figure 2.45b. The number of artifacts increases from 1 to 3 when  $\eta$  is 4 as shown in figure 2.45c. For  $\eta = 8$ , inversion includes a lot of artifacts at the surface of the left hill and along the surface. These artifacts reduce the resistivity value of the lower anomalies as shown in figure 2.45d.

The  $\eta$  parameter has an effect on the inverted results and also has effect on the convergence rate as shown in figure 2.46. The convergence rate is lowest when  $\eta = 1$  and significantly increases when  $\eta$  is 2, 3 or 4. Although  $\eta = 1$  has the lowest convergence rate, it returns the clearest inverted result and its recovered anomalies are close to actual anomalies. This is true for the locations, values, and shapes.

For noisy data from field surveys,  $\eta$  can be applied for controlling the clearness of the inverted model. By setting  $\eta = 1$ , the inversion returns a model which has a few anomalies as possible. By setting  $\eta = 8$ , the inversion returns a model which has the least data misfit but might have unreasonable anomaly due to noise in the observed data.

### 2.4.5 Real Case Test

Here, we tested our inversion code on real field data collected within the Kanchanaburi campus of Mahidol University, located about 200 km west of Bangkok (figure 2.47).

The field test area consists of many caves and cavities and also has steep slopes. Two profiles (L1 & L2) with 48 electrodes and about 4 m spacing (along the topography) of a Schlumberger array are laid out in the area as shown in figure 2.47. Both profiles lie next to the cave exposed to the surface. The main objective of the experiments is to detect and map the lateral network of the cavities beneath.

The details of the test are summarized in table 2.11. All runs set the error bars of the data to 1%. The observed data, forward response, and its final inverted model from our inversion code (FJC) and from the RES2DINV code are shown in figure 2.48 and 2.49 for L1 and L2, respectively.

The grid used for L1 is  $190 \times 82$  with a total of 12,159 unknown nodes and for L2 is  $173 \times 70$  with 7,673 unknown nodes. As with the synthetic example, the inversions were started with the homogeneous models with an average resistivity of 795  $\Omega$ -m for L1 and 1,170  $\Omega$ -m for L2. These values were computed from their



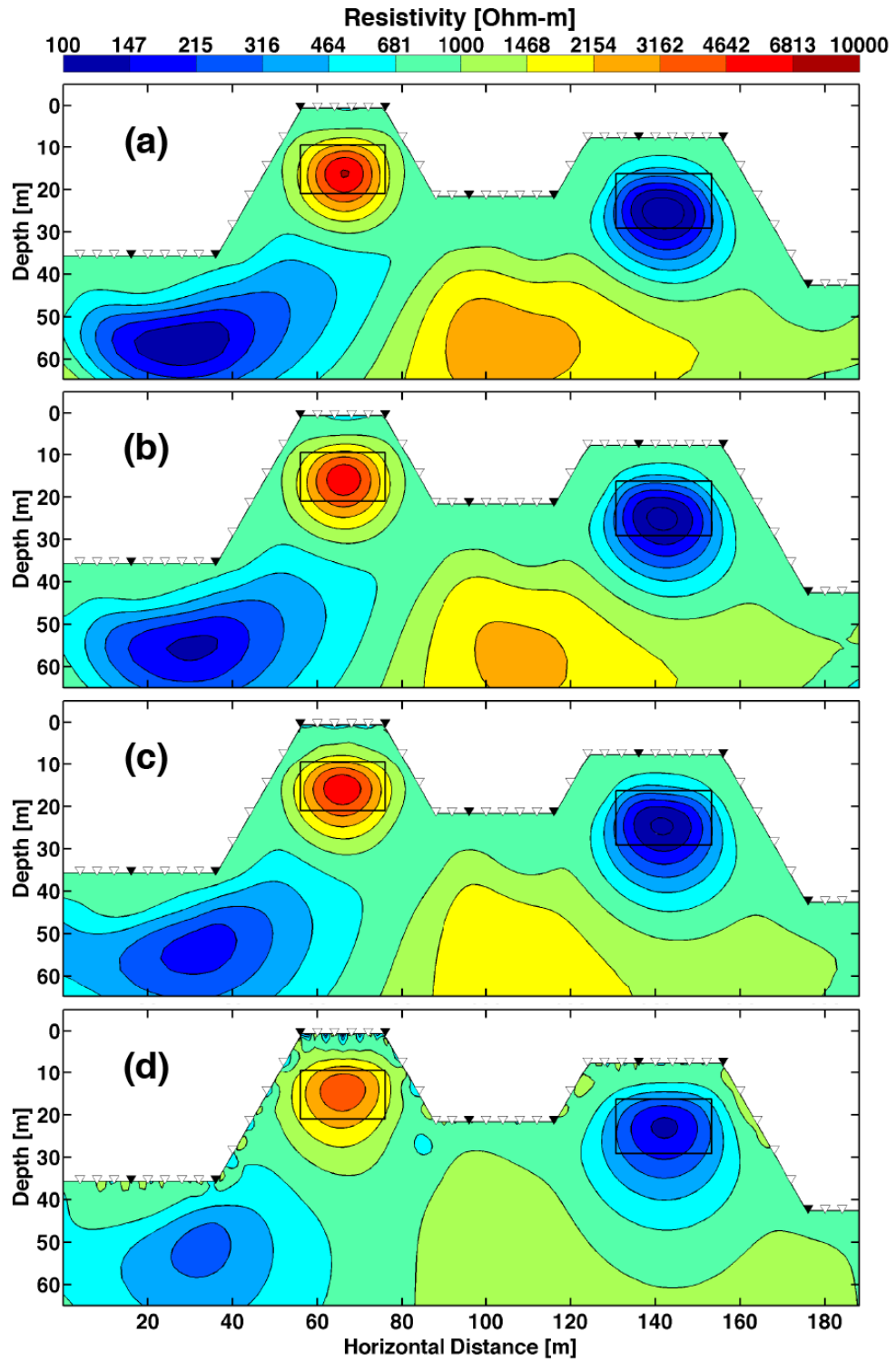


Figure 2.45: The inverted model of the Schlumberger data generated from an extreme topography model (Figure 2.25a) when the controlling parameter  $\eta$  is (a) 1, (b) 2, (c) 4 and (d) 8.

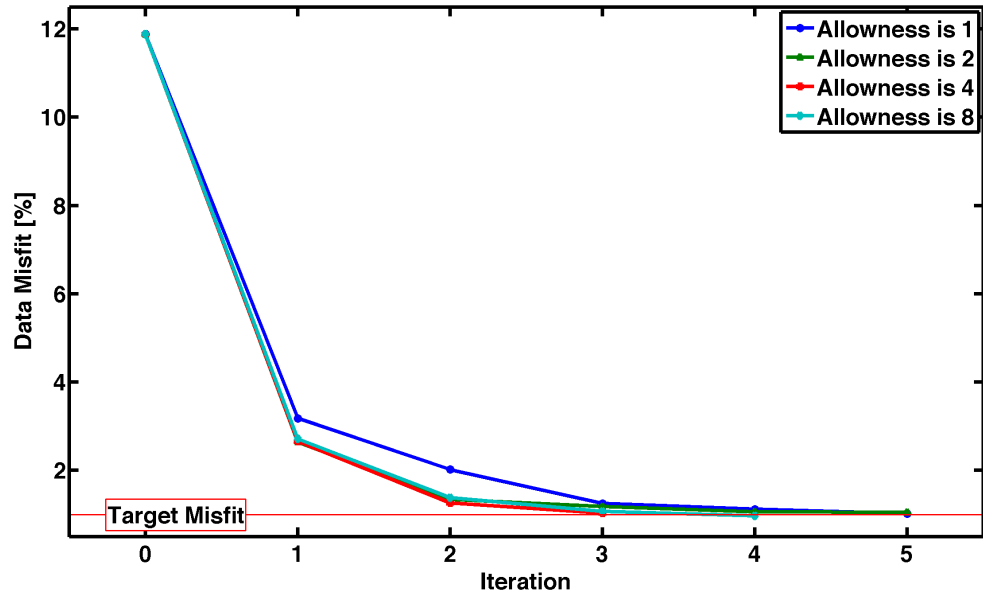


Figure 2.46: The change of data misfit with iteration for  $\eta$  is 1, 2, 4 and 8.

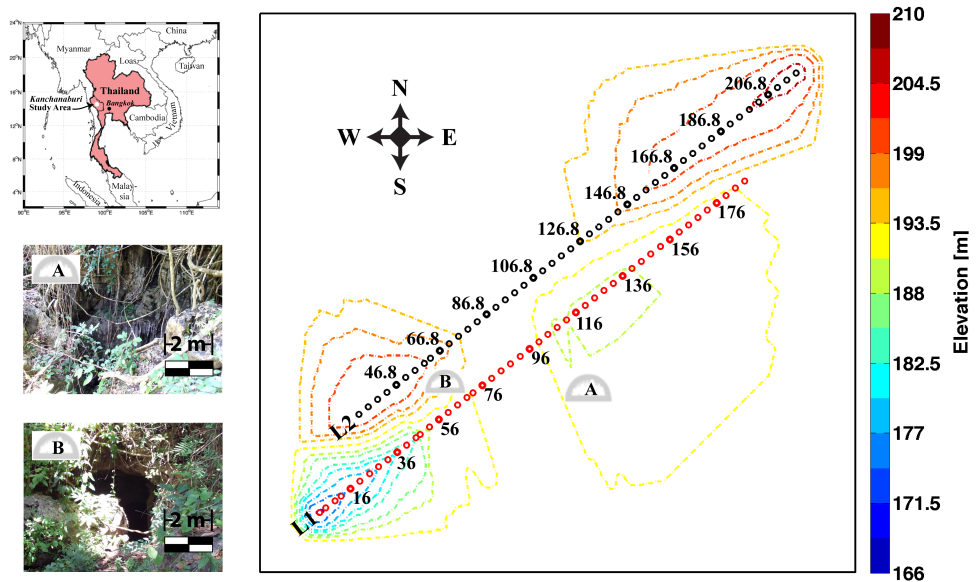


Figure 2.47: Field test area inside Mahidol University, Kanchanaburi campus, western Thailand. The two profiles (L1 & L2) are illustrated in the map with red and black profiles, respectively. The caves exposed at the surface are marked on the map as caves A and B (after Vachiratiengchai & Siripunvaraporn, 2013).

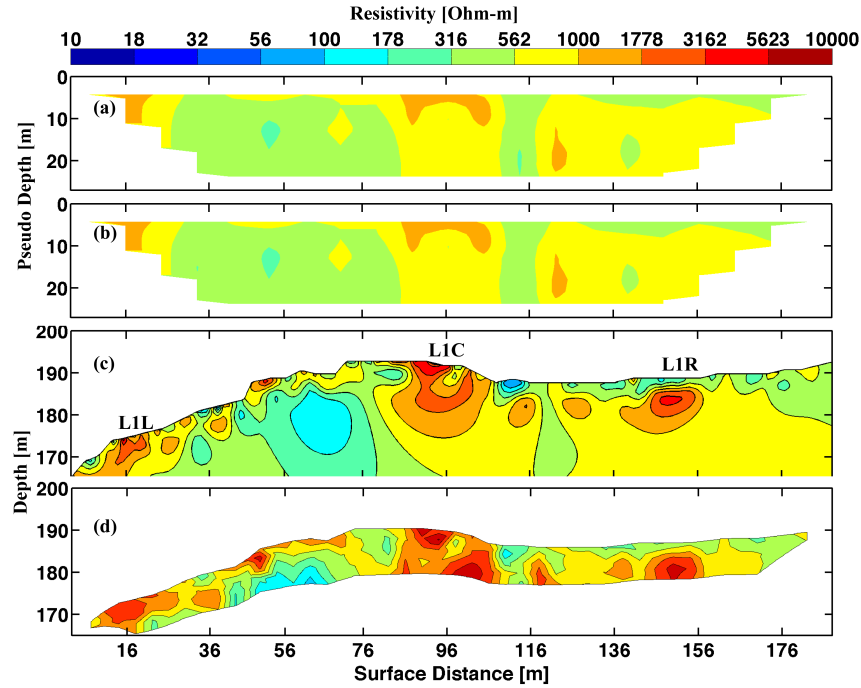


Figure 2.48: Line 1 showing (a) the observed Schlumberger data, (b) the forward response, (c) the inverted model from our inversion (FJC) and (d) the inverted model from RES2DINV. The RMS misfits and number of iterations for this figure can be seen in Table 2.11 (after Vachiratienchai & Siripunvaraporn, 2013).

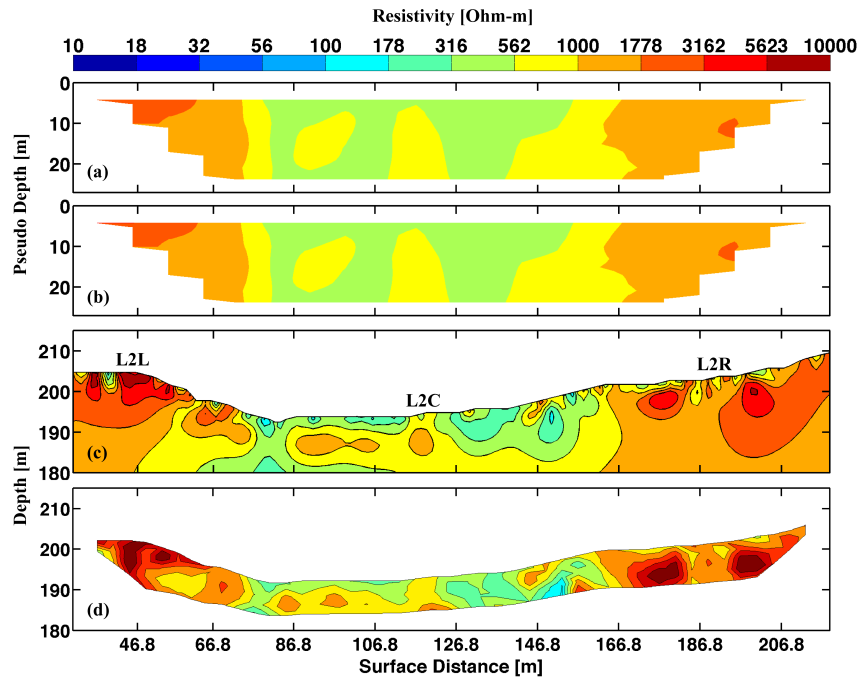


Figure 2.49: Line 2 showing (a) the observed Schlumberger data, (b) the forward response, (c) the inverted model from our inversion (FJC) and (d) the inverted model from RES2DINV. The RMS misfits and number of iterations for this figure can be seen in Table 2.11 (after Vachiratienchai & Siripunvaraporn, 2013).

apparent resistivity and led to an data misfit of 51.3% and 57.3%, respectively, for L1 and L2 (table 2.11). Both data sets were also run with RES2DINV. The slopes at some points of the data are too steep. RES2DINV needed to lower these slopes to make the topography smoother. Our inversion can reduce the data misfit of L1 to a minimum of 1.75% in 8 iterations taking 8.52 min and reach the target 1% RMS for L2 in 6 iterations in 3.79 min (table 2.11). RES2DINV can only reduce the RMS misfit to 3.09% in 25 iterations for L1 and 3.22% in 25 iterations for L2 before the program was automatically terminated. For both runs, RES2DINV requires less than 20 seconds CPU time which is 10-30 times faster than our code. However, our inversion code can fit the observed data better than the commercial code as shown in table 2.11.

The commercial code is significantly faster than ours because of several techniques used in their code. First, their code constructs and stores the initial Jacobian matrix when the program is first installed. Then, the Jacobian matrix for each iteration is estimated by Broyden's update as described in section 2.4.2. This process decreases the CPU time significantly. This RES2DINV code is therefore regarded as Broyden's update technique, while our code is a full Jacobian calculation (FJC) since we construct the real sensitivity at every iteration. We also applied Broyden's update (BU) technique to our data space inversion code. We found that a significant reduction of the CPU time from 40-60 s to less than 20-30 s per iteration can be obtained although this is still more than the CPU time of RES2DINV program. Most of the extra CPU time is for calls to the forward modeling routine. With the BU technique, the CPU time can be significantly decreased. However, its convergence is then not as good as with the FJC. The BU technique can reduce the data misfit to a minimum RMS of 2.77% for L1 and 2.44% for L2 (table 2.11) which are still higher than the FJC, and still better than the data misfit of RES2DINV. The BU technique cannot decrease the data misfit as well as using the FJC. This is shown by the runs of our code and the commercial code. Our experiment therefore demonstrates a tradeoff between the CPU time and the minimum

Table 2.11: The descriptions of the inversions for line 1 and line 2 of the real surveys by Occam's inversen for both full Jacobian calculation (FJC) and Broyden's update (BU) and the commercial RES2DINV code. After the 21st iteration, RES2DINV was terminated as the change in the model was relatively small.

Profile	Method	No. of Iter	CPU Time [min]	Final Misfit [%]
Line 1	Occam (FJC)	8	8.52	1.75
	Occam (BU)	12	6.53	2.77
	RES2DINV	21	0.27	3.16
Line 2	FJC	6	3.79	1.00
	BU	6	1.97	2.44
	RES2DINV	21	0.26	3.32

misfit obtained.

The CPU time of our code depends on the number of nodes used. L1 requires more unknown nodes and therefore requires more calculation time than L2. One major point to notice in our experiments is that to achieve the same data misfit as that of the RES2DINV program, the FJC version needs only 3 iterations to be at 3.06% for the L1 profile and required 3.32 min. Similarly, it uses only 3 iterations to be at 3.04 RMS for L2 and takes 1.94 min. On the other hand, the BU version needs 10 iterations (takes 5.55 min) for L1, and 4 iterations (taking 1.51 min) for L2 to be at about the same data misfit level as the FJC version. Based on this experiment, the CPU time of the BU version is more for L1 and slightly less for L2. Because the full sensitivity version can reach a lower data misfit, we prefer to use the FJC version rather than the BU version. Although, CPU times may be significantly larger than those of RESINV2D, they are still acceptable and practical in real field surveys.

The inversion models from our inversion and RES2DINV look similar for both profiles (figure 2.48c and d for L1, and figure 2.49c and d for L2). From figure 2.47, there are two caves, A and B, exposed to the surface. Cave A is on the right of L1 while cave B is in between both profiles. The paths, sizes and shapes of both caves are unknown and are investigated with the DC resistivity survey. The area is dominated by limestone to a depth of 100 m based on the drilling. Therefore, the high resistivity ( $> 3000 \Omega\text{-m}$ ) zone near the surface can only be interpreted as a cavity inside the limestone. Figure 2.48 shows that there are three notable high resistivity zones; the first (L1L) is at 14-25 m, the second (L1C) is 86-106 m, and the third zone (L1R) is 146-156 m but is not as near the surface as the first two cavities. For L2, three high resistivity zones which are broader and wider are located at 30-68 m (L2L), 86-126 m (L2C) but deeper, and 168-208 m (L2R). Associating these high resistivity zones with both caves, we found that cave A may be mapped as L1C. If it continues to L2, it may dip to a greater depth and appears as the high resistivity zone L2C beneath the profile L2. Cave B shows little correlation with high resistivity zones of L1, but matches well with L2L. This indicates that cave B dips and is wide beneath L2. The other caves cannot be related to caves A and B.

## 2.5 Conclusion

Here, we develop 2-D DCR forward modeling based on the hybrid finite difference-finite element technique and the inversion based on the data space Occam's inversion. This allows forward modeling to include steep topography ( $> 45^\circ$ ). Hybrid FD-FE technique needs less CPU time than either of the FD or FE methods alone. In addition, the full sensitivity calculation is based on the adjoint Green's function tech-

nique applied to the hybrid system of equations. This technique significantly decreases the computational time. Both techniques were applied inside the data space Occam's inversion. The number of iterations needed for convergence is smaller than when other methods are used, and the method is better at reducing the RMS misfit. Its weakness is only that it requires more CPU time than the commercial code. However, the CPU time is in the order of a few minutes even for a larger model. It is also acceptable and practical for applications in field surveys.

## CHAPTER III

# CONTROLLED-SOURCE ELECTROMAGNETIC INVERSION

In this chapter, we develop 3-D CSEM modeling and inversion on a ModEM modular system. The technique we used for the modeling and inversion is the scattered-field technique. We start the chapter by briefly describing the CSEM survey. Then we describe Maxwell's equations and how to solve Maxwell's equation by a scattered-field technique. Then we also describe ModEM and its mathematical framework. In the next section, we summarize the keys of modification for implementation of ModEM to work on CSEM data. Finally, we test 3-D CSEM modeling and inversion with synthetic models.

### 3.1 Controlled-Source Electromagnetic Surveys

A controlled-source electromagnetic (CSEM) survey is an offshore electromagnetic survey for studying resistivity structure beneath the seafloor. This technique energizes the Earth by an artificial electromagnetic (EM) source and measures the Earth's responses. Artificial EM sources are also used in various surveys such as controlled-source audio magnetotelluric (e.g. Qian & Pedersen, 1992; Yun-Feng & Ji-Feng, 2011; Chang-Hong *et al.*, 2012; Kalscheuer *et al.*, 2012; Wang *et al.*, 2012; Wu *et al.*, 2012), controlled-source radio magnetotelluric (e.g. Bastani *et al.*, 2011), crosswell electromagnetic (e.g. Wei *et al.*, 1999; Hoversten *et al.*, 2001, 2004; Kim *et al.*, 2004; Pardo *et al.*, 2008; Li *et al.*, 2010; Donadille & Al-Ofi, 2012), and marine DC resistivity (e.g. Goto *et al.*, 2008; Chiang *et al.*, 2011, 2012).

Controlled-source electromagnetic surveys have existed as academic techniques since the 1980s for studying the oceanic lithosphere (Constable & Srnka, 2007) and it was applied as a tool for evaluating reservoir resistivity in the hydrocarbon industry since the late 1990s. In 2000-2002, Statoil and ExxonMobil showed that CSEM data can be successfully used to evaluate reservoir resistivity for targets as deep as several thousand meters offshore Angola. Both companies leveraged instrumentation and expertise from the academic community to make big progress. This resulted in rapid growth in the use of marine CSEM methods for exploration. Now, CSEM data represents a commercial commodity within the exploration business, and acquisition services

are offered by three companies. The ability to determine the resistivity of deep targets from the seafloor makes marine CSEM the most important geophysical technique to emerge since 3D reflection seismology.

Figure 3.1 represents the basic diagram of marine CSEM. A horizontal electric-dipole transmitter is towed close to the seafloor to maximize the energy coupling to seafloor rocks. Other type of sources have been used, such as vertical electric and horizontal magnetic dipoles (e.g Edwards, 2005). Nowadays, only horizontal electric-dipole is available as the EM source in the hydrocarbon industry. At the seafloor, a series of electromagnetic receivers spaced at various ranges from the transmitter record the time-varying electric field and magnetic field over source-receiver ranges from several tens of kilometers to zero. The electric and magnetic fields are processed with various procedures such as time-domain stacking, Fourier transforms, and merging with navigation and position. Finally the recorded signal are converted into the amplitude and phase of the transmitted signal as functions of source-receiver offset and frequency (which is typically between 0.1 and 10 Hz).

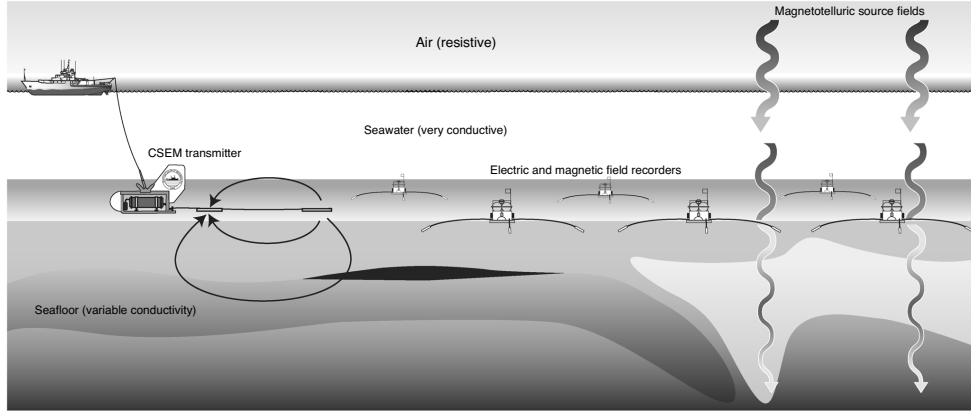


Figure 3.1: Schematic diagram represents the horizontal electric dipole-dipole CSEM method. An EM transmitter is towed close to the seabed to maximize the coupling of electric and magnetic fields with seafloor rocks. These fields are recorded by instruments deployed on the seafloor. The instruments are also able to record magnetotelluric fields that have propagated through the seawater layer (after Constable & Srnka, 2007).

### 3.1.1 CSEM Sounding

CSEM sounding is the method for studying the vertical variation of Earth's resistivity. This method fixes the position of the receiver and varies the transmitter position. Figures 3.4-3.8 show the sounding curve of the canonical model (Figure 3.2) when 200 A-m horizontal electric dipole in the  $x$ -direction is towed 50 meters above the seafloor. The canonical model consists of four layers which are (1) 1000 m thick and  $0.32 \Omega\text{-m}$  homogeneous seawater layer, (2) 1000 m thick and  $1.0 \Omega\text{-m}$  sediment layer,



(3) 100 m thick and 100  $\Omega$ -m oil/gas reservoir layer and (4) 1.0  $\Omega$ -m sediment layer (inspired by the Girassol prospect, Block 17, offshore Angola).

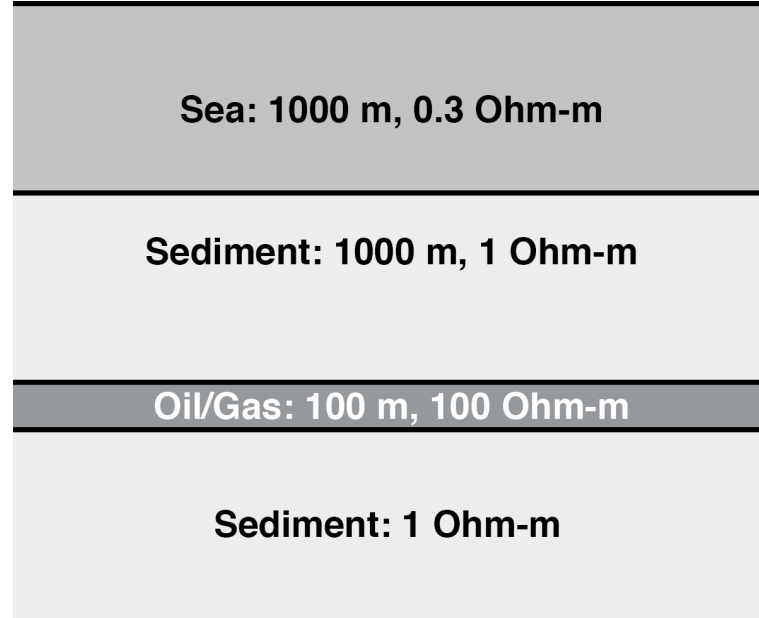


Figure 3.2: The canonical model for marine CSEM survey

Figure 3.3 shows the diagram of a CSEM receiver which consist of 3 induction coil magnetometers and 4 plastic arms for measuring 2 components of the electric field. Three induction coils measure three components of magnetic field which are (1) inline magnetic field, (2) broadside magnetic field and (3) vertical magnetic field. The other two components are (1) inline electric field and (2) broadside electric field. Inline and broadside are the words for indicating the orthogonality between the EM field and transmitter orientation. Inline means that EM field component is parallel to the transmitter orientation. In our case, inline means the magnetic or electric field is in the  $x$ -direction and broadside means the magnetic or electric field is in  $y$ -direction.

Although a seafloor receiver can record all of the EM components, only an inline electric field is used in real surveys. An inline electric field has the strongest signal and it is much greater than the error floor of an instrument as indicated by solid line in figure 3.4-3.8. For other components except  $B_y$ , their amplitudes are less than the error floor ( $10^{-16}$  V/Am<sup>2</sup> for an electric field and  $10^{-18}$  T for a magnetic field). Although the amplitude of a broadside magnetic field is also much greater than the error floor, an inline electric field is also well suited to operation in seawater (Constable & Srnka, 2007). This is because magnetic sensors are moved by water currents.

As shown in figure 3.8, the vertical magnetic field is not sensitive to the resistive layer. The amplitude and phase of the canonical model are similar to those of the homogeneous model. For other EM fields, their sounding curves are divided

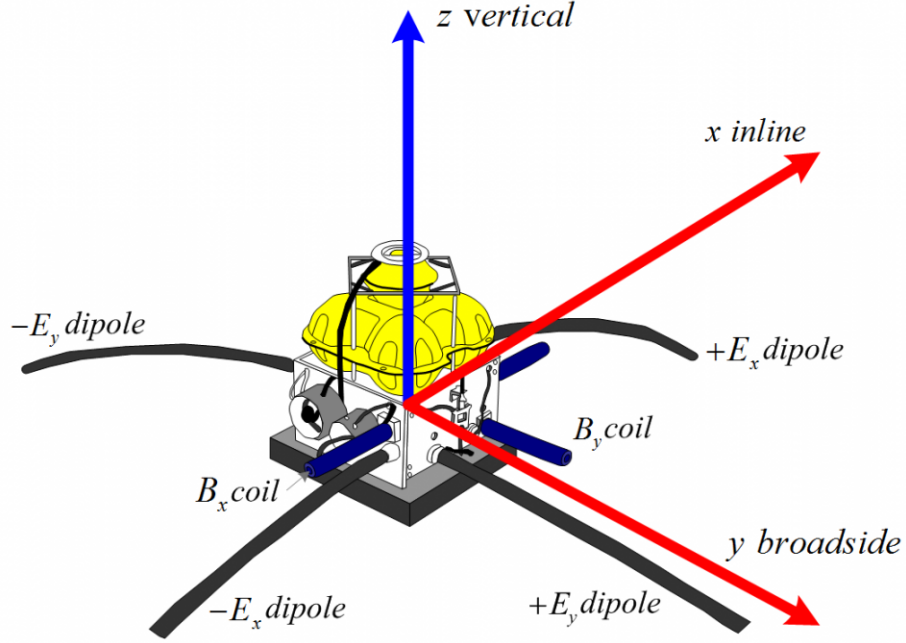


Figure 3.3: The diagram of a seafloor receiver. It consists of three induction magnetic coils and four plastic arms for measuring two components of the electric field (<http://marineemlab.ucsd.edu>).

into three regions which are (1) geometry and 1  $\Omega$ -m attenuation, (2) resistive layer attenuation and (3) airwave. The geometry attenuation region is the region where direct-wave attenuation dominates. This region has no information about the Earth's structure. The 1  $\Omega$ -m attenuation is the region where the EM field from the top sediment layer dominates. It cannot reflect or sense the resistive layer. The geometry and 1  $\Omega$ -m attenuation is about 2.0 km for inline ( $x$ ) electric field, 4.3 km for broadside ( $y$ ) electric field, 1.0 km for inline ( $x$ ) magnetic field and 1.3 km for broadside ( $y$ ) magnetic field. Next the resistive-layer-attenuation region is the region for which the response is dominated by the EM field from the resistive layer. It contains the most valuable information. The region is about 17 km for inline ( $x$ ) electric field, 13 km for broadside ( $y$ ) electric field, 10 km for inline ( $x$ ) magnetic field and 13 km for broadside ( $y$ ) magnetic field. The last one is the airwave region for which the response is dominated by airwaves. When the transmitter generates an EM wave, the EM wave propagates in all directions which are direct propagation to receiver, downward propagation into the Earth and upward propagation to the air-ocean interface. When the EM wave reaches the air-ocean interface, the EM wave will propagate along the interface and generate an EM field propagating downward to the receiver. This wave is called the "airwave" and it dominates when the offset is very long. In our case, the airwave shows up after 19 km for inline ( $x$ ) electric field, 17 km for broadside ( $y$ ) electric field, 11 km for inline ( $x$ )

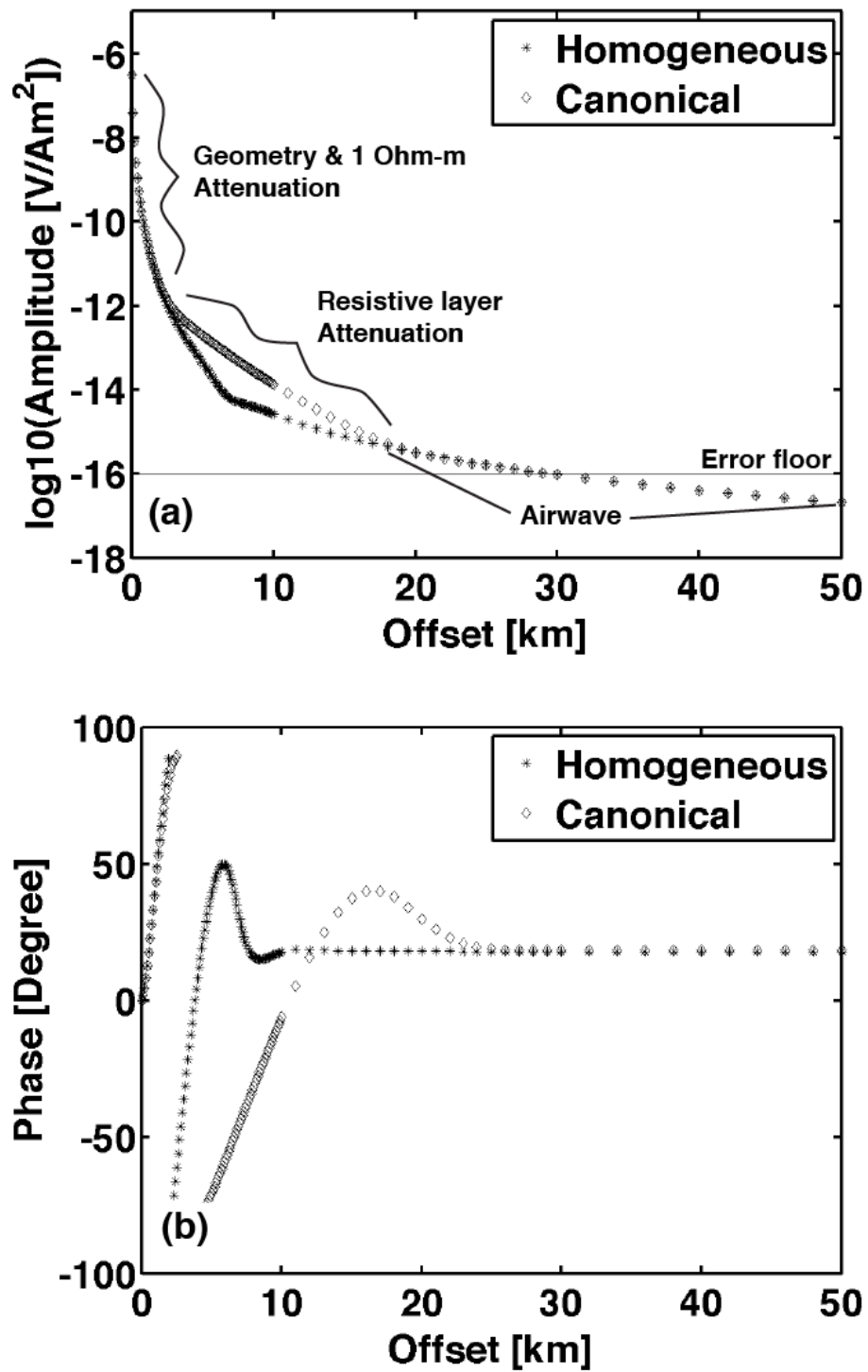


Figure 3.4: The sounding curve of inline ( $x$ ) electric field for the canonical model (indicated by asterisk) and homogeneous model (indicated by diamond). Figure (a) is amplitude and figure (b) is phase. The black solid line in figure (a) indicates the error floor of the receiver.

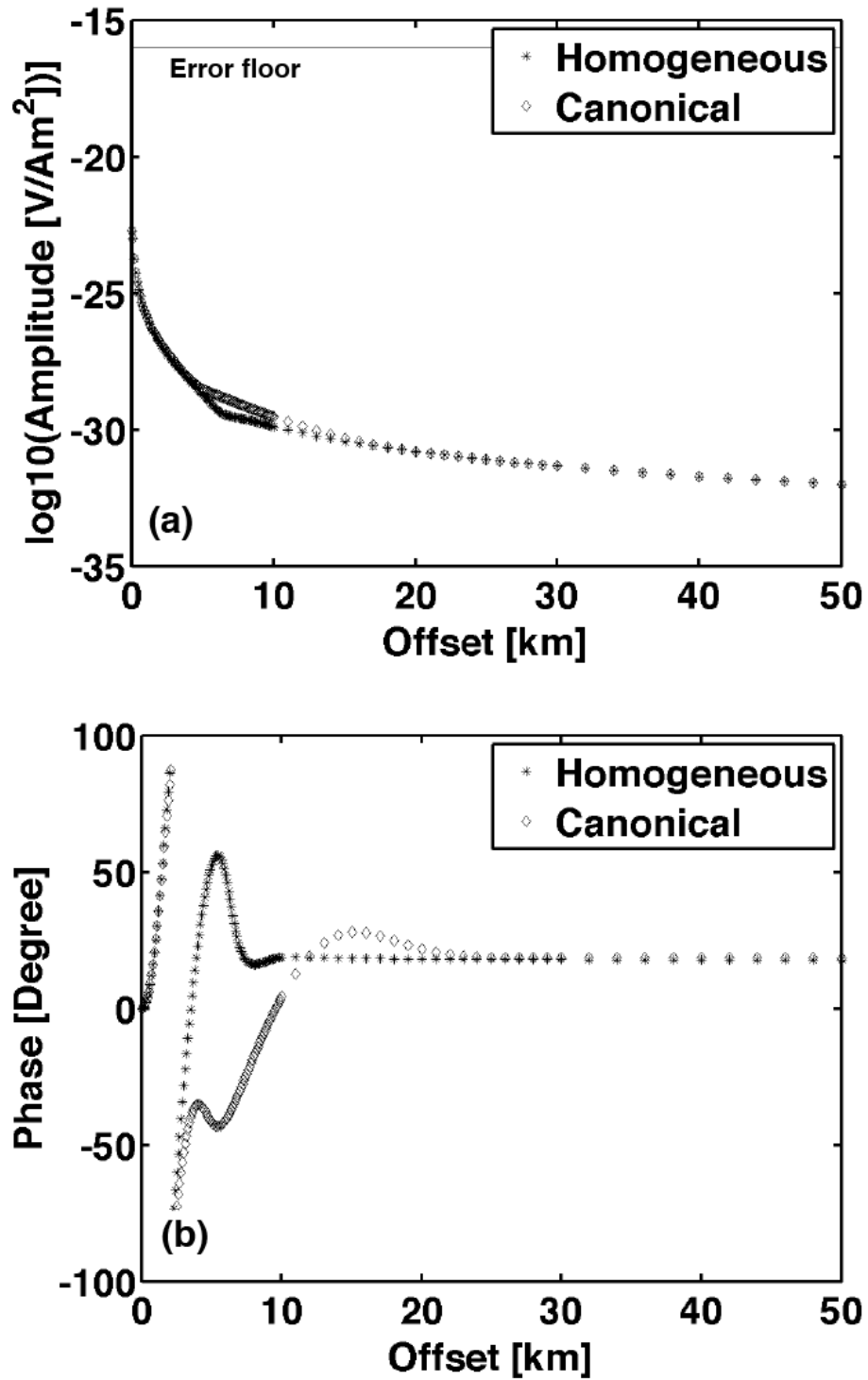


Figure 3.5: The sounding curve of broadside ( $y$ ) electric field for the canonical model (indicated by asterisk) and homogeneous model (indicated by diamond). Figure (a) is amplitude and figure (b) is phase. The black solid line in figure (a) indicates the error floor of the receiver.

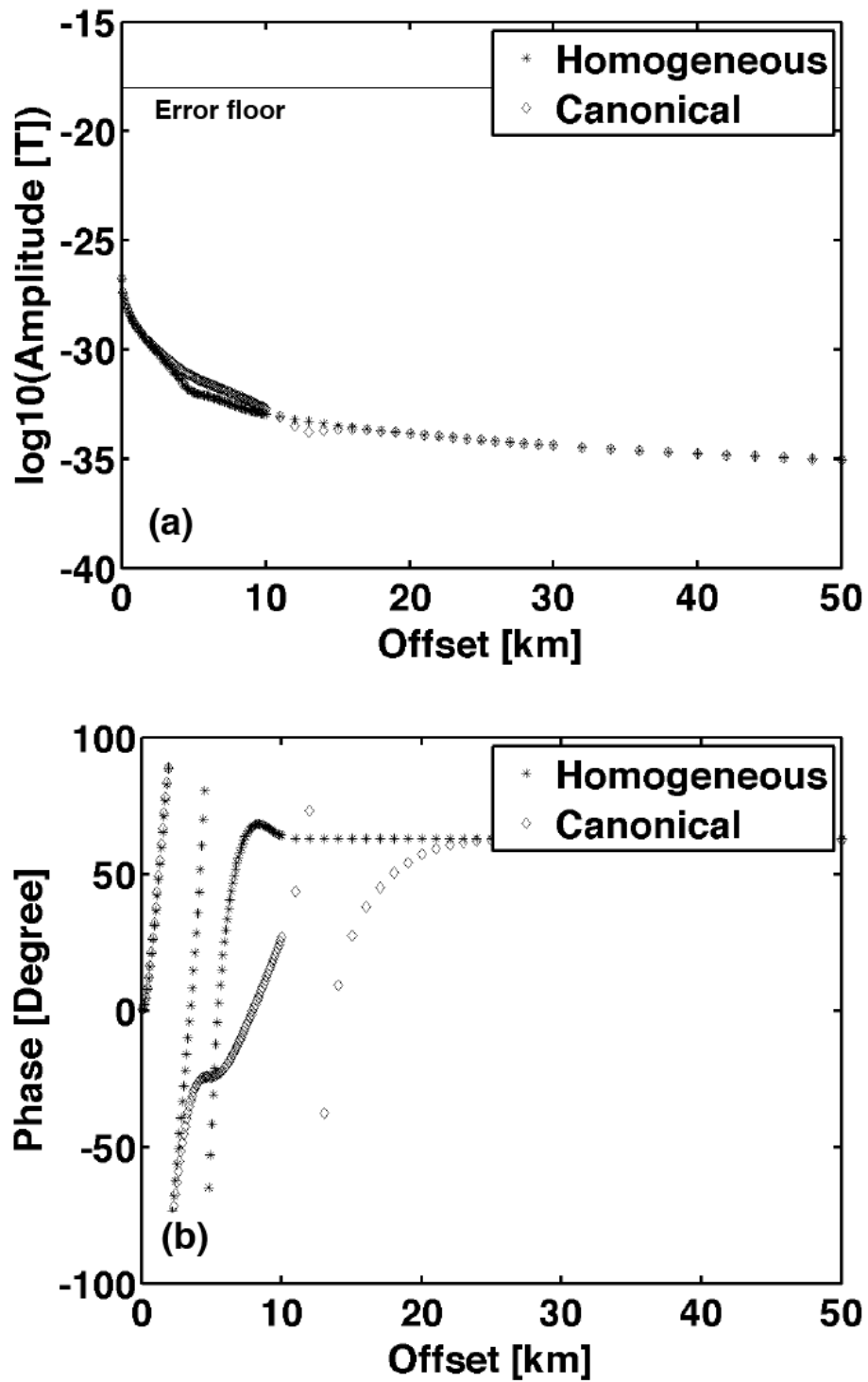


Figure 3.6: The sounding curve of inline ( $x$ ) magnetic field for the canonical model (indicated by asterisk) and homogeneous model (indicated by diamond). Figure (a) is amplitude and figure (b) is phase. The black solid line in figure (a) indicates the error floor of the receiver.

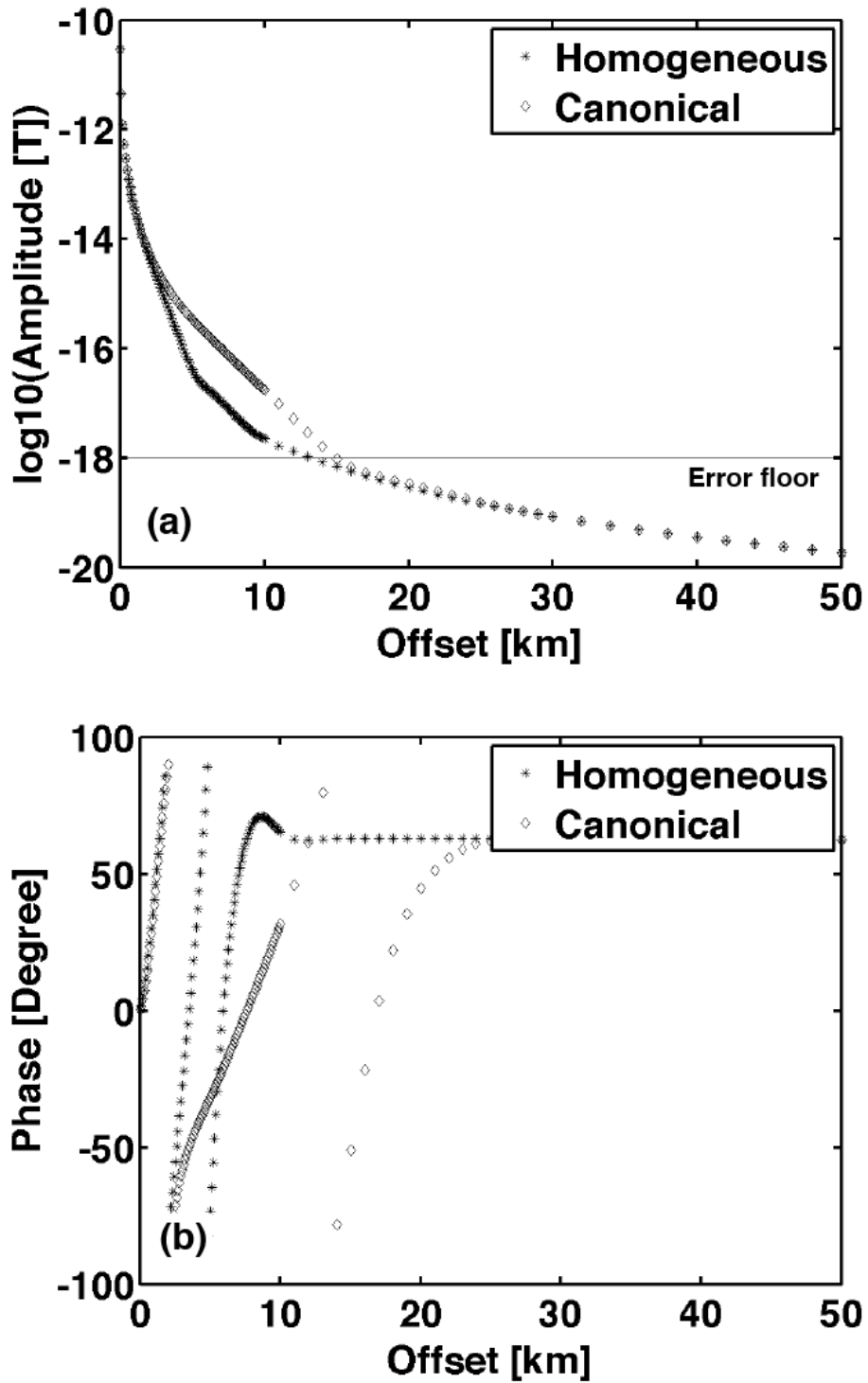


Figure 3.7: The sounding curve of broadside ( $y$ ) magnetic field for the canonical model (indicated by asterisk) and homogeneous model (indicated by diamond). Figure (a) is amplitude and figure (b) is phase. The black solid line in figure (a) indicates the error floor of the receiver.

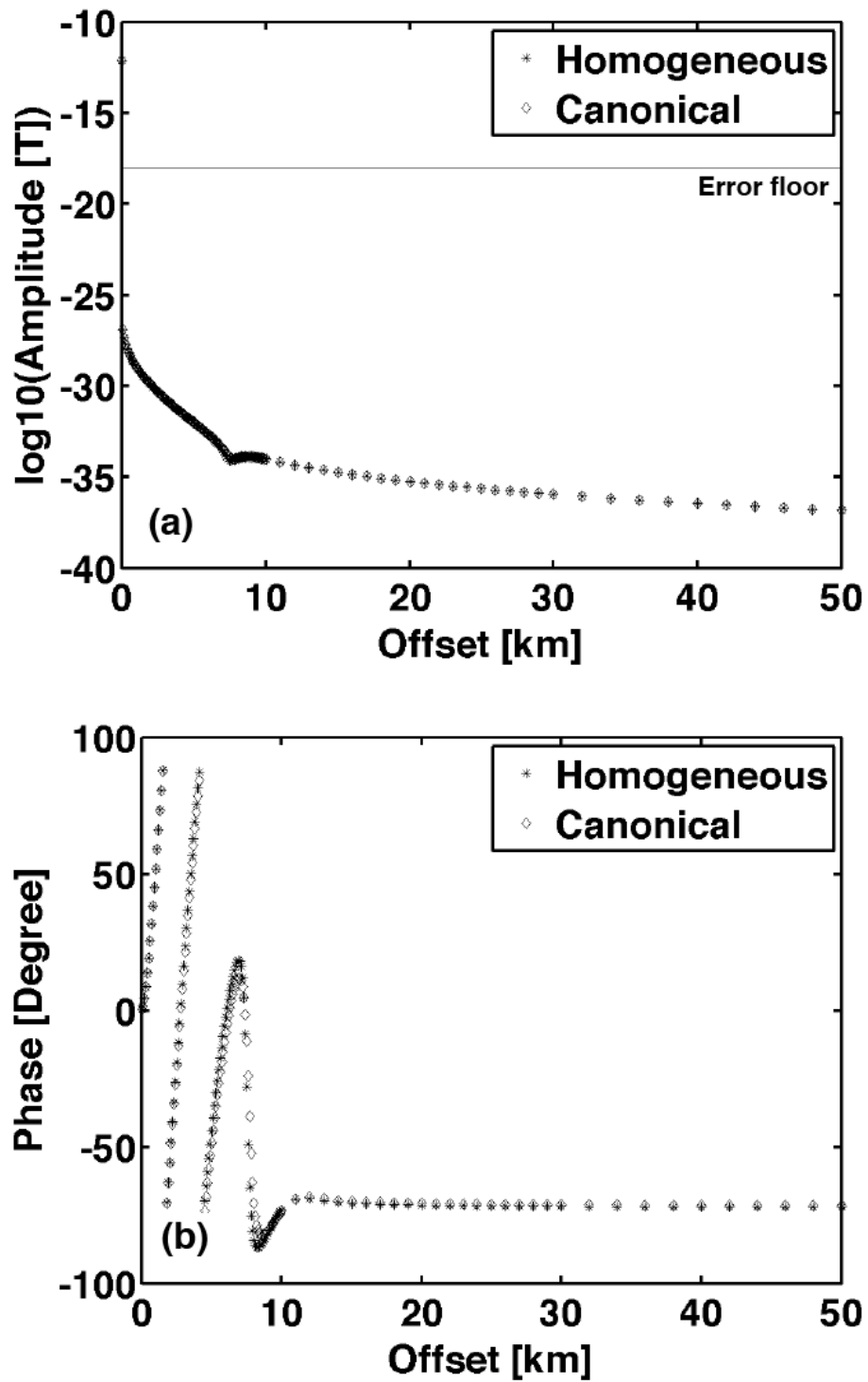


Figure 3.8: The sounding curve of vertical ( $z$ ) magnetic field for the canonical model (indicated by asterisk) and homogeneous model (indicated by diamond). Figure (a) is amplitude and figure (b) is phase. The black solid line in figure (a) indicates the error floor of the receiver.

magnetic field and 15 km for broadside ( $y$ ) magnetic field.

### 3.1.2 2-D and 3-D CSEM imagings

2-D and 3-D imagings are commonly used words for 2-D and 3-D resistivity images, respectively. For 2-D imaging, the receivers are placed in a straight line and the EM transmitter is towed over the receiver line. Their data are recorded in a similar way with CSEM sounding. In the hydrocarbon industry, 2-D CSEM imaging is only used for detecting the presence of hydrocarbons. To delineate hydrocarbon-filled reservoirs, 3-D CSEM imaging is required (Hesthammer *et al.*, 2010). For 3-D CSEM, the receiver array is placed at the seafloor as represented by circles in figure 3.9 and the EM transmitter is towed over the array as represented by the black arrow in figure 3.9. At each the

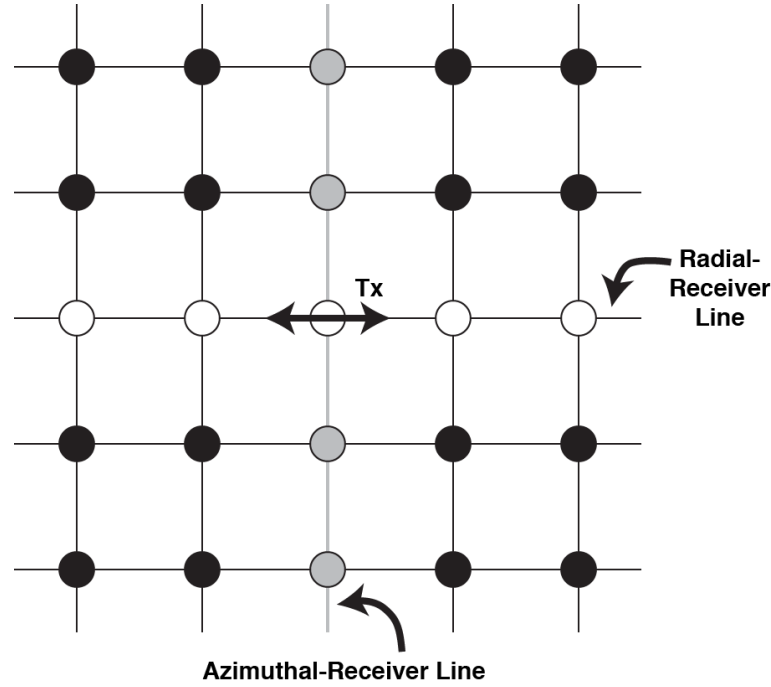


Figure 3.9: A schematic diagram of 3-D CSEM survey. The black arrow represents the transmitter and its orientation. Circles represent array of receivers where the white color indicates the radial receiver and the gray color indicates the azimuthal receiver.

transmitter positions, electric and magnetic field are recorded along the tow direction and along the perpendicular line of the tow direction. In 3-D CSEM, receivers along the tow direction are called radial receivers and its recorded electric and magnetic fields are called “radial” electric and magnetic fields. For the perpendicular line, receivers are called azimuthal receivers and their recorded data are called azimuthal fields. In general, the radial receiver records only the inline electric field, broadside magnetic field and vertical magnetic field while the azimuthal receiver records only the broadside electric field, inline magnetic field and vertical magnetic field (Constable, 2010). To



interpret 3-D CSEM data, 3-D CSEM modeling and inversion are required.

### 3.2 3D CSEM modeling and Inversion

To develop 3-D CSEM modeling for general resistivity structures, the frequency domain Maxwell's equations are solved by a finite difference method (e.g. Alumbaugh *et al.*, 1996; Champagne II *et al.*, 2001; Haber *et al.*, 2000; Haber & Ascher, 2001; Mackie *et al.*, 1993; Newman & Alumbaugh, 1995; Weiss & Newman, 2002; Weiss & Constable, 2006) or finite element method (e.g. Badea *et al.*, 2001). As in other numerical problem, the finite element method is more flexible for solving complicate geometry (Avdeev, 2005) but the finite difference method consumes fewer resource than the finite element method. Due to memory limitation and CSEM resolution, the finite difference method is more practical for developing 3-D CSEM modeling than the finite element method as shown by the number of publications.

For developing inversion, there are various inversion algorithms such as Gauss-Newton, quasi-Newton, Occam's inversion, and non-linear conjugate gradient. All of them have been used to develop inversion for various geophysical applications but non-linear conjugate gradient and quasi-Newton have only been used to develop inversion for 3-D CSEM. Although quasi-Newton inversion has been used to develop 3-D CSEM inversion, it has only one record which is published by Plessix & Mulder (2008). The remainders are developed using non-linear conjugate gradient (NLCG) inversion such as Gribenko & Zhdanov (2007), Newman & Boggs (2005), Commer & Newman (2008) and Newman *et al.* (2010). After the end of 2010, there have been no new publications about 3-D CSEM inversion.

Most of available 3-D CSEM modeling and inversions are developed using a scattered-field or secondary field technique to avoid the singularity problem at the source position. The scattered-field technique splits the total electric field or magnetic field into 2 parts. The first part is the primary field which is the electric or magnetic field of the simple model such as a homogeneous or 1-D layer model. The second part is the scattered-field where the response is scattered from the anomalous structure.

Here, we develop 3-D CSEM modeling to fit with the ModEM system in the hope that it can be readily used. In the following section, we describe Maxwell's equations and how to solve Maxwell's equations with the finite difference method. Then we describe the basics of the ModEM system and summarize how to develop 3-D CSEM modeling on the ModEM system.

### 3.3 Maxwell's Equations and the Governing Equations

In order to determine the electric or magnetic field, Maxwell's equations are necessary. Maxwell's equations in the time domain are

**Faraday's law of induction**

$$\nabla \times \mathbf{e} = -\frac{\partial \mathbf{b}}{\partial t}, \quad (3.1)$$

**Ampere's circuital law**

$$\nabla \times \mathbf{h} = \sigma \mathbf{e} + \mathbf{j}^e, \quad (3.2)$$

**Gauss's law for magnetism**

$$\nabla \cdot \mathbf{b} = 0, \quad (3.3)$$

and **Gauss's law**

$$\nabla \cdot \mathbf{d} = \rho, \quad (3.4)$$

where  $\mathbf{e}$  is the electric field,  $\mathbf{h}$  is the magnetic field,  $\mathbf{b} = \mu \mathbf{h}$  is the magnetic flux density,  $\mathbf{d}$  is the electric displacement,  $\mu$  is the magnetic permeability,  $\rho$  is the volume charge density,  $\sigma$  is the conductivity, and  $\mathbf{j}^e$  is the external source current density.

To transform the EM field from the time domain to the frequency domain, the Fourier transform is applied. To be compatible with ModEM (Egbert & Kelbert, 2012), the time dependent term is set as  $e^{-i\omega t}$  and the corresponding Fourier transforms are

$$F(\omega) = \int_{-\infty}^{+\infty} f(t) e^{i\omega t} dt. \quad (3.5)$$

and

$$f(t) = \frac{1}{2\pi} \int_{-\infty}^{+\infty} F(\omega) e^{-i\omega t} d\omega, \quad (3.6)$$

where the upper case letter is a function in the frequency domain and lower case is a function in the time domain.

Applying equation (3.5) to (3.1), (3.2), (3.3) and (3.4), we obtain Maxwell's equations in the frequency domain as

$$\nabla \times \mathbf{E} - i\omega\mu\mathbf{H} = -\mathbf{K}, \quad (3.7)$$

and

$$\nabla \times \mathbf{H} - (\sigma - i\omega\epsilon) \mathbf{E} = \mathbf{J}, \quad (3.8)$$

where  $\mathbf{E}$  and  $\mathbf{H}$  is electric field and magnetic fields,  $\mathbf{J}$  and  $\mathbf{K}$  are electric and magnetic source,  $\epsilon$  is dielectric permittivity and  $\omega$  is angular frequency. For most geophysical surveys, the frequency is very low such as 0.25-10 Hz in CSEM surveys or 100-0.001 Hz for magnetotelluric surveys. Therefore,  $i\omega\epsilon$  can be neglected and equation (3.8) can be reduced into

$$\nabla \times \mathbf{H} - \sigma \mathbf{E} = \mathbf{J}. \quad (3.9)$$

Equation (3.7) or (3.8) are the first order Maxwell's equations in the frequency domain. To obtain EM responses at the surface, one must solve for the  $\mathbf{E}$  and  $\mathbf{H}$  fields simultaneously via the first order Maxwell's equations. Solving the coupled system (3.8) and (3.15) requires substantial computer memory (Mackie *et al.*, 1994). Memory requirements can be significantly reduced by solving the second order Maxwell's equations, in  $\mathbf{E}$  form,

$$\nabla \times (\nabla \times \mathbf{E}) - i\omega\mu\sigma\mathbf{E} = -\nabla \times \mathbf{K} + \mathbf{J}, \quad (3.10)$$

or in  $\mathbf{H}$  form

$$\nabla \times (\sigma^{-1}\nabla \times \mathbf{H}) - i\omega\mu\mathbf{H} = -\mathbf{K} + \nabla \times (\sigma^{-1}\mathbf{J}). \quad (3.11)$$

For passive source surveys such as magnetotelluric, magnetic, or airborne surveys, the right hand sides of (3.10) and (3.11) are zero. For passive sources, both equations have been used to develop EM modeling such as Smith (1996); Alumbaugh *et al.* (1996); Newman & Alumbaugh (1997); Siripunvaraporn *et al.* (2005) for equation (3.10) and Mackie *et al.* (1994); Uyeshima & Schultz (2000) for (3.11).

For active source surveys, only equation (3.10) has been used to develop EM forward modeling because it is easier to exclude source-point singularities from the numerical computations (e.g. Newman & Alumbaugh, 1995). The technique for excluding source-point singularities is called scattered field or secondary field technique. It assumes that  $\mathbf{E}$  in equation (3.10) can be split into two parts

$$\mathbf{E} = \mathbf{E}_p + \mathbf{E}_s, \quad (3.12)$$

where  $\mathbf{E}_p$  is the primary electric field which can be evaluated analytically and  $\mathbf{E}_s$  is the secondary electric field which can be computed by solving

$$\nabla \times \nabla \times \mathbf{E}_s - i\omega\mu\sigma\mathbf{E}_s = i\omega\mu(\sigma - \sigma_p)\mathbf{E}_p, \quad (3.13)$$

where  $\sigma_p$  is for the primary model. Equation (3.11) is quite close to equation (3.10) except the term on the right hand side. The electric field from both equations have to satisfy two boundary conditions that are

1. the normal component of  $\sigma E$  must be continuous across each boundary of the physical property distribution ( $\sigma_1 E_1^\perp = \sigma_2 E_2^\perp$ ) and
2. the parallel component of  $E$  must be continuous across each boundary ( $E_1^\parallel = E_2^\parallel$ ).

To solve equation (3.10) or (3.13), a normal finite difference or finite volume grid which defines the unknowns at the corners as in figure 3.10 cannot satisfy the electric-field boundary condition and it produces inaccurate result. A staggered grid is therefore necessary.

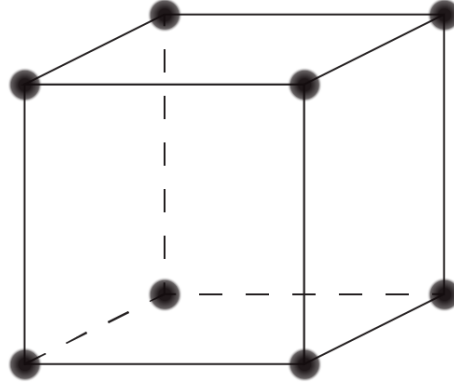


Figure 3.10: Normal 3D finite difference or finite volume grid. Unknowns are defined at the corners of the rectangular block.

### 3.4 Staggered Grid

Yee (1966) proposed a staggered grid for solving the boundary value problems of Maxwell's equation. Staggered grid has two types as shown in figures 3.11 and 3.12. For the first type, three electric fields are defined at the edges of the cube and three magnetic fields are defined at the faces of the cube (figure 3.11). The first type is suitable for solving equation (3.10). In this case, the total magnetic field is computed by

$$\mathbf{H} = \frac{1}{i\omega\mu} \nabla \times \mathbf{E}. \quad (3.14)$$

This grid type is used by Alumbaugh *et al.* (1996) and Newman & Alumbaugh (1997) for sideband electromagnetic 3D modeling and by Siripunvaraporn *et al.* (2005) and Egbert & Kelbert (2012) for 3D magnetotelluric modeling.

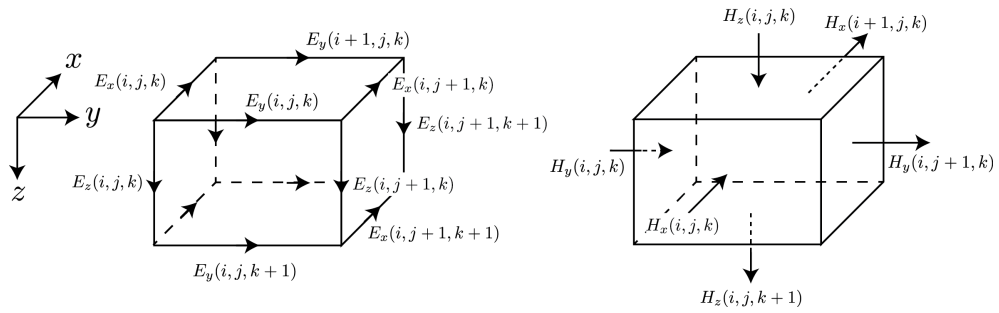


Figure 3.11: Staggered Grid Type I. Three components of electric field are defined at the edges on the cube and three components of magnetic field are defined at the face of the cube. The grid type is suitable for solving equation (3.10).

The second grid type defines all three components of the magnetic field on the edges of the cube and all three components of electric field at the face of the cube (figure 3.12) and it is suitable for solving equation (3.13). In this case, the total electric

field is then computed by

$$\mathbf{E} = \frac{1}{\sigma} \nabla \times \mathbf{H}. \quad (3.15)$$

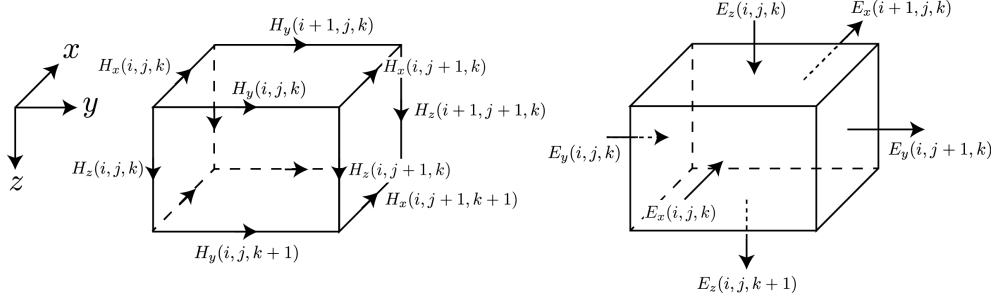


Figure 3.12: Staggered Grid Type II. Three components of electric field are defined at the faces on the cube and three components of magnetic field are defined at the edges of the cube. The grid type is suitable for solving equation (3.13).

This grid type is used by Mackie *et al.* (1994) for 3D MT modeling, by Smith (1996) for 3D EM modeling, by Uyeshima & Schultz (2000) for geomagnetic induction in a heterogeneous sphere and by Streich (2009) for CSEM modeling. The comparison of both grid types for MT data is done by Siripunvaraporn *et al.* (2002) and their conclusion is that for fine grid discretization both algorithms generate nearly identical solutions, but there are significant differences for a coarse grid discretization. On a coarse grid, the first type generally produces a solution that is closer than the second type to the exact solution. For ModEM, only the staggered grid type I is available for solving 3D EM forward problem.

### 3.5 ModEM

ModEM or modular electromagnetic inversion system has been developed by Prof. Gary Egbert and Anna Kelbert of Oregon State University. ModEM is developed and designed under a general mathematical framework for solving frequency-domain EM inverse problems as described in Egbert & Kelbert (2012).

For clearness we summarize the key points here. The unconstrained functional or penalty functional for EM inverse problems is

$$\mathcal{P}(\mathbf{m}, \mathbf{d}) = (\mathbf{d} - \mathbf{f}(\mathbf{m}))^T \mathbf{C}_d^{-1} (\mathbf{d} - \mathbf{f}(\mathbf{m})) + \nu (\mathbf{m} - \mathbf{m}_0)^T \mathbf{C}_m^{-1} (\mathbf{m} - \mathbf{m}_0), \quad (3.16)$$

where  $\mathbf{m}$  is the conductivity-model vector,  $\mathbf{m}_0$  is the prior conductivity-model vector or initial guess model,  $\mathbf{d}$  is the data vector,  $\mathbf{f}(\mathbf{m})$  is the forward mapping,  $\mathbf{C}_d$  is the data covariance,  $\mathbf{C}_m$  is the model covariance or regularisation term, and  $\nu$  is a trade-off parameter.

The forward mapping requires solution of the frequency domain EM partial differential equation (PDE) which is written as

$$\mathbf{S}_{\mathbf{m}}\mathbf{e} = \mathbf{b}, \quad (3.17)$$

where  $\mathbf{S}$  is the PDE operator on the left hand side of equation (3.13), the subscript  $\mathbf{m}$  denotes the dependence of the PDE operator on the unknown model parameter,  $\mathbf{e}$  is the discrete EM field solution, and  $\mathbf{b}$  is the forcing term that is the boundary condition and/or source term. For ModEM,  $\mathbf{e}$  represents only the electric field on the edges on the staggered grid. Then the magnetic field  $\mathbf{h}$  is computed by the simple transformation operator  $\mathbf{T}$

$$\mathbf{h} = \mathbf{T}\mathbf{e}. \quad (3.18)$$

Simulated observations are computed from the solution  $\mathbf{e}$  and/or  $\mathbf{m}$  by

$$d_i = f_i(\mathbf{m}) = \psi_i(\mathbf{e}(\mathbf{m}), \mathbf{m}). \quad (3.19)$$

Using the chain rule, a general expression for Jacobian matrix,  $\mathbf{J} = \partial \mathbf{f}(\mathbf{m}) / \partial \mathbf{m}$ , is given by

$$\mathbf{J} = \mathbf{L}\mathbf{S}_{\mathbf{m}_0}^{-1}\mathbf{P} + \mathbf{Q}. \quad (3.20)$$

In equation (3.20), the matrix

$$\mathbf{P} = -\frac{\partial}{\partial \mathbf{m}} (\mathbf{S}_{\mathbf{m}}\mathbf{e}_0) |_{\mathbf{m}=\mathbf{m}_0} \quad (3.21)$$

gives the sensitivity of  $\mathbf{S}_{\mathbf{m}}\mathbf{e}_0$  to perturbations in the model parameters.  $\mathbf{P}$  depends on the numerical implementation and the model parametrization. We assume the forward operator can be written as

$$\mathbf{S}_{\mathbf{m}}\mathbf{e} \equiv \mathbf{S}_0\mathbf{e} + \mathbf{U}(\pi(\mathbf{m}) \circ \mathbf{V}\mathbf{e}). \quad (3.22)$$

For equation (3.13),  $\mathbf{S}_0$  is the discrete curl-curl operator,  $\mathbf{U} \equiv i\omega\mu\mathbf{I}$ ,  $\mathbf{V} \equiv \mathbf{I}$ ,  $\mathbf{I}$  is the identity matrix,  $\pi(\mathbf{m}) \equiv \sigma(\mathbf{m})$  is a model mapping from the model parameter space to the cell edges and  $\circ$  denotes the component-wise multiplication of vectors. Therefore, the explicit expression for the operator  $\mathbf{P}$  is given by

$$\mathbf{P} = -\mathbf{U} \text{diag}(\mathbf{V}\mathbf{e}_0) \Pi_{\mathbf{m}_0}. \quad (3.23)$$

where  $\Pi_{\mathbf{m}_0}$  is the Jacobian of the model mapping  $\pi(\mathbf{m})$  evaluated at the background model parameter  $\mathbf{m}_0$ .

The matrix  $\mathbf{L}$  in equation (3.20) represents the linearised data functionals. It can be decomposed into two matrixes as

$$\mathbf{L} = \mathbf{A}^T \mathbf{\Lambda}^T, \quad (3.24)$$

where columns of  $\mathbf{A}$  are sparse vectors which represent evaluation functionals for point observations of the electric and magnetic fields. The matrix  $\mathbf{A}$  depends on the details of the observation functionals (e.g., impedance, apparent resistivity, amplitude, phase) which may combine magnetic and electric measurements from one or more locations. When the evaluation functionals have an explicit dependence on the model parameter, there is an additional term which is denoted  $\mathbf{Q}$  in equation (3.20). The Jacobian represents a linear mapping, giving the perturbation to data resulting from the model perturbation ( $\delta \mathbf{d} = \mathbf{J} \delta \mathbf{m}$ ). A gradient-based inversion uses this operator, along with the transpose or adjoint ( $\delta \mathbf{m} = \mathbf{J}^T \delta \mathbf{d}$ ). ModEM does not form  $\mathbf{J}$  or the components in equation (3.20) but rather implements the solver for the discrete system  $\mathbf{S}_{\mathbf{m}}^{-1}$ , the operators  $\mathbf{P}$ ,  $\mathbf{L}$ ,  $\mathbf{Q}$  and the compound Jacobian operator  $\mathbf{J}$ .

ModEM is organized into 5 layers and 3 levels as shown in figure 3.13. Each layer has no intrinsic dependence on other layers of the system. The first layer is the “Data Space” layer that is designed for handling and managing data vector  $\mathbf{d}$ . Its structure is fixed but suitable for supporting multivariate EM data. The data vector  $\mathbf{d}$  can handle multicomponent data via three attributes which are *transmitter*, *data type* and *receiver*.

The *transmitter* attribute is uniquely used for defining the forward problem that must be solved, including both the specific partial differential equation as well as sources and boundary conditions. The *data type* and *receiver* are used to define the measurement process that must be applied to the forward solution to get the response. These attributes are treated abstractly at the “data space” layers. To perform modeling or inversion, the actual information associated with these attributes are stored into the *dictionaries*. The *transmitter* (TX) dictionary has an entry for each forward problem, providing any data such as frequency, geometry or orientation of the source required to setup and solve each forward problem. In the *data type* (DT) dictionary, each entry defines general data functional types included in the inversion such as the impedance and vertical field transfer function for MT. The information about site location, site configuration or number of sites are provided through the entry of the *receiver* dictionary. The lists of possible dictionary entries will depend on the application. For 3D MT, the *transmitter* defines only the frequency and the *data type* defines the complex impedance and apparent resistivity/phase. For 3D CSEM, the *transmitter* defines the source orientation, position, moment, type and frequency while the *data type* defines either the real/imaginary part or amplitude/phase of the EM field. For the *receiver*, only the site orientation and position are defined for both 3D MT and 3D CSEM.

The second layer is level I of ModEM, which implements the inversion search algorithm, handles parallelization of the inversion and manages computations with Jacobian matrix  $\mathbf{J}$  such as matrix-vector multiplications  $\mathbf{J}^T \mathbf{d}$  and  $\mathbf{J} \mathbf{m}$ . This level consists

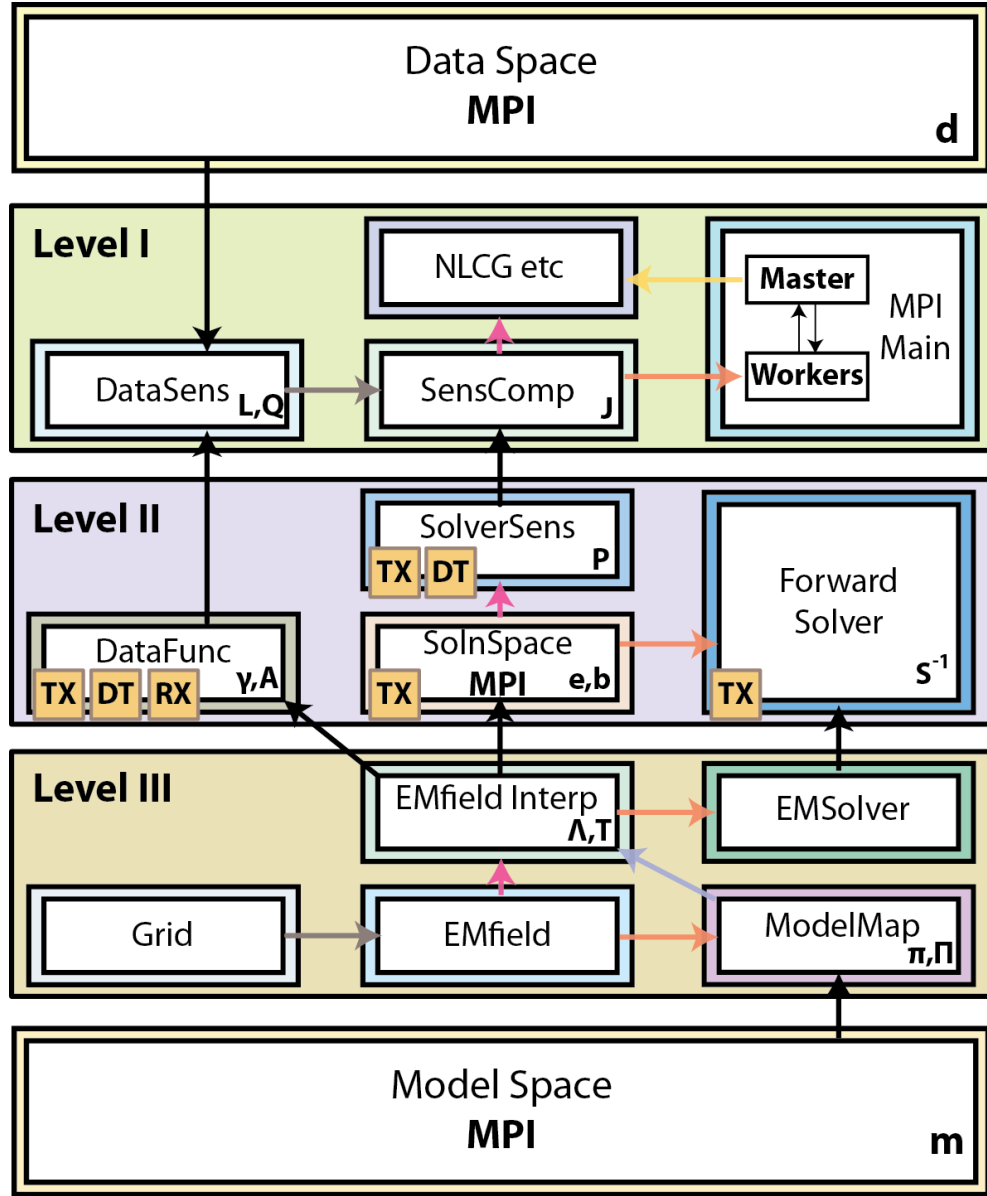


Figure 3.13: The schematic overview of ModEM. Individual modules are denoted by boxes, with dependencies indicated by arrows. Some boxes are marked with symbols to indicate the vectors and operators from Egbert & Kelbert (2012). The shaded small boxes indicate which dictionaries are used in each module.

of 4 modules **DataSens**, **SensComp**, **NLCG** and **MPI**. **DataSens** module implements multiplication by  $\mathbf{L}$ ,  $\mathbf{Q}$  and its transpose through four routines. The first,  $Lmult$ , is the linearized counterpart of the non-linear response  $\psi(\mathbf{e}, \mathbf{m})$  and returns the perturbation in the data for small perturbation in  $\mathbf{e}$  and  $\mathbf{m}$ , i.e.,  $\mathbf{L}\delta\mathbf{e} = \delta\mathbf{d}$ . The second,  $LmultT$ , implements the transpose of operator  $\mathbf{L}$  and returns  $\mathbf{L}^T\delta\mathbf{d} = \delta\mathbf{e}$ . The third,  $Qmult$ , computes the component of the data perturbation due to direct dependence of  $\psi$  on model parameter  $\mathbf{m}$ , which is  $\mathbf{Q}\delta\mathbf{m} = \delta\mathbf{d}$ . The last one,  $QmultT$ , implements transpose of  $\mathbf{Q}$  and returns  $\mathbf{Q}^T\delta\mathbf{d} = \delta\mathbf{m}$ . **SensComp** module puts all of  $\mathbf{L}$ ,  $\mathbf{S}_m^{-1}$ ,  $\mathbf{P}$



and  $\mathbf{Q}$  together to implement the full Jacobian calculation. In contrast the **DataSens** module deals with multiple objects. There are four public routines. The first, *Jmult*, implements  $\mathbf{J}\delta\mathbf{m}$  multiplication and returns  $\delta\mathbf{d}$ . The second, *JmultT*, implements  $\mathbf{J}^T\delta\mathbf{d}$  multiplication and returns  $\delta\mathbf{m}$ . The third, *fwdPred*, implements the full forward problem and returns the full predicted data for a given model parameter ( $\mathbf{d} = \mathbf{f}(\mathbf{m})$ ). The final routine, *calcJ*, is a routine for computing the full Jacobian matrix for all *transmitters*, *data type* and *receiver*. The **NLCG** module provides non-linear conjugate gradient inverse algorithm which is adopted from the standard Polak-Ribière algorithm (see figure 3.14 for pseudo-code). See section 3.6 more details. The **MPI main** module is designed for parallelization forward, inverse and Jacobian calculation over transmitter, data type and receiver. To minimize interaction, one processor is assigned as the master and the rest as workers. The workers enter a queue inside **MPI main** and wait for messages from the master. Only the master executes the actual inversion. To execute any statement in parallel, the master enters **MPI main** and distributes messages to all workers indicating tasks to perform. Thus, all MPI communication are hosted inside **MPI main**.

The third layer is a interface layer which is the second level of ModEM. This level provides modules for communicating between level I and level III. Each module in this level is specific to an application. They extensively use *transmitter*, *data type* and *receiver* dictionaries. Most of modifications from 3D MT to 3D CSEM are done at this level. This layer consists of 4 main modules. The first one is **SolnSpace** where the derived data type and its operator are defined. The derived data type is used to represent  $\mathbf{e}$  and  $\mathbf{b}$  in the forward equation  $\mathbf{S}_m\mathbf{e} = \mathbf{b}$ . The operators defined in this module are creation, destruction, I/O, copying, basic linear algebra and dot-product operators. These fundamental operators are used by the module in Level I. The second one is **ForwardSolver** which provides modules for the interface between the specific application forward modeling routines and generic routines in Level I. They consist of 3 public routines which are *initSolver* for initializing main objects for solving forward problem, *exitSolver* for deallocation and clean up and *fwdSolver* for computing the EM field on the edge of the staggered grid. In CSEM, the background model, anomalous model and primary field solution are set up at *initSolver* routine. Then the forcing term  $\mathbf{b}$  for the secondary field solution is set up at *fwdSolver* routine. Level III routine (**EMSolver**) is called to compute the secondary field, which is added to the primary field solution. Finally, the total field solution is returned by *fwdSolver*. The third one is **DataFunc** which provides modules for computing the response from the forward solution. There are three public routines which are *dataRef* for evaluating the non-linear data functional  $\psi_j(\mathbf{e}, \mathbf{m})$ , *Lrows* and *Qrows* for computing linearizing data and its counterpart. For CSEM, **DataFunc** are very simple, it only uses the routine in Level

III (**EMfieldInterp**) to interpolate electric or magnetic field at the receiver positions. The last one is **SolverSens** which implements multiplication by matrices  $\mathbf{P}$  and  $\mathbf{P}^T$ .

The fourth layer is Level III of ModEM which provides fundamental tools for EM modeling. This layer consists of 4 modules which are specific to a particular numerical approach to discretize and solve the EM forward problem. For example, finite difference vs. finite element, 2D MT vs. 3D MT, spherical vs. Cartesian geometry, all require different instances of this group of modules. On other hand, the same set of modules can be used for any source/receiver configurations with a particular approach. For modify 3D MT to 3D CSEM, all of these modules are not changed. The first one is **Grid** which defines the basic data type for representing the staggered grid. Attributes of the object can be accessed by all routines in Level III modules. For higher level (I and II) modules, they do not directly access internal attributes but they have to access past instances of the object. The second one is **EMField** which defines the basic data type for representing the EM field and also provides its basic operators such as creation, deallocation, linear algebra, and dot product. The third one is **EMSolver** which is used to evaluate the EM field from the discrete system of equations (3.10) or (3.13). The iterative solver, quasi-minimum residual with a level-1 incomplete *LU* decomposition for pre-conditioning, is applied for solving the discrete system. The fourth one is **EMFieldInterp** which implements the interpolation function used to compute the electric and magnetic fields at an arbitrary point within the model domain. These function are represented by sparse vectors corresponding to volumes of the matrix  $\Lambda$ .

The last layer is the ModelSpace layer which is designed to decouple the model parameterization and regularization from the remaining of the inversion. This layer has one basic data type of which attributes are private and inaccessible from other parts of inversion. This guarantees that the rest of the inversion is independent of any specific details in model parameter implementation. There are three essential groups of routines. The first group is the standard routine for creation, deallocation, I/O, copying, and also for linear algebra and dot products. The second group is the group for implementation model covariance  $\mathbf{C}_m$ . The third group (denoted as ModelMap in figure 3.13) consists of mapping between the model parameter and the EM field such as the implementation of  $\pi(\mathbf{m})$ ,  $\Pi = \partial\pi/\partial\mathbf{m}$  and  $\Pi^T$ .

### 3.6 NLCG inversion

Non-linear conjugate gradient (NLCG) inversion is used in many geophysical inversions such as Newman & Alumbaugh (2000), Rodi & Mackie (2001), Commer & Newman (2008) for magnetotelluric data and Kelbert *et al.* (2008) for global EM induction. NLCG is directly applied to minimize the penalty functional (equation (3.16)).

The advantage of NLCG is that there is no need to construct any large matrices (e.g.,  $\mathbf{J}$ ,  $\mathbf{J}^T$ ,  $\mathbf{C}_m$ ); only a product of  $\mathbf{J}$  or  $\mathbf{J}^T$  with any vector is required (Siripunvaraporn, 2012). Because NLCG inversion needs less memory than other inversions, the NLCG algorithm has been gaining popularity among developers as shown in many publications in the past decade (Newman & Alumbaugh, 2000; Rodi & Mackie, 2001; Newman & Boggs, 2004; Commer & Newman, 2008; Kelbert *et al.*, 2008). There are two NLCG

---

```

mprior = prior model
ν = initial damping parameter
a = initial line search step α scaled by model norm
n = 0
m̃0 = 0
m0 = Cm1/2m̃0 + mprior = starting model
Evaluate P0 = (d - f(m0))TCd-1(d - f(m0)) + νm̃0Tm̃0
Evaluate P'(m̃)|m̃0 = -2Cm1/2JTCd-1(d - f(m0)) + 2νm̃0
g0 = -P'(m̃)|m̃0
h0 = g0
Set α0 = a/g0Tg0
While (d - f(mn))TCd-1(d - f(mn)) > T do
  n = n + 1
  Line search: choose â to minimize P(Cm1/2(m̃n-1 + αhn-1) + mprior)
  m̃n = m̃n-1 + âhn-1
  Pn = (d - f(mn))TCd-1(d - f(mn)) + νm̃nTm̃n
  gn = -P'(m̃)|m̃n
  α = 2(Pn - Pn-1)/gn-1Thn-1
  Adjust α for super-linear convergence: α = min(1.00, 1.01 * α)
  If α too small
    ν = 0.1 * ν
    α = a/gnTgn
    Restart: hn = gn
    Cycle do loop
  End if
  β = gnT(gn - gn-1)/gn-1Tgn-1
  If (gnTgn + βgnThn-1 > 0)
    hn = gn + βhn-1
  Else
    Restart to restore orthogonality: hn = gn
  End if
End do

```

---

Figure 3.14: Pseudo-code for non-linear conjugate gradient (NLCG) algorithm. Notation:  $\mathbf{f}(\mathbf{m})$  represents the responses obtained from forward modeling;  $\mathcal{P}_n$  and  $\mathcal{P}'_n$  are values of the penalty functional and its derivative at the  $n$ th iteration;  $\mathbf{m}_n$ ,  $\mathbf{h}_n$ ,  $\mathbf{g}_n$  are vectors in the model space;  $\alpha$  and  $\beta$  represent real scalars; other symbols are as in the text (*after Egbert, unpublished*).

algorithms which are the Fletcher-Reeves (Fletcher & Reeves, 1964) algorithm and the Polak-Ribière (Polak & Ribière, 1969) algorithm. The difference between both algorithms is the method for evaluating the conjugate direction  $\mathbf{h}_n$ . For ModEM, NLCG is developed by adapting the standard Polak-Ribière algorithm (see figure 3.14 for pseudo-code). The major modification is the  $\nu$  adaptation algorithm. For the original NLCG inversion,  $\nu$  is manually assigned by the user and it is constant for the whole inversion.

When the convergence of the inversion stalls, the original NLCG inversion terminates and returns the result. For ModEM, they add an automatic scheme for decreasing the value of  $\nu$  when the convergence of inversion stalls. That makes the new NLCG algorithm better at data fitting than the original one. Although ModEM implements an algorithm for adjusting the  $\nu$  value, its result is still based on the initial value of  $\nu$ . Unlike Occam's inversion, its damping factor is fully and automatically adjusted by a search algorithm. The initial value of  $\nu$  has almost no effect on the inverted result.

### 3.7 Adapting ModEM to CSEM

Here, we summarize the key modifications for adapting ModEM to work with CSEM data. The first one is to add new data types in the *data type* dictionary and new data functionals in the **DataFunc** module. The second one is to include new attributes in the *transmitter* dictionary which are dipole type, electric dipole moment, source position, and source orientation. The third one is to modify the **ForwardSolver** to support the scattered-field formulation which consists of 7 steps. The first step is the primary-model calculation to create a 1D layer model. Here, we use the weighted average over a 2D section to evaluate the conductivity of the 1D model. The second step is the anomalous-model calculation to create the secondary conductivity model. Because ModEM solves equation (3.13) on the edge of staggered grid, we start by mapping the cell conductivity to the edges and then subtracting conductivity model from the primary model at the edges. The third step is the primary field calculation. At this step, we put the 1D layer model into the 1D forward modeling developed by Key (2009) and then map the results to the edges of the staggered grid. The fourth step is to create the force term **b**. At this step, we create the forcing term **b** of equation (3.17) by following the right hand side of equation (3.13). The fifth step is to calculate the scattered field **E<sub>s</sub>**. After we prepared the essential parameter, we call the *fwdSolver* routine to obtain the scattered field. The sixth step is to compute the total field **E**. At this step, we add the primary field to the scattered field to get the total field at the edges of the grid. The final step is to evaluate the response. Here, we use routines in **EMfield Interp** to interpret and evaluate the electric or magnetic field at the receiver position.

### 3.8 Synthetic Test

Here, we test the accuracy and reliability of 3D CSEM forward modeling and inversion on the synthetic model. All of these tests were run on IBM X3755 M3 workstation, using up to 21 processing cores with 104 GB total available memory.

### 3.8.1 Forward Modeling

In this section, the 3D CSEM modeling is tested by comparing its results with the results generated from a 1D forward modeling program (Key, 2009). The synthetic model used in this test is inspired by the canonical model (figure 3.2). The synthetic model consists of three homogeneous layers and one resistive anomaly. The three layers are (1)  $10^{10}$   $\Omega$ -m air layer, (2) 0.32  $\Omega$ -m ocean layer and (3) 1  $\Omega$ -m sediment layer. One resistive layer is a 100  $\Omega$ -m layer intruding in the sediment at 700 m from the seafloor. Its horizontal and vertical dimensions are 10 km  $\times$  10 km  $\times$  0.1 km as be shown in figure 3.15.

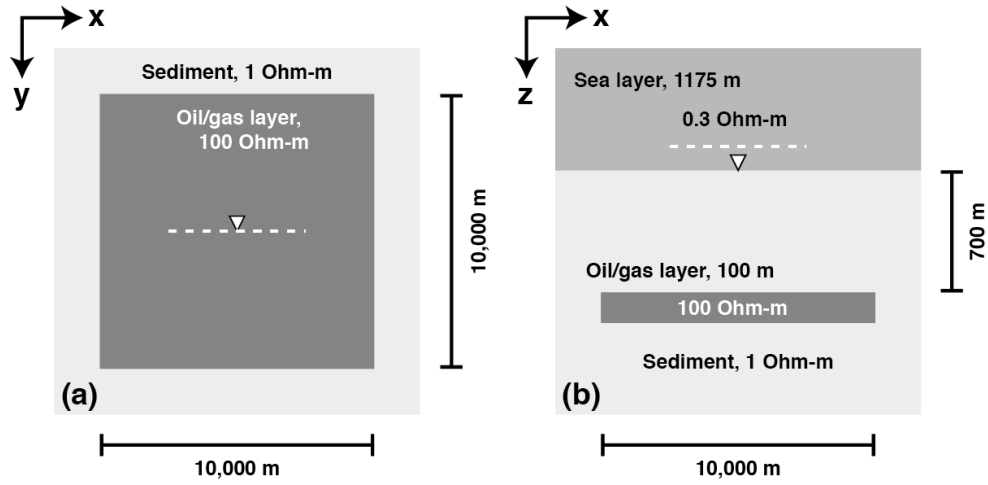


Figure 3.15: The synthetic model for testing the accuracy of CSEM modeling. Figure (a) is the top view at 1,000 m depth and figure (b) is the side view in the  $y$ -direction. The white triangle represents the receiver position and the white dashed line is the tow direction.

The resistivity model (figure 3.15) is discretized into 48 layers in the vertical direction. The first ten layers are automatically added by ModEM, which are represented by air layers. The next 13 layers are used for simulating the 1175-m thick ocean. The 700-meters top sediment are divided into 10 layers of which the smallest thickness is 10m at the first layer and the largest thickness is 200m at the sixth layer. The 100-m thick oil/gas layer is discretized into 4 uniform layers of thickness is 25 m. The thicknesses of the remaining layers continuously increases until reaching 20.8 km where the Dirichlet boundary condition can be applied. For horizontal ( $x$  and  $y$ ) directions, the grid is uniformly discretized in the area 10  $\times$  10 km. The grid size increases by the factor of 2 for the outside.

In this test, there is one seafloor receiver placed at the center of the model as indicated by the white triangle in figure 3.15. In this simulation, a 0.25 Hz  $x$ -horizontal electric dipole is towed at 50 meters above the receiver in the  $x$ -direction. The dipole

generates EM field every 100 meters starting from -3 km to 3 km as indicated by the white dashed line in figure 3.15. Under this setting, the calculated responses can be implied as the results from the 1-D model.

The reference 1-D data is generated from the 1-D model of which the grid discretization and resistivity are summarized in table 3.1. Its vertical grid discretization

Table 3.1: The 1-D resistivity model corresponding to the synthetic model (figure 3.15).

no.	Depth [km]	Resistivity [ $\Omega$ -m]	no.	Depth [km]	Resistivity [ $\Omega$ -m]
1	-1576	1.0e10	25	0.010	1.0
2	-590.1	1.0e10	26	0.025	1.0
3	-262.8	1.0e10	27	0.050	1.0
4	-153.5	1.0e10	28	0.100	1.0
5	-80.55	1.0e10	29	0.200	1.0
6	-31.95	1.0e10	30	0.400	1.0
7	-7.65	1.0e10	31	0.500	1.0
8	-2.250	1.0e10	32	0.600	1.0
9	-1.350	1.0e10	33	0.650	1.0
10	-1.200	1.0e10	34	0.700	100.0
11	-1.175	0.320	35	0.725	100.0
12	-1.150	0.320	36	0.750	100.0
13	-1.100	0.320	37	0.775	100.0
14	-1.000	0.320	38	0.800	1.0
15	-0.800	0.320	39	0.850	1.0
16	-0.500	0.320	40	0.900	1.0
17	-0.300	0.320	41	1.000	1.0
18	-0.200	0.320	42	1.300	1.0
19	-0.150	0.320	43	2.300	1.0
20	-0.100	0.320	44	3.800	1.0
21	-0.050	0.320	45	6.800	1.0
22	-0.025	0.320	46	10.80	1.0
23	-0.010	0.320	47	15.80	1.0
24	0.000	1.0	48	20.80	1.0

are the same vertical grid discretization that is used for the 3-D model. The reference 1-D data is represented by a solid black line in figure 3.16-3.19. Each figure consists of 6 data sets and 1 reference data. The first data set (u50) indicated by a diamond is the result when the spacing of a uniform grid is 50 m. The total number of grid points in the  $x$  and  $y$  directions is 208 and the number of model parameters is 2,076,672. The calculation time is 1 hour 44 minutes. The second data set (u100) indicated by a circle is the result when the spacing of the uniform grid is 100 m. The total number of grid points in the  $x$  and  $y$  directions is 108 and the number of model parameters is 559,872. The total calculation time is 28 minutes. The third one (u150) indicated by a plus is the result when the spacing of the uniform grid is 150 m. The total number of grid points in the  $x$  and  $y$  directions is 75 and the number of model parameters is 270,000. The total calculation time is 14 minutes. The fourth one (u200) indicated by a cross

is the result when the spacing is equal to 200 m. The total number of grid points in the  $x$  and  $y$  directions is 58 and the number of model parameters is 161,472. The total calculation time is 9 minutes. The fifth data set (u250) indicated by a square is the result when the spacing is equal to 250 m. The total number of grid points in the  $x$  and  $y$  directions is 48 and the number of model parameters is 110,592. The total calculation time is 6 minutes. The last data set (u500) indicated by a right-point triangle is the result when the spacing is equal to 500 m. The total number of grid points in the  $x$  and  $y$  directions is 28 and the number of model parameter is 37,632. The total calculation time is 2 minutes. The calculation time, the number of model parameter and grid for all these data sets are also summarized in table 3.2.

Table 3.2: The number of grid in  $x$  or  $y$  direction, the total number of model parameter and its calculation time for evaluating sounding curve for the synthetic model (figure 3.15).

	No. Grid	No. Model Parameter	CPU Time [min.]
<b>u50</b>	208	2,076,672	104
<b>u100</b>	108	559,872	28
<b>u150</b>	75	270,000	14
<b>u200</b>	58	161,472	9
<b>u250</b>	48	110,592	6
<b>u500</b>	28	37,632	2

Figure 3.16 represents the amplitude of the inline ( $x$ -direction) electric field for various uniform grids. Most of them can produce an accurate response when the offset is greater than 2 km. For a zero offset (transmitter above receiver), all of them cannot produce an accurate result. The minimum error at zero offset is about 71% evaluated by the 50m uniform grid. When offset increases, the relative error reduces and it is less than 1% when the offset is greater than 0.7 km for **u50**, 1.7 km for **u100** and **u150**, 2.5 km for **u200** and 2.7 km for **u250**. The relative error of **u500** is always greater than 1%. These situation also occurs in the other data types as shown in figure 3.17 for the phase of the inline electric field, figure 3.18 for the amplitude of broadside ( $y$ ) magnetic field and figure 3.19 for the phase of broadside magnetic field. The minimum distances of which the relative error is less than 1% or 2% are reported in table 3.3 and 3.4, respectively.

Although **u50** produces the most accurate result, its calculation time is greater than 1 hours for the forward modeling calculation and it is impractical for inversion. While **u500** spends only 2 minutes, its result is accurate when the offset is greater than 3 km. As discussed in the previous section, the information of the top layer sediment is measured in the offset 0-2.0 km for the inline ( $x$ ) electric field and

Table 3.3: The minimum offset of which its relative error is less than 1%. **Ex** is the inline electric field of which the sounding curves are represented in figure 3.16 for amplitude and figure 3.17 for phase. **By** is broadside magnetic field of which sounding curves are represented in figure 3.18 for amplitude and figure 3.19 for phase.

<b>Ex</b>	<b>u50</b>	<b>u100</b>	<b>u150</b>	<b>u200</b>	<b>u250</b>	<b>u500</b>
<b>Applitude</b>	> 0.7 km	> 1.7 km	> 1.7 km	> 2.5 km	> 2.7 km	-
<b>Phase</b>	> 0.6 km	> 1.1 km	> 1.1 km	> 1.6 km	> 1.7 km	-
<b>By</b>	<b>u50</b>	<b>u100</b>	<b>u150</b>	<b>u200</b>	<b>u250</b>	<b>u500</b>
<b>Applitude</b>	> 0.4 km	> 0.8 km	> 1.6 km	> 1.9 km	> 2.6 km	-
<b>Phase</b>	> 0.7 km	> 0.8 km	> 1.0 km	> 1.9 km	> 2.8 km	-

Table 3.4: The minimum offset for which its relative error is less than 2%. **Ex** is inline electric field of which the sounding curves are represented in figure 3.16 for amplitude and figure 3.17 for phase. **By** is broadside magnetic field of which sounding curves are represented in figure 3.18 for amplitude and figure 3.19 for phase.

<b>Ex</b>	<b>u50</b>	<b>u100</b>	<b>u150</b>	<b>u200</b>	<b>u250</b>	<b>u500</b>
<b>Applitude</b>	> 0.5 km	> 1.0 km	> 1.1 km	> 2.1 km	> 2.3 km	> 2.8 km
<b>Phase</b>	> 0.4 km	> 0.8 km	> 0.7 km	> 1.4 km	> 1.5 km	> 2.8 km
<b>By</b>	<b>u50</b>	<b>u100</b>	<b>u150</b>	<b>u200</b>	<b>u250</b>	<b>u500</b>
<b>Applitude</b>	> 0.4 km	> 0.6 km	> 1.1 km	> 1.3 km	> 1.7 km	-
<b>Phase</b>	> 0.6 km	> 0.8 km	> 0.9 km	> 1.3 km	> 1.6 km	-

0-1.3 km for the broadside ( $y$ ) magnetic field. With the 500m uniform grid, the top layer information is lost.

To solve the problem, we create two non-uniform grids based on the uniform grid study. The first and second grids are created based on the distances in table 3.3 and 3.4, respectively. The first non-uniform (**nu01**) grid consists of 94 grid points in  $x$  and  $y$  directions which are the 50m grid for 0-1.2 km, the 150m grid for 1.2-2.4 km, the 200m grid for 2.4-3.0 and the 250m grid for the remains. The total number of model parameters is 424,128. The amplitude and phase plot of the first non-uniform grid are shown in figure 3.20-3.23 as circles. The second non-uniform (**nu02**) grid consists of 88 grid points in  $x$  and  $y$  directions which are the 50m grid for 0-1.0 km, the 100m grid for 1.0-1.2 km, the 150m grid for 1.2-2.1 km, the 200m grid for 2.1-2.5 and the 250m grid for the remainders. Total number of model parameters is 371,712. The amplitude and phase plot of the second non-uniform grid are shown in figure 3.20-3.23 as pluses.

Both non-uniform grids take about 21 minutes to compute the response. Most of them fit quite well with the reference data. Their relative error is less than 2% when the offset is greater than or equal to 500 m. In figure 3.24-3.27, the relative error versus offset are plotted and the black solid lines represent 500m offset. Although both



non-uniform grids can reduce the number of model parameter and calculation time, the relative error at 0m offset is still about 71%. To solve this problem, we created a new non-uniform grid based on **nu02**. The new non-uniform (**nu03**) grid consists of 104 grid points in the  $x$  and  $y$  directions which are a 10m grid for 0-0.1 km for 0-100m, a 50m grid for 0.1-1.2 km, a 150m grid for 1.2-2.4 km, a 200m grid for 2.4-3.0 and a 250m grid for the remainders. The total number of model parameters is 519,168 and the CPU time is 26 minutes. Its amplitude and phase plot are shown in figure 3.20-3.23 and its relative errors are plotted in figure 3.24-3.27 as a right-point triangle.

By refining the grid between 0-0.1 km with a 10m grid, the relative errors of the inline electric field significantly reduce in 0.1-3.0 km as well. The maximum error is reduced from 71% to 4.3%. For the amplitude of broadside magnetic field, the relative errors increase after the grid is refined but they are less than 2% after 500m as shown in figure 3.26.

Following this study, the forward modeling can produce accurate results when the grid nearby the receiver is 10m. This is impractical for a real CSEM survey. For the real CSEM survey, the study area is greater than 10 km and it consists of numerous transmitters and receivers. The 100m and 150m grids are more practical than for a 10m grid, although they produce accurate results after 1.7 km. In the next section, we use a 100m grid model to test the reliability of the NLCG inversion.

### 3.8.2 Inversion

In this section, we test the reliability of 3D CSEM inversion with a two-blocks model which consists of one conductive (0.1  $\Omega$ -m) and one resistive (10  $\Omega$ -m) anomaly placed at the surface of a 1  $\Omega$ -m homogeneous sediment. The conductive anomaly is placed at south of the resistive anomaly as shown in figure 3.28. Both anomalies have the same horizontal and vertical dimensions which are  $1.2 \times 2.2 \times 0.4$  km. In this test, the two-blocks model is discretized with a 100m uniform grid in both N-S and E-W directions. The total number of grid points in the N-S or E-W direction is 32. For the vertical direction, the vertical grid in table 3.1 is used; therefore the total number of model parameters is 49,152.

In this test, 105 receivers are placed at the seafloor. A receiver is placed every 100 meters in the N-S direction and every 500 meters in the E-W direction as shown by white lines in figure 3.28a. In this simulation, three frequencies (0.25, 1, and 4 Hz) are used and the N-S horizontal-electric dipole is towed over with the leftmost, rightmost and mid lines of the receivers 50 meters from the seafloor. In each line, the transmitter generates an EM field every 200 m or 11 positions/line. The total number of data points is 5,148 (2079 for electric field in the N-S direction, 2079 for magnetic field in the E-W direction, 495 for electric field in the E-W direction and 495 for magnetic

field in the N-S direction).

NLCG inversion is used to inverse this data set. In these tests, we set the error bar as 1% of the data and we use a 1D homogenous sediment model as the prior model  $\mathbf{m}_{prior}$ . The initial RMS is about 200. NLCG inversion starts searching from  $\nu = 1.0$ . Inversion terminates after 10 iterations and it cannot reach the target RMS (1 RMS). The final RMS is about 22 and its inverse result is shown in figure 3.29. Resistive and conductive anomalies can be recovered by the inversion but the shapes and values are quite different from the actual model (figure 3.28). This might be an effect of the initial value of  $\nu$ . We try to vary the initial value  $\nu$  but most of them diverge. The result shown in figure 3.28 is the best result that NLCG inversion can do. This is the major disadvantage of NLCG inversion. For NLCG inversion, the convergent rate and inverted result strongly depend on  $\nu$ . To obtain reliable results from NLCG inversion, the inversion user has to manually vary  $\nu$  (Siripunvaraporn, 2012).

### 3.9 Conclusion

Here, we develop a 3-D CSEM forward modeling and inversion based on the scattered-field technique. All of the developments are done on the ModEM system. By applying the scattered-field technique to the ModEM system, we can develop an accurate 3-D CSEM forward modeling but a very fine grid near the receiver position is required. For the inversion, the NLCG algorithm coming with the ModEM system can function for 3-D CSEM data but it has stability concerns and it is not practical for real applications. All of this work is preliminary. To improve stability and reliability of 3-D CSEM modeling and inversion, further work is required.

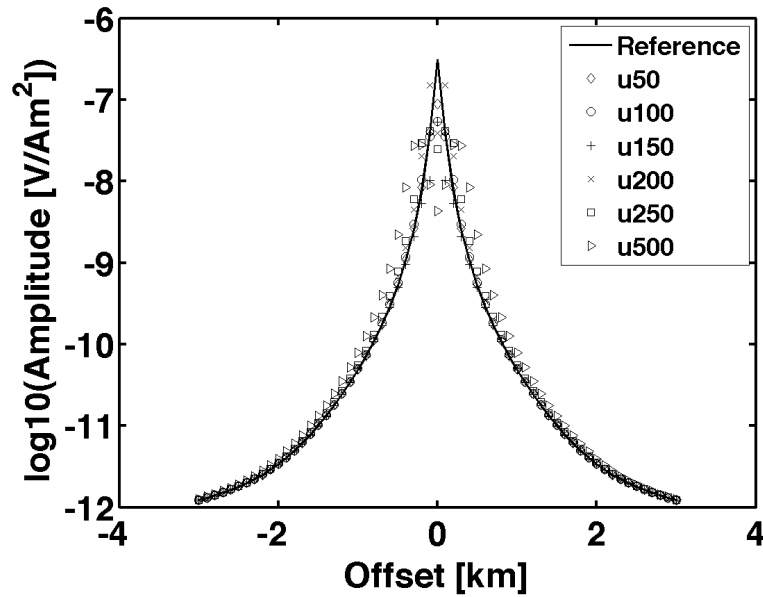


Figure 3.16: The amplitude of the inline ( $x$ ) electric field for the synthetic model (figure 3.15) when the 0.25 Hz  $x$ -direction horizontal electric dipole is towed at 50 meters above the seafloor receiver. The solid line is the reference data evaluated by the 1-D forward modeling program (Key, 2009), the diamond, circle, plus, cross, square and right-point triangle symbols are the numerical results from the 50m, 100m, 150m, 200m, 250m and 500m uniform grids, respectively.

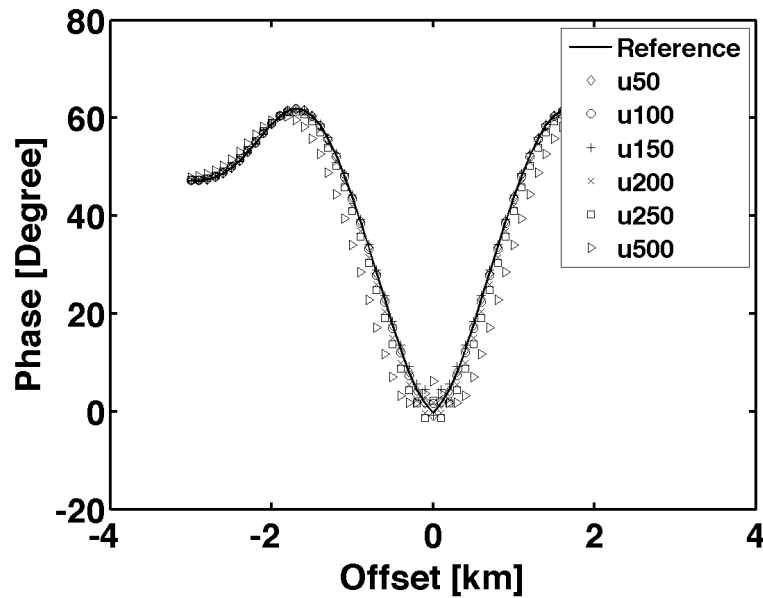


Figure 3.17: The phase of the inline ( $x$ ) electric field for the synthetic model (figure 3.15) when 0.25 Hz  $x$ -direction horizontal electric dipole is towed at 50 meters above the seafloor receiver. The solid line is the reference data evaluated by the 1-D forward modeling program (Key, 2009), the diamond, circle, plus, cross, square and right-point triangle symbols are the numerical results from the 50m, 100m, 150m, 200m, 250m and 500m uniform grids, respectively.

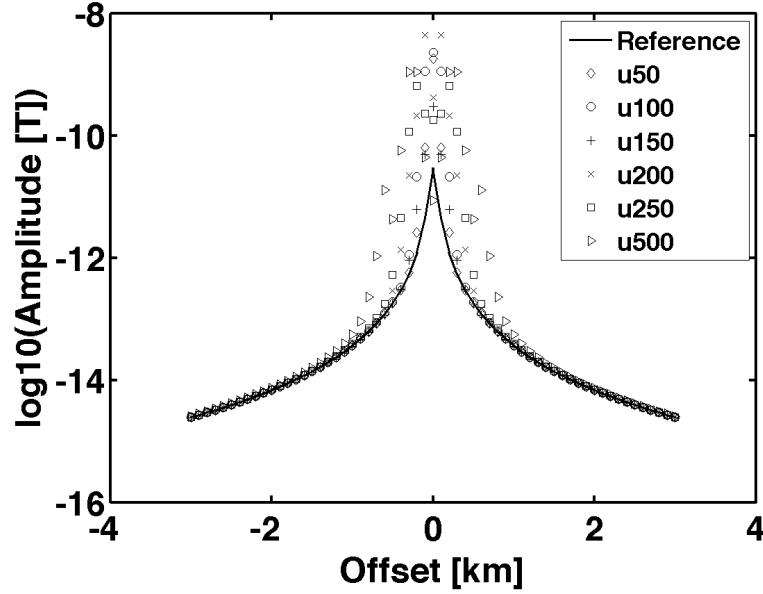


Figure 3.18: The amplitude of the broadside ( $y$ ) magnetic field for the synthetic model (figure 3.15) when 0.25 Hz  $x$ -direction horizontal electric dipole is towed at 50 meters above the seafloor receiver. The solid line is the reference data evaluated by the 1-D forward modeling program (Key, 2009), the diamond, circle, plus, cross, square and right-point triangle symbols are the numerical results from the 50m, 100m, 150m, 200m, 250m and 500m uniform grid model, respectively.

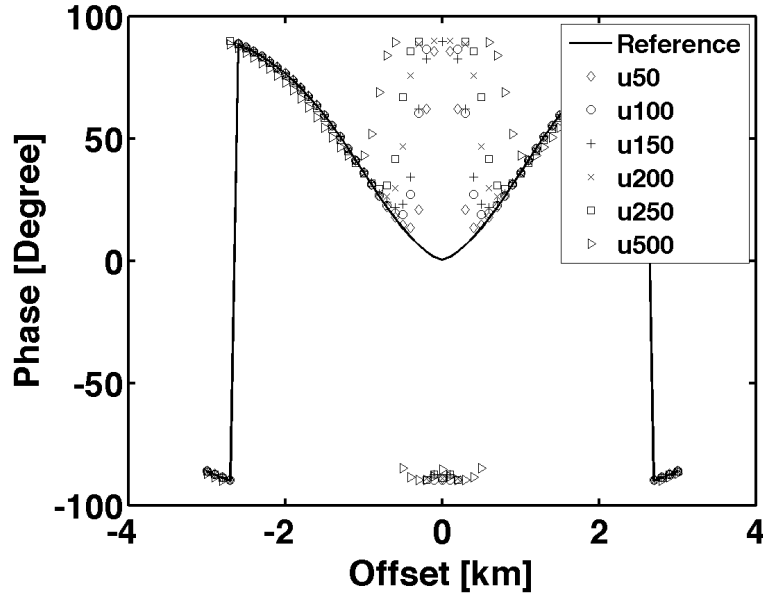


Figure 3.19: The phase of the broadside ( $y$ ) magnetic field for the synthetic model (figure 3.15) when the 0.25 Hz  $x$ -direction horizontal electric dipole is towed at 50 meters above the seafloor receiver. The solid line is the reference data evaluated by the 1-D forward modeling program (Key, 2009), the diamond, circle, plus, cross, square and right-point triangle symbols are the numerical results from the 50m, 100m, 150m, 200m, 250m and 500m uniform grids, respectively.

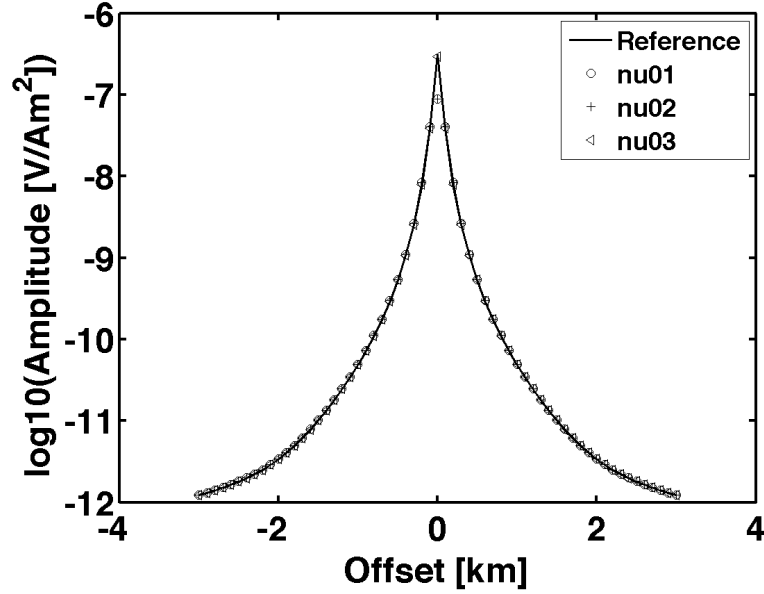


Figure 3.20: The amplitude of the inline ( $x$ ) electric field for the synthetic model (figure 3.15) when the 0.25 Hz  $x$ -direction horizontal electric dipole is towed at 50 meters above the seafloor receiver. The solid line is the reference data evaluated by the 1-D forward modeling program (Key, 2009), the circle, plus and left-point triangle symbols are the numerical results from the first, second and third non-uniform grids, respectively.

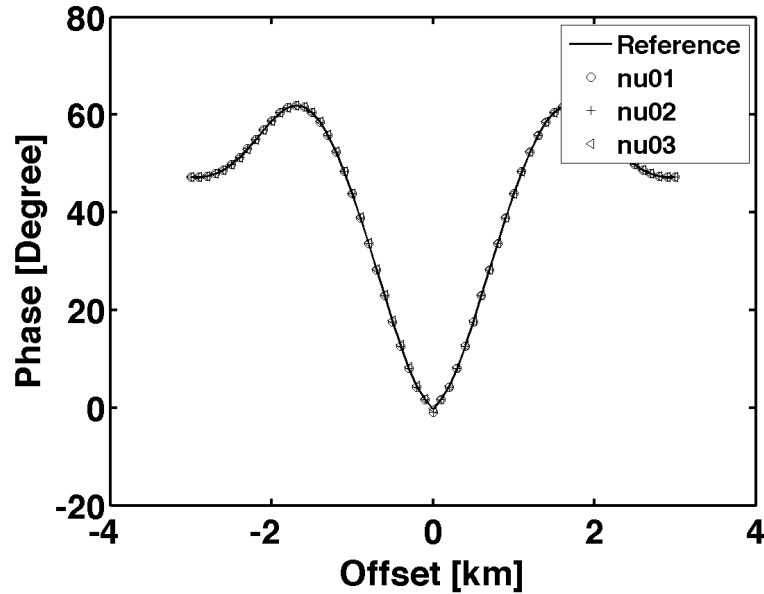


Figure 3.21: The phase of the inline ( $x$ ) electric field for the synthetic model (figure 3.15) when 0.25 Hz  $x$ -direction horizontal electric dipole is towed at 50 meters above the seafloor receiver. The solid line is the reference data evaluated by the 1-D forward modeling program (Key, 2009), the circle, plus and left-point triangle symbols are the numerical results from the first, second and third non-uniform grids, respectively.

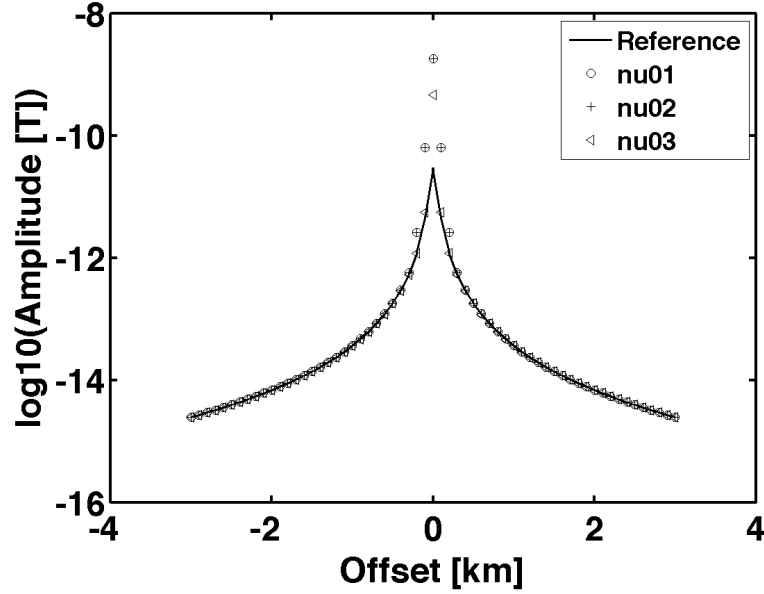


Figure 3.22: The amplitude of the broadside ( $y$ ) magnetic field for the synthetic model (figure 3.15) when 0.25 Hz  $x$ -direction horizontal electric dipole is towed at 50 meters above the seafloor receiver. The solid line is the reference data evaluated by the 1-D forward modeling program (Key, 2009), the circle, plus and left-point triangle symbols are the numerical results from the first, second and third non-uniform grids, respectively.

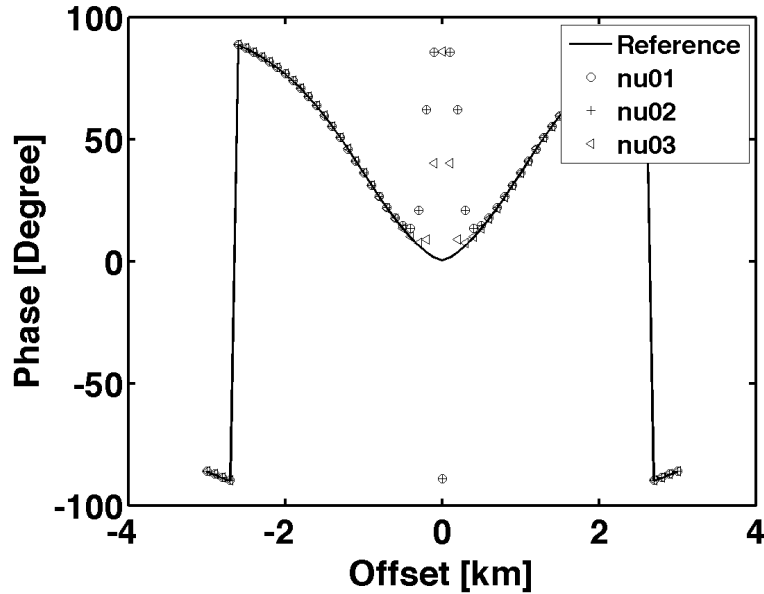


Figure 3.23: The phase of the broadside ( $y$ ) magnetic field for the synthetic model (figure 3.15) when 0.25 Hz  $x$ -direction horizontal electric dipole is towed at 50 meters above the seafloor receiver. The solid line is the reference data evaluated by the 1-D forward modeling program (Key, 2009), the circle, plus and left-point triangle symbols are the numerical results from the first, second and third non-uniform grids, respectively.

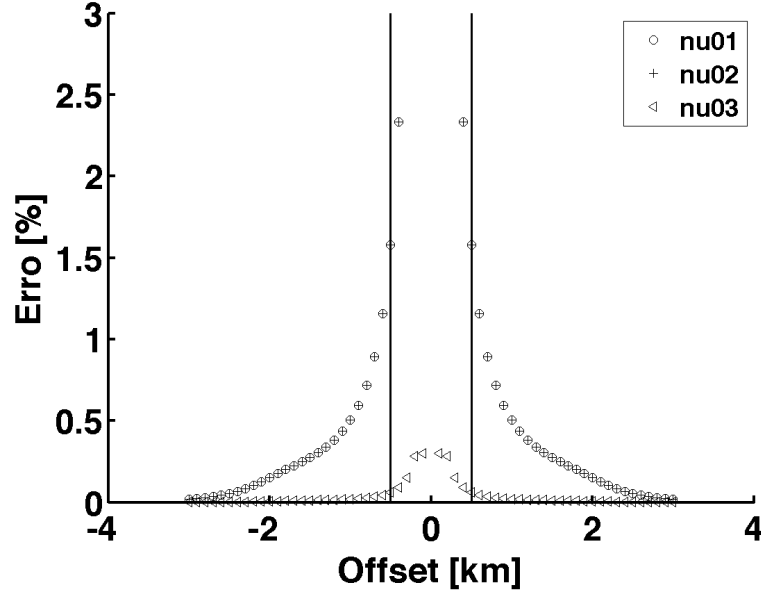


Figure 3.24: The error of the  $E_x$  amplitude for the synthetic model (figure 3.15) when 0.25 Hz  $x$ -direction horizontal electric dipole is towed at 50 meters above the seafloor receiver. The solid lines represent the 500m offset, the circle, plus and left-point triangle symbols are the numerical results from the first, second and third non-uniform grids, respectively.

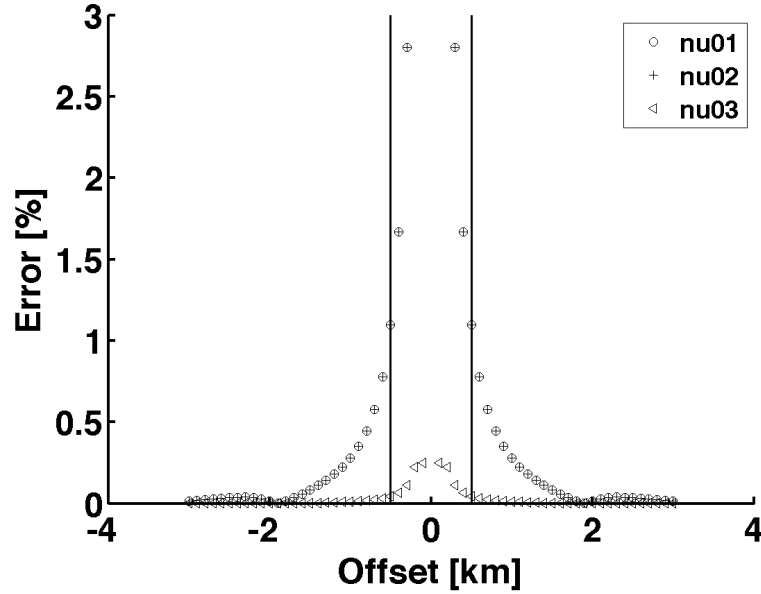


Figure 3.25: The error of the  $E_x$  phase for the synthetic model (figure 3.15) when 0.25 Hz  $x$ -direction horizontal electric dipole is towed at 50 meters above the seafloor receiver. The solid lines represent the 500m offset, the circle, plus and left-point triangle symbols are the numerical results from the first, second and third non-uniform grids, respectively.

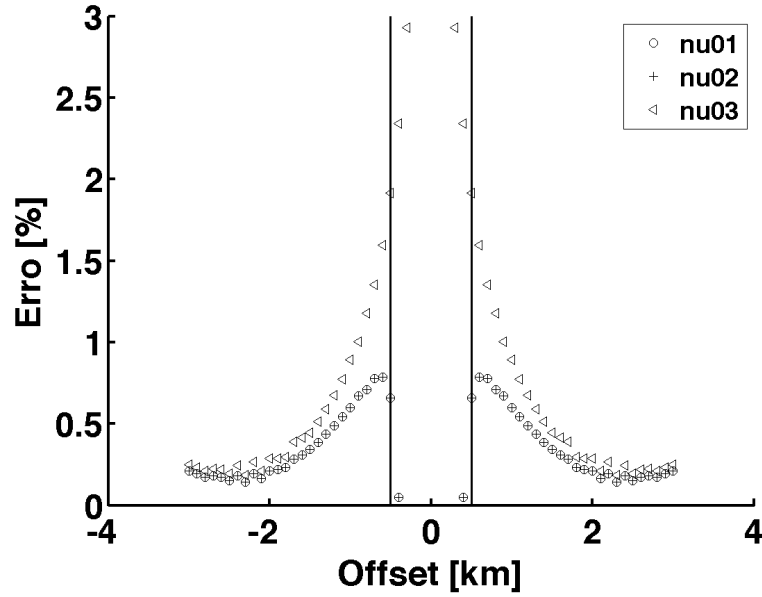


Figure 3.26: The error of the  $B_y$  amplitude for the synthetic model (figure 3.15) when 0.25 Hz  $x$ -direction horizontal electric dipole is towed at 50 meters above the seafloor receiver. The solid lines represent the 500m offset, the circle, plus and left-point triangle symbols are the numerical results from the first, second and third non-uniform grids, respectively.

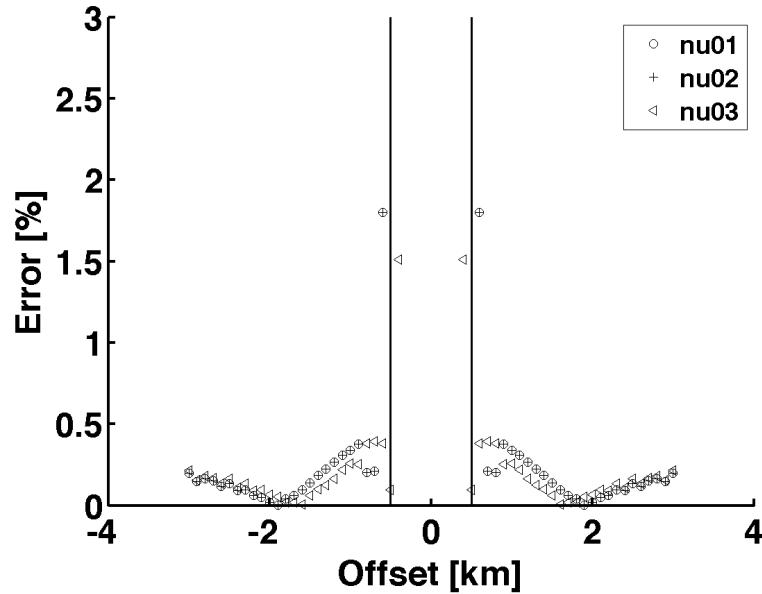


Figure 3.27: The error of the  $B_y$  phase for the synthetic model (figure 3.15) when 0.25 Hz  $x$ -direction horizontal electric dipole is towed at 50 meters above the seafloor receiver. The solid lines represent the 500m offset, the circle, plus and left-point triangle symbols are the numerical results from the first, second and third non-uniform grids, respectively.



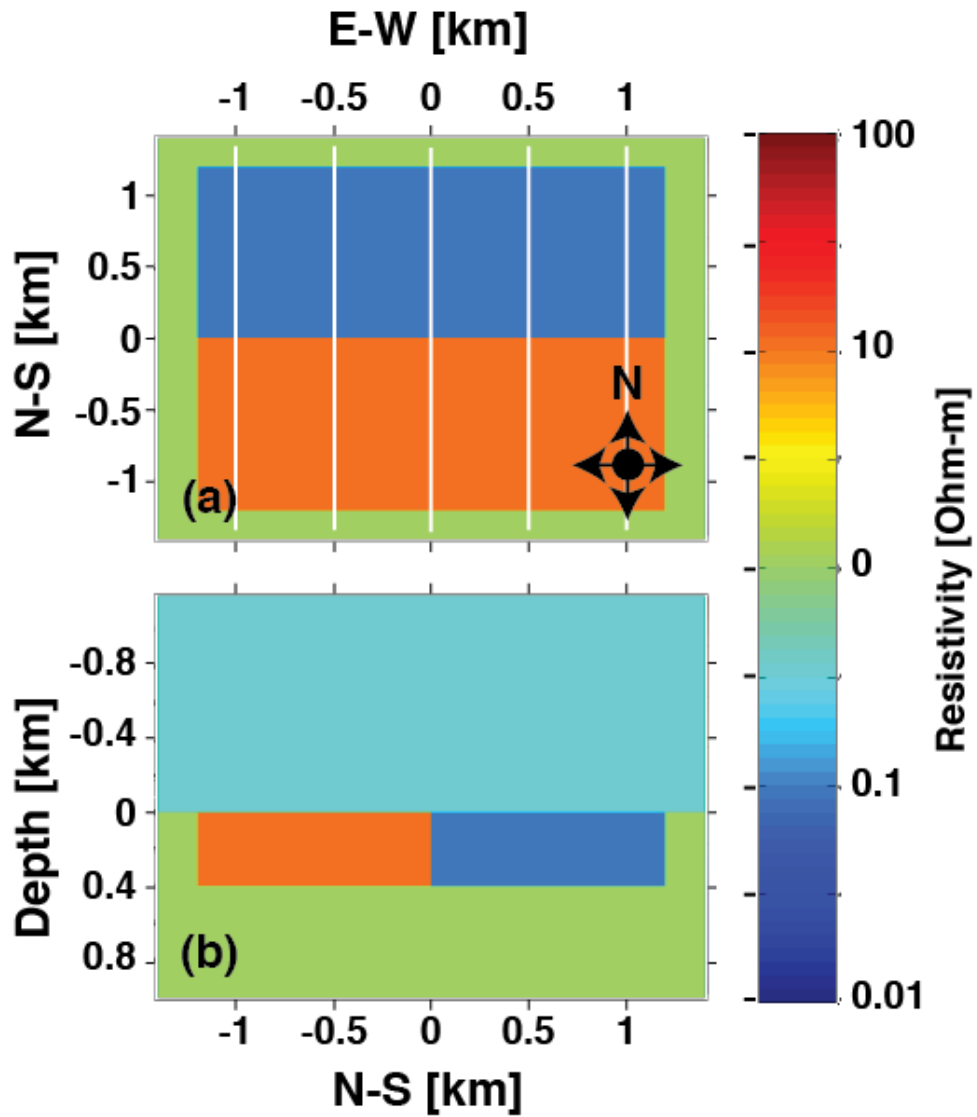


Figure 3.28: The two-blocks model for testing the reliability of CSEM inversion. The 0.1  $\Omega$ -m conductive and 10  $\Omega$ -m resistive anomalies are placed at the surface of 1  $\Omega$ -m sediment. The conductive anomaly is placed at the south of the resistive anomaly. Both anomalies have the same horizontal and vertical dimensions which are  $1.2 \times 2.2 \times 0.4$  km. The white lines in figure (a) represent the lines of the receiver.

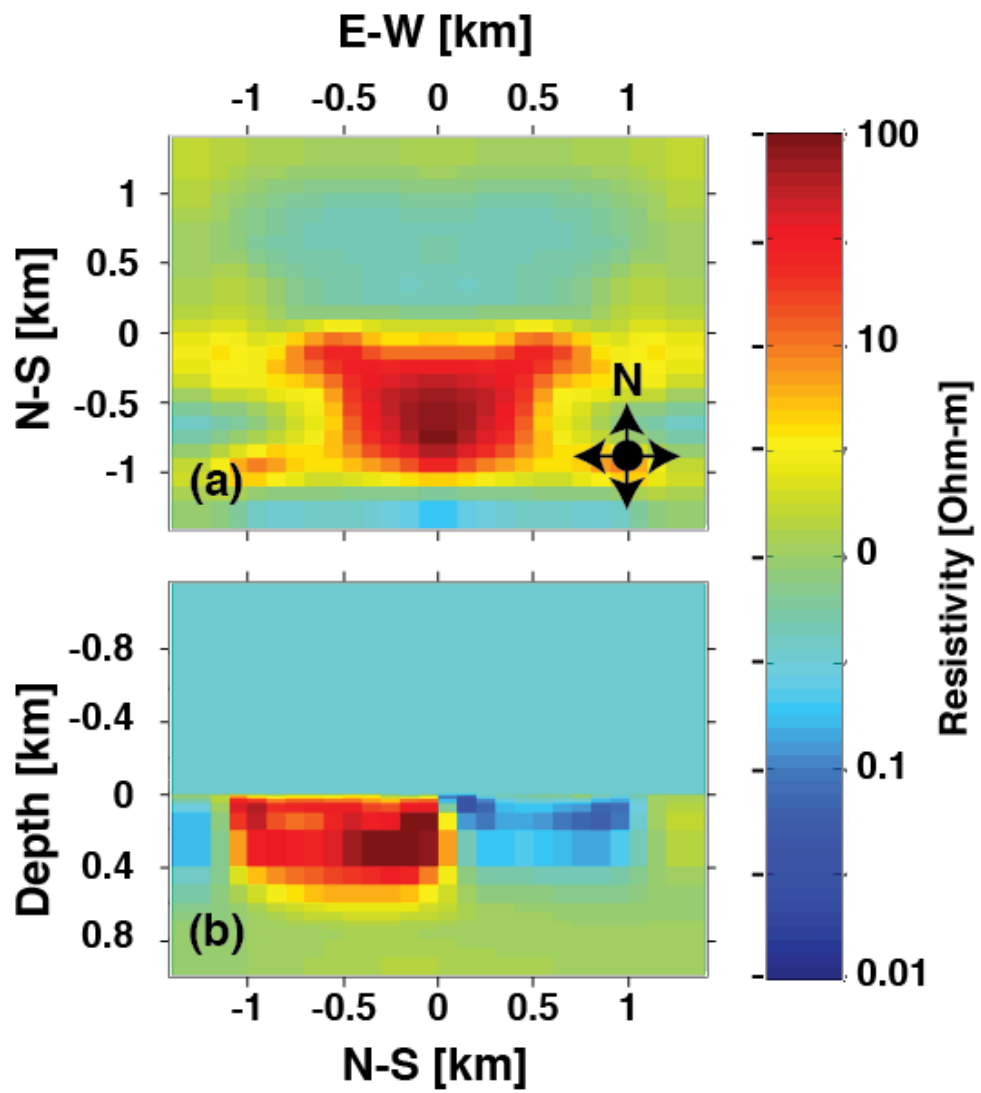


Figure 3.29: The inverted result is generated by NLCG inversion when  $\nu = 1.0$ .

## REFERENCES

- ALUMBAUGH, D. L., NEWMAN, G. A., PREVOST, L. & SHADID, J. N., 1996 “Three-Dimensional Wide Band Electromagnetic Modeling on Massively Parallel Computers,” *Radio Science* **31**, 1–23.
- ATHANASIOU, E., TSOURLOS, P., PAPAZACHOS, C. & TSOKAS, G., 2007 “Combined weighted inversion of electrical resistivity data arising from different array types,” *Journal of Applied Geophysics* **62**, 124–140.
- AVDEEV, D. B., 2005 “Three-dimensional electromagnetic modelling and inversion from theory to application,” *Surveys in Geophysics* **26**, 767–799.
- BABA, K. & SEAMA, N., 2002 “A new technique for the incorporation of seafloor topography in electromagnetic modeling,” *Geophysical Journal International* **150**, 392–402.
- BADEA, E. A., EVERETT, M. E., NEWMAN, G. A. & BIRO, O., 2001 “Finite-element analysis of controlled-source electromagnetic induction using Coulomb-gauged potentials,” *Geophysics* **66**, 786–799.
- BASTANI, M., SAVVAIDIS, A., PEDERSEN, L. B. & KALSCHUEER, T., 2011 “CSRMT measurements in the frequency range of 1-250 kHz to map a normal fault in the Volvi basin, Greece,” *Journal of Applied Geophysics* **75**, 180–195.
- BLOME, M., MAURER, H. & SCHMIDT, K., 2009 “Advances in three-dimensional geoelectric forward solver techniques,” *Geophysical Journal International* **176**, 740–752.
- BOONCHAIKUK, S., 2007 *Two-dimensional direct current resistivity inversion: finite element method*, Master’s thesis, Mahidol University.
- BOONCHAIKUK, S., SIRIPUNVARAPORN, W. & OGAWA, Y., 2013 “Evidence for middle Triassic to Miocene dual subduction zones beneath the Shan-Thai terrane, western Thailand from magnetotelluric data,” *Gondwana Research* **23**, 1607–1616.
- BOONCHAIKUK, S., VACHIRATIENCHAI, C. & SIRIPUNVARAPORN, W., 2008 “Two-dimensional direct current (dc) resistivity inversion: Data space Occam’s approach,” *Physics of the Earth and Planetary Interiors* **168**, 204 – 211.

- BROYDEN, C. G., 1965 “A Class of Methods for Solving Nonlinear Simultaneous Equations,” *Mathematics of Computation* **19**, 577–593.
- CHAMPAGNE II, N. J., BERRYMAN, J. G. & BUETTNER, H. M., 2001 “FDFD: A 3D finite-difference frequency-domain code for electromagnetic induction tomography,” *Journal of Computational Physics* **170**, 830–848.
- CHANG-HONG, L., HAN-DONG, T., QING, S., TUO, T. & JIA-YAN, T., 2012 “Three-dimensional conjugate gradient inversion of CSAMT data,” *Chinese Journal of Geophysics-Chinese Edition* **55**, 3829–3838.
- CHIANG, C.-W., GOTO, T.-N., CHEN, C.-C. & HSU, S.-K., 2011 “Efficiency of a Marine Towed Electrical Resistivity Method,” *Terrestrial Atmospheric and Oceanic Sciences* **22**, 443–446.
- CHIANG, C.-W., GOTO, T.-N., MIKADA, H., CHEN, C.-C. & HSU, S.-K., 2012 “Sensitivity of Deep-Towed Marine Electrical Resistivity Imaging Using Two-Dimensional Inversion: A Case Study on Methane Hydrate,” *Terrestrial Atmospheric and Oceanic Sciences* **23**, 725–732.
- CHRISTIANSEN, A. & AUKEN, E., 2004 “Optimizing a layered and laterally constrained 2D inversion of resistivity data using Broyden’s update and 1D derivatives,” *Journal of Applied Geophysics* **56**, 247–261.
- COGGON, J., 1971 “Electromagnetic and electrical modeling by the finite element method,” *Geophysics* **36**, 132–155.
- COMMER, M. & NEWMAN, G. A., 2008 “New advances in three-dimensional controlled-source electromagnetic inversion,” *Geophysical Journal International* **172**, 513–535.
- CONSTABLE, S., 2010 “Ten years of marine csem for hydrocarbon exploration,” *Geophysics* **75**, 75A67–75A81.
- CONSTABLE, S. & SRNKA, L. J., 2007 “An introduction to marine controlled-source electromagnetic methods for hydrocarbon exploration,” *Geophysics* **72**, WA3–WA12.
- CONSTABLE, S. C., PARKER, R. L. & CONSTABLE, C. G., 1987 “Occam’s inversion: A practical algorithm for generating smooth models from electromagnetic sounding data,” *Geophysics* **52**, 289–300.

- DEGROOT-HEDLIN, C. & CONSTABLE, S., 1990 "Occam's inversion to generate smooth, two-dimensional models from magnetotelluric data," *Geophysics* **55**, 1613–1624.
- DEY, A. & MORRISON, H. F., 1979 "Resistivity modeling for arbitrarily shaped two-dimensional structures," *Geophysical Prospecting* **27**, 106–136.
- DONADILLE, J.-M. & AL-OFI, S. M., 2012 "Crosswell electromagnetic response in a fractured medium," *Geophysics* **77**, D53–D61.
- EDWARDS, N., 2005 "Marine controlled-source electromagnetics: Principles, methodologies, future commercial applications," *Surveys in Geophysics* **26**, 675–700.
- EGBERT, G., BENNETT, A. F. & FOREMAN, M. G., 1994 "Topex/poseidon tides estimated using a global inversion model," *Journal of Geophysical Research: Oceans* **99**, 24821–24852.
- EGBERT, G. D. & KELBERT, A., 2012 "Computational recipes for electromagnetic inverse problems," *Geophysical Journal International* **189**, 251–267.
- ELLIS, R. G. & OLDENBURG, D. W., 1994 "The pole-pole 3-d dc-resistivity inverse problem: a conjugate-gradient approach," *Geophysical Journal International* **119**, 187–194.
- ERDOGAN, E., DEMIRCI, I. & CANDANSAYAR, M. E., 2008 "Incorporating topography into 2d resistivity modeling using finite-element and finite-difference approaches," *Geophysics* **73**, F135–F142.
- FLETCHER, R. & REEVES, C. M., 1964 "Function minimization by conjugate gradients," *Comput J* **7**, 149–154.
- FOX, R., HOHMANN, G., KILLPACK, T. & RIJO, L., 1980 "Topographic effects in resistivity and induced-polarization surveys," *Geophysics* **45**, 75–93.
- GABÀS, A., 2003 *Nous aspects metodològics en l'exploració elèctrica I electromagnètica, de la Universitat de Barcelona*.
- GALIS, M., MOCZO, P. & KRISTEK, J., 2008 "A 3-d hybrid finite-difference–finite-element viscoelastic modeling of seismic wave motion," *Geophysical Journal International* **175**, 153–184.
- GOTO, T.-N., KASAYA, T., MACHIYAMA, H., TAKAGI, R., MATSUMOTO, R., OKUDA, Y., SATOH, M., WATANABE, T., SEAMA, N., MIKADA, H., SANADA, Y. & KINOSHITA, M., 2008 "A marine deep-towed DC resistivity survey in a methane hydrate area, Japan Sea," *Exploration Geophysics* **39**, 52–59.

- GRANDIN, H., 1991 *Fundamentals of the Finite Element Method*. (Waveland).
- GREENHALGH, B. Z. G. A., S.A., 2006 “Solutions, algorithms and inter-relations for local minimization search geophysical inversion,” *Journal of Geophysics Engineering* **3**, 101–113.
- GRIBENKO, A. & ZHDANOV, M., 2007 “Rigorous 3d inversion of marine csem data based on the integral equation method,” *Geophysics* **72**, WA73–WA84.
- GRIFFITHS, D. H. & TURNBULL, J., 1985 “A multi-electrode array for resistivity surveying,” *First Break* **3**, 16–20.
- GRIFFITHS, D. H., TURNBULL, J. & OLAYINKA, A. I., 1990 “Two-dimensional resistivity mapping with a computer-controlled array,” *First Break* **8**, 121–129.
- HA, T., PYUN, S. & SHIN, C., 2006 “Efficient electric resistivity inversion using adjoint state of mixed finite-element method for Poisson’s equation,” *Journal of Computational Physics* **214**, 171–186.
- HABER, E. & ASCHER, U. M., 2001 “Fast finite volume simulation of 3D electromagnetic problems with highly discontinuous coefficients,” *SIAM Journal of Scientific Computing* **22**, 1943–1961.
- HABER, E., ASCHER, U. M., ARULIAH, D. A. & OLDENBURG, D. W., 2000 “Fast simulation of 3D electromagnetic problems using potentials,” *Journal of Computational Physics* **163**, 150–171.
- HESTHAMMER, J. & BOULAENKO, M., 2005 “The offshore EM challenge,” *First Break* **23**, 59–66.
- HESTHAMMER, J., STEFATOS, A., BOULAENKO, M., VERESHAGIN, A., GELTING, P., WEDBERG, T. & MAXWELL, G., 2010 “Csem technology as a value driver for hydrocarbon exploration,” *Marine and Petroleum Geology* **27**, 1872 – 1884.
- HOVERSTEN, G., MILLIGAN, P., BYUN, J., WASHBOURNE, J., KNAUER, L. & HARNESS, P., 2004 “Crosswell electromagnetic and seismic imaging: An examination of coincident surveys at a steam flood project,” *Geophysics* **69**, 406–414.
- HOVERSTEN, G., NEWMAN, G., MORRISON, H., GASPERIKOVA, E. & BERG, J., 2001 “Reservoir characterization using crosswell electromagnetic inversion: A feasibility study for the Snorre field, North Sea,” *Geophysics* **66**, 1177–1189.

- JIANFENG, Z. & TIELINM, L., 2002 “Elastic wave modeling in 3d heterogeneous media: 3d grid method.” *Geophysical Journal International* **150**, 780–799.
- KALSCHEUER, T., HUEBERT, J., KUVSHINOV, A., LOCHBUEHLER, T. & PEDERSEN, L. B., 2012 “A hybrid regularization scheme for the inversion of magnetotelluric data from natural and controlled sources to layer and distortion parameters,” *Geophysics* **77**, E301–E315.
- KALSCHEUER, T., JUANATEY, M., MEQBEL, N. & PEDERSEN, L., 2010 “Non-linear model error and resolution properties from two-dimensional single and joint inversions of direct current resistivity and radiomagnetotelluric data,” *Geophysical Journal International* **182**, 1174–1188.
- KELBERT, A., EGBERT, G. D. & SCHULTZ, A., 2008 “Non-linear conjugate gradient inversion for global EM induction: resolution studies,” *Geophysical Journal International* **173**, 365–381.
- KEY, K., 2009 “1d inversion of multicomponent, multifrequency marine csem data: Methodology and synthetic studies for resolving thin resistive layers,” *Geophysics* **74**, F9–F20.
- KIM, H. J., SONG, Y., LEE, K. H. & WILT, M. J., 2004 “Efficient crosswell EM Tomography using localized nonlinear approximation,” *Exploration Geophysics* **35**, 51–55.
- LABRECQUE, D. & WARD, S., 1990 “Two-dimensional cross-borehole resistivity model fitting. In: S. Ward (Ed.),” *Geotechnical and Environmental Geophysics* **1**, 51–57.
- LI, M., ABUBAKAR, A. & HABASHY, T. M., 2010 “Application of a two-and-a-half dimensional model-based algorithm to crosswell electromagnetic data inversion,” *Inverse Problems* **26**.
- LI, Y. & OLDENBURG, D. W., 1994 “Inversion of 3-d dc resistivity data using an approximate inverse mapping,” *Geophysical Journal International* **116**, 527–537.
- LI, Y. & SPITZER, K., 2002 “Three-dimensional dc resistivity forward modeling using finite elements in comparison with finite-difference solutions,” *Geophysical Journal International* **151**, 924–934.
- LOKE, M. H., 2000 “Tutorial: 2-d and 3-d electrical imaging surveys,” .

- LOKE, M. H. & BARKER, R. D., 1996 "Rapid least-squares inversion of apparent resistivity pseudosections by a quasi-newton method," *Geophysical Prospecting* **44**, 131–152.
- LOKE, M. H. & DAHLIN, T., 1997 "A combined gauss-newton and quasi-newton inversion method for the interpretation of apparent resistivity pseudosections," in *3rd Meeting of the European Association for Environmental and Engineering Geophysics*, pp. 139–142 (Aarhus, Denmark).
- LOKE, M. H. & DAHLIN, T., 2002 "A comparison of gauss-newton and quasi-newton inversion method in resistivity imaging inversion," *Journal of Applied Geophysics* **49**, 149–162.
- MA, Q., 2002 "The boundary element method for 3-d dc resistivity modeling in layered earth," *Geophysics* **67**, 610–617.
- MACKIE, R. L., MADDEN, T. R. & WANNAMAKER, P. E., 1993 "Three-dimensional magnetotelluric modeling using difference equations - Theory and comparisons to integral equation solutions," *Geophysics* **58**, 215–226.
- MACKIE, R. L., SMITH, J. T. & MADDEN, T. R., 1994 "Three-dimensional electromagnetic modeling using finite difference equations: The magnetotelluric example," *Radio Science* **29**, 923–935.
- MCGILLIVRAY, P. & OLDENBURG, D., 1990 "Methods for calculating Frechet derivatives and sensitivities for the non-linear inverse problem: a comparative study," *Geophysical Prospecting* **38**, 499–524. Cited By (since 1996) 73.
- MILSOM, J., 2003 *Field Geophysics*, The geological field guide series, third edn. (Wiley).
- NEWMAN, G. A. & ALUMBAUGH, D. L., 1995 "Frequency-domain modelling of airborne electromagnetic responses using staggered finite differences," *Geophysical Prospecting* **43**, 1021–1041.
- NEWMAN, G. A. & ALUMBAUGH, D. L., 1997 "Three-Dimensional Massively Parallel Electromagnetic Inversion-I., Theory," *Geophysical Journal International* **128**, 345–354.
- NEWMAN, G. A. & ALUMBAUGH, D. L., 2000 "Three-dimensional magnetotelluric inversion using non-linear conjugate gradient," *Geophysical Journal International* **140**, 410–424.



- NEWMAN, G. A. & BOGGS, P. T., 2004 "Solution accelerators for large-scale three-dimensional electromagnetic inverse problems," *Inverse Problems* **20**, S151–S170.
- NEWMAN, G. A. & BOGGS, P. T., 2005 "Solution accelerators for large-scale three-dimensional electromagnetic inverse problems," *Inverse Problems* **20**, S151–S170.
- NEWMAN, G. A., COMMER, M. & CARAZZONE, J. J., 2010 "Imaging csem data in the presence of electrical anisotropy," *Geophysics* **75**, F51–F61.
- OKABE, M., 1981 "Boundary element method for the arbitrary inhomogeneities problem in electrical prospecting," *Geophysical Prospecting* **29**, 39–59.
- OLAYINKA, A. & YARAMANCI, U., 2000 "Use of block inversion in the 2-D interpretation of apparent resistivity data and its comparison with smooth inversion," *Journal of Applied Geophysics* **45**, 63–81.
- OLDENBURG, D. & LI, Y., 1994 "Inversion of induced polarization data," *Geophysics* **59**, 1327–1341.
- PAIN, C., HERWANGER, J., WORTHINGTON, M. & DE OLIVEIRA, C., 2002 "Effective multidimensional resistivity inversion using finite element techniques," *Geophysical Journal International* **151**, 710–728.
- PARDO, D., TORRES-VERDÍN, C. & ZHANG, I. Z., 2008 "Sensitivity study of borehole-to-surface and crosswell electromagnetic measurements acquired with energized steel casing to water displacement in hydrocarbon-bearing layers," *Geophysics* **73**, F261–F268.
- PARKER, R. L., 1994 *Geophysical Inverse Theory* (Princeton University Press, Princeton, New Jersey).
- PIDLISECKY, A. & KNIGHT, R., 2008 "FW2.5D: a MATLAB 2.5-D electrical resistivity modeling code," *Computers and Geosciences* **34**, 1645–1654.
- PLESSIX, R.-E. & MULDER, W. A., 2008 "Resistivity imaging with controlled-source electromagnetic data: depth and data weighting," *Inverse Problems* **24**.
- POLAK, E. & RIBIÈRE, 1969 "Note sur la convergence de directions conjuguées," *Rev. Francaise Informat Recherche Opertionelle* **16**, 35–43.
- PRESS, W. H., TEUKOLSKY, S. A., VETTERLING, W. T. & FLANNERY, B. P., 1992 *Numerical Recipes in Fortran: the art of scientific computing*, 2 edn. (Cambridge University Press).

- QIAN, W. & PEDERSEN, L., 1992 “A new controlled source tensor array system,” *Journal of Applied Geophysics* **29**, 64 – 65.
- RODI, W. & MACKIE, R. L., 2001 “Nonlinear conjugate gradients algorithm for 2-D magnetotelluric inversion,” *Geophysics* **66**, 174–187.
- RÜCKER, C., GÜNTHER, T. & SPITZER, K., 2006 “Three-dimensional modeling and inversion of dc resistivity data incorporating topography. i. modelling,” *Geophysical Journal International* **166**, 495–505.
- SANTOS, F. & EL-KALIOUBY, H., 2011 “Quasi-2D inversion of DCR and TDEM data for shallow investigations,” *Geophysics* **76**, F239–F250.
- SASAKI, Y., 1994 “3-d resistivity inversion using the finite element method,” *Geophysics* **55**, 1839–1848.
- SHARMA, P. V., 1997 *Environmental and Engineering Geophysics* (Cambridge University Press, Cambridge, U.K., New York, USA).
- SIMPSON, C. T., M.J., 2003 “Comparison of finite difference and finite element solutions to the variably saturated flow equation,” *Journal of Hydrology* **270**, 49–64.
- SIRIPUNVARAPORN, W., 2012 “Three-Dimensional Magnetotelluric Inversion: An Introductory Guide for Developers and Users,” *Surveys in Geophysics* **33**, 5–27. 20th Workshop on Electromagnetic Induction in the Earth, Giza, EGYPT, SEP 18-24, 2010.
- SIRIPUNVARAPORN, W. & EGBERT, G., 2000 “An efficient data-subspace inversion method for 2-d magnetotelluric data,” *Geophysics* **65**, 791–803.
- SIRIPUNVARAPORN, W. & EGBERT, G., 2007 “Data space conjugate gradient inversion for 2-d magnetotelluric data,” *Geophysical Journal International* **170**, 986–994.
- SIRIPUNVARAPORN, W., EGBERT, G. & LENBURY, Y., 2002 “Numerical accuracy of magnetotelluric modeling: A comparison of finite difference approximations,” *Letter Earth Planets Space* **54**, 721–725.
- SIRIPUNVARAPORN, W., EGBERT, G., LENBURY, Y. & UYESHIMA, M., 2005 “Three-dimensional magnetotelluric inversion: data-space method,” *Physics of the Earth and Planetary Interiors* **150**, 3–14.

- SIRIPUNVARAPORN, W., UYESHIMA, M. & EGBERT, G., 2004 "Three-dimensional inversion for network-magnetotelluric data," *Earth Planets Space* **56**, 893–902.
- SMITH, J. T., 1996 "Conservative modeling of 3-D electromagnetic fields, Part II: Biconjugate gradient solution and an accelerator," *Geophysics* **61**, 1319–1324.
- STANLEY, W. D., MOONEY, W. D. & FUIS, G. S., 1990 "Deep crustal structure of the cascade range and surrounding regions from seismic refraction and magnetotelluric data," *J. Geophys. Res.* **95**, 19419–19438.
- STREICH, R., 2009 "3d finite-difference frequency-domain modeling of controlled-source electromagnetic data: Direct solution and optimization for high accuracy," *Geophysics* **74**, F95–F105.
- SUN, Z., SUN, J. & ZHANG, D., 2009 "2d dc electric field numerical modeling including surface topography using coordinate transformation method," *Journal of Jilin University(Earth Science Edition)* **39**, 528–534.
- TELFORD, W. M., GELDART, L. P. & SHERIFF, R. E., 1990 *Applied Geophysics*, 2nd edn. (Cambridge University Press).
- TONG, L. & YANG, C., 1990 "Incorporation of topography into 2-d resistivity inversion," *Geophysics* **55**, 354–361.
- TSOURLES, P., SYMANSKI, J. & TOSKAS, G., 1999 "The effect of terrain topography on commonly used resistivity arrays," *Geophysics* **64**, 1357–1363.
- TSOURLOS, P. I., SZYMANSKI, J. E. & TSOKAS, G. N., 1998 "A smoothness constrained algorithm for the fast 2-d inversion of dc resistivity and induced polarization data," *Journal of The Balkan Geophysics Society* **1**, 3–13.
- ULUGERGERLI, E., 2011 "Two dimensional combined inversion of short- and long-normal dc resistivity well log data," *Journal of Applied Geophysics* **73**, 130–138.
- UYESHIMA, M. & SCHULTZ, A., 2000 "Geomagnetic induction in a heterogeneous sphere: a new three-dimensional forward solver using a conservative staggered-grid finite difference method," *Geophysical Journal International* **140**, 636–650.
- VACHIRATIENCHAI, C., 2007 *Two-dimensional direct current resistivity inversion: finite difference method*, Master's thesis, Mahidol University.

- VACHIRATIENCHAI, C., BOONCHAIKUK, S. & SIRIPUNVARAPORN, W., 2010 "A hybrid finite difference-finite element method to incorporate topography for 2d direct current (dc) resistivity modeling," *Physics of the Earth and Planetary Interiors* **183**, 426 – 434.
- VACHIRATIENCHAI, C. & SIRIPUNVARAPORN, W., 2010 "Hybrid Finite Difference-Finite Element Inversion for two-dimensional direct current resistivity data," in *5th International Conference on Applied Geophysics* (Phuket, Thailand).
- VACHIRATIENCHAI, C. & SIRIPUNVARAPORN, W., 2013 "An efficient inversion for two-dimensional direct current resistivity surveys based on the hybrid finite difference-finite element method," *Physics of the Earth and Planetary Interiors* **215**, 1–11.
- WANG, R., YIN, C., WANG, M. & WANG, G., 2012 "Simulated annealing for controlled-source audio-frequency magnetotelluric data inversion," *Geophysics* **77**, E127–E133.
- WARD, S. H., 1990 "Geotechnical and environmental geophysics," *Investigations in Geophysics* **5**, 147–189.
- WEI, B. J., ZHENG, G. J. & ZENG, W. C., 1999 "The iterative inversion algorithm in Crosswell electromagnetic imaging," *Chinese Journal of Geophysics-Chinese Edition* **42**, 711–719.
- WEISS, C. J. & CONSTABLE, S., 2006 "Mapping thin resistors and hydrocarbons with marine EM methods, Part II - Modeling and analysis in 3D," *Geophysics* **71**, G321–G332.
- WEISS, C. J. & NEWMAN, G. A., 2002 "Electromagnetic induction in a fully 3D anisotropic earth," *Geophysics* **67**, 1104–1114.
- WU, G., HU, X., HUO, G. & ZHOU, X., 2012 "Geophysical Exploration for Geothermal Resources: An Application of MT and CSAMT in Jiangxia, Wuhan, China," *Journal of Earth Science* **23**, 757–767.
- XU, S.-Z., DUAN, B.-C. & ZHANG, D.-H., 2000 "Selection of the wavenumbers  $k$  using an optimization method for the inverse fourier transform in 2.5d electrical modelling," *Geophysical Prospecting* **48**, 789–796.
- XU, S.-Z., ZHAO, S. & NI, Y., 1998 "A boundary element method for 2-d dc resistivity modeling with a point current source," *Geophysics* **63**, 399–404.

- YEE, K., 1966 “Numerical solution of initial boundary value problems involving maxwell’s equations in isotropic meida,” *IEEE Transactions on Antennas and Propagation* **14**, 3022–307.
- YUN-FENG, X. & JI-FENG, Z., 2011 “Three dimensional controlled source electromagnetic numerical simulation based on the rock properties of the west line of South-to-North Water Diversion Project using Finite Element Method,” *Chinese Journal of Geophysics-Chinese Edition* **54**, 2160–2168.
- ZHANG, J., MACKIE, R. L. & MADDEN, T. R., 1995 “3-D resistivity forward modeling and inversion using conjugate gradients,” *Geophysics* **60**, 1313–1325.
- ZHAO, S. & YEDLIN, M., 1996 “Some refinements on the finite-difference method for 3-d dc resistivity modeling,” *Geophysics* **61**, 1301–1307.
- ZIENKIEWICZ, O. & CHEUNG, Y., 1965 “Finite element in the solution of field problems,” *The Engineer* **220**, 507–510.

## BIOGRAPHY

<b>NAME</b>	Mr. Chatchai Vachiratienchai
<b>DATE OF BIRTH</b>	29 <sup>th</sup> August 1982
<b>PLACE OF BIRTH</b>	Bangkok, Thailand
<b>INSTITUTIONS ATTENDED</b>	Mahidol University, 2000-2004 Bachelor of Science (Physics) Mahidol University, 2004-2007 Master of Science (Physics) Mahidol University, 2008-2013 Doctor of Philosophy (Physics)
<b>SCHOLARSHIPS</b>	Teaching assistant, Mahidol University, 2008-2009 Research assistant, Royal Golden Jubilee, 2009-2013
<b>HOME ADDRESS</b>	14, Phet Kasem 48, Bangwa, Khet Phasi Charoen, Bangkok, Thailand, 10160
<b>E-MAIL</b>	chatchai.vac@gmail.com